



TECHNISCHE UNIVERSITÄT MÜNCHEN

Fakultät für Physik

Lehrstuhl für Topologie korrelierter Systeme

**Low-temperature properties
and magnetic structure of
 CrB_2 , MnB_2 , and CuMnSb**

Dipl.-Phys. Univ. Alexander Regnat

Vollständiger Abdruck der von der
Fakultät für Physik der Technischen Universität München
zur Erlangung des akademischen Grades eines

Doktors der Naturwissenschaften (Dr. rer. nat.)

genehmigten Dissertation.

Vorsitzender: Prof. Dr. Frank Pollmann

Prüfer der Dissertation: 1. Prof. Dr. Christian Pfleiderer
2. Prof. Dr. Christian Back

Die Dissertation wurde am 29.11.2018 an der Technischen Universität München eingereicht
und durch die Fakultät für Physik am 10.07.2019 angenommen.

Abstract	1
Local-Moment versus Itinerant Magnetism	3
1 Experimental Methods	7
1.1 Crystal Growth and Samples	7
1.1.1 Preparation of Polycrystalline CrB ₂	7
1.1.2 Single Crystal Growth of CrB ₂ and MnB ₂	8
1.1.3 Single Crystal Growth of CuMnSb	9
1.1.4 Samples	10
1.2 Apparatus for High-Pressure Experiments	11
1.2.1 Piston-cylinder Cell	16
1.2.2 Uniaxial Pressure Cell	17
1.2.3 Bridgman Pressure Cell	18
1.2.4 Data Treatment	24
1.2.5 Pressure Determination	25
1.3 Low-temperature Bulk and Transport Measurements	29
1.3.1 Adiabatic Demagnetization Refrigeration	29
1.3.2 Electrical Resistivity and Hall Effect	32
1.3.3 Magnetization	33
1.3.4 Heat Capacity	33
1.4 X-ray and Neutron Diffraction	33
1.4.1 X-ray Diffraction	34
1.4.2 Powder Neutron Diffraction	34
1.4.3 Single Crystal Neutron Diffraction	34
1.4.4 Polarized Neutron Scattering	35

1.5	Representation Analysis and Magnetic Structure Refinement	37
1.5.1	The Superspace Approach to Modulated Structures	37
1.5.2	Magnetic Structure Refinement from Diffraction Data	40
2	The Weak Itinerant Antiferromagnet CrB₂	43
2.1	Introduction to C32 diborides	43
2.2	Introduction to CrB ₂	44
2.3	Nuclear Structure of CrB ₂	50
2.3.1	Powder X-Ray Diffraction	50
2.3.2	Single Crystal X-Ray Diffraction	53
2.3.3	Polarized Single Crystal Neutron Diffraction	53
2.3.4	Discussion	56
2.3.5	Summary	57
2.4	Magnetic Structure of CrB ₂	58
2.4.1	Powder Neutron Diffraction	58
2.4.2	Single Crystal Neutron Diffraction at RESI	60
2.4.3	Single Crystal Neutron Diffraction at HEiDi	63
2.4.4	Representation Analysis and Magnetic Structure Refinement	68
2.4.5	Discussion of the Non-trivial Topology of the Triple-k Structures	77
2.4.6	Summary	85
2.5	Low-temperature Bulk and Transport Properties of CrB ₂	87
2.5.1	Magnetization	87
2.5.2	Specific Heat	89
2.5.3	Electrical Resistivity and Hall Effect	91
2.5.4	Discussion	95
2.5.5	Summary	99
2.6	High-pressure Transport Properties of CrB ₂	99
2.6.1	Piston-cylinder and Uniaxial Pressure Cells	99
2.6.2	Bridgman Cells	105
2.6.3	Discussion	113
2.6.4	Summary	117
2.7	Conclusions	118

3	The Local Moment Antiferromagnet MnB₂	119
3.1	Introduction to MnB ₂	119
3.2	Nuclear Structure of MnB ₂	122
3.2.1	Powder X-Ray Diffraction	122
3.2.2	Polarized Single Crystal Neutron Diffraction	125
3.3	Magnetic Structure of MnB ₂	127
3.3.1	Powder Neutron Diffraction	128
3.3.2	Single Crystal Neutron Diffraction	131
3.3.3	Representation Analysis and Magnetic Structure Refinement	132
3.4	Low-temperature Bulk Properties of MnB ₂	138
3.4.1	Specific Heat	138
3.4.2	AC Susceptibility	139
3.4.3	Magnetization	140
3.4.4	Electrical Resistivity and Hall Effect	142
3.5	Summary	144
 4	 The Half-Heusler Antiferromagnet CuMnSb	 147
4.1	Introduction to Heusler Compounds	147
4.2	Introduction to CuMnSb	149
4.3	Low-temperature Bulk and Transport Properties of CuMnSb	152
4.3.1	AC Susceptibility	152
4.3.2	Specific Heat	152
4.3.3	Magnetization	154
4.3.4	Electrical Resistivity and Hall Effect	159
4.4	Nuclear Structure of CuMnSb	162
4.4.1	Powder X-ray and Neutron Diffraction	162
4.4.2	Polarized Neutron Scattering	164
4.5	Magnetic Structure of CuMnSb	167
4.5.1	Representation Analysis	168
4.5.2	Powder Neutron Diffraction	170
4.5.3	Single Crystal Neutron Diffraction	173
4.6	Summary	182
 Conclusions		 185
 Acknowledgments		 187
 Bibliography		 206

Abstract

The low-temperature bulk and transport properties as well as the nuclear and magnetic structure of three metallic antiferromagnets - CrB_2 , MnB_2 , and CuMnSb - are studied using single-crystals grown from high-purity starting elements. For all compounds measurements of the magnetization, ac susceptibility, specific heat, resistivity, Hall effect, and the x-ray and neutron scattering are reported. Further, high-pressure resistivity data of CrB_2 are presented.

Kurzzusammenfassung

Die Tieftemperaturvolumen- und -transporteigenschaften von drei metallischen Antiferromagneten - CrB_2 , MnB_2 und CuMnSb - werden anhand von einkristallinen Proben, die aus hochreinen Ausgangselementen synthetisiert wurden, untersucht. Für alle Verbindungen werden Messungen der Magnetisierung, der Wechselfeldsuszeptibilität, der spezifischen Wärme, des spezifischen Widerstands und Hall-Effekts sowie der Röntgen- und Neutronenstreuung berichtet. Ferner werden Widerstandsdaten von CrB_2 unter hohem Druck präsentiert.

Contents

Local-Moment versus Itinerant Magnetism

Historically the magnetic properties of condensed matter are explained from two diametrically opposed points of view. In a local-moment picture they are derived from the magnetic attributes of the individual magnetic atoms, i.e., they are constructed from electronic states that are localized in real space. In contrast, in the itinerant electron scenario, which may be applied to magnetic metals, their description starts from electronic states which are localized in reciprocal space and the magnetic properties are derived from the Fermi surface.

In transition metals and transition metal compounds the orbital angular momentum of the d electrons tends to be quenched due to crystalline electric fields and the (partial) covalency. In a local-moment description the magnetic properties of the d electrons should hence be determined by the total spin quantum number S . Due to the overlap of their orbitals, however, the d electrons usually possess an itinerant character. Consequently, their atomic spin is no longer well-defined and the applicability of a local-moment description is questionable.

The example of d -electron metals and their alloys illustrates a dichotomy and long-standing issue which has inspired numerous experimental and theoretical investigation, namely as to whether metallic magnetism is better accounted for by the local-moment or itinerant electron treatment. It turned out that actually many real metals exhibit a combination of properties which are either characteristic of local-moment or itinerant magnetism. Particularly all elemental d -electron ferromagnets display a mixture of features which have been attributed to either model.

Historically, the following observations were believed to be hallmarks of local-moment magnetism

- (i) A Curie-Weiss temperature dependence of the susceptibility in the paramagnetic regime,
- (ii) atomic magnetic form factors which compare to the free atoms, and
- (iii) well-defined spin wave excitation.

This was believed to be contrasted in itinerant electron magnets by

- (i) a low-temperature magnetization which is unsaturated even in high magnetic fields,
- (ii) a reduced, non-integer ordered moment, and
- (iii) a spin split Fermi surface.

The discovery and extensive investigation of so-called weak itinerant ferromagnets - such as ZrZn_2 , MnSi , and Ni_3Al - finally helped to resolve this seeming inconsistency. Starting from the 1960's novel theories established that the local-moment properties observed in this material class and in the elemental ferromagnets are attributed to spin fluctuations of the itinerant electrons. By taking into account these spin fluctuations in a self-consistent way MORIYA and LONZARICH provided a new mechanism which was based on the variance of the local magnetization rather than on fluctuating local moments. Their theoretical approach accounted for the paramagnetic Curie-Weiss susceptibility. Moreover, their model yielded a good quantitative agreement with experimental observations, e.g., the Curie temperature T_C and the ratio of the ordered and the effective fluctuating moment m_{eff}/m_s [1, 2]. Owing to this considerable progress the importance of spin fluctuations for the magnetic properties of archetypical itinerant magnets is nowadays widely accepted.

Archetypical local-moment magnetism has been identified in a variety of magnetic insulators and a profound understanding of the exchange mechanisms - such as direct exchange, double exchange, and superexchange - has been established. Empirically it was found that the Heisenberg model of local magnetic moments can be successfully applied to many real materials, including also magnetic metals. However, magnetic metals at the border of local-moment magnetism are still poorly understood.

The properties of metals at the border of magnetism have been addressed within the DFG-funded research framework "Transregional Collaborative Research Center TRR80: From Electronic Correlations to Functionality". The work reported as part of this thesis has been carried out as part of the TRR80 project "Stabilizing Magnetic Order under Extreme Conditions" and focuses on the structural and magnetic properties of three magnetic metals, namely CrB_2 , MnB_2 , and CuMnSb .

For a classification of these material either as local-moment, itinerant electron, or intermediate magnets a comprehensive understanding of their magnetic properties is required. Therefore investigations of the low-temperature bulk and transport properties were carried out. Neutron diffraction was employed to determine the ordered magnetic moment as well as the long-range magnetic order of all three compounds. As in many magnetic materials crystalline imperfections and magnetic impurities may easily conceal or alter the intrinsic magnetic properties, high-quality single crystal samples were examined. Their nuclear structures were confirmed and carefully checked for putative short-range ordering of defects by means of diffuse neutron scat-

tering. Finally, the evolution of the properties in one compound, CrB_2 , has been studied as a function of pressure by means of the electrical resistivity.

This thesis is organized as follows. Chapter 1 introduces the experimental methods used as part of the studies reported here and gives an account on the sample preparation and the samples studied. Several measurements carried out as part of this thesis required extensive further development of existing devices. Thus novel high-pressure equipment such as Moissanite-anvil Bridgman cells and a ruby fluorescence pressure gauge have been set up. Furthermore strong effort has been put into the optimization of a cryogen-free demagnetization refrigerator. The mains aspects of this technical work are also briefly summarized in Chapter 1.

Chapter 2 gives a short introduction into the physics of the C32 metal diborides. This material class contains several d - and f -electron based diborides which exhibit the same layered hexagonal structure. It therefore allows to investigate a cornucopia of electronic and magnetic ground states with their fundamental excitations in an overall unchanged crystallographic environment. Two compounds studied as part of this thesis, CrB_2 and MnB_2 crystallize in the C32 nuclear lattice.

Chapter 2 then reports on the investigations of CrB_2 . Low-temperature bulk and transport measurements of high-quality single crystal material establish weak itinerant antiferromagnetism par excellence. This finding is corroborated by the small ordered moment and the complex incommensurate cycloidal spin structure observed in magnetic neutron diffraction. The latter may be understood in terms of an triple-k state on a triangular Cr lattice. Its analysis suggests a highly non-trivial topology which is characterized by 120° spin correlations and the formation of a \mathbb{Z}_2 vortex crystal candidate. In a comprehensive series of high-pressure transport measurements finally the stability of the itinerant magnetic order in CrB_2 is studied. Measurements using hydrostatic, uniaxial, and quasi-hydrostatic pressure conditions suggest that the electronic and magnetic properties of CrB_2 are essentially determined by the ratio of the hexagonal lattice parameters. As $T_N = 89\text{ K}$ is suppressed using moderate quasi-hydrostatic pressure an incipient electronic instability, presumably superconductivity, is revealed.

Chapter 3 covers the studies of the first large single crystals of MnB_2 . Their residual resistivity is characteristic of a good metal and corroborates a high crystalline quality. Magnetic neutron diffraction of powder and single crystal specimens suggest commensurate local-moment antiferromagnetism with a extraordinary high Néel temperature, $T_N \approx 1130\text{ K}$. The long-range spin order is characterized by ferromagnetically coupled hexagonal Mn layers which mutually couple antiferromagnetically. The Mn moment initially lie within the hexagonal planes but are canted at $T_{\text{flop}} \approx 130\text{ K}$ resulting in a net ferromagnetic moment. This spin-flop transition is consistent with the bulk measurements which show a significant enhancement of the magnetization and the ac susceptibility as well as a ferromagnetic hysteresis below T_{flop} . Finally, specific heat data corroborate weak electronic correlation, hence supporting the local-moment picture.

Chapter 4 reports on the investigations of the very first single crystal samples of the half-Heusler compound CuMnSb . Due to the high chemical miscibility of their constituents Heuslers are

prone to crystalline defects and antisite-disorder. These imperfections of the nuclear lattice may easily conceal or alter the intrinsic electronic and magnetic properties of Heusler compounds. Therefore in the study of CuMnSb two single crystal ingots grown from a stoichiometric and Sb-rich initial composition, respectively, were examined. Consistent with previous reports the crystal grown from a stoichiometric mixture of starting elements contained a small amount of the ferrimagnetic impurity phase Mn_2Sb . In contrast the second ingot turned out to be phase-pure and was studied extensively employing bulk, transport, and diffraction measurements. These experiments strongly suggest local-moment antiferromagnetism with $T_N = 55$ K and pronounced spin fluctuation even at temperature far above T_N . Distinct anomalies were observed at $T^* \approx 34$ K in essentially all properties studied. Based on our magnetic neutron scattering data these features were attributed to a canting of the large, almost integer Mn moments which above T^* form a type-II antiferromagnetic lattice and point along $\langle 111 \rangle$ directions. Below T^* the moments tilt by about 11° . Magnetization measurements show that the canting is not associated with a net ferromagnetic moment, hence suggesting that antiferromagnetically coupled Mn spins cant in opposite directions. This finding is in excellent agreement with theoretical investigations of the magnetic ground state of defect-free CuMnSb.

Finally, [4.6](#) summarizes the main experimental results and conclusions reported in this thesis.

1.1 Crystal Growth and Samples

1.1.1 Preparation of Polycrystalline CrB₂

As part of this thesis polycrystalline samples of CrB₂ were studied to determine their crystal structure and lattice parameters by means of x-ray and neutron scattering. All polycrystalline samples were prepared by GEORG BENKA as part of his Ph.D. thesis. Here only the most important aspects of the manufacturing process are mentioned. The reader is referred to Refs. [3, 4] for further details.

The synthesis of polycrystalline CrB₂ started from a stoichiometric mixture of high purity elements, viz. pellets of 5N Cr and coarse powder of 5N B. 98 % isotopically enriched ¹¹B was used to reduce absorption during neutron scattering experiments. The starting materials were placed in an all-metal sealed arc melting furnace. Then the vacuum chamber of the arc melter was pumped to ultra-high vacuum for 12-18 hours. Finally the mixture was molten under a high purity inert gas atmosphere (9N Ar) by means of a plasma arc. A lanthanum-doped tungsten welding electrode was employed to light up the plasma arc. For a uniform temperature profile the arc was constantly moved over the molten zone. After the plasma arc was turned off the melt cooled down within a few minutes and finally solidified thereby forming a shiny, metallic batch as shown in Fig. 1.1f and Fig. 1.1g. To maximize its homogeneity the latter was subsequently molten and solidified several times.

The polycrystalline CrB₂ batches were studied using scattering techniques (powder x-ray diffraction and powder neutron diffraction) in order to analyze their stoichiometric composition. As will be reported in Sec. 2.4.1 all arc-melted samples studied consisted mainly of CrB₂ (65 % to

95 %). The sample fractions which did not crystallize in the CrB_2 target phase were identified as Cr_3B_4 and CrB . Despite the presence of these impurity phases our polycrystalline samples allowed to determine the nuclear structure and lattice parameters of the CrB_2 target phase.

1.1.2 Single Crystal Growth of CrB_2 and MnB_2

As part of this thesis single crystal samples of CrB_2 and MnB_2 were studied with respect to their nuclear and magnetic structure using x-ray and neutron diffraction. Furthermore low-temperature bulk and transport measurements as well as high-pressure transport measurements of the same single crystals were carried out.

All CrB_2 and MnB_2 single crystals studied have been synthesized by ANDREAS BAUER as part of his Ph.D. thesis. A detailed description of the single crystal growth has been reported in Ref. [5]. In the following the most important steps of the production process are summarized.

High purity starting elements were used for the preparation of both materials. 4N5 Cr powder with 4N5 B powder and 4N Mn powder prepared from pre-cast rods with 4N5 B powder were chosen for the synthesis of CrB_2 and MnB_2 , respectively. To allow for comprehensive neutron scattering investigations 99.9% ^{11}B -enriched B powders were used in both cases. First, stoichiometric amounts of the powders were mixed and filled into a bespoke tungsten crucible. The crucibles were inductively heated under an inert gas (Ar) atmosphere. Sintered metallic rods of CrB_2 and MnB_2 formed by an exothermic solid state reaction at $T \approx 1500^\circ\text{C}$ and $T \approx 1300^\circ\text{C}$, respectively. They had a relatively low density, e.g., $\sim 2.6 \text{ g cm}^{-3}$ for CrB_2 which corresponds to $\sim 50\%$ of crystalline CrB_2 . The sintering procedure was repeated to obtain several rods which in the case of CrB_2 were directly used as seed and feed rods for the subsequent single crystal growth. An intermediate step was added for MnB_2 where the relatively low melting temperature of $\sim 2000^\circ\text{C}$ allowed to melt and cast the sinters into seed and feed rods of higher density.

For the single crystal growth of both materials an optical float-zone technique using a high-pressure furnace (Smart Floating Zone, SFZ) at IFW Dresden was employed. To reduce the loss of B the melt was exposed to a flowing inert gas (Ar) atmosphere of 15 bar to 18 bar pressure. Two ingots of CrB_2 , SFZ-118 and SFZ-162, and one ingot of MnB_2 , SFZ-158, were prepared this way. Laue x-ray diffraction was used to ensure that the float-zoned ingots were single crystals and to identify the crystalline axis along which the ingot was grown. In contrast to CrB_2 which grew along its hexagonal c axis, the growth direction of MnB_2 was found to be along an a axis. While the cross-section of the MnB_2 ingot was significantly flattened along the c axis x-ray Laue diffraction confirmed that the c axis rotated by $\sim 4^\circ$ along the $\sim 10 \text{ mm}$ of the single crystal. Photographs of the crystals and typical Laue x-ray images are shown in Fig. 1.1.

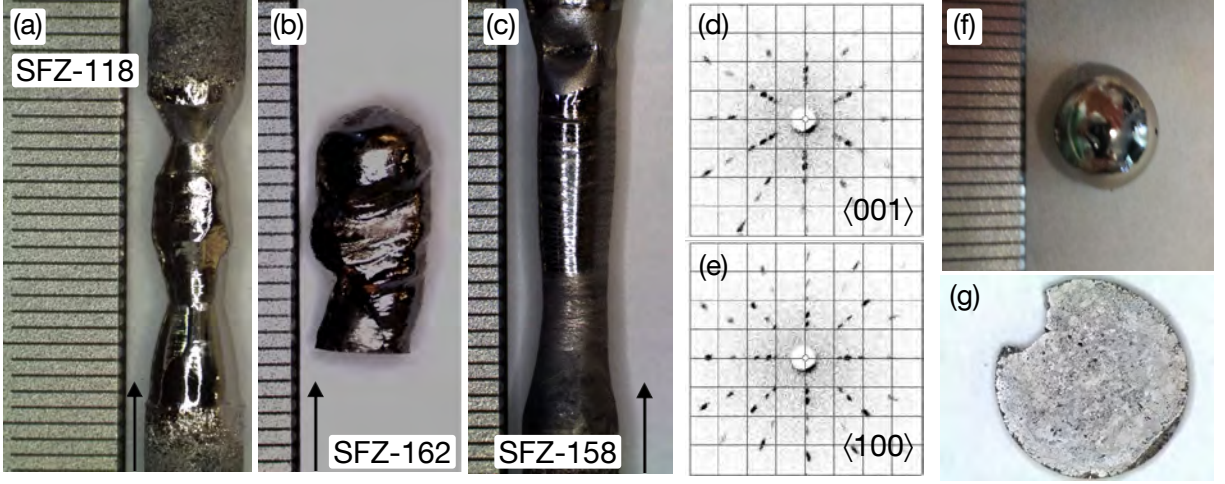


Figure 1.1: Crystal growth of CrB_2 and MnB_2 . (a) Float-zoned single crystal CrB_2 , ingot SFZ-118. (b) Float-zoned single crystal CrB_2 , ingot SFZ-162. (c) Float-zoned single crystal MnB_2 , ingot SFZ-158. (d,e) Typical Laue x-ray diffraction of hexagonal diborides, here CrB_2 . A sixfold and twofold symmetry are observed along the c -axis ($\langle 001 \rangle$) and a -axis ($\langle 100 \rangle$), respectively. (f) Polycrystalline batch of CrB_2 prepared by arc-melting. (g) Cut through the batch. The uniform appearance suggest a rather high crystalline homogeneity.

1.1.3 Single Crystal Growth of CuMnSb

As part of this thesis x-ray and neutron scattering of single crystal CuMnSb were carried out to analyze its nuclear and magnetic structure. Moreover, the low-temperature bulk and transport measurements of the same single crystal samples were examined.

All single crystal CuMnSb studied was synthesized by ANDREAS BAUER as part of his Ph.D. thesis using the preparation chain and apparatus described in Ref. [5]. In a first step the high-purity starting elements - 6N copper pieces, pre-cast 4N manganese rods, and 6N antimony shots - were inductively heated and cast into polycrystalline feed and seed rods using a rod-casting furnace. Subsequently, a float-zone technique using an optical furnace (Optical Floating Zone, OFZ) at TUM was employed to prepare single crystal from the casted rods. To minimize the oxygen contamination of the ingot the float-zoning was carried out under a flowing inert gas (Ar) atmosphere.

The growth procedure was carried out two times: While a stoichiometric initial mixture of starting elements was chosen for the first growth attempt the second growth attempt was performed using a starting composition with 3.5 % Sb excess. The single crystals grown are denoted OFZ-75 and OFZ-98, respectively (cf. Tab. 1.3). For consistency with Ref. [5] these crystals are referred to as CuMnSb-A and CuMnSb-B , respectively.

A detailed metallurgical characterization was carried out in order to determine the crystalline composition and quality of both ingots. As reported in Ref. [5] powder x-ray diffraction with

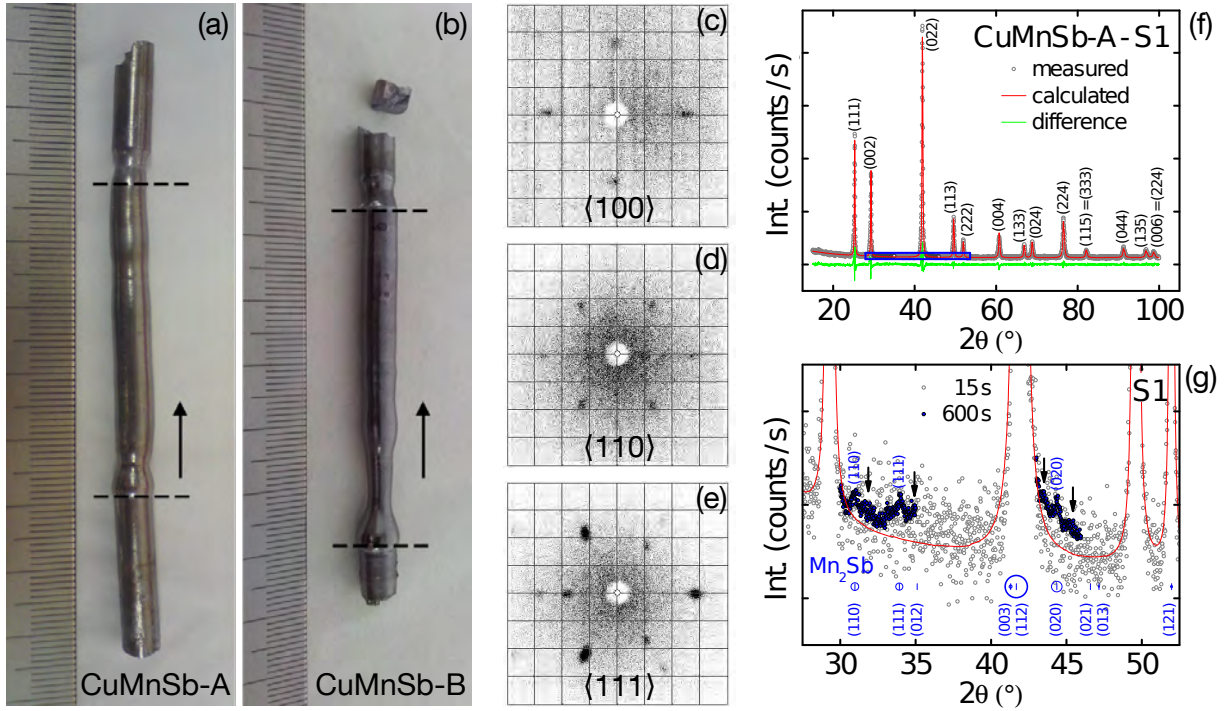


Figure 1.2: Single crystal growth of CuMnSb. (a) Float-zoned single crystal CuMnSb as grown from stoichiometric feed rods, referred to as CuMnSb-A. (b) Float-zoned single crystal CuMnSb grown from an initial weight with an Sb excess of 0.035, referred to as CuMnSb-B. Arrows indicate the growth direction. Vertical dashed lines mark the beginning and end of the float-zoning. (c)-(e) Laue x-ray diffraction of CuMnSb-A along high symmetry directions. As expected for a cubic structure fourfold, twofold and threefold diffraction patterns are observed for the $\langle 100 \rangle$, $\langle 110 \rangle$, and $\langle 111 \rangle$ direction, respectively. (f) X-ray powder diffraction of CuMnSb-A. A Rietveld refinement corroborates the $C1_b$ structure. (g) At long exposure times tiny amounts of Mn_2Sb (blue) and a further unidentified impurity phase (black arrows) are resolved. Figure adapted from Ref. [5].

very long exposure times was performed in order to resolve even tiny amounts of impurity phases. These measurements suggest the presence of a small volume fraction ($< 1\%$) of Mn_2Sb in the first ingot, CuMnSb-A. In contrast, the crystal which was grown from a slightly off-stoichiometric initial weight, CuMnSb-B, turned out to be phase-pure. This is consistent with a report by ENDO ET AL. [6, 7] who showed that during the single crystal growth of CuMnSb a small Sb excess in the initial weight effectively prevents the formation of Mn_2Sb without changing the lattice parameters of the target phase, i.e., of CuMnSb.

1.1.4 Samples

Tab. 1.1 through Tab. 1.3 summarize the samples examined. In the first column the abbreviations “SC” and “PC” denote single crystal and polycrystalline material, respectively. The

1.2 Apparatus for High-Pressure Experiments

sample names given in the second column indicate the preparation procedure, where “AMP” denotes a polycrystalline batch prepared by arc-melting and both “SFZ” and “OFZ” indicate single crystal samples prepared by optical float-zoning using the “Smart Floating Zone furnace” (IFW Dresden) and “Optical Floating Zone furnace” (TUM), respectively. As concerns the single crystal specimens, the sample names moreover allow to infer the part of the ingot from which the sample was cut using the sample maps shown in Fig. 1.3.

The abbreviations “XRD” and “ND” mean x-ray and neutron diffraction, respectively. “pc”, “ux”, and “bc” refer to three types of pressure cells, namely piston-cylinder cell, uniaxial pressure cells, and Bridgman pressure cells, respectively.

Bulk samples used in the investigations of the low-temperature specific heat, susceptibility, magnetization and electrical transport properties were cut using a wire saw and carefully polished. Powder samples for x-ray and neutron diffractions studies were prepared using a RETSCH cryo-mill. In some cases the powders were additionally ground in an agate stone mortar in order to remove residual grains. The powder samples of CrB_2 were prepared from the float-zoned growth start of the single crystal ingot SFZ-118. An additional powder specimen was prepared from arc-melted polycrystalline material AMP-008. The MnB_2 powder sample was prepared from the growth start of the single crystal ingot SFZ-158 and a polycrystalline casted feed rod. Both specimens were first ground by means of a cryo-mill. Subsequently, the individual powders were added to obtain a reasonably large sample. Finally, a powder sample of CuMnSb was prepared from the single crystal ingot OFZ-98. Samples employed for powder neutron diffraction had typical masses of 1 g to 2 g. For powder x-ray diffraction few mg of the same specimens were used.

1.2 Apparatus for High-Pressure Experiments

High-pressure transport measurements of CrB_2 were carried out using three different types of pressure cells: A piston-cylinder cell, pc-1, with a liquid pressure transmitter was used for the generation of moderate hydrostatic pressure, $p < 2$ GPa. Several Bridgman cells, bc-1 to bc-3, with solid pressure medium were set up to achieve high pressures, $2 \text{ GPa} < p < 8 \text{ GPa}$. A He-activated uniaxial pressure cell was used in two measurements series, ux-1 and ux-2, to study effects of uniaxial pressure. In the studies using Bridgman and uniaxial pressure cells the pressure p was stepwise increased during a measurement series. In contrast, p was successively decreased in the experiment with the piston-cylinder cell. Photographs of typical transport samples of CrB_2 as prepared for the three different types of pressure cells are shown in Fig. 1.4. Tab. 1.4 summarizes all samples studied together with the corresponding pressure cells. Below the details of the pressure cell preparation, pressure determination, the sample geometries used, as well as the data treatment are reported.

type	name	dimensions (mm)	orientation	experiment	section
PC	AMP-008			powder XRD (TUM, XRC Vienna)	2.3.1
SC	SFZ-118-3-1-1			powder XRD (TUM)	2.3.1
SC	SFZ-118-3-1-1			powder ND (SPODI)	2.4.1
SC	SFZ-118-3-1-2	$\sim 0.5 \times 0.5 \times 0.5^1$	$\langle 100 \rangle \times \langle 120 \rangle \times \langle 001 \rangle$	single crystal XRD (XRC Vienna)	2.3.1
SC	SFZ-118-3-2-3-ab	$1.2 \times 0.5 \times 0.3$	$\langle 001 \rangle \perp$ circular cut plane	single crystal XRD (TUM)	2.3.3
SC	SFZ-118-3-3	$\emptyset 4 \times 9$	$\langle 001 \rangle \times \langle 120 \rangle \times \langle 001 \rangle$	single crystal ND (RESI, HEiDi, DNS)	2.4.2, 2.4.3, 2.3.3
SC	SFZ-162-3-3-1	$3.5 \times 3.5 \times 3.6$	$\langle 100 \rangle \times \langle 120 \rangle \times \langle 001 \rangle$	single crystal ND (HEiDi, DNS)	2.4.3, 2.3.3
SC	SFZ-118-3-2-1	$2.5 \times 2.2 \times 0.9$	$\langle 100 \rangle \times \langle 001 \rangle \times \langle 120 \rangle$	magnetization, heat capacity	2.5.1, 2.5.2
SC	SFZ-118-3-2-3-ac	$1.0 \times 0.4 \times 0.3$	$\langle 100 \rangle \times \langle 120 \rangle \times \langle 001 \rangle$	electrical transport	2.5.3
SC	SFZ-118-3-2-3-ca	$1.2 \times 0.5 \times 0.3$	$\langle 001 \rangle \times \langle 120 \rangle \times \langle 100 \rangle$	electrical transport	2.5.3
SC	SFZ-118-3-2-3-ca-2	$1.2 \times 0.5 \times 0.3$	$\langle 001 \rangle \times \langle 120 \rangle \times \langle 100 \rangle$	electrical transport	2.5.3
SC	SFZ-162-3-3-ac	$2.0 \times 1.0 \times 0.2$	$\langle 100 \rangle \times \langle 120 \rangle \times \langle 001 \rangle$	electrical transport	2.5.3
SC	SFZ-162-3-3-ca	$2.0 \times 1.0 \times 0.2$	$\langle 001 \rangle \times \langle 120 \rangle \times \langle 100 \rangle$	electrical transport	2.5.3
PC	Batch-2 ²	$1.5 \times 0.5 \times 0.6$	$\langle 001 \rangle \times \langle 120 \rangle \times \langle 100 \rangle^2$	high-pressure transport: pc-1	2.6.1
SC	SFZ-162-3-3-ca	$0.7 \times 0.7 \times 0.7$	$\langle 100 \rangle \times \langle 120 \rangle \times \langle 001 \rangle$	high-pressure transport: ux-1	2.6.1
SC	SFZ-162-3-3-ac	$0.7 \times 0.7 \times 0.7$	$\langle 001 \rangle \times \langle 120 \rangle \times \langle 100 \rangle$	high-pressure transport: ux-2	2.6.1
SC	SFZ-118-3-2-3-ac	$\sim 0.5 \times 0.2 \times 0.1^3$	$\langle 100 \rangle \times \langle 120 \rangle \times \langle 001 \rangle$	high-pressure transport: bc-1	2.6.2
SC	SFZ-118-3-2-3-ca	$\sim 0.5 \times 0.2 \times 0.1^3$	$\langle 001 \rangle \times \langle 120 \rangle \times \langle 100 \rangle$	high-pressure transport: bc-1	2.6.2
SC	SFZ-162-3-3-ac	$0.5 \times 0.2 \times 0.1$	$\langle 100 \rangle \times \langle 120 \rangle \times \langle 001 \rangle$	high-pressure transport: bc-2	2.6.2
SC	SFZ-162-3-3-ca	$0.7 \times 0.2 \times 0.1$	$\langle 001 \rangle \times \langle 120 \rangle \times \langle 100 \rangle$	high-pressure transport: bc-2	2.6.2
SC	SFZ-162-3-1-ca	$1.3 \times 0.4 \times 0.1$	$\langle 001 \rangle \times \langle 120 \rangle \times \langle 100 \rangle$	high-pressure transport: bc-3	2.6.2

Table 1.1: Summary of the CrB₂ samples studied. ¹Irregularly shaped sample of unknown crystallographic orientation which was cleaved of the single crystal. ²Strongly texturised polycrystalline sample prepared by B EUF as part of his Ph.D. thesis by inductive heating in a graphite crucible [8, 9]. The crystallographic orientation was inferred from measurements of the anisotropy of the electrical resistivity [9]. ³No photographs have been taken of these samples. Their dimensions were estimated from the size of similar samples which were cut the same way. The geometry factors were determined by scaling the resistivity data recorded at the lowest pressure studied with respect to the resistivity of a sample cut from the same single crystal ingot and measured at ambient pressure, cf. Sec. 1.2.4.

type	name	dimensions (mm)	orientation	experiment	section
SC	SFZ-158-4			powder XRD (XRC Vienna)	3.2.1
PC, SC	SFZ-158-2+4 ¹			powder ND (SPODI)	3.3.1
SC	SFZ-158-3-1-1	$\varnothing 4.5 \times 2.6$	$\langle 100 \rangle \perp$ circular cut plane	SC ND (DNS)	3.2.2
SC	SFZ-158-3-1-1	$\varnothing 4.5 \times 2.6$	$\langle 100 \rangle \perp$ circular cut plane	SC ND (RESI)	3.3.2
SC	SFZ-158-3-2-1	$2.7 \times 2.8 \times 1.7$	$\langle 100 \rangle \times \langle 110 \rangle \times \langle 001 \rangle$	heat capacity	3.4.1, [5]
SC	SFZ-158-3-2-1	$2.7 \times 2.8 \times 1.7$	$\langle 100 \rangle \times \langle 110 \rangle \times \langle 001 \rangle$	ac susceptibility	3.4.2, [5]
SC	SFZ-158-3-2-1 ²	$2.7 \times 2.8 \times 1.7$	$\langle 100 \rangle \times \langle 110 \rangle \times \langle 001 \rangle$	magnetization	3.4.3
SC	SFZ-158-3-2-a-ab	$2.6 \times 0.5 \times 0.1$	$\langle 100 \rangle \times \langle 001 \rangle \times \langle 110 \rangle$	electrical transport	3.4.4

Table 1.2: Summary of the MnB_2 samples studied. ¹Mixture of two powders which were prepared from a polycrystalline casted feed rod and the float-zoned growth start of the MnB_2 ingot SFZ-158. ²From the sample dimension demagnetization factors $N_a = 0.283$ and $N_c = 0.445$ were calculated for field along the a -axis and c -axis, respectively [10].

type	name	dimensions (mm)	orientation	experiment	section
SC	OFZ-98-3-1-1			powder XRD (XRC Vienna)	4.4.1
SC	OFZ-98-3-1-2			powder ND (SPODI)	4.5.2
SC	OFZ-98-3-2-3	$\varnothing 6 \times 9$	$\langle 110 \rangle \perp$ circular cut plane	SC ND (DNS)	4.4.2
SC	OFZ-98-3-2	$\varnothing 6 \times 11$	$\langle 110 \rangle \perp$ circular cut plane	SC ND (RESI)	4.5.3
SC	OFZ-98-3-2-1	$3.0 \times 3.0 \times 2.0$	$\langle 100 \rangle \times \langle 110 \rangle \times \langle 110 \rangle$	SC ND (HEiDi)	4.5.3
SC	OFZ-75-3-3-a	$4.8 \times 1 \times 1$	$\langle 100 \rangle \times \langle 110 \rangle \times \langle 110 \rangle$	heat capacity	4.3.2, [5]
SC	OFZ-98-3-3-a	$5.6 \times 1 \times 1$	$\langle 100 \rangle \times \langle 110 \rangle \times \langle 110 \rangle$	heat capacity	4.3.2, [5]
SC	OFZ-75-3-3-a	$4.8 \times 1 \times 1$	$\langle 100 \rangle \times \langle 110 \rangle \times \langle 110 \rangle$	magnetization	4.3.3
SC	OFZ-75-3-2-2-a	$5.7 \times 1 \times 1$	$\langle 100 \rangle \times \langle 110 \rangle \times \langle 110 \rangle$	magnetization	4.3.3
SC	OFZ-98-3-3-a	$5.6 \times 1 \times 1$	$\langle 100 \rangle \times \langle 110 \rangle \times \langle 110 \rangle$	magnetization	4.3.3
SC	OFZ-75-3-3-c	$5.0 \times 0.9 \times 0.2$	$\langle 100 \rangle \times \langle 110 \rangle \times \langle 110 \rangle$	electrical transport	4.3.4
SC	OFZ-75-3-3-e	$3.0 \times 0.9 \times 0.2$	$\langle 110 \rangle \times \langle 110 \rangle \times \langle 100 \rangle$	electrical transport	4.3.4
SC	OFZ-98-3-3-d	$5.0 \times 1.0 \times 0.2$	$\langle 100 \rangle \times \langle 110 \rangle \times \langle 110 \rangle$	electrical transport	4.3.4

Table 1.3: Summary of the CuMnSb samples studied. The single crystal ingot OFZ-75 was grown from a stoichiometric initial weight of starting elements and is referred to as CuMnSb-A. Ingot OFZ-98 was grown from an initial weight which contained a 3.5% excess of Sb; it is denoted CuMnSb-B.

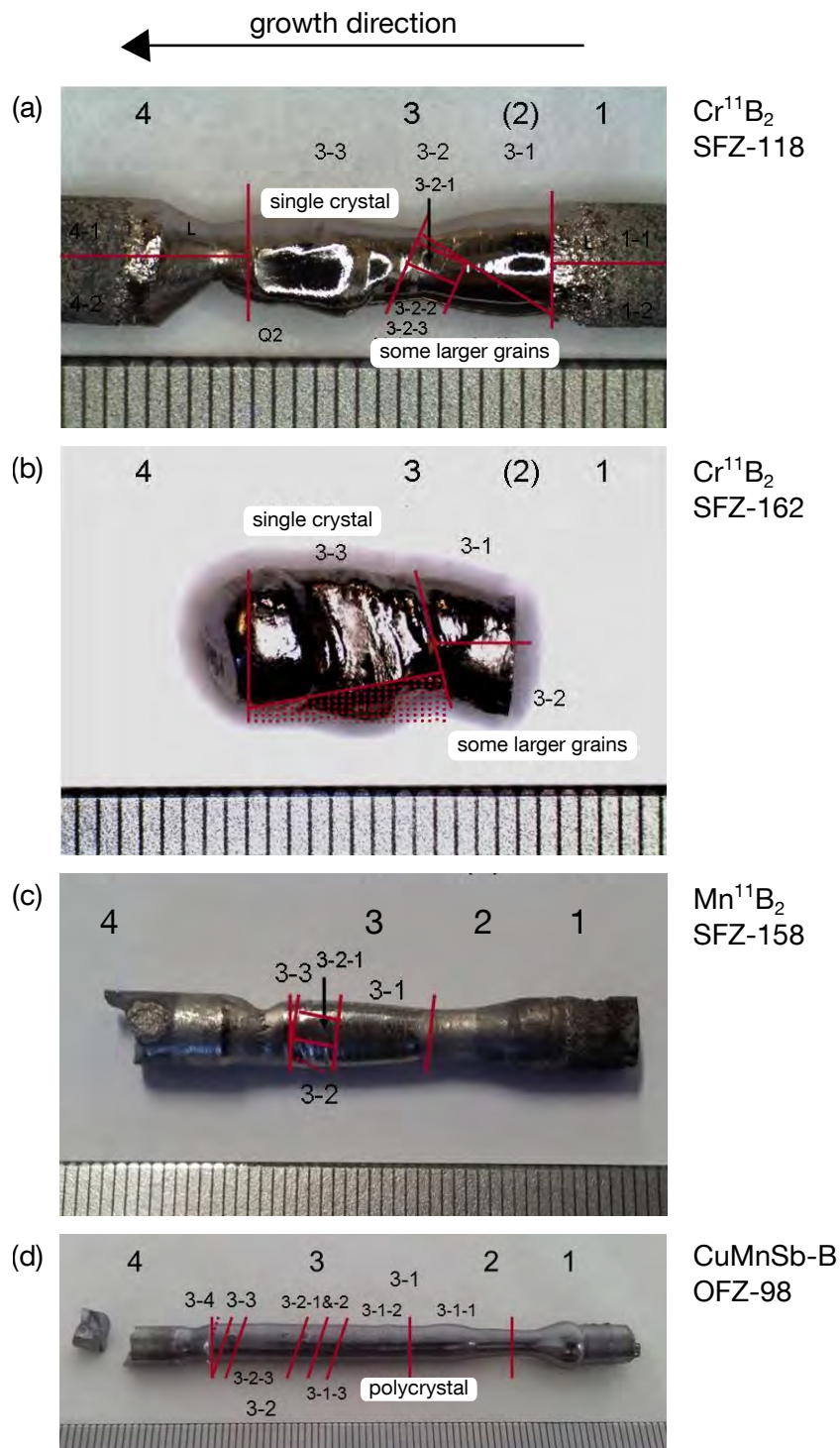


Figure 1.3: Photographs of the ingots of CrB_2 , MnB_2 , and CuMnSb studied as part of this thesis. Red lines indicate how the ingots were cut. For all ingots the growth direction was from left to right. (a) ^{11}B -enriched CrB_2 , SFZ-118. (b) ^{11}B -enriched CrB_2 , SFZ-162. (c) ^{11}B -enriched MnB_2 , SFZ-158. (d) CuMnSb-B , i.e., CuMnSb grown from an initial weight which contained a 3.5% Sb excess, OFZ-98. Courtesy of ANDREAS BAUER.

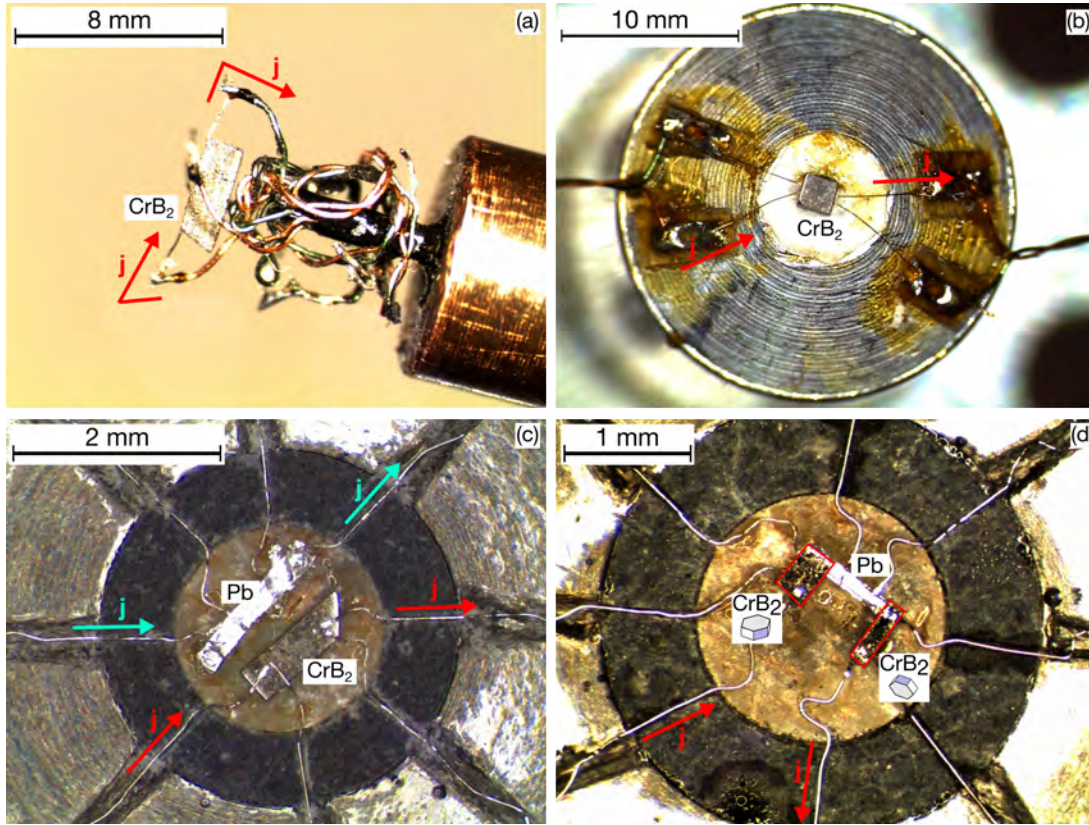


Figure 1.4: Typical set-up of high-pressure transport samples of CrB₂ prepared for measurements with different pressure cells. (a) Cuboid polycrystalline sample, spot-welded and mounted on the feed-through of a piston-cylinder cell. (b) Cubic single crystal sample, spot-welded and mounted on the lower anvil of a uniaxial stress cell. (c) Single crystal sample and superconducting manometer (Pb) both contacted using press contacts and mounted on the lower anvil of a Bridgman cell. (d) Two single crystal samples in a “crossed” geometry with a superconducting manometer (Pb), each contacted using press contacts and mounted on the lower anvil of a Bridgman cell. Arrows indicate the terminals that were used to apply the excitation current.

1.2.1 Piston-cylinder Cell

A detailed account of the piston-cylinder cell used in this thesis has been given in Ref. [11]. Pressure was generated by compression of a liquid pressure transmitter. The sample was mounted on an electrical feed-through, and the pressure transmitter sealed with a PTFE cap. The cell body was machined from hardened copper-beryllium (trade name Berylco25, Cu:Be with 2.5 % Be) and prevented bagging of the capsule. Obstrutors, sealing rings, and locknuts were also made from copper-beryllium.

A Fluorinert FC72:FC84 mixture with volume ratio 1:1 was chosen as pressure transmitter. It has a hydrostatic limit of ~ 2 GPa which is rather low compared to, e.g., methanol-ethanol mixtures [12–14]. This is, however, sufficiently high to rule out significant uniaxial stress for

1.2 Apparatus for High-Pressure Experiments

name	description	samples	F (kN)	p (GPa)
pc-1	piston-cylinder cell:	texturized polycrystalline cuboid:	20	1.1
	non-magnetic WC anvil	$1.5 \times 0.5 \times 0.6 \text{ mm}^3$, $\langle 001 \rangle \times \langle 120 \rangle \times \langle 100 \rangle$	25	1.7
	liquid pressure medium: Fluorinert mix		35	2.2
	pressure gauge: Sn			
ux-1	He-activated uniaxial stress cell:	single crystal cube, SFZ-162:	0	0
	Al_2O_3 -sputtered Al anvils	$0.7 \times 0.7 \times 0.7 \text{ mm}^3$, $\langle 001 \rangle \times \langle 120 \rangle \times \langle 100 \rangle$		0.05
	no pressure medium			0.1
	no pressure gauge			0.2 ^a
ux-2	He-activated uniaxial stress cell:	single crystal cube, SFZ-162:	0	0
	Al_2O_3 -sputtered Al anvils	$0.7 \times 0.7 \times 0.7 \text{ mm}^3$, $\langle 100 \rangle \times \langle 120 \rangle \times \langle 001 \rangle$		0.05
	no pressure medium			0.1
	no pressure gauge			0.2
				0.3
			0.4	
bc-1	Bridgman cell:	single crystal platelets, SFZ-118-3-2-3:	5	2.2
	non-magnetic WC anvils, 3.5 mm culet	$0.5 \times 0.15 \times 0.1 \text{ mm}^3$, $\langle 100 \rangle \times \langle 120 \rangle \times \langle 010 \rangle$	9	2.8
	solid pressure medium: steatite powder	$0.5 \times 0.15 \times 0.1 \text{ mm}^3$, $\langle 001 \rangle \times \langle 120 \rangle \times \langle 100 \rangle$	12	3.5 ^{a,b}
	pressure gauge: Sn			
bc-2	Bridgman cell:	single crystal platelets, SFZ-162-3-3:	20	3.3
	Alumina anvils, 3.0 mm culet	$0.5 \times 0.2 \times 0.08 \text{ mm}^3$, $\langle 100 \rangle \times \langle 120 \rangle \times \langle 010 \rangle$	30	5.1
	solid pressure medium: steatite powder	$0.7 \times 0.2 \times 0.08 \text{ mm}^3$, $\langle 001 \rangle \times \langle 120 \rangle \times \langle 100 \rangle$	40	6.3
	pressure gauge: Pb		50	6.9
			60	7.0
			70	7.3
		80	7.3	
bc-3	Bridgman cell:	single crystal platelet, SFZ-162-3-1:	5	1.3
	non-magnetic WC anvils, 3.5 mm culet	$0.6 \times 0.3 \times 0.1 \text{ mm}^3$, $\langle 100 \rangle \times \langle 120 \rangle \times \langle 010 \rangle$	15	3.4 ^a
	solid pressure medium: steatite powder			
	pressure gauge: Sn			

Table 1.4: Summary of samples and pressure cells used in the high-pressure transport study of CrB_2 . Sample dimensions and orientations are specified using the format $a \times b \times c$ where $a \perp b \perp c$. In this notation a corresponds to the direction of the excitation current \mathbf{j} . c is the direction of the loading force, \mathbf{F} , and magnetic field, $\mu_0 \mathbf{H}$. ^a Resistivity scaled to account for the formation of cracks in the sample. ^b Pressure estimated because pressure gauge failed.

the pressure range studied, i.e., the pressure generated with this technique may be considered hydrostatic.

1.2.2 Uniaxial Pressure Cell

The uniaxial pressure cell was developed by ALFONSO CHACÓN and JULIAN BECKER as part of their master's and bachelor's thesis, respectively [15, 16]. It has been designed as a scaled-down version of a pressure cell described in Ref. [17]. The operating principle is based on stainless steel bellows which are activated by pressurized He gas. When the bellows are filled they act

Experimental Methods

on the upper anvil which, in turn, is moved against the fixed lower anvil. Since no pressure medium is employed, a sample that is placed between both anvils is stressed uniaxially. The amount of stress acting on the sample depends on the gas pressure p_{He} and the sample cross section A . It can be calculated as $\sigma = p_{\text{He}}A_{\text{eff}}A^{-1}$ where $A_{\text{eff}} = 235 \text{ mm}^2$ is the effective area of the bellows. The anvils were machined from aluminium and insulated by depositing a $d \approx 1 \mu\text{m}$ thin layer of Al_2O_3 . For measurements at temperatures $1.8 \text{ K} \leq T \leq 300 \text{ K}$ the cell was mounted to a bespoke sample stick and inserted into the variable temperature insert (VTI) of a OXFORD INSTRUMENTS 14/16 T magnet cryostat. Measurements at lower temperatures, e.g., by means of the ADR cryostat described in Sec. 1.3.1, are hitherto prohibited due to the heat leak generated by the He capillary.

1.2.3 Bridgman Pressure Cell

A schematic drawing and a photograph of the Bridgman pressure cell are shown in Fig. 1.5. Pressure is generated by two opposed anvils which, between their anvil flats, compress a pressure medium. The sample is embedded in this pressure medium. A thin gasket, $h \approx 0.2 \text{ mm}$, which exerts a high friction force with respect to the anvils prevents the medium from flowing out of the pressurized area and serves as a wire-feedthrough. Within the operating limits set by the yield strength of the anvil material, the accessible pressure p can be estimated as $p = F/A = 4F/(\pi d^2)$, where F is the loading force and d the diameter of the anvil flat, which is commonly called *culet*. By decreasing d the accessible pressure can be increased while keeping F and, consequently, the cell body small. On the other hand, the available sample volume decreases.

1.2.3.1 Anvils

Several anvil materials and culet sizes have been used. They are summarized in Tab. 1.5 and shown in Fig. 1.5d.

Anvils made from tungsten-carbide (WC) are very hard and thus allow the generation of high pressures while providing a sufficiently large sample space. There are, however, two major disadvantages connected with WC anvils. First, due to their metallicity, they often cause shorts of the sample wiring. Second, though being nominally non-magnetic, WC anvils still possess a small magnetic moment which can affect the measurement in an undesired way. This is a consequence of the manufacturing (sintering) process of WC in which either Ni or Co, both ferromagnets, are used as binder. Due to these limitations of WC alternative anvil materials with similarly high compressive strength, alumina (Al_2O_3) and moissanite (SiC:6H), have been tested.

Alumina is a widely-used, non-conducting ceramic. It is produced in a sintering process without the addition of magnetic binders and may therefore be considered non-magnetic. Owing to the smaller yield strength of alumina, the maximum pressures generated with alumina anvils are smaller than those created using WC anvils of the same size.

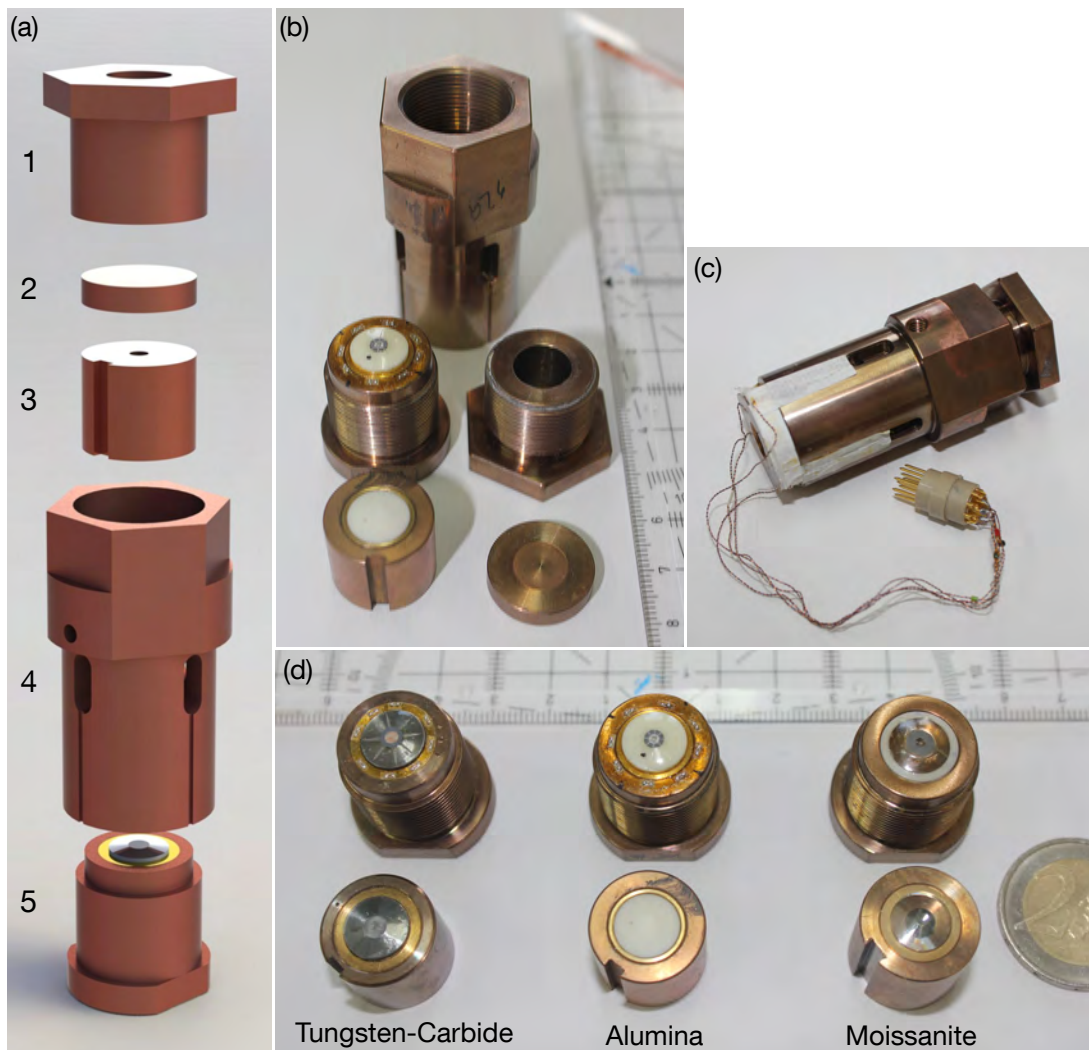


Figure 1.5: Bridgman cell for high-pressure transport measurements. (a) Schematic drawing showing all parts of the Bridgman cell assembly, (1) locknut, (2) washer disc, (3) upper anvil, (4) cell body, and (5) lower anvil. (b) Photograph of the parts of the assembly. (c) Photograph of the assembled Bridgman cell. The sample wiring is fed through windows in the Cu:Be cell body. (d) Photograph of the different anvil types used, from left to right: tungsten-carbide, alumina, and moissanite.

Moissanite is the $6H$ polytype of single crystal SiC, a non-conducting and non-magnetic synthetic material with exceptional hardness [18]. An important advantage of moissanite is its transparency in the visible spectral range. As described in Sec. 1.2.5 this allows to measure the pressure inside the Bridgman cell already at room temperature by means of optical, contactless techniques, e.g., the ruby fluorescence method [19, 20]. Unlike sintered materials single crystal anvils such as those manufactured from moissanite are prone to cleavage. The risk of anvil failure is particularly high for large anvils as they are more likely to show crystalline imperfections. The latter may then nucleate cracks once the anvil is stressed. This limits the use of moissanite

Experimental Methods

culet- \varnothing (mm)	material
3.5	non-magnetic tungsten-carbide (WC), tradename TRANSCERAM TC-NM12, compressive strength 3.1 GPa
3.0	alumina (ceramic Al ₂ O ₃), tradename TRANSCERAM Al ₂ O ₃ , 99.7%, compressive strength 2.9 GPa
4.0	moissanite (single crystal SiC:6H), manufacturer CHARLES&COLVARD LTD.

Table 1.5: Summary of Bridgman cell anvil sizes and materials. Compressive strengths of tungsten-carbide and alumina as specified by the manufacturer TRANSCERAM.

to either small anvils or to special cells which allow for a very precise alignment of the anvils. On the other hand large moissanite single crystals are still affordable when compared to, e.g., diamond anvils. The latter represents to date the hardest and most commonly used transparent anvil material. The high costs of natural diamond however limit its application to small anvil sizes and hence tiny samples. This rules out the use of diamond anvil cells for any kind of measurement where large sample volumes are essential, for instance, neutron scattering. As an affordable alternative synthetic moissanite might enable such high-pressure neutron studies, hence opening up new experimental possibilities to address a variety of exciting physical problems. Recent technical developments of pressure cells which employ moissanite as anvil material are very promising [21, 22].

1.2.3.2 Gaskets and Pressure Media

All Bridgman cell gaskets were prepared from pyrophyllite. Electrical feedthroughs were cut into the gasket using a razor blade. The height h of the gasket strongly affects both the maximum pressure obtained per unit force and the pressure distribution within the sample space [23, 24]. A gasket height of 0.2 mm was chosen to obtain a reasonably large sample space with an (initially) flat pressure distribution.

A solid pressure medium, steatite powder, was used to avoid difficulties regarding the feedthroughs. The use of a gasket reduces shear stresses in solid pressure media significantly [14]. Still, in comparison with liquid pressure transmitters, steatite has a low hydrostatic limit and develops uniaxial stress components. The pressure generated with this technique should therefore be considered as a combination of hydrostatic pressure p_0 plus a uniaxial stress component σ_{dev} , i.e., the pressure is no longer perfectly hydrostatic but exhibits a certain anisotropy.

1.2.3.3 Pressure Anisotropy and Inhomogeneity

As has been stated above the use of a solid pressure medium (steatite) results in an uniaxial stress component σ_{dev} which adds to the hydrostatic average pressure p_0 . Consequently, p exhibits a certain anisotropy. Even though the pressure anisotropy is in most cases an unwanted by-product of the solid pressure medium it may in fact also be used intentionally to tune the lattice parameters of a material unevenly. If the studied material itself exhibits an elastic anisotropy the effect of the pressure anisotropy can be amplified or reduced depending on whether σ_{dev} coincides with a soft or hard crystal axis, respectively. Thus certain distortions of the crystallographic unit cell may be achieved which are not accessible by means of purely hydrostatic pressure. This method has been applied to CrB_2 as part of this thesis. As will be detailed in Sec. 2.6 CrB_2 exhibits a hard a and a soft c axis. Quasi-hydrostatic pressure $p_0 + \sigma_{\text{dev}}$ can thus be used to achieve an increased compression of the c lattice parameter if σ_{dev} is aligned along c . In turn the ratio c/a can be tuned to values which are not accessible using hydrostatic pressure.

In order to apply the pressure anisotropy in a controlled way and to analyze its effect on the pressurized sample an adequate sample geometry must be chosen. One sample arrangement which serves this purpose is the “crossed” sample geometry described in Sec. 1.2.3.5. The pressure anisotropy must not be confused with the spatial variations of the pressure, the pressure inhomogeneity $\Delta p_0/p_0$. The latter arises naturally from the pressure distribution in a Bridgman cell. As shown schematically in Fig. 1.6a the pressure distribution in an ideal Bridgman cell is characterized by ring-shaped concentric isobars. Hence the effect of the inhomogeneity can be reduced significantly if the samples are aligned along these isobars. Such ring-shaped sample arrangements have therefore been used for all measurements. Nonetheless the samples will be exposed to an increasing pressure inhomogeneity when the cell is loaded. As shown in Fig. 1.6b the pressure distribution over the sample space is initially flat. With increasing load the pressure profile steepens. Consequently, the isobars close in on each other and the inhomogeneity $\Delta p_0/p_0$ acting on the samples increases. If superconducting manometers are employed $\Delta p_0/p_0$ can be estimated from the width of the superconducting transitions (cf. Sec. 1.2.5). Fig. 1.6c shows the superconducting transition of a Pb manometer for various loading forces F . As F is increased the transition broadens hence indicating an increase of the pressure inhomogeneity. As shown in Fig. 1.6d $\Delta p_0/p_0$ in fact increases slightly, in particular at high pressures. For the Bridgman cells used in this thesis a typical inhomogeneity of $\Delta p_0/p_0 \approx 15\%$ was obtained.

1.2.3.4 Standard Sample Geometry

Fig. 1.7a shows the standard sample geometry for high-pressure transport measurements with Bridgman cells. It comprises of a single sample and a pressure gauge, each connected in a four-terminal configuration. The lower anvil of the cell was prepared according to the following procedure [9]: First, the pyrophyllite gasket was glued onto the anvil culet using a small amount of varnish. Then the culet was insulated by gluing a thin steatite disc, $d \approx 60\ \mu\text{m}$, into the

Experimental Methods

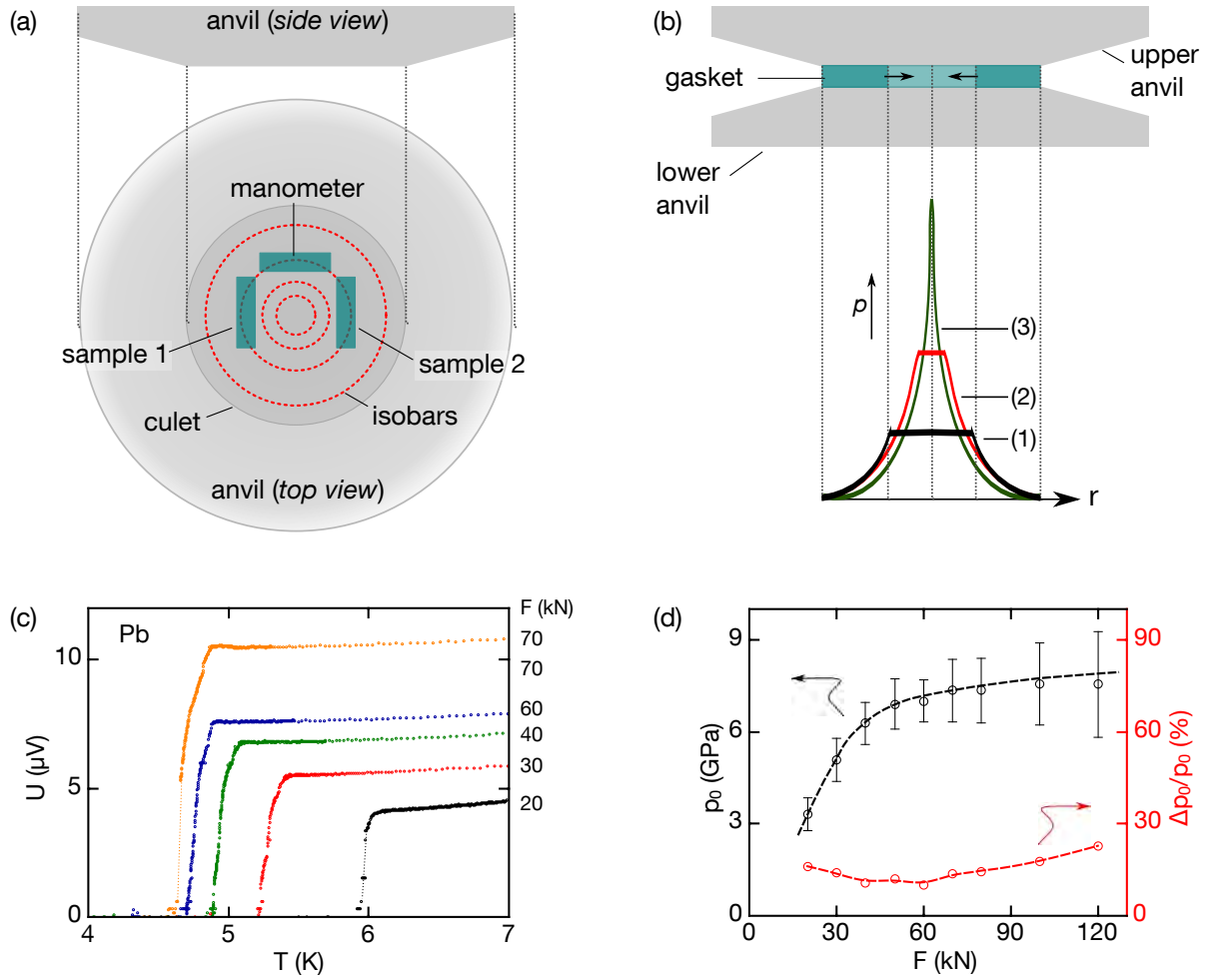


Figure 1.6: Pressure inhomogeneity in the Bridgman cells. (a) The pressure distribution in the sample space is characterized by ring-shaped concentric isobars. For all measurements the samples were aligned along these lines of constant pressure in order to reduce the pressure inhomogeneity seen by the samples. (b) Evolution of the pressure profile with increasing p . The profile is initially flat but steepens with increasing p , (1) \rightarrow (2) \rightarrow (3), hence increasing the pressure inhomogeneity seen by the samples. Drawing reproduced from Ref. [23]. (c) Superconducting transitions of a Pb manometer for various loads. Thin dotted lines serve as a guide to the eye. (d) Average pressure p_0 and pressure inhomogeneity $\Delta p_0/p_0$ estimated from the width of the manometer's superconducting transition.

gasket. These steatite discs were prepared such that their diameter fitted exactly the inner diameter of the gasket. The anvil surface outside of the culet was insulated by means of a two-component epoxy resin. As the resin additionally serves as a massive support for the gasket the latter preparation step was also carried out for insulating (alumina) anvils. After curing of the resin wire-feedthroughs were cut into the gasket using a razor blade. Samples were prepared as thin platelets. They were glued onto the steatite disc inside the gasket using a tiny amount

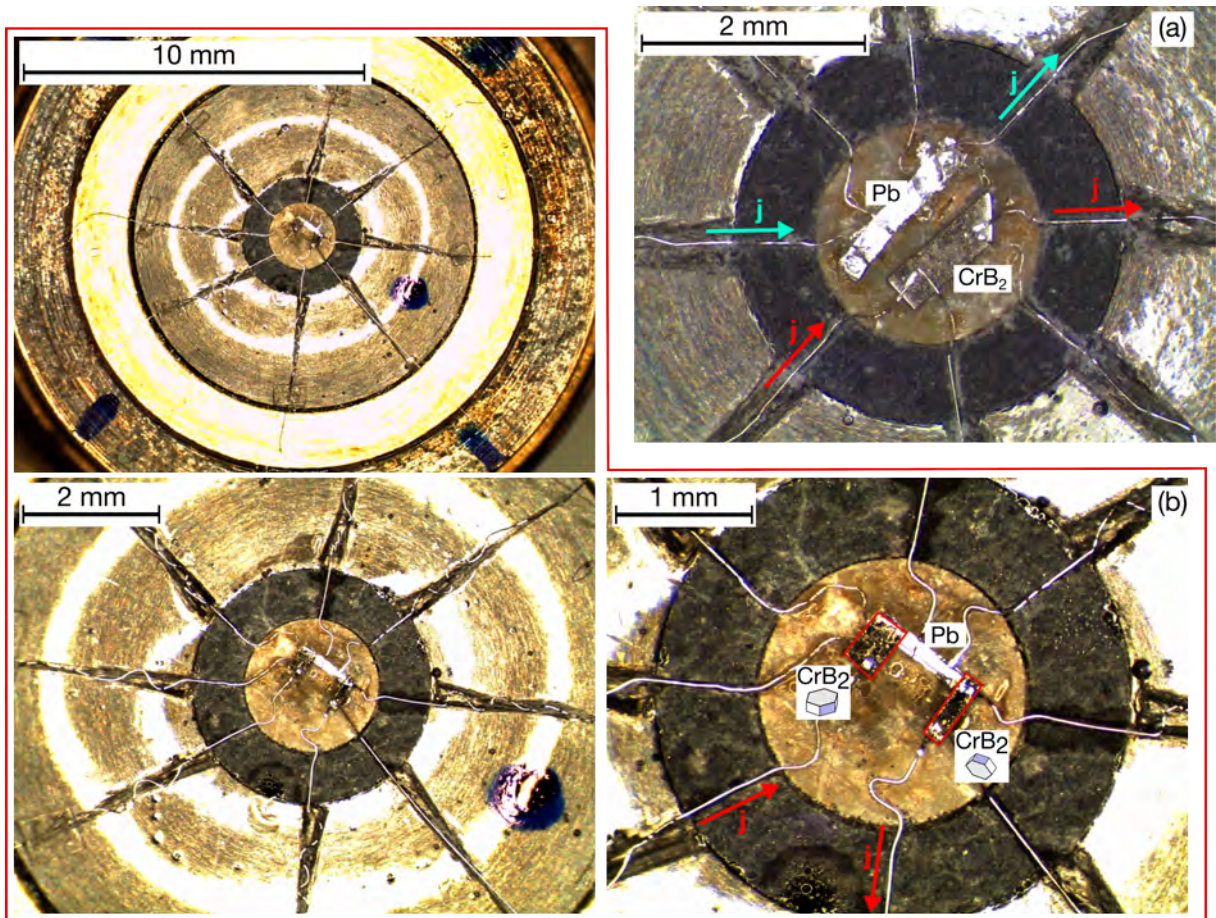


Figure 1.7: Sample geometries for high-pressure transport measurements with Bridgman cells. The photographs show top views of the lower cell anvil. Arrows indicate the excitation current flow. (a) The standard geometry comprises a single sample and a superconducting pressure gauge (here Pb), both connected in a standard four-terminal configuration. (b) Two single crystal samples are aligned in a “crossed” geometry which allows to analyze the effect of uniaxial stress that develops due to the solid pressure medium: The c -axis of the left sample points parallel to the loading force \mathbf{F} whereas the c -axis of the right sample stands perpendicular on \mathbf{F} . To reduce the number of wire-feedthroughs both samples are electrically connected by the superconducting manometer (here Pb) resulting in a U-shaped arrangement.

of a fast-curing two-component epoxy resin. A thin foil of Sn or Pb which served as pressure gauge was added in an analogous way (cf. Sec. 1.2.5). Press contacts were created by laying the flattened tips of annealed Pt wires, $\varnothing 25\ \mu\text{m}$, on the sample surface. These wires got pressed on the sample surface and established an electrical contact only when the cell was loaded. The wire-feedthroughs in the gasket were filled with pyrophyllite powder. Finally the sample was covered with a small amount of steatite powder and a second steatite disc.

1.2.3.5 Crossed Sample Geometry

It is well known that pressure anisotropies arising, for instance, from the use of solid pressure media can strongly influence the physical properties of some materials. This particularly applies to materials which exhibit a crystalline anisotropy such as the hexagonal diborides studied as part of this thesis, CrB₂ (Sec. 2) and MnB₂ (Sec. 3). Therefore for several high-pressure transport measurements of CrB₂ a “crossed” sample geometry was chosen. Fig. 1.7b show this sample arrangement in more detail. In this geometry two samples are placed within the same Bridgman cell - the first one with its c -axis parallel, the second one with its c -axis perpendicular to the anvil plane. In turn, the force \mathbf{F} which is used to load the cell is oriented perpendicular to the c -axis of the first sample and parallel to the c -axis of the second sample. As stated above the solid pressure medium will give rise to an additional uniaxial stress component σ_{dev} . As σ_{dev} develops preferentially along this loading direction it follows that, besides the volume changes associated with hydrostatic pressure p_0 , the c -axis of the first sample will be stretched while the c -axis of second sample will experience an additional compression. Indicating the different quasi-hydrostatic pressure conditions by the symbols p_{\perp} and p_{\parallel} , respectively, it follows

$$p = p_0 + \sigma_{\text{dev}} = \begin{cases} p_0 + \sigma_{\perp} \equiv p_{\perp}, & \text{if } \mathbf{F} \perp c, \\ p_0 + \sigma_{\parallel} \equiv p_{\parallel}, & \text{if } \mathbf{F} \parallel c. \end{cases} \quad (1.1)$$

Accordingly, the resistivity data is denoted ρ_{\perp} and ρ_{\parallel} .

For the “crossed” sample geometry the preparation of the lower anvil follows the same above-mentioned procedure as for the standard geometry. To reduce the number of leads the samples were connected by means of the superconducting manometer resulting in a U-shaped arrangement. The first and the last terminal along this U-shaped arrangement, I^+ and I^- , are used to apply the excitation current for sample 1, sample 2, and the manometer. The voltage drop at each sample and the manometer is measured in a two terminal configuration. As in the standard sample geometry thus only eight wires exit the pressure cell.

1.2.4 Data Treatment

All high-pressure resistivity data were scaled with respect to the resistivity measured at ambient pressure. This was necessary to eliminate uncertainties of the geometry factor which may arise due to changes of the contact geometry and the contact quality when closing the pressure cell.

Transport samples for uniaxial stress measurements were prepared in the pressure cell and investigated at ambient pressure, $\sigma = 0$, prior to loading the cell. Normalization of these data with respect to the ambient pressure resistivity measured without pressure cell provided a factor ν_0 applied to all resistivity data of the same measurement series recorded at uniaxial stress $\sigma > 0$.

Samples for piston-cylinder cells or Bridgman cells could not be investigated at ambient pressure.

1.2 Apparatus for High-Pressure Experiments

Instead, ambient pressure resistivity data were obtained by scaling the resistivity data which were recorded at the lowest pressure, p_{\min} , using a factor ν_0 . Fig. 1.8 shows the procedure that was used to determine ν_0 .

All data of the same measurement series were scaled to the resistivity taken at p_{\min} using a pressure dependent scaling factor ν for each measurement of the series (Fig. 1.8b and Fig. 1.8d). Deviations of the scaled curves, $\nu\rho(T, p) - \rho(T, p_{\min})$, are small and occur mainly at temperatures $T < T_N$ where the magnetic ordering temperature shifts as a function of pressure (Fig. 1.8c). The hypothetical ambient pressure resistivity is then given by $\tilde{\rho}(T) = \rho(T, p_{\min})\nu_0^{-1}$ where ν_0 is found by linear extrapolation of $\nu(p)$ for $p \rightarrow 0$.

Deviations of this hypothetical ambient pressure curve from the ambient pressure resistivity (measured without pressure cell) are due to a sample dependent geometry factor μ . As in the case of uniaxially stressed samples μ is determined by scaling the hypothetical ambient pressure curve to the well-known resistivity at $p = 0$: $\rho(T, p = 0) = \tilde{\rho}(T)\mu = \rho(T, p_{\min})\nu_0^{-1}\mu$. This is illustrated in Fig. 1.8e. For all measurements the sample dependent geometry factor μ is by far larger than ν_0^{-1} .

For a few measurements data had to be scaled using an additional factor because the resistivity had changed abruptly after increasing the pressure, hence making the determination of ν_0 and consequently μ impossible. These measurements are listed in Tab. 1.4. The additional scaling factor was determined by normalizing the high-temperature resistivity data to the data recorded at a lower pressure. Abrupt changes of the resistivity are not uncommon for Bridgman cell experiments, especially if a solid pressure medium or press contacts are employed. Such discontinuous behavior is often attributed to the formation of micro cracks in the sample or movement of the contact wiring.

1.2.5 Pressure Determination

1.2.5.1 Superconducting Pressure Gauges

Pressure determination was carried out by means of superconducting Sn or Pb manometers for all piston-cylinder and Bridgman cells. For this purpose a thin platelet of the manometer material was placed inside the pressure cell and close to the sample. The superconducting transition temperature T_c of both, Sn and Pb, decreases with increasing pressure according to the empirical pressure dependencies

$$T_c^{\text{Sn}} = T_{c,0}^{\text{Sn}} - 4.63 \cdot 10^{-2}p + 2.16 \cdot 10^{-4}p^2 \quad (1.2)$$

$$T_c^{\text{Pb}} = T_{c,0}^{\text{Pb}} - 4.02 \cdot 10^{-2}p + 7.4 \cdot 10^{-5}p^2 \quad (1.3)$$

where $T_{c,0}^{\text{Sn}} = 3.7 \text{ K}$ and $T_{c,0}^{\text{Pb}} = 7.2 \text{ K}$ are the critical temperatures at ambient pressure [25, 26]. T_c is determined by measuring the resistivity of the manometer as a function of temperature. As shown in Fig. 1.9 the latter drops abruptly once the manometer becomes superconducting.

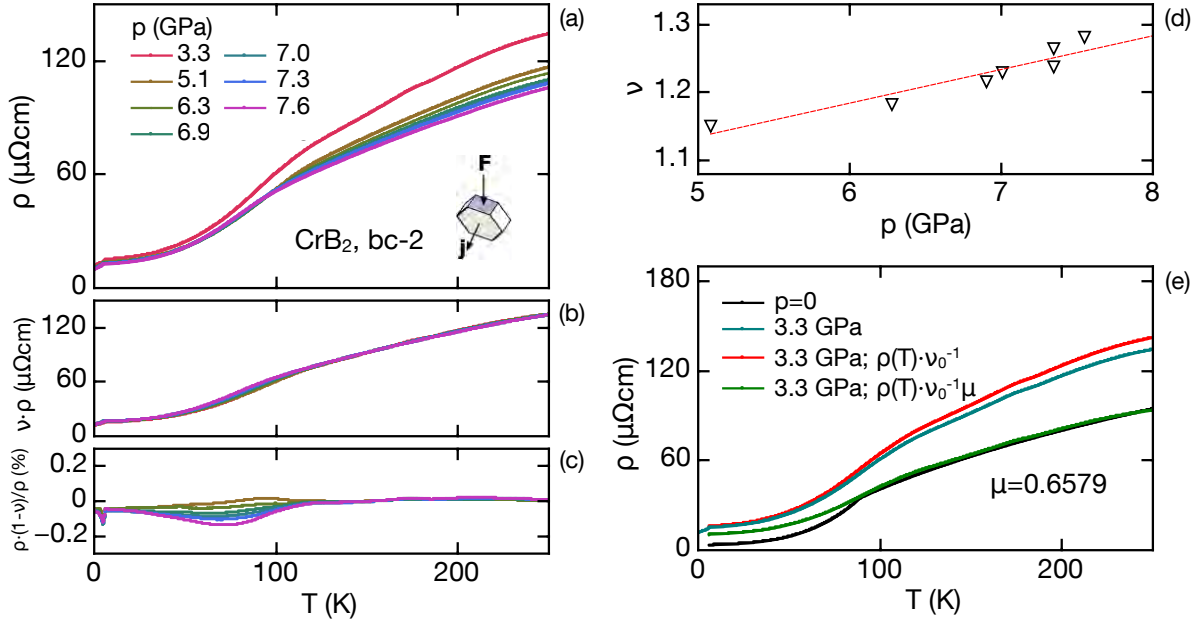


Figure 1.8: Normalization procedure applied to the high-pressure resistivity data of CrB₂. (a) Measurement series where $\rho(T)$ was recorded for various pressures p . (b) Each curve $\rho(T)$ was scaled to the curve recorded at the lowest pressure, here $p = 3.3$ GPa, using a scaling factor ν . (c) Relative deviation of the scaled curves. (d) Scaling factor ν as a function of pressure p . (e) Comparison of the ambient pressure resistivity (black curve), high-pressure resistivity (blue curve), hypothetical ambient pressure resistivity ($\rho(T) \cdot \nu_0^{-1}$, red curve) and normalized high-pressure resistivity ($(\rho(T) \cdot \nu_0^{-1})\mu$, green curve)

Due to the finite width of the transition a certain ambiguity of T_c and consequently of p_0 arises. For most measurements a full superconducting transition has been detected and T_c was chosen as the temperature where ρ dropped by 50% of its normal-state residual resistivity, ρ_0 (midpoint criterion). For those measurements where only a partial superconducting transition has been detected T_c was chosen as the onset temperature of the transition (onset criterion). The same criterion for T_c was used consistently for all measurements of a series. This ensures that changes in pressure, Δp_0 , between two measurements of the same series are correct even if the absolute values of p_0 were inexact. The relative error in p as determined either from the midpoint or from the onset criterion is typically smaller than 10%. Hence data of two measurement series may still be compared even if different criteria have been used in the pressure determination.

1.2.5.2 Ruby-Fluorescence Pressure Gauge

Superconducting gauges provide a simple tool to determine the pressure inside a pressure cell. There are however several disadvantages connected to this method, namely (i) it can be applied only at cryogenic temperatures, (ii) it is very sensitive to magnetic fields, (iii) it requires addi-

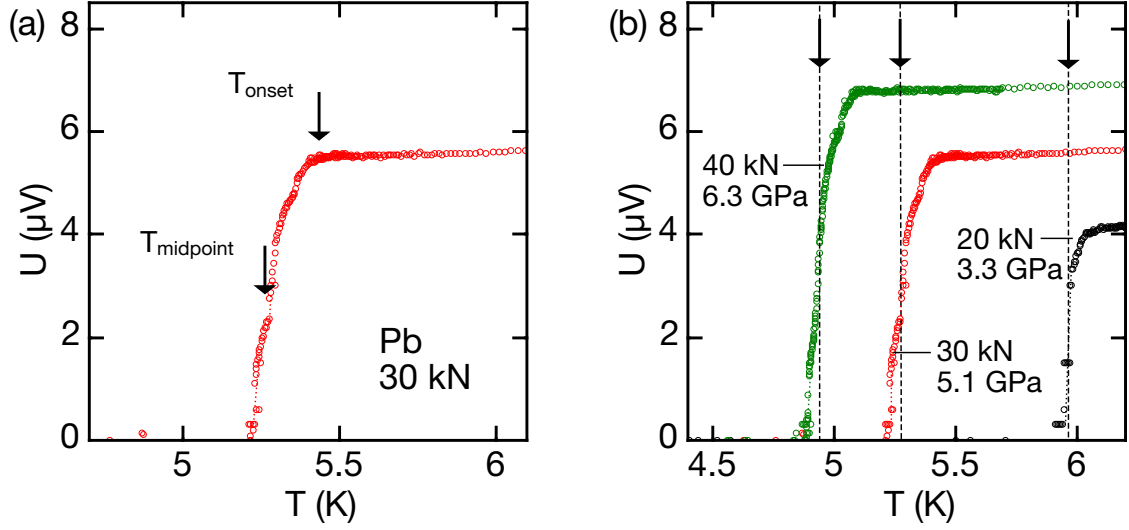


Figure 1.9: Pb as a superconducting pressure gauge. (a) The manometer becomes superconducting at a pressure-dependent critical temperature T_c . T_c was determined from the onset temperature or the midpoint temperature if a partial or a full transition was observed, respectively. (b) With increasing pressure T_c decreases according to Eq. 1.3. Arrows and vertical dashed lines indicate T_c as determined by the midpoint criterion.

tional wiring and wire-feedthroughs. An alternative approach which overcomes these limitations is the ruby-fluorescence technique. A small piece of ruby (Cr-doped $\alpha\text{-Al}_2\text{O}_3$) is put next to the sample inside the pressure cell and serves as a pressure gauge. It is excited by means of a laser and relaxes under the emission of two characteristic lines, R1 = 694.25 nm and R2 = 692.86 nm. Upon the application of pressure the energy level scheme of ruby changes and the R lines shift as [27]:

$$\frac{dp}{d\lambda} = 0.2746(140) \text{ GPa } \text{\AA}^{-1}. \quad (1.4)$$

Measuring the line shift $\Delta\lambda$ allows to determine the pressure inside the cell. The ruby-fluorescence is a contactless method and can be applied already at room temperature. It can still be useful to apply this technique also at low temperatures, particularly for the following two reasons: (i) The pressure seen by a sample will change due to the thermal contraction of the pressure cell upon cooling to cryogenic temperatures. The ruby method will allow to determine the actual low-temperature pressure. (ii) With increasing pressure the ruby fluorescence lines broaden and weaken hence rendering their measurement at room temperature difficult. However, with decreasing temperature the R1 and R2 lines narrow again and their intensity increases. Measuring the ruby lines at cryogenic temperatures therefore allows pressure determination using small amounts of ruby and at high pressure where the emission intensity would be significantly lowered at room temperature.

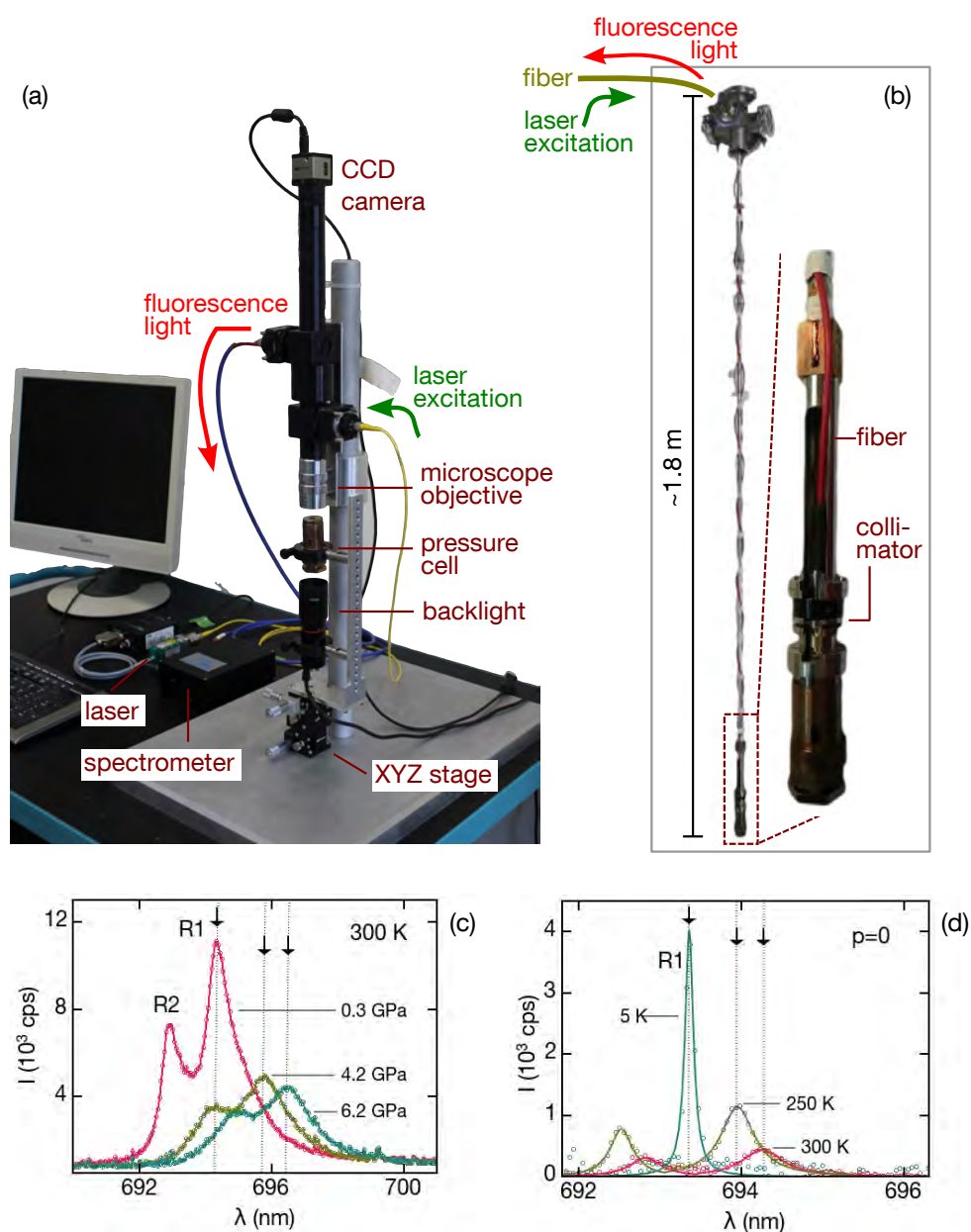


Figure 1.10: Optical pressure determination by means of the ruby fluorescence technique. (a) Ruby fluorescence manometer. The set-up serves to excite the ruby inside the pressure cell and to collect and analyse the emitted fluorescence light. (b) Sample stick for the measurement of the ruby fluorescence at cryogenic temperatures. (c) Room temperature spectra of the ruby fluorescence lines R1 and R2 at various pressures. Courtesy of PAU JORBA (d) Low-temperature spectra of the ruby R1 fluorescence line at zero pressure. Courtesy of FLORIAN SIGGER

The moissanite anvils shown in Fig. 1.5d are transparent and thus provide an optical access to the sample space. As this already allows to apply the fluorescence technique and a ruby-fluorescence manometer was set up. Its design follows a suggestion by KARL SYASSEN which allows to apply

the fluorescence technique both at room temperature and at cryogenic temperatures [28]. The optical apparatus is shown in Fig. 1.10a. It comprises a solid state laser ($\lambda = 532$ nm) to excite the ruby, a microscope objective which focuses the laser beam on the ruby and collects the emitted fluorescence light, and a spectrometer to analyse the R1 and R2 lines. A CCD camera allows to inspect the sample space and check the correct position of the laser focus. The latter can be adjusted by moving the cell using a XYZ micrometer stage. For safe operation all optical components are fiber-coupled. Laser, spectrometer, and camera can be controlled via a computer interface. The setup is mounted on a mobile rack.

For measurements of the ruby lines at cryogenic temperatures a bespoke sample stick for the use with an OXFORD INSTRUMENTS magnet cryostat was built by FLORIAN SIGGER as part of his Bachelor thesis [29]. As shown in Fig. 1.10b the Bridgman cell is mounted at the bottom end of the sample stick. A multimode fiber is used to guide the laser light to the pressure cell and the emitted fluorescence light back to the spectrometer. Focussing is achieved by means of a micro-collimator. Fig. 1.10c and Fig. 1.10d provide typical fluorescence spectra to demonstrate the proper operation of the manometer both at room temperature and at cryogenic temperatures. As the ruby-fluorescence manometer was set-up as part of this thesis but has not been applied for high-pressure measurements reported here the reader is referred to Refs. [22, 29] for further details.

1.3 Low-temperature Bulk and Transport Measurements

Several measurement techniques have been applied to study the low-temperature bulk and transport properties of samples at zero pressure and high-pressure. They are summarized in the following sections. Whereas some measurements were carried out in standard Helium flow cryostats the vast majority of experiments was performed in a cryogen-free demagnetization cryostat. This became possible due to extensive enhancements of the cryostat which are shortly reviewed in Sec. 1.3.1.

1.3.1 Adiabatic Demagnetization Refrigeration

Adiabatic demagnetization refrigeration (ADR) is a cooling technique that exploits the magnetic field dependence of the entropy S of a paramagnetic spin system. The working principle for a single-shot refrigeration procedure was independently proposed by Debye and Giauque [30, 31] and is shown schematically in Fig. 1.11: Starting from an initial temperature T_i which is provided by a heat bath the paramagnet is isothermally magnetized. Thereby its magnetic entropy is lowered. The heat of magnetization $\Delta Q_{\text{mag}} = -T_i[S(B_i, T_i) - S(0, T_i)]$ is absorbed by the heat bath. Subsequently the paramagnet is thermally decoupled from the heat bath and demagnetized adiabatically. During the demagnetization its temperature decreases from T_i to $T_f = T_i \sqrt{(B_f^2 + B_{\text{int}}^2)/(B_i^2 + B_{\text{int}}^2)}$. Here B_i and B_f denote the initial and final magnetic fields,

Experimental Methods

respectively. B_{int} is the internal magnetic field of the paramagnetic cooling medium and limits the final temperature to $T_f > 0$. Due to heat leaks the paramagnet finally warms up to T_i along the $S(B_f)$ curve thereby absorbing the heat $\Delta Q_{\text{spin}} = \int_{T_f}^{T_i} C(B_f) dT$, where C is the (field dependent) specific heat of the refrigerant.

If during the demagnetization process the magnetic field is lowered not to zero but only to an intermediate field $B_f > 0$ this residual field may be used to adjust the temperature in a controlled way. Depending on the specific experimental requirements T can be raised, lowered, or kept at a constant value only by variation of the residual magnetic field. Unlike classical temperature control loops which are realized, e.g., in Helium flow cryostats and which commonly employ resistive heaters and valves the ADR method hence allows to control T in a very elegant way, namely simply by regulation of a magnetic field or, more precisely, by regulation of the current which powers the ADR magnet. Thus the ADR method offers temperature control almost without any time lag and at an outstanding precision.

After a desired target temperature has been tuned in the hold time Δt which is available for low-temperature experiments depends on the amount of the residual magnetic field B_f : if T_f is large, B_f is large and so is the hold time Δt ; in turn the hold time Δt is low at low temperatures. It is worth noting that depending on the specific technical realization of the refrigeration process hold times of several hours at milli-Kelvin temperatures are feasible.

Cryogen-free ADR cryostat

Most low-temperature transport measurements reported in this thesis were carried out using a cryogen-free ADR cryostat DRYOGENIC DMS-1000 which makes use of the above-mentioned cooling principle. The key components of the system are assembled in a vacuum vessel, comprising a superconducting 7 T ADR magnet, a superconducting 10 T sample magnet, and a pulse tube cryocooler which serves as the ADR heat bath at $T_i \approx 3.8$ K. A sample stick carries both the sample, a mechanical heatswitch, and the paramagnetic cooling agent. The latter is realized by a paramagnetic salt, ferric ammonium alum (FAA), which is sealed in a vacuum-tight cylinder, the so-called salt pill. The sample is rigidly connected to this salt pill and will therefore cool down upon demagnetization. During the demagnetization process the heatswitch allows to decouple the salt pill thermally from the cryostat heat bath.

The DRYOGENIC DMS-1000 was purchased as a prototype cryostat requiring extensive modifications. These were carried out as part of the author's diploma thesis and this Ph.D. thesis [9] as well as the bachelor's and master's theses of JAN SPALLEK [32, 33]. The necessary improvements of the cryostat cover essentially all technical aspects including the hardware, measurement electronics, and control software. Only the most important changes are listed below.

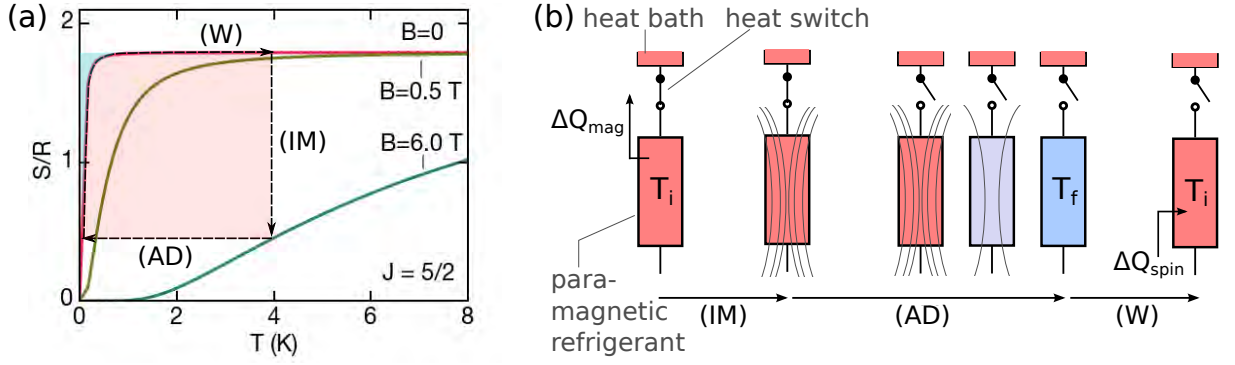


Figure 1.11: Working principle of the single-shot demagnetization refrigeration method. In an optimal implementation the ADR procedure comprises three steps - isothermal magnetization (“IM”), adiabatic demagnetization (“AD”), and warmup (“W”). (a) S - T diagram of the refrigeration process employing an ideal $J = 5/2$ spin system as refrigerant. The heat of magnetization ΔQ_{mag} which must be absorbed by the heat bath corresponds to the sum of the red and blue shaded areas. The heat ΔQ_{spin} that can be absorbed by the refrigerant during its warmup corresponds to the area underneath its entropy curve $S(B_f, T)$. For instance, ΔQ_{spin} corresponds to the the small blue shaded area if $B_f = 0$. ΔQ_{spin} is increased substantially if B is not lowered to zero but to a finite magnetic field, e.g., $B_f = 0.5$ T. (b) Flow chart representation of the refrigeration process. In its technical realization the ADR cooling method requires at least a heat bath, a paramagnetic refrigerant, and a heat switch which allows to decouple the refrigerant from the heat bath during the quasistatic demagnetization.

Modifications of the Cryostat

- Renewal of the mechanical support structure to ensure the correct alignment of the cryostat assembly and the magnet system.
- Exchange of thermal buses by copper strands of high thermal conductivity to minimize temperature gradients and reduce the bath temperature T_i .
- Redesign of the sample stick for improved reliability, shorter cooldown times, and longer hold times.
- Redesign of the heatswitch resulting in a sturdier mechanical support while keeping the heat leak through the support structure low.
- Preparation of robust and long-lasting paramagnetic salt pills for use under high vacuum conditions.
- Manufacture of bespoke sample holders for measurements at zero pressure and at high-pressure using piston-cylinder and Bridgman pressure cells.

Modifications of the Measurement Electronics

Experimental Methods

- Renewal of the heatswitch motor and motor driver.
- Replacement of the magnet power supplies to allow for smooth, bipolar field sweeps, e.g., for Hall effect measurements (only unipolar measurements were previously possible).
- Integration of additional lock-in amplifiers for simultaneous measurements of several samples without multiplexing.
- Integration of high precision current sources and nanovoltmeters for heat capacity and thermal transport measurements.

Modifications of the Measurement and Control Software

- Replacement of the original control software, which was based on NATIONAL INSTRUMENTS LABVIEW.
- Implementation of a new software based on the PYTHON programming language and the open-source software packages NICOS¹ and SLAVE².

Altogether these modifications guarantee a routine operation of the ADR cryostat from room temperature down to $T_{\min} \leq 80$ mK and at sample magnetic fields up to ± 10 T. Measurements can be controlled and automated in a flexible and straightforward way. Several sample sticks are available and have been used for various low-temperature experiments including electrical and thermal transport measurements both at zero pressure and high-pressure as well as ac susceptibility measurements [34]. Moreover a platform for heat capacity measurements at milli-Kelvin temperatures has been set up as part of the Ph.D. thesis of CHRISTOPHER DUVINAGE [35].

1.3.2 Electrical Resistivity and Hall Effect

All electrical transport data were measured using either SIGNAL RECOVERY model 7225 or model 7230 digital lock-in amplifiers. Low excitation currents and an excitation frequency of 22.08 Hz were used to avoid parasitic stray signals. Room temperature low-noise transformers SIGNAL RECOVERY, model 1900, were employed for signal amplification and impedance matching. All transport samples were contacted in a standard four-terminal configuration for measurements of the longitudinal resistivity. For simultaneous measurements of the resistivity and the Hall effect a six-terminal configuration was used. The magneto-resistance and the Hall resistivity were inferred from the measured longitudinal and transverse voltage pickup by symmetrization and anti-symmetrization, respectively.

Wherever applicable, contacts were made by spot welding gold wires of $\varnothing 25$ μm on the sample surface. This includes measurements at zero pressure, high-pressure transport measurements

¹<https://forge.frm2.tum.de/wiki/projects:nicos:index>

²<http://slave.readthedocs.org/en/develop/>

using piston-cylinder cells, and high-pressure transport measurement using uniaxial pressure cells. Due to the small size of samples used with Bridgman cells spot welding is typically not possible. Instead, press contacts of $\varnothing 25 \mu\text{m}$ annealed platinum wire were employed. The leads attached to the sample were soldered to twisted copper pairs.

All transport measurements were carried out either in the helium-free ADR cryostat described in section 1.3.1 or an OXFORD INSTRUMENTS 14/16 T magnet cryostat. Geometry factors were determined from digital photographs recorded with an optical microscope. A conservative estimate of the resulting uncertainty of the resistivity data reported in this thesis is $\sim 25\%$, where contacts were made by means of spot welding. Larger errors of up to 100% may apply to resistivity data recorded with Bridgman pressure cells, where the electrical terminals were made by means of flat press contacts. For better comparison these data were therefore scaled with respect to the data recorded at ambient pressure, see Sec. 1.2.4.

1.3.3 Magnetization

Magnetization measurements were carried out under magnetic fields up to 9 T using an OXFORD INSTRUMENTS vibrating sample magnetometer at an excitation frequency of 62.35 Hz and an excitation amplitude of ~ 1 mm. Samples were glued to a non-magnetic sample holder and fastened using PTFE tape and GE varnish.

Due to their relatively small magnetization no correction for demagnetization effects was required for antiferromagnetic CrB_2 and CuMnSb . For the corresponding magnetization measurements $H = H_{\text{int}}$ was assumed. In contrast MnB_2 develops a significant ferromagnetic moment at low temperatures. For the corresponding susceptibility and magnetization measurements the internal field was calculated as $H_{\text{int}} = H - NM(H)$, where N denotes a geometry-dependent demagnetization factor.

1.3.4 Heat Capacity

Measurements of the heat capacity reported in the context of the studies pursued as part of this thesis have been carried out by ANDREAS BAUER as part of his Ph.D. thesis [5]. Data were recorded using a QUANTUM DESIGN Physical Properties Measurement System (PPMS) and different sizes of heat pulses, 0.1% and 0.5% ; both measurement configurations yielded identical results.

1.4 X-ray and Neutron Diffraction

Magnetic neutron diffraction from polycrystalline (powder) and single crystal samples was used to clarify the nuclear and magnetic structure of CrB_2 (Sec. 2.4), MnB_2 (Sec. 3.3), and CuMnSb (Sec. 4.5). Measurements were carried out at the diffractometers SPODI, RESI, and HEiDi, at the Heinz Maier-Leibnitz Zentrum (MLZ), Garching. The data collected in these experiments

Experimental Methods

were analyzed by means of Rietveld refinements using the software packages FullProf [36] and Jana2006 [37]. Additionally, for all three materials polarized neutron scattering was carried out at the time-of-flight spectrometer DNS at MLZ, Garching.

1.4.1 X-ray Diffraction

The nuclear structure was studied by means of powder and single crystal x-ray diffraction. The x-ray diffraction experiments were carried out by ANATOLIY SENYSHYN (MLZ, Garching) and KLAUDIA HRADIL (X-ray Center Vienna, Technische Universität Wien). As part of the studies of CrB₂ powder x-ray diffraction was carried out using Cu- $K_{\alpha 1}$ radiation with a STOE diffractometer, model STADI P. Single crystal x-ray diffraction was carried out using Mo- $K_{\alpha 1}$ radiation. In Vienna a RIGAKU diffractometer, model AFC7, equipped with a Graphite monochromator and a CCD detector was employed. In Garching a STOE, model Stadijadi diffractometer was used. A PANALYTICAL, model X'Pert3 diffractometer with Cu- $K_{\alpha 1}$ and Cu- $K_{\alpha 2}$ radiation was used during the x-ray powder diffraction study of MnB₂. Finally, for the powder study of CuMnSb a BRUKER, model D8 Advance x-ray diffractometer with Cu- $K_{\alpha 1}$ and Cu- $K_{\alpha 2}$ radiation was employed. In all experiments closed-cycle cryostats were used to provide low temperatures.

1.4.2 Powder Neutron Diffraction

Powder diffraction data were collected at the instrument SPODI at the MLZ, Garching [38]. All measurements were carried out in a Debye-Scherrer geometry using a neutron wavelength of 1.548(1) Å. Higher order contamination were suppressed by means of a Ge(551) monochromator at a scattering angle of 155°. The diffraction data were corrected for geometrical aberrations and the curvature of the Debye-Scherrer rings. Cryogenic and high temperatures were generated by means of a closed-cycle cooler and a vacuum furnace, respectively. For measurements at room temperature and low temperatures the powders were filled into thin-walled Va tubes. For high-temperature measurements of MnB₂ thin-walled Nb cylinders were used instead.

1.4.3 Single Crystal Neutron Diffraction

Single crystal neutron diffraction data were recorded at the four-circle diffractometers RESI and HEiDi at the MLZ, Garching [39, 40]. Measurements at RESI were carried out using thermal neutrons at a wavelength of 1.0408(10) Å. The wavelength was set by means of a Cu(422) monochromator at a fixed scattering angle of 90°. For scans of full reciprocal space planes a MAR345 image plate detector was used. Scattering intensities were integrated using the EVAL-14 method [41]. The use of an image plate detector allowed to scan large portions of the reciprocal space in a short time. This proved to be particularly useful for the determination of the incommensurate magnetic structure of CrB₂. Another benefit of the image plate detector was its ability to reveal diffuse scattering. A counting tube was used for studies of specific

positions in reciprocal space notably to record the temperature dependence of selected Bragg peaks.

Measurements at HEiDi were carried out using hot neutrons at a wavelength of $0.794(1)$ Å. The wavelength was selected by means of a Ge(422) monochromator at a scattering angle of 40° . For the studies of CrB_2 the wavelength was chosen as $1.1659(10)$ Å in order to reduce the peak overlap. Therefore the monochromator was changed to the Ge(331) Bragg reflection while keeping the scattering angle constant at 40° . For all measurements an Er filter was used to remove the $\lambda/2$ -contamination of the monochromatized beam. A 16 mm tube was placed in front of the sample and of a 25 mm tube, followed by a rectangular aperture of size $18 \times 27 \text{ mm}^2$ and $31 \times 25 \text{ mm}^2$ for CuMnSb and CrB_2 , respectively. All data were recorded with a counting tube. Scattering intensities were integrated using the Lehmann-Larsen algorithm [42].

Closed-cycle cryostats were used for studies at low-temperatures at RESI and HEiDi. For measurements at cryogenic temperatures at both instruments the samples were glued to pin-shaped sample holders made of Al using a small amount of low-temperature varnish. An image furnace was used for the high-temperature diffraction study of single crystal MnB_2 at RESI. The sample was glued to a pin-shaped sample holder using a heat resistant ceramic glue.

1.4.4 Polarized Neutron Scattering

Polarized single crystal neutron scattering data were recorded at the cold time-of-flight spectrometer DNS at the MLZ, Garching [43]. All experiments were carried at a neutron wavelength of $4.20(4)$ Å. Scattering intensities were integrated around zero energy transfer with an energy range of 2 meV to 3 meV . Since no selector or filters were available at the time of the measurements the scattered neutrons contained a considerable $\lambda/2$ contamination. These spurious reflections were manually removed from the data. A closed-cycle cryostat was employed to cool the samples below their magnetic ordering temperatures. The samples were glued to a bespoke sample holder made of Al using a small amount of GE varnish. The orientation of the samples was determined using x-ray Laue diffraction. Deviations from the desired orientation were manually reduced to $\leq 1^\circ$ by carefully bending the sample holder.

Polarization analysis was performed to discriminate nuclear and magnetic scattering. Polarized neutron data were recorded using a local coordinate frame which rotates together with the scattering vector $\mathbf{Q} = \mathbf{k}_f - \mathbf{k}_i$ where

- $\mathbf{x} \parallel \mathbf{Q}$,
- $\mathbf{y} \perp \mathbf{Q}$ in the scattering plane,
- $\mathbf{z} \perp \mathbf{Q}$ out of the scattering plane.

Three configurations were used in the polarization analysis (PA) where \mathbf{P} describes the polarization of the incident neutron beam,

- "x-PA":

- polarization of the incident beam: $\mathbf{P} \parallel \mathbf{x} \parallel \mathbf{Q}$
- analyze I_x of the scattered beam given by

$$I_x^{\text{SF}} = \frac{2}{3}I_{\text{inc}}^{\text{spin}} + I_{\text{mag}}^y + I_{\text{mag}}^z \quad (1.5)$$

$$I_x^{\text{NSF}} = \frac{1}{3}I_{\text{inc}}^{\text{spin}} + I_{\text{inc}}^{\text{isot}} + I_{\text{coh}} \quad (1.6)$$

- "y-PA":

- polarization of the incident beam: $\mathbf{P} \parallel \mathbf{y} \perp \mathbf{Q}$
- analyze I_y of the scattered beam given by

$$I_y^{\text{SF}} = \frac{2}{3}I_{\text{inc}}^{\text{spin}} + I_{\text{mag}}^z \quad (1.7)$$

$$I_y^{\text{NSF}} = \frac{1}{3}I_{\text{inc}}^{\text{spin}} + I_{\text{inc}}^{\text{isot}} + I_{\text{coh}} + I_{\text{mag}}^y \quad (1.8)$$

- "z-PA":

- polarization of the incident beam: $\mathbf{P} \parallel \mathbf{z} \perp \mathbf{Q}$
- analyze I_z of the scattered beam given by

$$I_z^{\text{SF}} = \frac{2}{3}I_{\text{inc}}^{\text{spin}} + I_{\text{mag}}^y \quad (1.9)$$

$$I_z^{\text{NSF}} = \frac{1}{3}I_{\text{inc}}^{\text{spin}} + I_{\text{inc}}^{\text{isot}} + I_{\text{coh}} + I_{\text{mag}}^z \quad (1.10)$$

Here SF and NSF denote spin-flip scattering and non spin-flip scattering, respectively. The x, y, and z subscripts refer to the direction of the incident and scattered beam polarization. $I_{\text{inc}}^{\text{spin}}$ is the nuclear spin incoherent scattering. $I_{\text{inc}}^{\text{isot}}$ is the nuclear isotope incoherent scattering. I_{coh} denotes nuclear coherent Bragg scattering. Finally, $I_{\text{mag}}^{y,z}$ is the magnetic scattering intensity resulting from the y and z components of the orbital momentum operator (in the instrumental coordinate system), respectively. The benefits of polarization analysis are twofold. Firstly, nuclear and magnetic scattering can be discriminated by using the "x-PA" configuration. In this setting, besides an isotropic incoherent (background) signal, the SF and NSF channels each contain solely magnetic and nuclear scattering, respectively. Secondly, the polarization components of the magnetic scattering can be determined independently. For instance, I_{mag}^y is obtained by subtracting Eq. 1.7 from Eq. 1.5. Likewise I_{mag}^z can be calculated by subtracting Eq. 1.9 from Eq. 1.5 [44, 45]. This polarization information may eventually be used for magnetic structure determination. As a more detailed account of the neutron polarization method and

its applications would exceed the scope of this thesis, the reader is referred to the standard textbooks.

1.5 Representation Analysis and Magnetic Structure Refinement

The magnetic order of CrB₂, MnB₂, and CuMnSb where determined using a superspace approach as summarized in the following.

1.5.1 The Superspace Approach to Modulated Structures

Modulated structures are characterized by the presence of additional Bragg peaks. These satellite peaks appear irrespective of the physical origin of the modulation which may be, e.g., atomic displacements, occupancies, strains, or magnetic moments. Most importantly, in aperiodic structures where the modulation is incommensurate they cannot be indexed using three integer numbers h , k , and l . Instead, $(3+d)$ indices are required, where $d=1, 2$, or 3 . This reflects a loss of periodicity in three dimensions. Consequently, classical approaches and programs which are all based on periodicity are not suited for the determination of aperiodic structures.

To overcome this limitation the concept of higher-dimensional superspace was developed [46, 47], effectively restoring periodicity. This technique cannot only be applied to the above-mentioned aperiodic (incommensurately modulated) but to any kind of structure. An excellent introduction has been given by WAGNER and SCHÖNLEBER [48]. Within the superspace description of a modulated structure three integer numbers h , k , and l are used to index the main reflections and the reciprocal unit cell associated with these main reflections is established. In some cases both the main and the satellite reflections can be indexed using integer values for h , k , and l alone. The modulation is then referred to as being commensurate, meaning that the periodicity of the modulation matches an integer number of lattice translations of the basic cell. In such a situation besides the superspace approach covered here other techniques may be used to describe the modulation. For instance, the concept of supercells is applicable. In this approach the modulation is handled by choosing the direct space primitive cell such that it fully covers one period of the modulation. Depending on the modulation length the primitive cell can become very large and hence is referred to as supercell. On the other hand, in many cases there is no set of integer numbers h , k , and l , which allows to index all main and satellite reflections, notably incommensurate structures. Since h , k , and l are insufficient for a complete description of the main and the satellite peaks an additional reciprocal vector, referred to as modulation wavevector \mathbf{k} , is introduced. It may be expressed with the help of fractional components of the reciprocal primitive translations \mathbf{b}_i , $\mathbf{k} = \alpha\mathbf{b}_1 + \beta\mathbf{b}_2 + \gamma\mathbf{b}_3$, describing the position of the satellite peaks with respect to their main reflections. Each satellite peak of m th order is located $m \cdot \mathbf{k}$ away from its main reflection. This relationship is illustrated in Fig. 1.12a which displays a schematic depiction of the reciprocal space of a one-dimensionally modulated crystal as shown

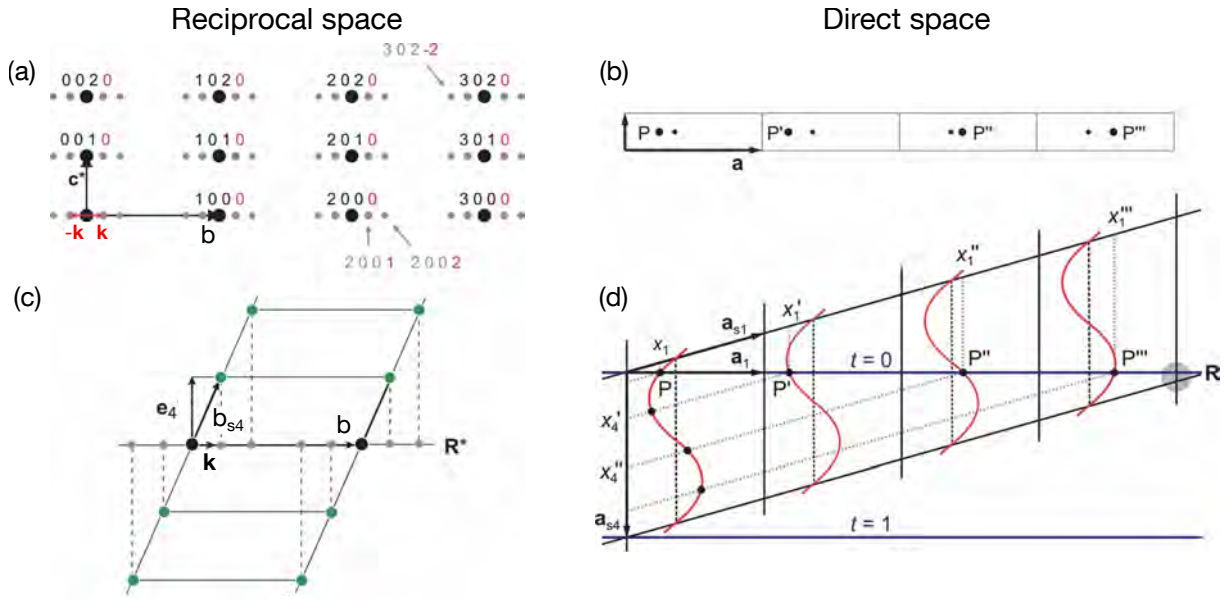


Figure 1.12: Superspace approach to modulated structures. (a) Schematic depiction of the scattering pattern of a one-dimensionally modulated structure which comprises of main reflections (bold black dots) and satellite peaks (small gray dots). The satellite peaks can be indexed only if in addition to the main indices h , k , and l a further index m , which corresponds to the modulation wavevector \mathbf{k} , is introduced. (b) Schematic depiction of a one-dimensionally modulated crystal structure. Small black dots correspond to the atomic positions of the unmodulated basic structure. Bold black dots indicate the atomic positions in the modulated structure, P , P' , P'' , and P''' . In three-dimensional space the structure is aperiodic. (c) Schematic depiction of the reciprocal superspace. For the definition of the vectors \mathbf{e}_4 and \mathbf{b}_{s4} see text. The satellite peaks (grey dots) can be interpreted as projections from superspace (green dots) along \mathbf{b}_{s4} into the three-dimensional reciprocal space. (d) Schematic depiction of the direct superspace. For the definition of the vectors \mathbf{a}_1 , \mathbf{a}_{s1} and \mathbf{a}_{s4} see text. In higher-dimensional superspace the atoms must be understood as one-dimensional objects, so-called *atomic domains*. Their mathematical representations are the *atomic modulation functions* (AMF, red curves). Along \mathbf{a}_{s1} the AMFs exhibit translational symmetry, i.e., in superspace the periodicity of the modulated structure is recovered. The real (three-dimensional) space atomic positions are found by horizontal intersections \mathbf{R} with the AMF. All images adapted from Ref. [48].

in Fig. 1.12b.

The number of wavevectors needed to account for the satellite peaks is referred to as the dimension d of superspace which describes the modulated structure. For a single \mathbf{k} -vector the modulated structure may be described using a (3+1)-dimensional superspace. Accordingly, (3+2)- and (3+3)-dimensional superspaces are employed in the description of double- \mathbf{k} and triple- \mathbf{k} structures. In the interest of simplicity in the following only the case of four dimensions

is considered, i.e. $d = 1$. The presentation is also limited to atomic displacive modulations since they can be visualized more easily than, for instance, magnetic modulations. Any other kind of modulation as well as higher-dimensional ($d = 2, 3$) modulations can be treated in a fully analog way.

To begin with, the concept of higher-dimensional reciprocal superspace is considered. As illustrated in Fig. 1.12c for $d = 1$ the additional fourth dimension of the reciprocal superspace is defined by the unity vector \mathbf{e}_4 which stands perpendicular on the usual reciprocal primitive translations \mathbf{b}_{si} , $i = 1, 2, 3$, (only $\mathbf{b} = \mathbf{b}_{s1}$ is drawn). Here the subscript index “s” was added to indicate that the vector belongs to superspace rather than to three-dimensional space. Then a fourth primitive reciprocal vector \mathbf{b}_{s4} is introduced as the linear combination of \mathbf{k} and \mathbf{e}_4 . With this choice of vectors every satellite peak can be understood as a projection along \mathbf{b}_{s4} into the three-dimensional reciprocal space.

Higher-dimensional reciprocal superspace is connected to a higher-dimensional direct superspace. As illustrated in Fig. 1.12d for $d = 1$ the direct superspace is spanned by four primitive translations \mathbf{a}_{si} , $i = 1, 2, 3, 4$. In higher-dimensional superspace any modulation, even if it was aperiodic in three-dimensional space, can now be described as a periodic (superspace) structure (Fig. 1.12c). For that purpose two basis vectors, \mathbf{a}_{s1} (or \mathbf{a}_{s2} or \mathbf{a}_{s3}) and \mathbf{a}_{s4} are chosen. Here \mathbf{a}_{s4} is perpendicular to the three-dimensional axis that corresponds to the first basis vector (\mathbf{a}_1 if \mathbf{a}_{s1} is chosen). The angle between \mathbf{a}_{s1} and \mathbf{a}_1 is defined by the associated component of the ordering wavevector \mathbf{k} as $\tan(\mathbf{a}_1, \mathbf{a}_{s1}) = \alpha/|\mathbf{a}_1|$.

As a consequence of the higher-dimensional superspace atoms are no longer points but should be understood as one-dimensional objects, referred to as *atomic domains*, along the fourth dimension \mathbf{a}_{s4} and represented by a curve that is periodic along \mathbf{a}_{s4} . The periodic curve along \mathbf{a}_{s4} is termed *atomic modulation function* (AMF). Its shape is determined by experiment. The same holds for the AMFs in the sections $(\mathbf{a}_{s2}, \mathbf{a}_{s4})$ and $(\mathbf{a}_{s3}, \mathbf{a}_{s4})$. In any of these two-dimensional sections - $(\mathbf{a}_{s1}, \mathbf{a}_{s4})$, $(\mathbf{a}_{s2}, \mathbf{a}_{s4})$, and $(\mathbf{a}_{s3}, \mathbf{a}_{s4})$ - the AMF displays a translational symmetry. For $(\mathbf{a}_{s1}, \mathbf{a}_{s4})$ this is shown in Fig. 1.12d. Thus the modulation, even if it is aperiodic in three dimensional space, becomes periodic again in higher-dimensional superspace and translational symmetry is recovered.

To deduce the three-dimensional modulated structure from the superspace description cuts \mathbf{R} were employed that are perpendicular to \mathbf{a}_{s4} and run parallel to \mathbf{a}_1 (or \mathbf{a}_2 or \mathbf{a}_3). The intersections of \mathbf{R} with the AMFs yield the atom positions in three-dimensional space. Different cuts \mathbf{R} only differ in the component x_4 of the vector \mathbf{a}_{s4} . Since the AMFs are wavefunctions with a period of 1 different \mathbf{R} correspond to different phases t of the AMFs. Consequently, different cuts \mathbf{R} will yield different intersections with the AMFs and hence result in different sets of atomic positions. The latter are however related by simple origin shifts, i.e., valid results are obtained from any cut \mathbf{R} . The periodicity of the AMFs enables us to examine the key aspects of a modulated structure by considering only a single AFM intersection rather than an infinite

number thereof: Varying t from $t = 0$ to $t = 1$ provides all atomic displacements occurring anywhere in the three-dimensional structure along \mathbf{R} . Visualizations of the t -dependence of a modulated parameter are commonly referred to as t -plots.

As stated above the superspace approach may also be used to describe other types of modulations. Specifically, in AMFs the size and direction of the magnetic moment vectors may be described.

Recently, the superspace approach for solving modulated structures has been made available through the crystallographic software JANA2006 [37]. In JANA2006 the magnetic structure refinement corresponds to fitting the AFMs to the experimentally observed structure factors. As the result of the refinement procedure the Fourier coefficients of the modulation functions are obtained. Together with the superspace group and k -vectors they fully describe the modulated structure.

1.5.2 Magnetic Structure Refinement from Diffraction Data

The basic procedure applied for the magnetic structure refinement from diffraction data is outlined in Fig. 1.13. For each material powder x-ray, powder neutron diffraction, and single crystal neutron diffraction measurements were carried out. First, the powder diffraction data were refined using the FULLPROF software to confirm the nuclear space group and determine the lattice parameters [36]. Below the magnetic ordering temperature the powder neutron diffraction pattern contained an additional magnetic contribution. These magnetic Bragg peaks were analyzed using the program K-SEARCH which is part of the FULLPROF software suite to find the magnetic modulation wavevectors.

Second, a representation analysis based on the nuclear symmetry, lattice parameters, and modulation vectors was carried out. A built-in tool of JANA2006 was employed for the 1-dimensionally modulated (single- k) magnetic structures of CuMnSb and MnB₂. In the case of CrB₂ where a 3-dimensionally modulated (triple- k) structure must be considered the web applet ISODISTORT was used instead [49]. As a result of the representation analysis, for each material studied several isotropy subgroups of the paramagnetic parent structure were determined. Isotropy subgroups contain those symmetry elements which are preserved during a symmetry-lowering transition, e.g., magnetic ordering. Isotropy subgroups which allow for long-range magnetic order are also referred to as *magnetic superspace groups* or *Shubnikov groups*. For the analysis only these Shubnikov groups were considered. In the case of CrB₂, however, none of the tested Shubnikov groups resulted in satisfactory fits of the observed neutron scattering. Therefore non-isomorphic subgroups of the Shubnikov groups were taken into account. Finally, the magnetic isotropy groups (or their subgroups) served as magnetic model structures and were evaluated by Rietveld refinements of the nuclear and magnetic structure factors obtained from single crystal neutron diffraction. During this last step the JANA2006 crystallographic software which implements the above-mentioned superspace approach [37] was used. Among the

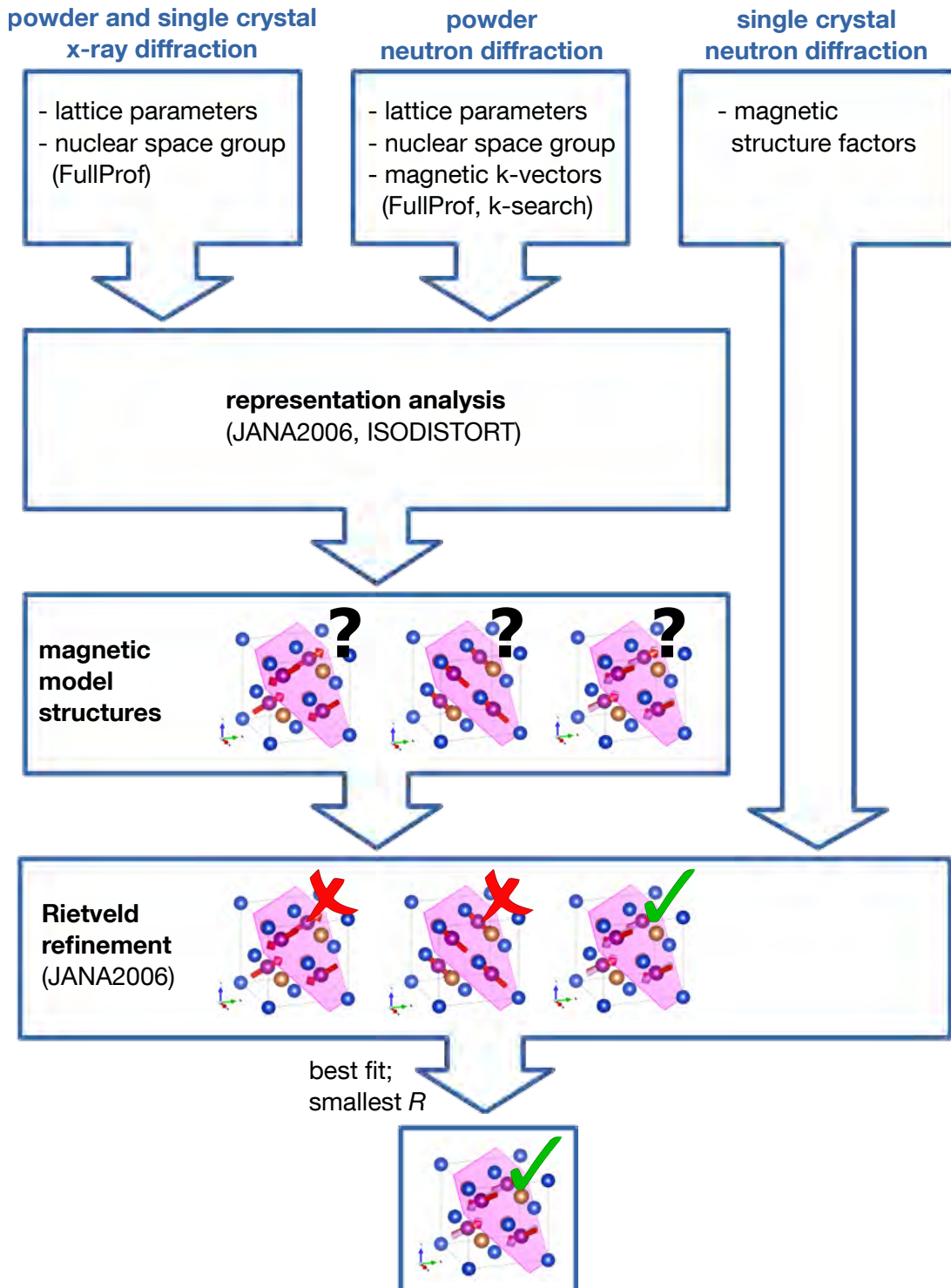


Figure 1.13: Basic procedure for the magnetic structure refinement from diffraction data.

Experimental Methods

various model structures the one which fitted best with the observed scattering and which hence resulted in the smallest R value was selected as the presumably correct magnetic structure.

2.1 Introduction to C32 diborides

The series of C32 diborides, MB_2 , where M is a transition-metal or rare-earth element, has first attracted interest in terms of their mechanical and thermal stability, chemical inertness, and high electrical and thermal conductivity [50, 51]. These properties make the C32 diborides favorable for many technical applications. In addition, despite their common crystal structure the C32 diborides differ strongly with respect to their electronic and magnetic properties. This allows to study an abundance of electronic and magnetic ground states with their fundamental excitations in an overall unchanged crystallographic environment.

The C32 structure is shown schematically in Fig. 2.1. It is characterized by an alternating sequence of hexagonal M and honeycomb B layers which are stacked along the [001] direction. Within the honeycomb B sheets each B atom has three nearest B neighbors. Each M atom

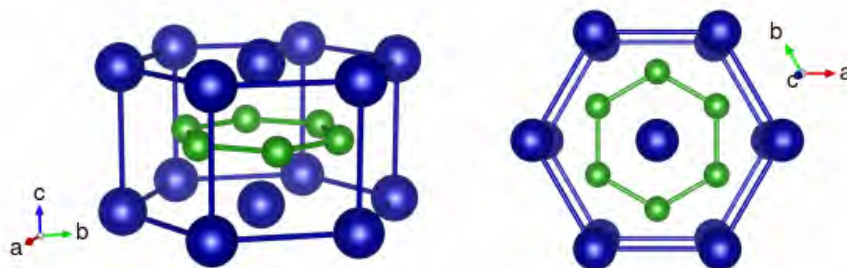


Figure 2.1: Schematic depiction of the C32 crystal structure. Hexagonal metal layers (blue) and honeycomb boron layers (green) are stacked along the [001] direction.

is coordinated by twelve nearest B atoms. In a simple picture the B $2s$ and $2p$ orbitals can be understood in terms of a sp^2 hybrid orbital and a p_z orbital. While the former extends only in the B plane the latter stands vertical on it. The strong σ bonding between neighboring sp^2 orbitals results in a large energy splitting of the bonding and anti-bonding states [52–55]. Altogether a dense packing with strong interlayer interactions is realized.

Recent investigations of the C32 diborides have mainly been motivated by the discovery of superconductivity in MgB₂ [56, 57]. The superconducting phase of MgB₂ is interesting for two reasons: On the one hand it is a showcase for two-band superconductivity with two essentially independent condensates which form in the π and σ bands. On the other hand MgB₂ has a record-high transition temperature, $T_c \approx 39$ K, for a conventional phonon mediated superconductor. The high T_c results from the strong coupling of the conduction electrons with the E_{2g} optical phonon of the B in-plane motion. To date MgB₂ is the only known stoichiometric superconductor among the C32 metal diborides [56, 58]. In NbB₂ superconductivity can be induced by B doping [59–61] whereas in ZrB₂ superconductivity arises presumably from a ZrB₁₂ impurity phase [62, 63]. The superconducting diborides RuB₂ and OsB₂ crystallize in the orthorhombic Pmmm structure [64, 65].

In contrast to the rare occurrence of superconductivity ferromagnetism has been observed in a larger number of C32 diborides, all of which are rare-earth based, e.g., TbB₂, DyB₂, TmB₂, HoB₂ and ErB₂ [66–69]. These compounds have low ordering temperatures of a few K. Antiferromagnetic order in rare-earth based diborides is less common and, like ferromagnetism, observed at low ordering temperatures, for instance in YbB₂ [70].

In contrast antiferromagnetism at moderate and high temperatures is found in transition-metal based C32 compounds, e.g. CrB₂, $T_N \approx 88$ K [71, 72], and MnB₂, $T_N \approx 760$ K [73, 74], which are subject of this chapter and chapter 3, respectively.

2.2 Introduction to CrB₂

CrB₂ has been the subject of theoretical and experimental solid-state research since the mid-1960s. The crystal structure of CrB₂ was first reported by KIESSLING based on powder x-ray diffraction. It was identified as a hexagonal AlB₂ structure, Strukturbericht designation C32, space group P6/mmm (#191), with lattice constants $a = 2.969$ Å and $c = 3.066$ Å [75, 76]. In the crystal lattice the Cr and B atoms occupy the 1a and 2d Wyckoff position, respectively. These findings have been corroborated later in single crystal x-ray and neutron diffraction studies which find similar values for the lattice parameters [71, 77, 78]. A schematic depiction of the C32 structure is shown in Fig. 2.1. The layered structure is characterized by an alternating sequence of hexagonal Cr and honeycomb B sheets which are stacked along the [001] direction. As in any layered material defects, e.g., stacking faults, are likely to occur. However, no account of putative defects or short-range defect structures has been given before.

Band structure calculations hint towards strong electronic correlations in CrB₂ [52–55]. They further suggest consistently that the density of states at the Fermi level is high, dominated by electrons with Cr *d* character, and hence results in a strong Stoner enhancement favoring the development of a magnetic instability. Experimentally an antiferromagnetic character of the electronic correlations was first demonstrated by susceptibility measurements in the paramagnetic high-temperature phase which revealed a large negative Curie-Weiss temperature $\Theta_{\text{CW}} = -1550 \text{ K}$ and an effective fluctuating moment $\mu_{\text{eff}} = 2.07 \mu_{\text{B}}$ [79]. Later BARNES and CREEL identified antiferromagnetic order with $T_{\text{N}} = 88 \text{ K}$ by means of NMR spectroscopy [71].

Details of the antiferromagnetic structure were first addressed in the theoretical investigation by LIU and coworkers [52, 80]. In order to account for powder neutron diffraction data by CASTAING they proposed the formation of a spin density wave (SDW) due to Fermi surface nesting with $\mathbf{k} = 0.26\boldsymbol{\tau}_{001}$ where $\boldsymbol{\tau}_{001}$ is the reciprocal lattice vector of *c*, hence $|\boldsymbol{\tau}_{001}| = 2\pi/c$. Later the SDW type order was rejected by FUNAHASHI ET AL. who suggested on the basis of single crystal neutron diffraction a basically cycloidal spin structure with propagation vector $0.285\boldsymbol{\tau}_{110}$ and an ordered moment $\mu_{\text{s}} = 0.5 \pm 0.1 \mu_{\text{B}}/\text{Cr}$ where the moment vector is turning in the *a-c*-plane [77]. Here $\boldsymbol{\tau}_{110}$ is the reciprocal lattice vector of $\langle 110 \rangle$ and accordingly $|\boldsymbol{\tau}_{110}| = 2\pi/(a/2)$.

The measurements presented in Ref. [77] provide a basic account of the magnetic structure of CrB₂. However the proposed cycloidal spin order was not checked for compatibility with the symmetry of the paramagnetic parent phase. Moreover, considering the small number of Bragg peaks recorded as well as the comparatively large scatter of the magnetic structure factors the quality of the diffraction data reported in Ref. [77] was clearly insufficient for a detailed magnetic structure refinement. Although this measurement hints at a cycloidal structure, more complex spin modulations could not be ruled out. This limitation is due to a variety of difficulties arising in magnetic neutron diffraction of CrB₂.

First, the ordered moment is small resulting in a low magnetic scattering intensity. Second, the magnetic structure is complex, e.g., due to the incommensurate modulation and the hexagonal nuclear symmetry which may result in multiple magnetic domains. Third, significant broadening of nuclear and magnetic Bragg peaks may occur even in high-quality crystals of CrB₂ due to crystalline defects: As any close-packed structure the C32 diborides are prone to planar defects such as stacking faults and small angle grain boundaries. Both types of defects increase the crystalline mosaicity and hinder data analysis. Fourth and final, the scattering signal is dramatically reduced due to the strong neutron absorption of ¹⁰B. To overcome this limitation FUNAHASHI and coworkers have studied thin platelets prepared with natural boron. The drawbacks of the approach are twofold. First, the reduced sample volume causes an overall reduction of the scattering signal. Second, the large neutron absorption due to ¹⁰B requires an accurate extinction correction of the scattering intensities. The latter is technically complex and enhances the scatter of the recorded scattering amplitudes significantly.

More recently KAYA ET AL. have reported spherical neutron polarimetry on single crystal

Cr¹¹B₂ [81]. By using ¹¹B-enriched samples the above-mentioned problems arising from ¹⁰B were avoided. Comparing the polarization of four magnetic satellite peaks to values calculated for different magnetic models the authors confirm a cycloidal spin structure. Their data is fitted best for a cycloid which propagates within a plane that is inclined by $\pm 7.6^\circ$ from the $\langle 110 \rangle^* - c^*$ reciprocal plane, where the \pm sign correspond to two different magnetic domains which were assumed to be equally populated. The investigations by KAYA ET AL. corroborate the cycloidal character of the long-range antiferromagnetic order in this compound. Still the authors consider only on a small number of potential magnetic structures and do not take into account the symmetry of the paramagnetic phase, e.g., by means of a representation analysis. Moreover, only four satellite peaks have been studied. Altogether, other cycloidal spin structures with similar polarization as the one reported in Ref. [81] cannot be ruled out.

The field dependence of the magnetic structure was addressed in a single study only, where NMR spectroscopy at $\mu_0 H \approx 7.5$ T on single crystal samples hinted at a combination of commensurate and incommensurate order. These NMR data further seem to be inconsistent with the cycloidal spin structures proposed so far [82].

Several experimental investigations addressed the character of the antiferromagnetism in CrB₂. On the one hand, NMR spectroscopy suggested that CrB₂ shares characteristics of local-moment and itinerant magnetism [83–85]. On the other hand measurements of the magneto-volume effect indicated a thermal expansion coefficient comparable with weak itinerant ferromagnets such as ZrZn₂, hence suggesting an itinerant character [86–88]. Itinerant antiferromagnetism is also supported by low-temperature resistivity and specific heat measurements [89].

Investigations of the low-temperature bulk and transport properties of CrB₂ established that this compound is a good metal and, most importantly, exhibits strong spin fluctuations and a magnetic phase transition at about $T_N = 88$ K. AC susceptibility measurements in zero field were reported, e.g., in Refs. [72, 79, 88, 90–94]. They found consistently a Curie-Weiss behavior at high temperatures with a pronounced maximum at T_N . A large negative Curie-Weiss temperature, $-\Theta_{CW} \gg T_N$, indicated strong antiferromagnetic correlations.

Coarse heat capacity data at zero magnetic field were reported in Ref. [72, 89]. A lambda-shaped anomaly at T_N was suggestive of a second-order phase transition. The relatively large Sommerfeld coefficient to the electronic specific heat, $\gamma = 13.6$ mJ mol⁻¹ K² was typical for *d*-metals with moderate correlations.

A few investigations addressed the electrical transport properties of CrB₂. They reported consistently low values of the resistivity characteristic of good metallic behavior. With decreasing temperature ρ drops monotonically exhibiting a kink around T_N . The analysis of the temperature dependence in the framework of the Landau Fermi liquid theory hints towards strong spin fluctuations, consistent with the enhancement of the magnetic susceptibility and the large electronic specific heat. Early work provided, again, only coarse low-temperature data recorded using a polycrystalline sample [89, 91]. Polycrystalline samples were examined in a more re-

cent unpublished study by BŒUF as well [8]. TANAKA ET AL. reported measurements of the resistivity and Hall effect of single crystal samples. They addressed, for the first time, the role of crystalline anisotropies which appeared to be small. Again only coarse data were presented. The effect of an external magnetic field on the normal resistivity has not been accounted for in any study at all.

Several studies addressed the elastic properties of CrB₂. High-temperature measurements were reported by OKAMOTO ET AL. revealing an elastic anisotropy characterized by a hard *a* and a soft *c*-axis [95]. More recently measurements of the elastic constants between room temperature down to just above T_N were reported [96]. The room temperature elastic constants given in Ref. [96] are consistent with Ref. [95]. Their variation upon cooling to T_N is $< 10\%$ for the diagonal elements of the elastic tensor as well as for c_{13} . A significant elastic hardening was observed only for c_{12} which increases by about 50% . It is interesting to note that depending on the measurement technique employed, namely resonant ultrasound spectroscopy or inelastic x-ray scattering, the authors observed different elastic properties near the magnetic ordering transition. Significant elastic anomalies close to T_N were observed only with the ultrasound technique, whereas no anomalies could be detected by x-rays. These discrepancies were attributed to the movement of magnetic domain walls in response to ultrasound waves attenuating the resonance signal. In contrast, measurement techniques which probe the elastic properties microscopically, e.g., x-ray scattering, are insensitive to the domain wall motion.

Investigation of the high-pressure phase diagram of CrB₂, reported in this thesis, were motivated by the systematic search for superconductivity in the class of C32 diborides and quantum criticality of an itinerant antiferromagnet [8, 58]. Due to the small magnetization of antiferromagnetic CrB₂ which prohibits, e.g., magnetization and susceptibility measurements in conjunction with pressure cells high-pressure studies have so far concentrated on the electrical resistivity. Within the pressure range studied, no pressure-induced electronic instabilities were observed [8, 97]. Conflicting results were reported concerning the effect of pressure on T_N . While BŒUF reported a small suppression, $dT_N/dp \approx -2.5 \text{ K GPa}^{-1}$, a tiny enhancement was found by GRECHNEV ET AL., $dT_N/dp \approx 1 \text{ K GPa}^{-1}$. Measurements carried out as part of the author's diploma thesis suggested that this discrepancy was attributed to small deviations from perfectly hydrostatic conditions [9]. Due to the elastic anisotropy of CrB₂ small uniaxial pressure components may result in significant changes of the bulk and transport properties in the high-pressure phase of this compound. Still in none of the previous studies these technical difficulties were taken into consideration.

Almost all previous experiments were carried out on polycrystalline samples and hence did not allow to study the role of crystalline and magnetic anisotropies. In fact this question was to date addressed only in a single study by TANAKA and coworkers who have grown single crystal CrB₂ by means of radio-frequency heated float zoning [92]. With the exception of Ref. [92], in essentially all previous studies fairly pronounced Curie tails were observed in the low-temperature

susceptibility suggesting the presence of ferromagnetic impurities. Particularly in *d* and *f* metal compounds such ferromagnetic impurities may easily influence the intrinsic physical properties and even suppress subtle correlation effects, e.g., magnetic order or superconductivity. Most samples studied contained natural B (19.9 % ¹⁰B, 80.1 % ¹¹B) prohibiting detailed neutron scattering studies of the magnetic structure and excitations of CrB₂.

With this in mind high-quality single crystal samples which have been synthesized from high-purity starting elements [5, 98] were studied as part of this thesis. In addition these crystals were grown with an ¹¹B enrichment which significantly reduces neutron absorption. Therefore these high-quality samples allowed, for the first time, extensive neutron scattering investigations on large single crystals of CrB₂. As part of this thesis single crystal neutron diffraction was employed to study the complex magnetic structure of CrB₂ (Sec. 2.4). Moreover, polarized neutrons were used to investigate the diffuse scattering which may originate from short-range order of crystalline defects or magnetic frustration (Sec. 2.3.3). Inelastic neutron scattering experiments were carried out by GEORG BRANDL as part of his Ph.D. thesis. They reveal the presence of an abundance of strongly damped spin excitations both above and below the Néel temperature [99].

The high crystalline quality of our single crystal samples is consistently inferred from both our scattering experiments and low-temperature bulk and transport measurements. It is further corroborated by the very first demonstration of the de Haas-van Alphen (dHvA) effect in CrB₂ where measurements at magnetic fields up to $\mu_0 H = 14$ T and at a minimum temperature of 300 mK allowed to map out the angular dependence of three distinct dHvA frequencies [100, 101]. A comparison with band structure calculations and the resulting Fermi surface allowed to attribute two frequencies to electron-like Fermi surface sheets derived from bands with strong B *p_{x,y}* character whereas the third frequency may be related to Cr *d* bands.

This chapter reports on the results of an extensive experimental investigation of single crystal CrB₂. The nuclear and magnetic structure determined on the basis of comprehensive x-ray and neutron diffraction measurements of both powder and single crystal samples will be addressed first. Unlike the authors of Ref. [77] who studied thin platelets prepared with natural boron in the neutron scattering experiments reported below powder samples and large high-quality single crystal samples of Cr¹¹B₂ were investigated. The ¹¹B enrichment allows for sensible scattering intensities despite the overall small magnetic moment. Moreover, no extinction correction of the diffraction data is necessary hence reducing the technical complexity and boosting the accuracy of the structural refinement significantly.

X-ray and neutron diffraction data confirmed consistently the layered C32 nuclear structure of CrB₂. The question of crystal defects and defect structure formation was addressed for the first time by means of single crystal polarized neutron scattering. The experiment reveals well-defined diffuse streaks within the hexagonal basal plane suggesting the presence and short-range ordering of crystalline defects.

Magnetic neutron diffraction confirms the formation of long-range antiferromagnetic order below a moderate Néel temperature, $T_N = 88.5$ K, consistently observed in the transport, magnetization, specific heat, and neutron scattering data. Based on a state-of-the-art representation analysis and Rietveld refinements potential magnetic structures were considered. Whereas earlier reports suggested a simple cycloidal magnetic order [77] our analysis supports a complex incommensurate multi-k state with a small ordered moment $m_s \approx 0.59 \mu_B/\text{Cr}$. Its topological character is highly non-trivial and corresponds to a triangular vortex lattice. In fact, it may represent the first example for such a state in an itinerant magnet (Secs. 2.3 and 2.4).

Next, comprehensive measurements of the low-temperature heat capacity, magnetization, resistivity and Hall effect are reported. Accurate data with high point density were recorded using the same high-quality single crystal samples studied in the diffraction experiments. Taken together these establish CrB₂ as a weak itinerant antiferromagnet par excellence: As a hallmark of itinerant magnetism all bulk and transport properties reflect a remarkable stability of the magnetic order. The ordered moment $m_s \approx 0.59 \mu_B/\text{Cr}$ determined from magnetic neutron diffraction is strongly exceeded by the effective fluctuating moment $m_{\text{eff}} = 2.2 \mu_B$ seen in magnetization measurements. The latter also suggest an unsaturated magnetization up to the highest field studied. Finally, a metallic resistivity with a low-temperature residual value of a few $\mu\Omega \text{ cm}$ is observed.

The experiments reported here do not only corroborate weak itinerant antiferromagnetism in CrB₂ but also address the question of geometric frustration and magnetic anisotropies not addressed before for this hexagonal compound. From the ratio of the large negative Curie-Weiss temperature, $\Theta_{\text{CW}} = -750$ K and the ordering temperature $T_N = 88.5$ K strong geometric frustration may be inferred. Moreover, the magnetization and resistivity measurements hint at a small easy-plane anisotropy and an abundance of spin fluctuations even at $T > T_N$ (Sec. 2.5).

Finally, the possibility of electronic instabilities in CrB₂ other than long-range magnetic order were explored. This interest is mainly driven by the observation of superconductivity in several isostructural compounds, in particular MgB₂ and NbB₂ [56, 58, 59] as well as the specific heat and magnetic neutron diffraction data. The latter suggest additional electronic excitations at intermediate temperatures which could be connected to an incipient electronic instability, e.g., charge order or superconductivity.

In a search for such potential electronic instabilities a comprehensive series of high-pressure transport measurements combining hydrostatic, purely uniaxial, and quasi-hydrostatic pressure conditions was carried out. The experiments allowed, for the first time, to analyze the effect of uniaxial pressure components on the transport properties of this compound suggesting a high-pressure phase diagram of CrB₂ which is essentially determined by the ratio of the lattice parameters c/a . Consistently, a pronounced low-temperature resistivity anomaly which may be attributed to an incipient electronic instability is observed under quasi-hydrostatic pressure when c/a exceeds a critical value. The experimental signature of this instability is strongly

reminiscent of incipient superconductivity (Sec. 2.6).

2.3 Nuclear Structure of CrB₂

The nuclear structure of CrB₂ was investigated by means of powder and single crystal x-ray diffraction as well as powder and single crystal neutron diffraction. Furthermore the diffuse nuclear scattering was studied to check for a putative defect structure which may develop, e.g., due to stacking faults or the formation of short-range ordered atomic vacancies.

The results of the x-ray diffraction of single crystal and polycrystalline (powder) samples will be presented first. These data confirm the C32 hexagonal nuclear structure of CrB₂ and demonstrate the high crystalline quality and purity of the single crystals. Following this the temperature dependence of the lattice parameters is discussed. In the last part of this section the results of our diffuse single crystal neutron scattering study are reported. The use of polarized neutrons allowed to discriminate nuclear and magnetic scattering contributions. While no magnetic diffuse scattering was observed sharply confined diffuse streaks expanding within the hexagonal basal plane suggested the formation of a nuclear defect structure.

2.3.1 Powder X-Ray Diffraction

Powder x-ray diffraction was carried out for two samples. In one case the powder was prepared from a single crystal specimen cut off the ingot SFZ-118. (Samples for single crystal x-ray and neutron diffraction were cut from the same ingot; these data will be presented in Sec. 2.3.2) In the other case the powder was prepared from a polycrystalline batch, AMP-008, which was prepared by GEORG BENKA using an arc melting furnace [3].

Fig. 2.2 shows typical x-ray diffraction data which were used for refinements of the structural parameters of CrB₂. In accordance with the hitherto reported structural data a single C32 phase was chosen as nuclear model for all fits. Fig. 2.2a shows a typical room temperature powder x-ray diffraction pattern of the first sample, i.e., powder prepared from single crystal material. The structural refinement agrees well with the experimental data, thus confirming the reported C32 crystal structure of CrB₂. Particularly, the absence of any additional reflections corroborates the phase purity of our sample SFZ-118. Fig. 2.2b collects several x-ray powder diffraction patterns recorded for sample AMP-008 at various temperatures. Our refinement confirms the C32 crystal symmetry both at room temperature and at cryogenic temperatures. Besides the nuclear Bragg peaks of CrB₂ additional weak reflections were observed suggesting that, in contrast to the first sample, powders prepared from the arc-melted sample AMP-008 contain a small fraction of impurity phases.

As the preparation of CrB₂ by means of arc-melting is straightforward when compared to, e.g., optical float-zoning it is interesting to consider the quality of the polycrystalline specimens obtained with this method more carefully. Therefore the composition of two powder samples

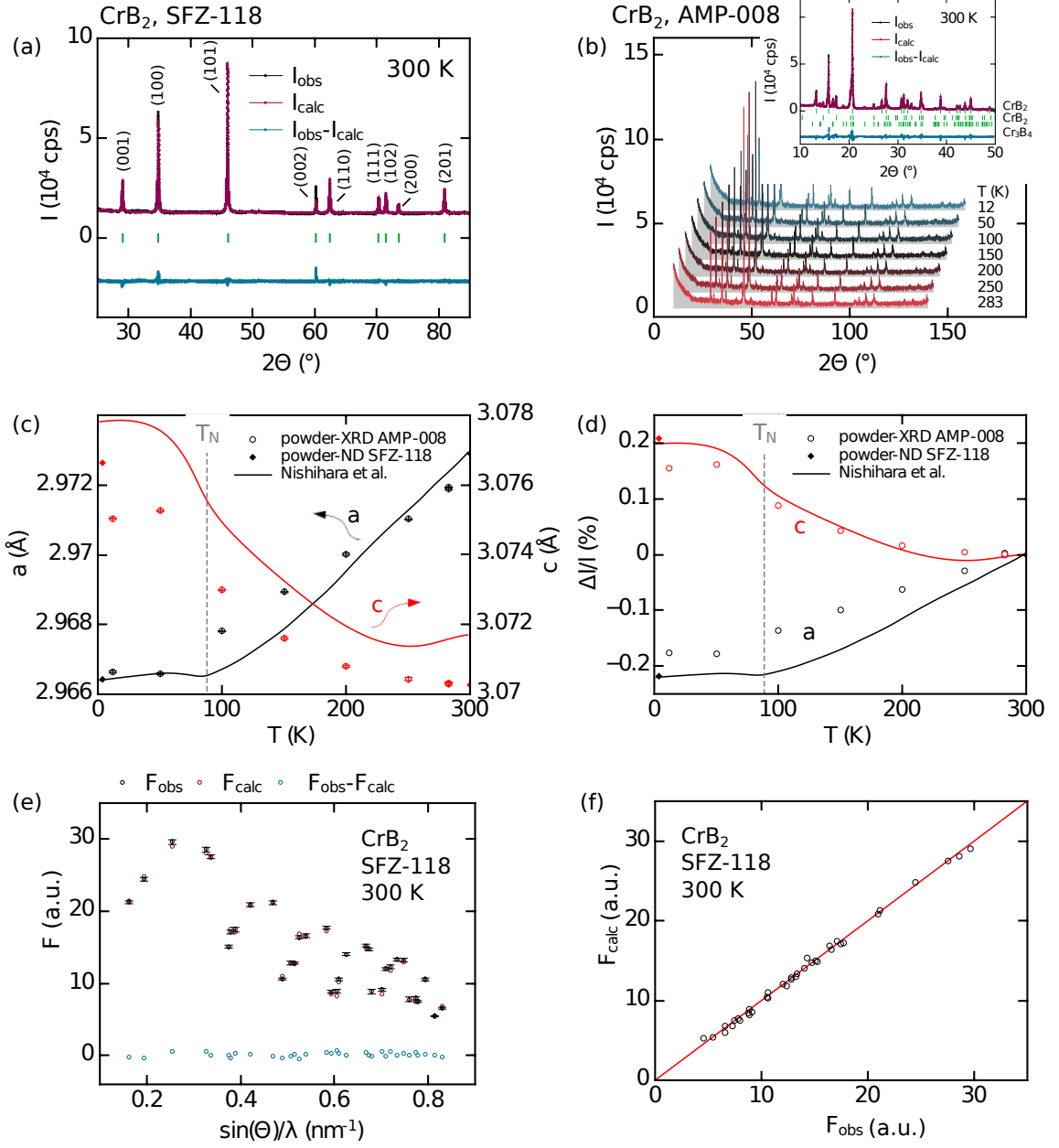


Figure 2.2: X-ray diffraction of CrB_2 . (a) Powder x-ray diffraction and refinement of the C32 crystal structure. (b) Powder x-ray diffraction at various temperatures. The inset shows data taken at 300 K with the corresponding refinement. Three phases have been identified, CrB_2 , CrB , and Cr_3B_4 . (c) Absolute change of the lattice parameters as a function of temperature. Data indicated by the solid lines were taken from Ref. [88] (d) Relative change of of the lattice parameters as a function of temperature. Data indicated by the solid lines were taken from Ref. [88] (e) Single crystal x-ray diffraction data along with their refinement based on the C32 crystal structure. F_{obs} and F_{calc} are the recorded and calculated structure factors, respectively. (f) Calculated structure factors compared to the ones observed in single crystal x-ray diffraction.

prepared from AMP-008 were analyzed quantitatively. By refining the observed diffraction data the impurity phases could be identified as Cr₃B₄ (space group # 71, Immm) and CrB (space group # 63, Cmcm), cf. inset of Fig. 2.2b. The volume fractions of all three phases, CrB₂, Cr₃B₄, and CrB, were determined as 64:17:19 and 94:6:0 for sample 1 and sample 2, respectively. The large variation of the chemical composition indicates a rather strong heterogeneity of the arc-melted batch AMP-008. On the other hand CrB₂ clearly represents the largest volume fraction, particularly when the second sample is considered. The latter sample was therefore used to study the evolution of the lattice parameters as a function of temperature.

Temperature Dependence of the Lattice Parameters

As mentioned above the C32 crystal symmetry remains unchanged down to cryogenic temperatures. Fig. 2.2c shows the hexagonal lattice constants $a = 2.97 \text{ \AA}$ and $c = 3.07 \text{ \AA}$ as a function of temperature. With decreasing temperature a first decreases. Around the Néel temperature, $T_N = 89 \text{ K}$, a passes through a faint minimum and eventually increases again. The opposite behavior is observed for the c axis: With decreasing temperature c first increases, exhibits a maximum around T_N , and finally shrinks again. The relative change of the lattice parameters is shown in Fig. 2.2d. It is negative for a and positive for c with a minimum of $\Delta a/a \approx -0.18 \%$ and a maximum of $\Delta c/c \approx 0.16 \%$, respectively.

The observed temperature dependence of the lattice parameters is in fair agreement with thermal expansion measurements reported by NISHIHARA ET AL. [88]. For a direct comparison the data from Ref. [88] were added as solid lines in Fig. 2.2c and Fig. 2.2d. Clearly the same qualitative temperature dependence is observed. Considering the absolute size of the lattice parameters x-ray diffraction and thermal expansion measurements almost coincide for the a axis. Compared to the data recorded as part of this thesis the c axis reported in Ref. [88] exhibits an almost temperature independent offset of $\sim 1 \cdot 10^{-3} \text{ \AA}$, i.e. 0.03 % at high temperatures. At the lowest temperature studied the difference is larger, reaching 0.09 %. As concerns the relative length change, $\Delta l/l$, x-ray diffraction and thermal expansion measurements almost coincide for the c axis, whereas a small deviation at high temperatures is observed for the a axis. In fact these discrepancies may be either due to the different methods used or subtle differences in the sample preparation. The samples both in Ref. [88] and in this study were prepared by arc-melting. The samples in Ref. [88] were however additionally annealed. It is well known that arc-melted samples can suffer from internal strain due to the abrupt temperature changes, notably fast cooling (“quenching”). Annealing is suited to reduce such internal strain. Furthermore, annealing commonly supports the growth of grains. In some cases, such as Ni₃Al, this may even allow to transform polycrystalline into single crystal grains. Taken together it seems plausible that the crystalline quality of annealed CrB₂ polycrystals is superior compared to as-grown polycrystalline samples and that their physical properties resemble more closely those of single crystals. The latter is consistent with powder neutron diffraction measurements of samples

prepared from single crystal material, SFZ-118, where data taken at room temperature and at 4 K fit the thermal expansion data of Ref. [88] almost perfectly, cf. full symbols in Fig. 2.2c and Fig. 2.2d. A more detailed discussion of these powder neutron diffraction experiments is presented in Sec. 2.4.1. It is conceivable that the polycrystalline samples studied in this thesis may exhibit a very similar temperature dependence as those studied in Ref. [88] when annealed. This question is currently addressed by GEORG BENKA as part of his Ph.D. thesis [4].

2.3.2 Single Crystal X-Ray Diffraction

Single crystal x-ray diffraction was carried out at room temperature using a small sample that was cleaved off the single crystal ingot SFZ-118. The experimental data are shown in Fig. 2.2e along with the refinement. The structural model, which is again based on the C32 structure, describes nicely the observed scattering. All Bragg peaks are accounted for and may be fitted within the experimental error. This may be seen better by plotting the calculated structure factors F_{calc} versus the observed structure factors F_{obs} , as shown in Fig. 2.2f. The measurement also demonstrates that both the powder and the single crystal sample prepared from ingot SFZ-118 are phase-pure. Together with the bulk and transport data presented below this corroborates the extraordinary high crystalline quality of this sample.

2.3.3 Polarized Single Crystal Neutron Diffraction

Investigations of the diffuse scattering of CrB₂ were carried out using a monochromatic and polarized neutron beam, $\lambda = 4.2 \text{ \AA}$, at the instrument DNS, located at the MLZ, Garching. The instrument was configured to allow for a discrimination of magnetic and nuclear scattering. Hence scattering recorded in the spin-flip channel (SF) was purely magnetic in origin whereas scattering recorded in the non spin-flip channel (NSF) was purely nuclear in origin. The reciprocal hexagonal basal plane ($hk0$), was studied by rotating the single crystal sample around the axis perpendicular to the scattering plane, i.e., the crystallographic c -axis. To ensure that the observed scattering was intrinsic to the material and not a specific feature of an individual sample the same measurements were carried out for two samples which were cut from different single crystal ingots of ¹¹B-enriched CrB₂, SFZ-118 and SFZ-162. Sample SFZ-118 was a cylindrical rod with dimensions $\varnothing 4 \text{ mm} \times 9 \text{ mm}$. Sample SFZ-162 was a cube with an edge length of 3.5 mm. The results obtained from both specimens are fully consistent. The presentation and discussion is therefore limited to the first set of measurements on sample SFZ-118.

Typical data taken at a temperature of 3.6 K are shown in Fig. 2.3. The top row presents the intensity distribution recorded in the spin-flip channel, i.e., magnetic scattering. At high intensity, Fig. 2.3a, several magnetic Bragg peaks are observed which form a sixfold magnetic scattering pattern around each nuclear main reflection. Note that the full sixfold pattern cannot be resolved due to instrumental constraints. However, adding the Friedel partner associated to each observed satellite peak the sixfold symmetry becomes evident. This agrees nicely with our

The Weak Itinerant Antiferromagnet CrB₂

sample	T K	phase	a (Å)	b (Å)	c (Å)	R	wR
powder x-ray diffraction							
SFZ-118	~ 300	CrB ₂	2.9722	2.9722	3.0707	1.04	1.91
AMP-008, sample #1	~ 300	CrB ₂	2.9732	2.9732	3.0715	6.37	8.87
		CrB	2.9674	7.8750	2.9326		
		Cr ₃ B ₄	2.989	13.0304	2.9517		
AMP-008, sample #2	283	CrB ₂	2.9719	2.9719	3.0703	4.33	6.82
		Cr ₃ B ₄	2.9839	13.02	2.9525		
AMP-008, sample #2	250	CrB ₂	2.9710	2.9710	3.0704	4.41	6.57
		Cr ₃ B ₄	2.9821	13.0191	2.9522		
AMP-008, sample #2	200	CrB ₂	2.9700	2.9700	3.0708	4.39	6.47
		Cr ₃ B ₄	2.9804	13.0186	2.9516		
AMP-008, sample #2	150	CrB ₂	2.9689	2.9689	3.0716	4.40	6.51
		Cr ₃ B ₄	2.9788	13.0177	2.9512		
AMP-008, sample #2	100	CrB ₂	2.9678	2.9678	3.073	4.38	6.48
		Cr ₃ B ₄	2.9774	13.0176	2.9510		
AMP-008, sample #2	50	CrB ₂	2.9666	2.9666	3.0753	4.38	6.45
		Cr ₃ B ₄	2.9763	13.0182	2.9507		
AMP-008, sample #2	12	CrB ₂	2.9666	2.9666	3.0750	4.47	6.56
		Cr ₃ B ₄	2.9763	13.0177	2.9506		
single crystal x-ray diffraction							
SFZ-118	~ 300	CrB ₂	2.9729	2.9722	3.0717	3.32	4.25
powder neutron diffraction							
SFZ-118, growth start	~ 300	CrB ₂	2.9729	2.9729	3.0703	4.51	6.00
		Cr ₃ B ₄	2.9852	13.0204	2.9523		
SFZ-118, growth start	4	CrB ₂ (mag.)	2.9664	2.9664	3.0767	4.25	5.66
		Cr ₃ B ₄	2.9757	13.0177	2.9508		

Table 2.1: Refinements of the nuclear structure of CrB₂. The structural model was based on the hexagonal C32 space group symmetry. Impurity phases, Cr₃B₄ and CrB, were fitted based on the orthorhombic Immm and Cmcmm space group symmetry, respectively. The volume fractions of CrB₂, Cr₃B₄, and CrB were 64:17:19 and 94:6:0 for AMP-008 sample #1 and sample #2, respectively. For powder diffraction data R and wR are the reliability factors of the powder profiles' fits. For single crystal data R and wR refer to the refinement of the structure factors F^2 . The simple spin cycloid suggested in Ref. [77] was chosen as magnetic model structure to account for the magnetic Bragg peaks observed in powder neutron diffraction of SFZ-118 at 4K, cf. Sec. 2.4.1.

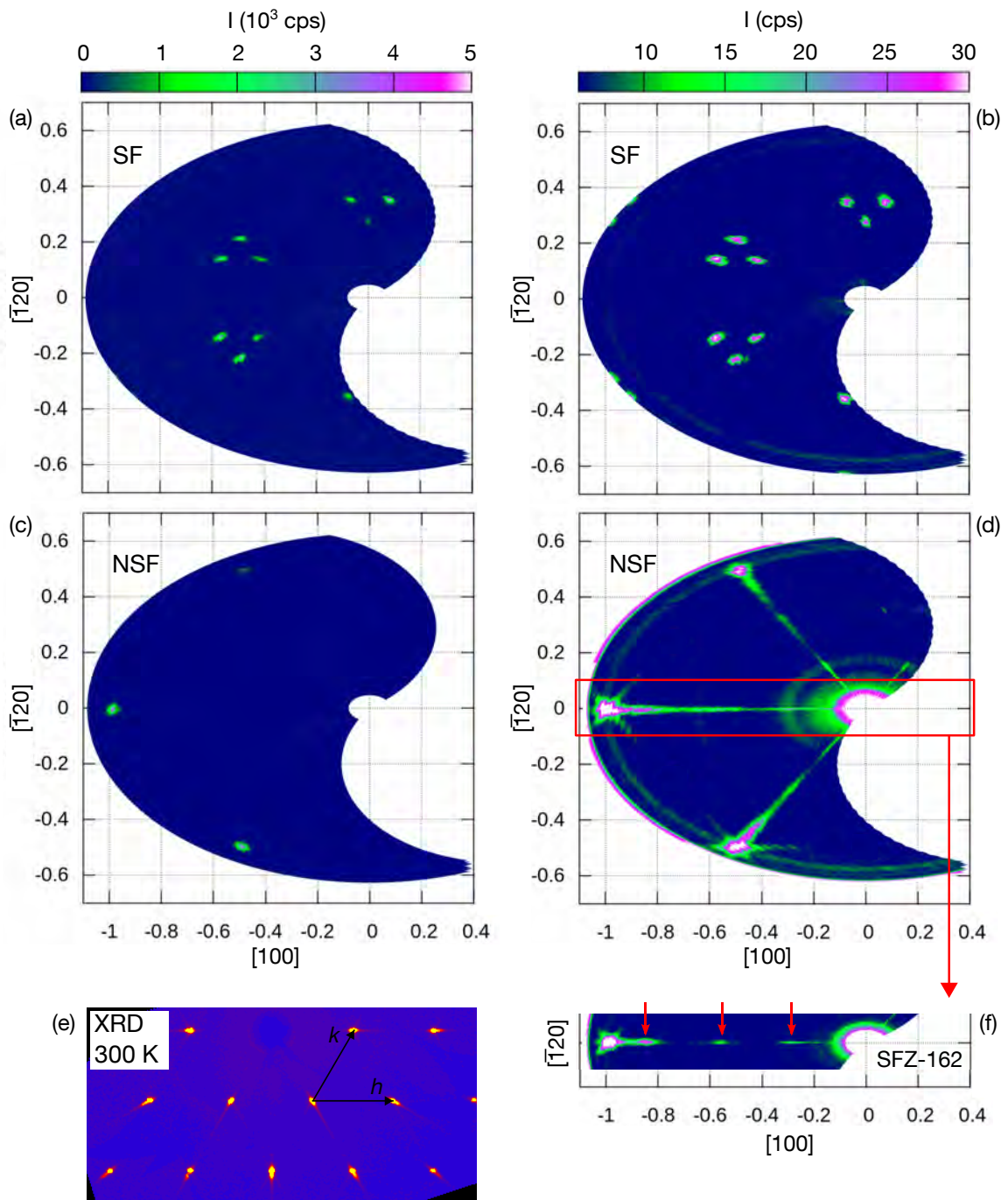


Figure 2.3: Polarized neutron scattering in the $(hk0)$ reciprocal space plane of CrB₂, $T = 3.6$ K. Polarization analysis allows to discriminate nuclear and magnetic scattering. Top row: Spin-flip channel showing only magnetic contributions. Neither at high, (a), nor at low scattering intensity, (b), diffuse scattering is observed. Bottom row: Non spin-flip channel containing only nuclear contributions. At high intensity, (c), three nuclear Bragg peaks are observed. Closer inspection of the nuclear scattering at low intensity, (d), reveals diffuse streaks in between the Bragg peaks. (e) Room temperature single crystal x-ray diffraction with long exposure times corroborates the nuclear diffuse scattering. (f) Faint maxima of intensity are distributed along the diffuse streaks as shown here for the second sample studied, SFZ-162.

data taken at the single crystal diffractometers RESI and HEiDi (Secs. 2.4.2 and 2.4.3). As will be discussed below, the sixfold pattern may be explained by the complex incommensurate magnetic structure shown in Fig. 2.13. At low intensity, Fig. 2.3b, the magnetic signal in the $(hk0)$ plane is essentially unchanged. In particular there are no indications of diffuse scattering.

Turning to the non spin-flip signal, i.e., the nuclear scattering shown in Fig. 2.3c, three nuclear Bragg peaks are observed, namely (anti-clockwise from top to bottom) $(\bar{1}10)$, $(\bar{1}00)$, and $(0\bar{1}0)$. At low intensity, Fig. 2.3d, diffuse streaks are observed which expand in between the Bragg peaks and the direct beam. Closer inspection reveals additional faint Bragg peaks distributed along these lines of diffuse scattering. They may arise from a nuclear periodic structure that is incommensurate with the C32 lattice, i.e., a superstructure. The superstructure peaks are more pronounced for the second sample, SFZ-162, as shown in Fig. 2.3f.

The observation of both diffuse streaks and superstructure peaks is consistent with the neutron diffraction at RESI and HEiDi, cf. Sec. 2.4.3 and Sec. 2.4.2. As the latter employed unpolarized neutrons the origin of both experimental signatures could however not be clarified unambiguously from the data recorded at RESI and HEiDi. In contrast, the polarization analysis available at DNS allows to attribute both features to the nuclear scattering. In turn the diffuse scattering should also be observable by means of x-ray diffraction. Indeed single crystal x-ray diffraction with long exposure times recorded very recently corroborates the presence of the diffuse streaks even at room temperature, cf. Fig. 2.3e. The observation of the faint superstructure peaks could so far been not be confirmed in x-ray scattering due to instrumental limitations.

2.3.4 Discussion

The diffraction data recorded do not display any diffuse magnetic scattering. Instead, the observation of distinct diffuse streaks hints at the formation of a crystalline defect structure. Moreover, additional peaks distributed along the diffuse streaks suggest a nuclear superstructure. Even though both effects may not necessarily be connected a mutual interplay may be inferred from the observation that the superstructure peaks are distributed exclusively along the lines of diffuse scattering. This is also supported by the single crystal diffraction data which confirm the existence of the superstructure peaks. As presented in Sec. 2.4.3 it seems as if the latter can be indexed using a modulation wave vector which is mathematically closely connected to the magnetic propagation vector.

Several types of crystalline defect structures may cause diffuse streaks. For instance, similar diffuse streaks are frequently observed for layered fcc and hcp structures which are prone to stacking faults. The latter, however, give rise to diffuse streaks along the direction of the close-packed stacking, i.e., along the $[111]$ and $[001]$ direction, respectively. Considering CrB₂ as hcp structure with stacking faults, diffuse streaks along the $[001]$ direction would be expected. It is thus unlikely that this microscopic mechanism can account for our observation of diffuse scattering within the $(hk0)$ reciprocal space plane.

Alternatively, the diffuse scattering may be due to the short-range ordering of point defects, e.g., B vacancies. In fact vacancy ordering has been observed in several materials stabilizing in an AlB₂ prototype structure and related structures. Moreover, theoretical investigations suggest vacancy ordering in elemental B as well as two-dimensional B layers [102–107]. In the case of CrB₂, the high vapor pressure of B may cause B losses during crystal growth. This may result in deviations from the stoichiometric starting composition and eventually trigger the formation of B vacancies in the crystal lattice. The dependence of the nuclear structure of CrB₂ on its B content has been the subject of a recent theoretical investigation. Based on first-principles calculations the authors of Ref. [108] argue that the AlB₂ structure of CrB₂ is destabilized upon introduction of B vacancies in favor of the ReB₂-type structure (space group P6₃/mmc). Since x-ray and neutron diffraction data are fully consistent with the AlB₂-type structure the presence of ReB₂-type impurity phase may be ruled out in the samples studied in this thesis. It suggests, moreover, that the B deficiency of the samples is small, corroborating the high quality of the single crystals. At present it is not clear whether a pronounced lack of B will drive a structural transformation to ReB₂-type CrB₂. By growing a series of B-depleted single crystals CrB_{2-x} GEORG BENKA currently addressed this question as part of his Ph.D. thesis [4].

2.3.5 Summary

In summary the x-ray and neutron scattering experiments carried out as part of this thesis confirm C32 structure of CrB₂ both at room temperature and at cryogenic temperatures. The main results of our refinements are summarized in Tab. 2.1, where small R factors underscore the excellent agreement between the refinement and the experimental data. Moreover these measurements confirm excellent phase purity and high quality of the single crystal samples studied. It is also helpful to remark that all structural information obtained from powder and single crystal neutron diffraction are fully consistent with the x-ray data but, due to less satisfactory statistics, have a lower accuracy. These neutron scattering data were used for the determination of the magnetic structure and will be presented in Sec. 2.4.

Investigations of the diffuse scattering in the $(hk0)$ scattering plane of single crystal CrB₂ show no indications of magnetic diffuse scattering. In contrast, nuclear diffuse streaks in the $(hk0)$ hexagonal basal plane are observed. Additional maxima of intensity are distributed along these streaks. These features may be attributed to a short-range defect order or a nuclear superstructure, respectively. In order to clarify the microscopic origin of the diffuse scattering further investigations are needed to search for diffuse scattering also apart from the $(hk0)$ plane. Moreover, the spatial distribution of the diffuse scattering must be analyzed on the basis of detailed defect structure simulations. To identify the modulation associated with the observed superstructure peaks the latter must be examined with respect to the spatial distribution, extinction rules, intensity distribution, and compatible space groups. This may allow to identify the corresponding superstructure by standard structure solution methods, e.g., the charge flipping

algorithm [109, 110].

2.4 Magnetic Structure of CrB₂

The account of the neutron diffraction investigation on the magnetic properties begins with the results obtained in powders. These suggest the onset of long-range antiferromagnetic order at $T_N \approx 89$ K and an incommensurate k-vector $\tau = 0.283\tau_{110}$ which are essentially consistent with the low-temperature measurements and the k-vector reported in the literature [77]. Following this the investigation of the magnetic structure of CrB₂ by means of magnetic single crystal neutron diffraction will be reported. The short presentation of typical scattering data obtained from the four-circle diffractometers RESI and HEiDi is followed by the refinement of the magnetic structure. As a main result the magnetic order in CrB₂ may be far more complex than the spin cycloid proposed so far. In fact, the structure may represent an incommensurate multi-k structure.

2.4.1 Powder Neutron Diffraction

Powder neutron diffraction was carried out at the instrument SPODI (cf. Sec. 1.4.2) using a powder sample prepared from the growth start of SFZ-118. Data have been recorded at 300 K and at 4 K. The corresponding diffraction patterns are shown Fig. 2.4a and b, respectively. A structural refinement of the measurement at 300 K showed that the sample was not phase-pure, instead containing CrB₂ and Cr₃B₄ at a volume ratio of 85:15. The existence of an impurity phase is not too surprising as during the float-zoning process the growth start of a single crystal rod commonly solidifies before chemical equilibrium is reached. Therefore this part of the ingot may contain parasitic phases. Besides revealing the precise chemical composition the refinement corroborates the C32 structure of CrB₂, which is fully consistent with the x-ray data.

2.4.1.1 Determination of the magnetic k-vector

The powder profile recorded at 4 K, shown in Fig.2.4b, may be fully accounted for by two phases, CrB₂ and Cr₃B₄. A few weak additional reflections at low scattering angles are due to the long-range magnetic structure (cf. Fig. 2.4c). The corresponding peak positions are labeled "CrB₂ (mag.)" in Fig.2.4b. In order to determine the k-vector describing the magnetic periodicity an analysis employing the program K-SEARCH which is part of the FULLPROF software suite was carried out. The best fit was obtained for $\tau = 0.283\tau_{110}$, in good agreement with the reported k-vector, $\tau = 0.285\tau_{110}$ [77].

The data was also refined using the spin-cycloid proposed in Ref. [77] as structural model. Both the small R value, $R=4.25$, and a visual inspection of the refined powder pattern (Fig. 2.4b) show that the model is in fair agreement with our data. Thus, the magnetic structure of CrB₂ represents either a spin cycloid or a closely related spiral structure. Since powder diffraction can

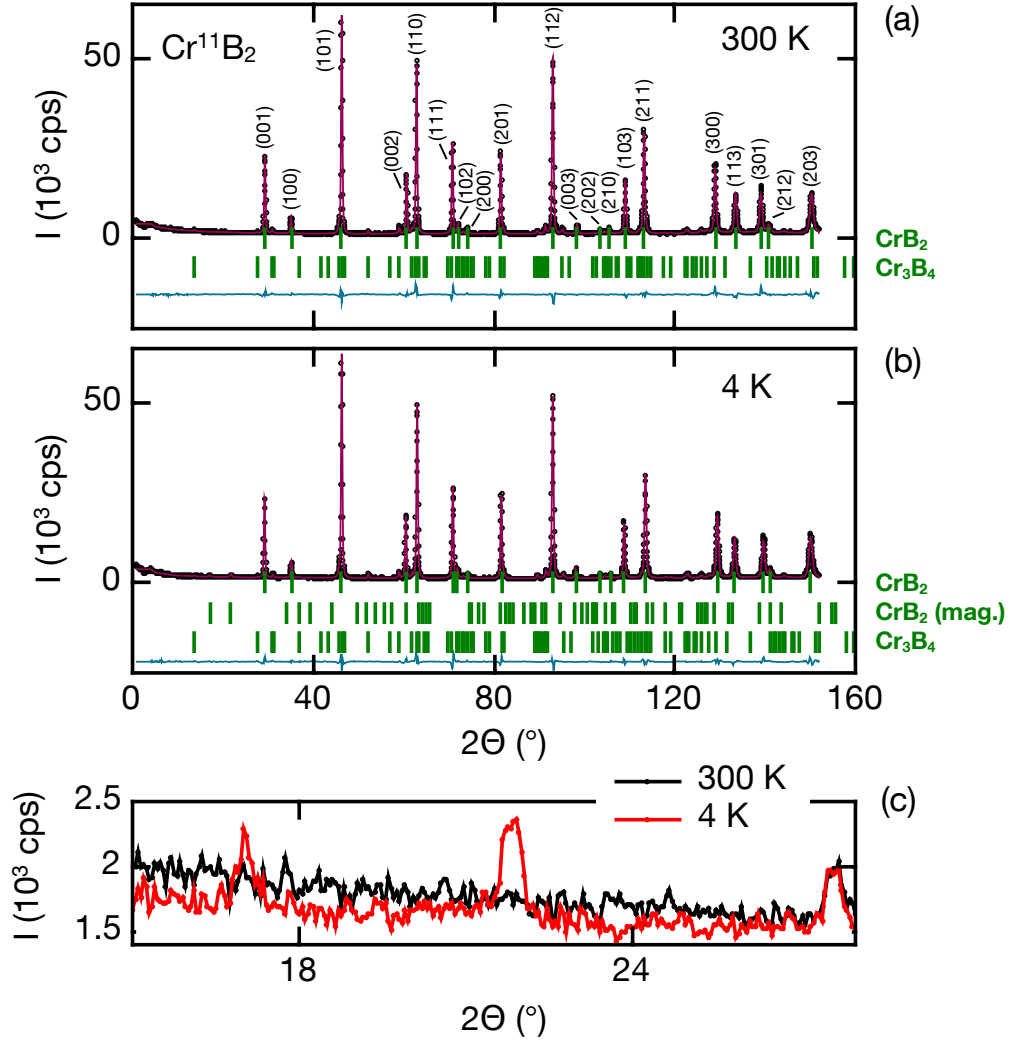


Figure 2.4: Powder neutron diffraction of CrB₂ at 300 K, (a), and 4 K, (b). Full lines correspond to structural refinements of the scattering data. (a) At 300 K only nuclear scattering from CrB₂ and an impurity phase, Cr₃B₄, is observed. (b) At 4 K additional Bragg peaks appear due to scattering from magnetic CrB₂. (c) Comparison of both diffraction patterns at low scattering angles highlighting the appearance of additional magnetic Bragg peaks at low temperature.

only discriminate scattering by structures with different values d_{hkl} these results imply that the magnetic structure of CrB₂ may be described by at least one k-vector of length $|\boldsymbol{\tau}|$. However, they do not rule out multi-k structures where all k-vectors have the same length but point in different directions. An improved refinement will therefore require single crystal data as recorded at RESI and HEiDi.

2.4.2 Single Crystal Neutron Diffraction at RESI

The single crystal studies began with measurements at RESI. Using large ¹¹B-enriched samples of CrB₂ scans of large portions of reciprocal space at three different temperatures, 100 K, 80 K, and 3 K were performed. The central results of these scans may be summarized as follows.

- (i) At high temperature, $T = 100 \text{ K} > T_N$, 33 strong Bragg peaks were recorded all of which are consistent with the C32 structure and the lattice parameters given in Sec. 2.3.1.
- (ii) At low temperature, $T = 3 \text{ K} \ll T_N$, apart from 48 nuclear main reflections 64 additional magnetic satellite peaks were detected. The magnetic Bragg peaks form a six-fold scattering pattern around each nuclear main peak clearly demonstrating that the magnetic structure is incommensurate with respect to the nuclear lattice. The pattern may be indexed using three k-vectors, $\boldsymbol{\tau} = (0.286, 0.286, 0)$, $\boldsymbol{\chi} = (-0.572, 0.286, 0)$, and $\boldsymbol{\epsilon} = (0.286, -0.572, 0)$, where $\boldsymbol{\tau} = 0.286\boldsymbol{\tau}_{110}^*$ is almost identical with the reported propagation vector $\boldsymbol{\tau} = 0.285\boldsymbol{\tau}_{110}^*$ [77] and close to the value found by powder neutron diffraction. Consistent with powder neutron diffraction $\boldsymbol{\tau}$, $\boldsymbol{\chi}$, and $\boldsymbol{\epsilon}$ have the same length, i.e., satellite peaks arising from these k-vectors cannot be discriminated in powder diffraction. $\boldsymbol{\chi}$ and $\boldsymbol{\epsilon}$ result from $\boldsymbol{\tau}$ by $R^+(\boldsymbol{\tau})$ and $R^-(\boldsymbol{\tau})$, respectively, where R^\pm denotes a rotation by $\pm 120^\circ$ about $[001]^*$. Hence the sum $\boldsymbol{\tau} + \boldsymbol{\chi} + \boldsymbol{\epsilon} = 0$.

Temperature scans of several individual satellite peaks show increasing intensity with decreasing temperature, strongly suggestive of a continuous, i.e., second order, magnetic phase transition.

- (iii) At all temperatures studied diffuse streaks are observed between neighboring nuclear Bragg peaks. They are observed in all scattering planes studied, most clearly however in the $(hk\bar{1})$ plane. As discussed in Sec. 2.3.3 these streaks may be attributed to short-range order of crystalline defects, e.g., B vacancies.
- (iv) Distributed along the diffuse streaks 52 additional Bragg peaks ($T = 3 \text{ K}$) could be identified. They are incommensurate with the nuclear C32 structure but cannot be indexed using the magnetic k-vectors $\boldsymbol{\tau}$, $\boldsymbol{\chi}$, or $\boldsymbol{\epsilon}$ either. The reflections have similar intensities as the magnetic satellites, i.e., they are by 3-4 orders of magnitude weaker than the main nuclear Bragg peaks. However, as has been clarified by our measurements carried out at HEiDi (cf. Sec. 2.4.3), they are observed both below and above T_N . The reflections may therefore be attributed to a nuclear superstructure, which is fully consistent with our polarized neutron scattering study reported in Sec. 2.3.3.

Typical scattering data recorded at RESI are shown in Fig. 2.5 for both $T > T_N$ and $T < T_N$. Since the l component of the magnetic propagation vector is zero these results can be visualized most intuitively by projecting all collected reflections into the reciprocal hexagonal basal plane

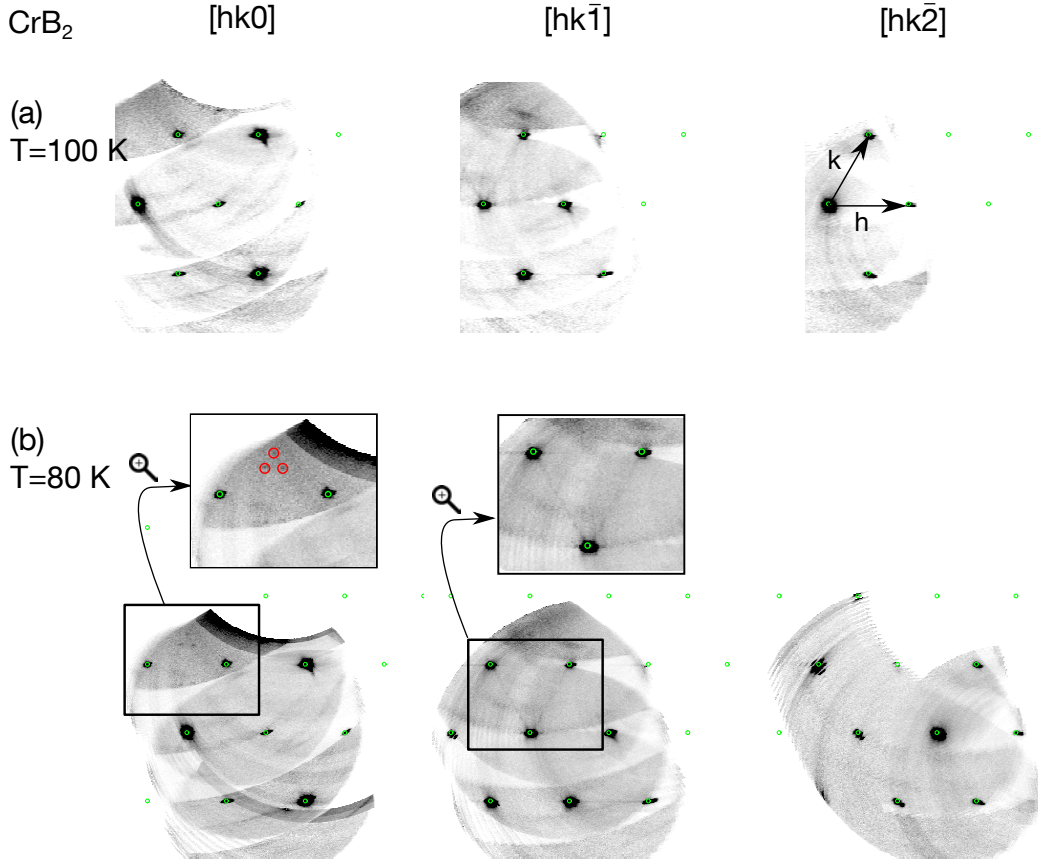


Figure 2.5: Single crystal neutron diffraction of CrB₂ recorded at RESI above and below T_N . The left, middle, and right column show the reciprocal $(hk0)$, $(hk\bar{1})$, and $(hk\bar{2})$ plane, respectively. (a) Scan at 100 K. Strong nuclear Bragg peaks, marked by green open circles, are consistent with the C32 structure. Diffuse streaks expand in between the nuclear peaks. They can be seen most clearly in the $(hk\bar{1})$ scattering plane. (b) Scan at 80 K. Besides the nuclear Bragg reflections magnetic satellite peaks appear (red circles in the left inset). The diffuse streaks are essentially unchanged.

$(hk0)$. This provides the reciprocal space map shown in Fig. 2.6 for $T = 3$ K. It contains 48 nuclear and 64 magnetic Bragg peaks that fulfill a 3σ -criterion. Due to the projection into the $(hk0)$ plane Bragg peaks with identical h and k values overlap. Clearly a sixfold magnetic scattering (red circles) around the nuclear Bragg peaks (black circles) is observed. Thin dotted lines indicate the directions of streaks of diffuse scattering. Several superstructure peaks (green circles) are distributed along these diffuse streaks.

The temperature dependence of the magnetic Bragg peaks was recorded using a counter tube detector, where the intensity of four satellite reflections as a function of the sample temperature was tracked. All data have been taken while heating the sample from base temperature, 3 K, to well above T_N . Magnetic Bragg peaks that are associated to the three different k -vectors were studied, namely $(0, 0, 0) - \tau$, $(0, 1, 0) - \tau$, $(1, \bar{1}, 0) + \chi$, and $(0, 0, 0) + \epsilon$. Fig. 2.7 shows

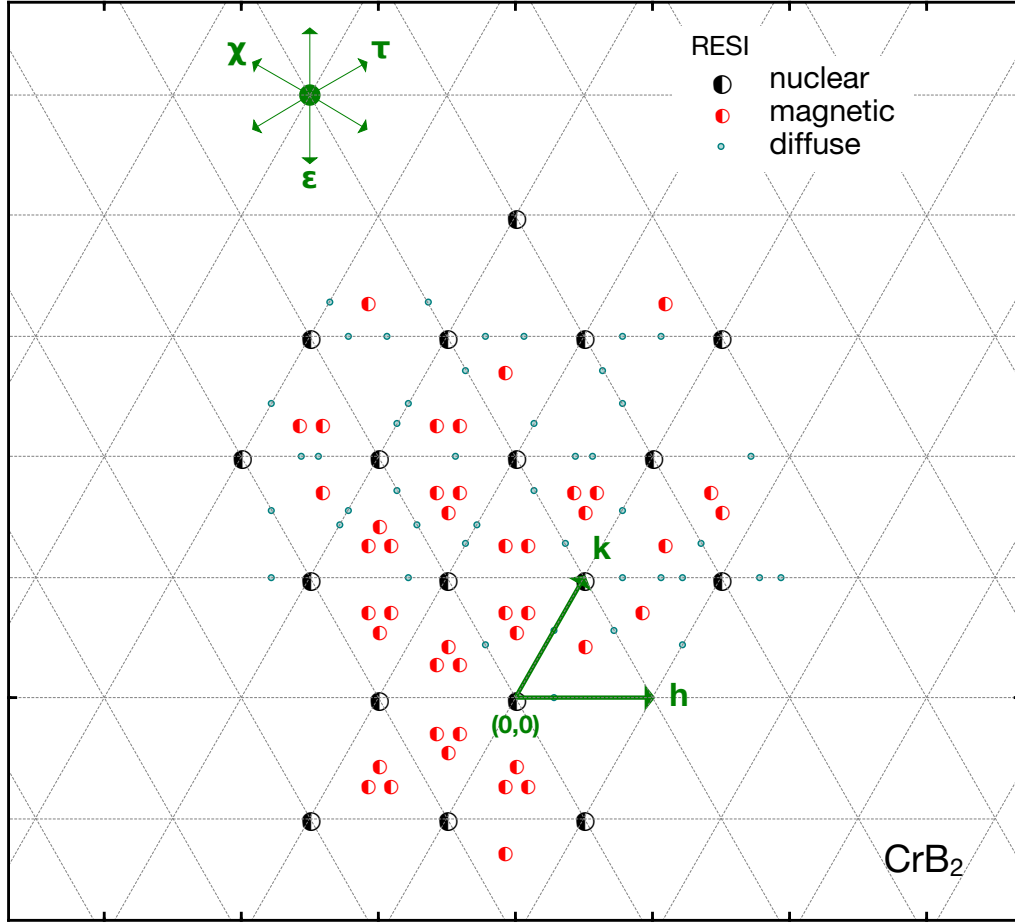


Figure 2.6: Reciprocal space map highlighting locations where intensity was observed in single crystal neutron diffraction of CrB₂ at RESI, $T = 3$ K. All reflections have been projected into the reciprocal $(hk0)$ plane.

the integrated intensity of these peaks as a function of T . The magnetic scattering signal vanishes continuously at $T_N \approx 89$ K, characteristic of a second order phase transition. This agrees nicely with our bulk and transport data reported in Sec. 2.5. Below T_N the scattering signal increases monotonically with decreasing temperature and levels off around 40 K. For $(1, \bar{1}, 0) + \chi$ the temperature dependence displays additionally a faint shoulder between 40 K and 60 K. The other curves may possibly exhibit a similar feature but the error bars are too large to be conclusive.

The data were analyzed using the empirical expression

$$I = I_0 \cdot \left[1 - \left(\frac{T}{T_N} \right)^a \right], \quad (2.1)$$

where T_N was fixed at 89 K while I_0 and the exponent a are free parameters of the fit. A

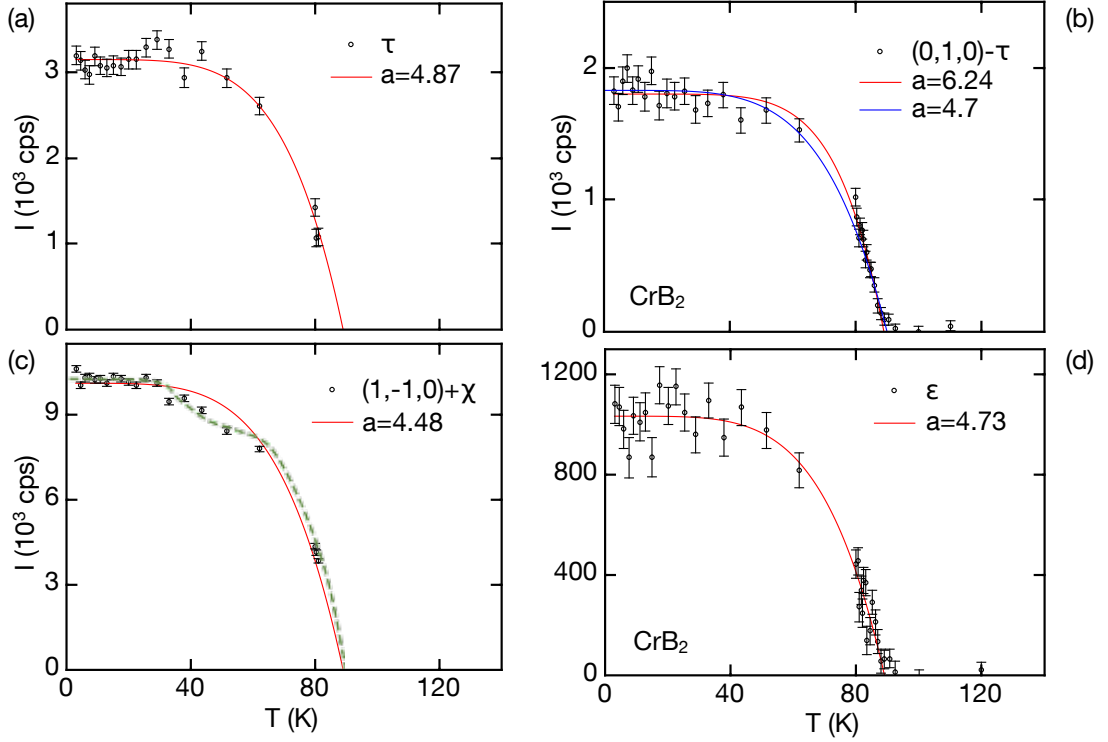


Figure 2.7: Magnetic neutron scattering of single crystal CrB₂ recorded at RESI. Temperature dependence of the integrated intensity of the (a) τ , (b) $(0, 1, 0) - \tau$, (c) $(1, \bar{1}, 0) + \chi$, and (d) ϵ satellite peaks. Red lines are fits of the experimental data to Eq. 2.1. The blue line in panel (b) also corresponds to Eq. 2.1 with $a = 4.7$. The green dashed line in (c) serve as a guide to the eye.

summary of all fit results is given in Tab. 2.2. For three Bragg peaks the exponent a varies slightly from 4.48 to 4.87, giving an average exponent of $a \approx 4.7$. The temperature dependence of a single satellite, $(0, 1, 0) - \tau$, seems to differ strongly as it is best fitted by $a = 6.24$. Yet, closer inspection shows that these data may be fitted similarly well by an exponent $a \approx 4.7$. The fit curves deviate from each other mainly in the temperature range $60 \text{ K} \leq T \leq 80 \text{ K}$ where, due to an instrumental error of the measurement software no data points were taken. Furthermore, fits of Eq. 2.1 to the more precise data recorded at HEiDi result in $a = 4.58$ and $a = 4.59$. Averaging the different values obtained for a suggests that Eq. 2.1 describes $I(T)$ best for $a \approx 4.65$

2.4.3 Single Crystal Neutron Diffraction at HEiDi

All single crystal neutron diffraction at HEiDi was carried out using a counter tube detector. Fig. 2.8a shows typical peak profiles of some nuclear Bragg peaks which are representative for the full set of reflections in two aspects. On the one hand, the peaks are very broad exhibiting a typical full width of half maximum of about 3° to 4° . On the other hand, there are some reflections

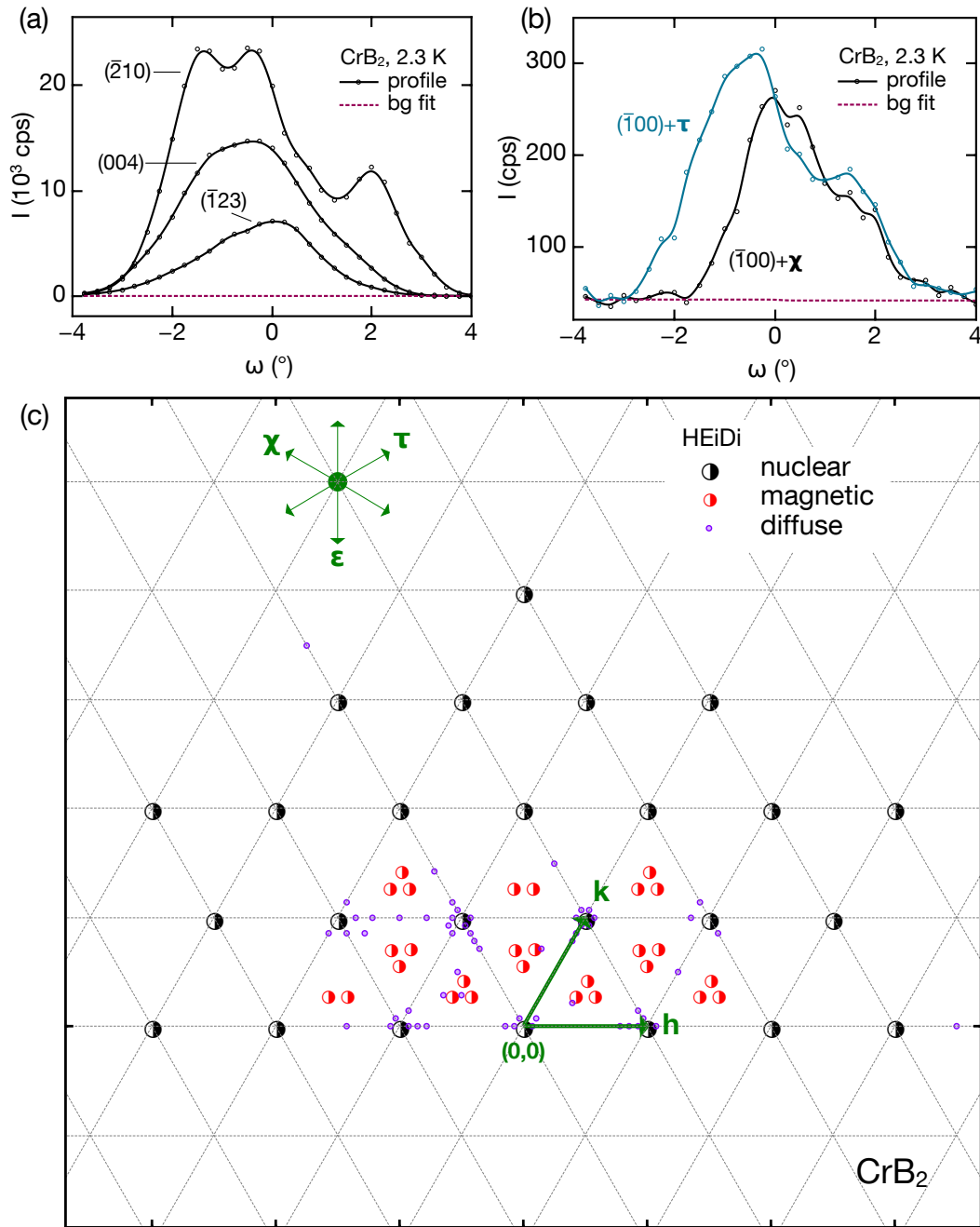


Figure 2.8: Single crystal neutron diffraction of CrB₂ recorded at HEiDi at $T = 2.3$ K. (a, b) ω -scans showing typical profiles of (a) nuclear Bragg peaks and (b) magnetic Bragg peaks. The purple dashed lines correspond to background fits. Note the different scale for nuclear and magnetic reflections. (c) Reciprocal space map highlighting locations where intensity was observed. All reflections have been projected into the reciprocal $(hk0)$ plane.

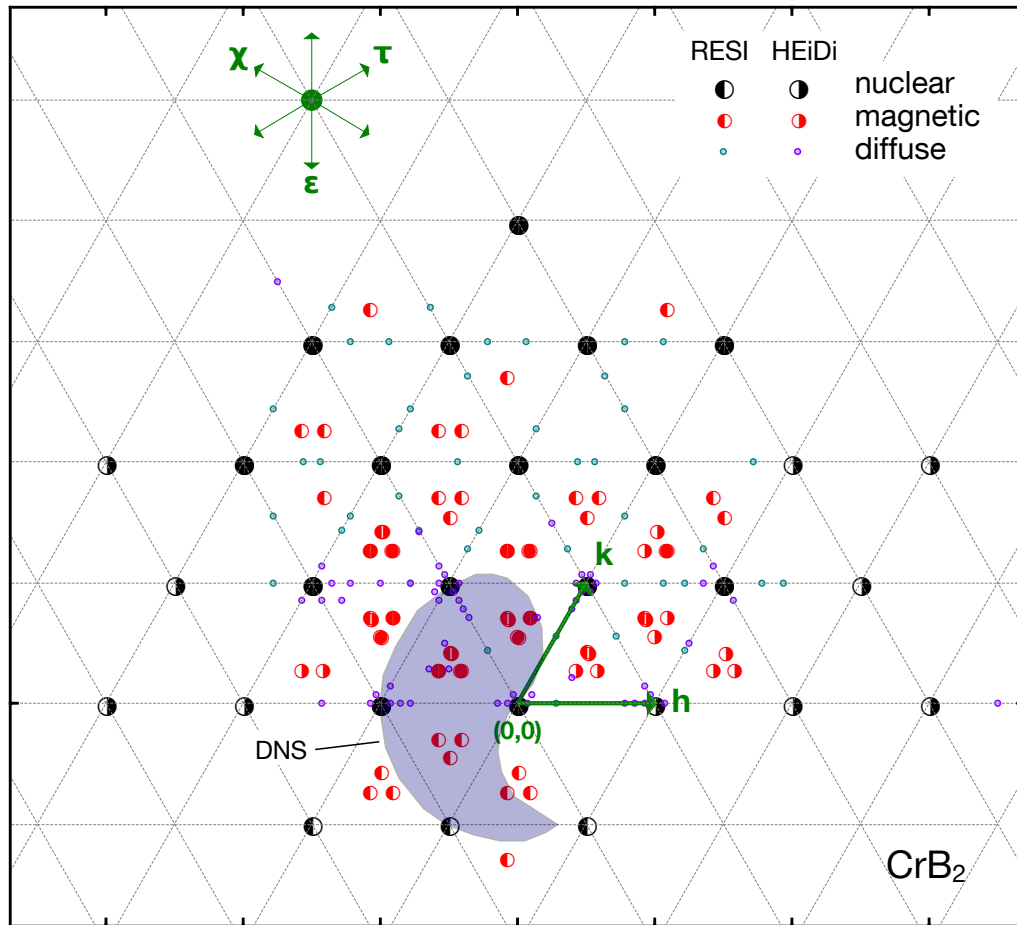


Figure 2.9: Reciprocal space map highlighting locations where intensity was observed in single crystal neutron diffraction of CrB₂. Data have been combined from the measurement at RESI ($T = 3$ K) and HEiDi ($T = 2.3$ K). All reflections have been projected into the reciprocal $(hk0)$ plane. The blue shaded area indicates the reciprocal space studied at DNS using polarized neutrons, cf. Sec. 2.3.3

which are clearly split into two or even three distinct peaks. Both the peak broadening and the peak splitting arise most likely from small angle grain boundaries and apply also to the magnetic scattering. As shown in Fig. 2.8b typical magnetic Bragg peaks exhibit a similarly broad shape. Despite the much lower intensity as compared to the nuclear scattering the peak splitting is again clearly visible. For the magnetic structure refinement the peak intensities were integrated using a Lehmann-Larsen algorithm [42], not taking into account the peak splitting. Doing so would have increased the complexity of the refinement dramatically without providing any additional insights.

A comprehensive set of reflections suitable for a magnetic structure refinement was recorded at $T = 2.3$ K. It contains 70 nuclear, 67 magnetic, and 71 superstructure peaks all of which fulfill

a 10σ -criterion. The results of a magnetic structure refinement of these data will be presented below. As for the measurements at RESI the dataset is visualized by a projection into the $(hk0)$ reciprocal space plane. This is shown in Fig. 2.8c. Albeit covering a slightly different portion of reciprocal space the scattering pattern closely resembles the scattering observed at RESI. Again a large number of magnetic satellites peaks may be noticed which are consistent with the three k-vectors $\boldsymbol{\tau}$, $\boldsymbol{\chi}$, and $\boldsymbol{\epsilon}$, forming a sixfold pattern around each nuclear main Bragg peak. For better comparison both the low-temperature datasets recorded at RESI and at HEiDi are plotted into a single map shown in Fig. 2.9. For the sake of completeness Fig. 2.9 also shows the part of the reciprocal $(hk0)$ plane which has been studied at DNS, cf. Sec. 2.3.3.

It is important to note, that a large number of additional superstructure reflections may neither be explained by the nuclear C32 structure nor by the magnetic modulation. The vast majority of these reflections is distributed along straight lines which connect neighboring nuclear Bragg peaks. From the above-mentioned experiments carried out at DNS and RESI it is already known that these are lines of diffuse scattering. As the experiments at RESI and HEiDi employed unpolarized neutrons the origin of the additional Bragg peaks was initially not clear, i.e., they could either be due to a nuclear or a magnetic superstructure. In an effort to distinguish the two possibilities an additional, smaller dataset was collected at HEiDi at a high sample temperature $T = 100 \text{ K} > T_N$. These data demonstrate the presence of the weaker superstructure peaks in the paramagnetic CrB₂, hence supporting a nuclear superstructure. This is fully consistent with data recorded at DNS using polarized neutrons which already suggested a nuclear scattering mechanism for both the diffuse streaks and the superstructure peaks, cf. Sec. 2.3.3. This is underpinned by diffuse single crystal x-ray data mentioned above, which prove the existence of the characteristic streaks of diffuse scattering at room temperature.

Considering now the distribution of the superstructure peaks it is interesting to note, that the peak positions cannot be accounted for by a single k-vector. They may, however, be indexed using a set of three independent modulation vectors

$$\boldsymbol{\tau}_{\text{nuc}} = \frac{1}{4}\boldsymbol{\tau}, \quad \boldsymbol{\epsilon}_{\text{nuc}} = \frac{1}{4}\boldsymbol{\epsilon}, \quad \boldsymbol{\chi}_{\text{nuc}} = \frac{1}{4}\boldsymbol{\chi}.$$

Furthermore, the empirical mathematical relationship between the nuclear and magnetic k-vectors hints at a close connection between the corresponding modulations. For instance, this may be understood in terms of the long-range magnetic order driven by the nuclear superstructure. To clarify this question a deeper understanding of the nuclear superstructure will be needed.

The temperature dependence $I(T)$ of the magnetic scattering signal was recorded at HEiDi with high resolution for the two satellite peaks $\boldsymbol{\chi}$ and $(\bar{1}, 1, 0) + \boldsymbol{\epsilon}$. Again all curves were recorded upon heating of the sample. These data are shown in Fig. 2.10. The continuous onset of long-range magnetic order may be clearly seen in the steep increase of the scattering intensity I below

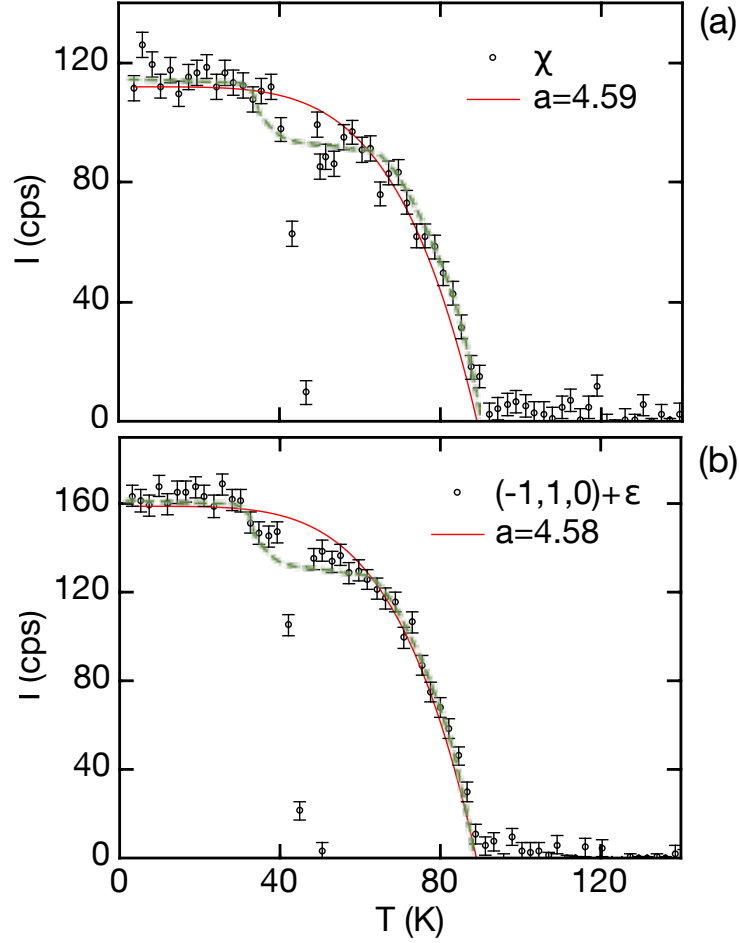


Figure 2.10: Magnetic neutron scattering of single crystal CrB₂ recorded at HEiDi. (a) Temperature dependence of the integrated intensity of the χ satellite. (b) Temperature dependence of the integrated intensity of the $(\bar{1}, 1, 0) + \epsilon$ satellite. Red lines are fits of the experimental data to Eq. 2.1. The green dashed lines serve as a guide to the eye.

$T_N = 89$ K, consistent with a second order phase transition. A faint shoulder may be discerned between 40 K and 60 K before I finally levels off at lower temperatures. In the center of the shoulder, i.e., around 50 K, a sudden loss of intensity has been detected. Both the shoulder and the loss of intensity are not due to failure of the apparatus, e.g., an accidental movement of the sample or a spontaneous reduction of the neutron flux. Even though the physical origins of both the shoulder and the sudden drop in $I(T)$ are still not clear, these features seem not to be an artifact of the measurement, but intrinsic properties of the sample. Least-square fits of Eq. 2.1 to our experimental data are summarized in 2.2 resulting in exponents $a = 4.58$ and $a = 4.59$, in good agreement with the results obtained at RESI.

instrument	satellite	I_0	a
RESI	$-\tau$	3147	4.87
RESI	$(0, 1, 0) - \tau$	1801	6.24 [†]
RESI	$(1, \bar{1}, 0) + \chi$	10109	4.48
RESI	ϵ	1033	4.73
HEiDi	χ	111	4.59
HEiDi	$(\bar{1}, 1, 0) + \epsilon$	159	4.58

Table 2.2: Summary of fits of the temperature dependence of several magnetic satellite peaks to Eq. 2.1. Data from RESI and HEiDi are on different scales. Therefore values of I_0 cannot be compared directly. [†] Fixing a at 4.7 fits both experimental datasets similarly well; see text for details.

2.4.4 Representation Analysis and Magnetic Structure Refinement

The program JANA2006 was used to fit different structural models to the single crystal neutron scattering data collected at HEiDi [37]. In order to identify the isotropy subgroups of the paramagnetic parent structure of CrB₂, which allow for a magnetic ordering, a representation analysis was performed. In the version available at the time of this project JANA2006 did not allow for representation analyses of superspace groups of dimension higher than (3+1), i.e., only a single modulation was supported. Since a first refinement approach assuming only a single modulation did not result in a satisfactory fit of the experimental data the representation analysis was finally carried out using the program ISODISTORT, version 6.1.11, which is part of the ISOTROPY SOFTWARE SUITE and which allows for up to three incommensurate modulations [49]. Consistent with both measurements and literature, the nuclear structure was assumed as hexagonal P6/mmm space group with lattice parameters $a = b = 2.97 \text{ \AA}$ and $c = 3.03 \text{ \AA}$, where the Cr and B atoms were located at the 1a (0, 0, 0) and 2d (1/3, 2/3, 1/2) site, respectively. With respect to the magnetic modulation only magnetic distortions of the Cr ion were considered; no strain, occupational, or displacement waves were taken into account. The search for compatible irreducible representations was carried out over a specific k point only, namely LD (a,a,0), where a=0.286. This corresponds to the experimentally observed k-vector τ . The superposition of more than a single representation was prohibited.

In a first series of refinements the magnetic superspace groups obtained in the ISODISTORT analysis were tested for their compatibility with the experimental diffraction data. Among all tested model structures those groups that gave the best fits of the scattering data were selected and their non-isomorphic subgroups were derived. In a second series of refinements the latter were additionally tested for their agreement with the measured data. As will be reported below the best fitting model structures are actually based on these non-isomorphic subgroups.

As part of the magnetic structure refinement the experimental data were fitted to the individual

magnetic superspace groups. All refinements were based on the dataset recorded at HEiDi at a sample temperature of 2.3 K. The HEiDi data were favored over the data recorded at RESI as it contained a much larger number of nuclear and magnetic Bragg peaks and, due to the use of a counter tube detector and longer counting times during the measurement, had a higher accuracy. Reflections not fulfilling a 10σ -criterion were removed manually. Moreover, weak superstructure peaks located along diffuse streaks were excluded as well. Taken together, the HEiDi dataset contained 75 nuclear Bragg peaks and 67 magnetic satellite peaks.

For the fitting procedure the atomic positions were kept constant, i.e., deviations from the C32 nuclear symmetry were prohibited. To account for the ¹¹B-enrichment of the sample the coherent scattering length of the B atoms was set to $b_{\text{coh}} = 6.65$ fm. The magnetic form factor of the Cr³⁺ ion was used to calculate the magnetic scattering. An isotropic extinction model (type 1, Lorentzian) was chosen to account for extinction effects. In order to account for the formation of magnetic domains the model structure was assumed to be twinned and the twin fractions were refined as well. For better comparison all refinements were first carried out on the raw data, i.e., the symmetry of the individual model structures was not used to average the scattering intensities prior to the refinement. Eventually, averaging of the scattering intensities has been applied to the best fitting model structures. The results of our fits are summarized in Tab. 2.3. The second column, “ R factors”, specifies the number of fitted reflections and fitted parameters in the format $n_{\text{all}} = n_{\text{obs}} + n_{\text{weak}}/n_{\text{params}}$, where n_{params} is the number of free parameters of the fit. n_{all} , n_{obs} , and n_{weak} refer to the number of all fitted Bragg peaks, the number of the observed Bragg peaks ($I > 3\sigma$), and number of weak Bragg peaks ($I < 3\sigma$), respectively. As any reflections with $I < 10\sigma$ were manually removed from the dataset beforehand n_{weak} is zero for all refinements. Consequently, the R values for all fitted reflections are the same as the R values for the observed reflections and hence not indicated individually in the table. The fit quality is indicated by their R value, i.e., the smaller R the better the agreement with the experimental data. Thus the most probable structural models are eventually determined from the smallest R values.

Altogether four different magnetic models fit our diffraction data satisfactorily. They are highlighted in Tab. 2.3 by boldface type. For each model structure a mathematical description of the spatial magnetic moment distribution is given by the expression

$$\mathbf{m}(\mathbf{r}) = \sum_{\mathbf{i}} (\mathbf{A}_{\mathbf{i}} \sin \mathbf{q}_{\mathbf{i}}\mathbf{r} + \mathbf{B}_{\mathbf{i}} \cos \mathbf{q}_{\mathbf{i}}\mathbf{r}),$$

where the summation runs over the number of modulation waves and where the corresponding Fourier coefficients $\mathbf{A}_{\mathbf{i}}$ and $\mathbf{B}_{\mathbf{i}}$ are summarized in Tab. 2.4.

All four structures are aperiodic, i.e., the magnetic modulation is incommensurate with respect to the nuclear lattice. Moreover, as the l component of the \mathbf{k} -vector is zero the magnetic modulation is limited to the hexagonal basal plane. This means that the magnetic textures of

The Weak Itinerant Antiferromagnet CrB₂

SpcGrp	R factors	R	wR	R_{nuc}	wR_{nuc}	R_{mag}	wR_{mag}
Single-k Structures							
P2/m(a0g)0s [†]		100	100	100	100	100	100
C2/m(a0g)0s	142=142+0/6	47.36	50.26	48.11	51.6	31.47	38.37
Cmm2(a00)000	142=142+0/4	6.29	16.54	4.89	6.91	36.06	40.27
Cmmm.1'(a00)00ss	142=142+0/4	6.26	16.54	4.87	6.91	35.99	40.27
C2/m(a0g)00	142=142+0/5	6.21	16.52	4.81	6.86	36.02	40.26
C222(a00)000	142=142+0/4	6.02	20.8	4.85	6.91	30.94	51.89
Cmmm.1'(a00)0sss	142=142+0/4	5.99	20.82	4.82	6.91	30.92	51.88
Amm2(0b0)s00	142=142+0/5	5.42	10	4.84	6.91	17.81	20.54
Amm2(0b0)s00	142=142+0/5	5.42	10	4.84	6.91	17.81	20.54
Amm2(0b0)000	142=142+0/4	5.32	9.38	4.85	6.91	15.47	18.44
P2/m(a0g)0s	142=142+0/6	5.3	9.96	4.72	6.8	17.88	20.6
Cmmm.1'(a00)0s0s	142=142+0/4	5.3	9.38	4.82	6.91	15.47	18.44
C222(a00)s00	142=142+0/5	5.26	9.12	4.84	6.91	14.16	17.45
C222(a00)s00	142=142+0/5	5.26	9.12	4.84	6.91	14.15	17.45
P2/m(a0g)00	142=142+0/5	5.22	9.2	4.74	6.8	15.44	18.39
Cmm2(a00)0s0	142=142+0/10	4.84	6.82	4.83	6.91	5.18	6.21
C2/m.1'(a0g)0ss	142=142+0/10	4.84	6.80	4.83	6.91	5.04	6.10
Double-k Structures							
Ammm1'(0,b,g)000s(0,-b,g)s00s	142=142+0/6	6.59	23.16	4.82	6.74	24.11	25.12
Ammm1'(0,b,g)000s(0,-b,g)000s	142=142+0/5	6.57	23.28	4.77	6.77	24.97	26.26
Triple-k Structures							
P $\bar{6}$ 2'm'	142=142+0/6	100	153.9	6.38	8.17	100	100
P6'/m'mm'	142=142+0/5	7.06	21.67	5.94	8.5	30.88	51.89
P6'/m'm'm	142=142+0/5	6.23	15.55	4.83	6.73	36.1	40.44
P6'/mmm'	142=142+0/5	5.28	9.34	4.79	6.73	15.66	18.71
P6'/m	142=142+0/5	5.28	9.34	4.8	6.73	15.66	18.71
P $\bar{6}$ m2	142=142+0/6	5.23	9.27	4.74	6.66	15.63	18.66
P6'2'2	142=142+0/6	5.23	9.08	4.8	6.73	14.32	17.74
P $\bar{3}$ 'm1	142=142+0/6	5.23	9.08	4.8	6.73	14.32	17.74
P6'mm'	142=142+0/6	5.01	7.3	4.84	6.73	8.64	10.19
P $\bar{3}$ '1m'	142=142+0/6	5.01	7.3	4.84	6.73	8.64	10.19

Table 2.3: Magnetic structure refinement of CrB₂. Space group names and values of R_{mag} printed in boldface type mark the best fits. [†]Refinement did not converge.

neighboring $\{001\}$ sheets are identical. Among the four magnetic models two are single-k and two are triple-k. Note that the triple-k structures explain our experimental data similarly well as the single-k solutions albeit requiring only 6 rather than 10 free parameters.

2.4.4.1 Model 1: Monoclinic Single-k Structure C2/m.1'(a0g)0ss

A schematic depiction of the monoclinic single-k structure C2/m.1'(a0g)0ss is shown in Fig. 2.11. It may be understood in terms of a spin density wave which, as shown in Fig. 2.11a, expands along the a -axis of the standard cell. While the b -component of the moment vector vanishes m_a and m_c are strongly modulated. Consequently, there are Cr atoms along the propagation direction which carry no magnetic moment. The modulation of neighboring directions is phase

Single-k structures					
direct cell	2.970000	5.144200	3.070000	90.000	90.000 90.000
reciprocal cell	0.336700	0.194394	0.325733	90.000	90.000 90.000
wave 1	$\mathbf{k}_1 = (0.571429, 0.000000, 0.000000)$				
Centrosymmetric super-space group: C2/m.1'(a0g)0ss, #12					
	along a	along b	along c	length	
\mathbf{A}_1	0.000(0)	0.000(0)	0.000(0)	0.000(0)	
\mathbf{B}_1	-0.534(48)	0.000(0)	0.616(28)	0.815(56)	
	along a^{hex}	along b^{hex}	along c^{hex}	length	
\mathbf{A}_1	0.000(0)	0.000(0)	0.000(0)	0.000(0)	
\mathbf{B}_1	-0.534(48)	-0.534(48)	0.616(28)	0.815(73)	
Non-centrosymmetric super-space group Cmm2(a00)0s0, #35					
	along a	along b	along c	length	
\mathbf{A}_1	0.000(0)	0.000(0)	0.613(26)	0.613(26)	
\mathbf{B}_1	0.530(39)	0.000(0)	0.000(0)	0.530(39)	
	along a^{hex}	along b^{hex}	along c^{hex}	length	
\mathbf{A}_1	0.000(0)	0.000(0)	0.613(26)	0.613(26)	
\mathbf{B}_1	0.530(39)	0.530(39)	0.000(0)	0.530(55)	
Triple-k structures					
direct cell	2.970000	2.970000	3.070000	90.000	90.000 120.000
reciprocal cell	0.388788	0.388788	0.325733	90.000	90.000 60.000
wave 1	$\mathbf{k}_1 = (0.286, 0.286, 0)$				
wave 2	$\mathbf{k}_2 = (-0.572, 0.286, 0)$				
wave 3	$\mathbf{k}_3 = (-0.286, 0.572, 0)$				
Centrosymmetric superspace group P $\bar{3}$ '1m', #162					
	along a	along b	along c	length	
\mathbf{A}_1	0.335(31)	0.335(31)	0.381(26)	0.507(51)	
\mathbf{B}_1	0.000(0)	0.000(0)	0.000(0)	0.000(0)	
\mathbf{A}_2	-0.335(31)	0.000(0)	0.381(26)	0.507(41)	
\mathbf{B}_2	0.000(0)	0.000(0)	0.000(0)	0.000(0)	
\mathbf{A}_3	0.000(0)	0.335(31)	-0.381(26)	0.507(41)	
\mathbf{B}_3	0.000(0)	0.000(0)	0.000(0)	0.000(0)	
Non-centrosymmetric super-space group: P6'mm', #183					
	along a	along b	along c	length	
\mathbf{A}_1	0.000(0)	0.000(0)	0.371(20)	0.371(20)	
\mathbf{B}_1	-0.321(26)	-0.321(26)	0.000(0)	0.321(37)	
\mathbf{A}_2	0.000(0)	0.000(0)	0.371(20)	0.371(20)	
\mathbf{B}_2	0.321(26)	0.000(0)	0.000(0)	0.321(26)	
\mathbf{A}_3	0.000(0)	0.000(0)	-0.371(20)	0.371(20)	
\mathbf{B}_3	0.000(0)	0.321(26)	0.000(0)	0.321(26)	

Table 2.4: Modulation functions of the refined magnetic superspace groups. For the single-k structures, where the standard cell differs from hexagonal settings, projections of the ordered moment along the hexagonal axes are indicated additionally.

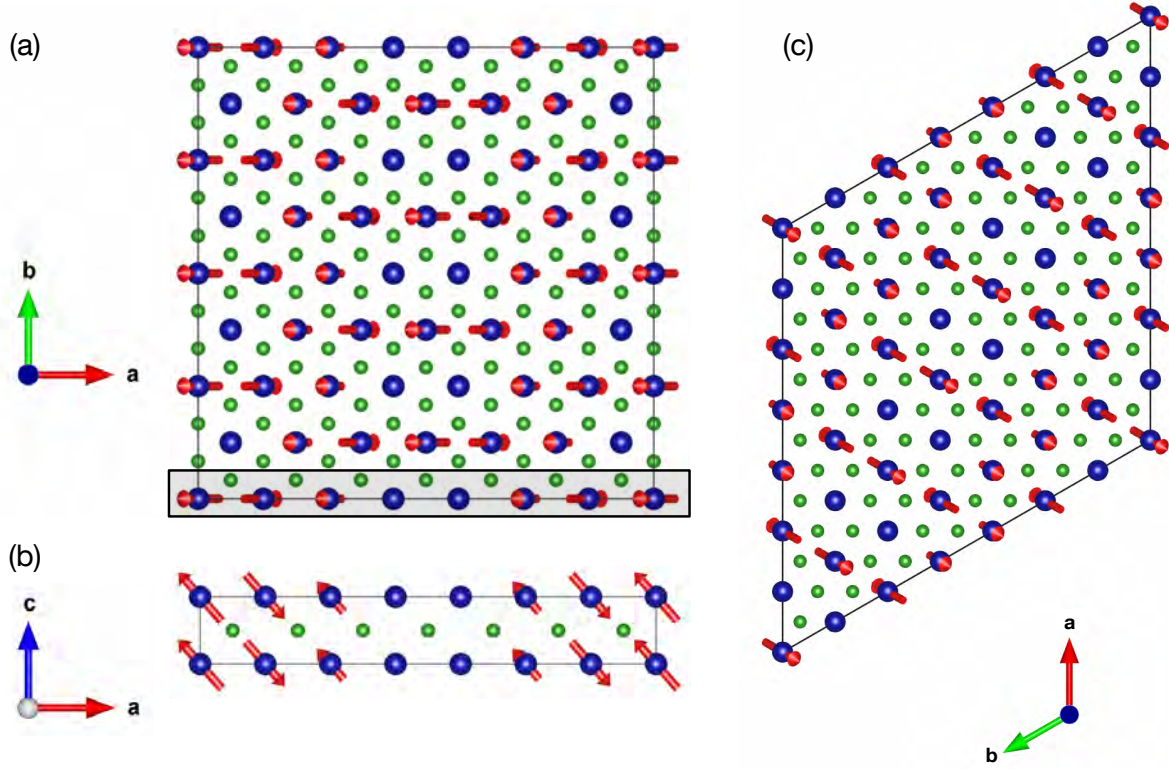


Figure 2.11: Schematic depiction of the $C2/m.1'(a0g)0ss$ structure. (a) Viewing direction along the standard settings *c*-axis. (b) Viewing direction along the standard settings *b* axis. (c) Viewing direction along *c*-axis of the hexagonal nuclear parent cell.

shifted. Comparison with Fig. 2.11c shows that in the hexagonal cell the density wave points along the $\langle 110 \rangle$ direction, while the magnetic moments lie in the $\langle 110 \rangle$ -*c*-plane. This results in wave fronts which are perpendicular to $\langle 110 \rangle$ and wherein all Cr moments possess an equal size and direction. Due to the high symmetry of the triangular nuclear lattice the *a*-axis and $\langle 110 \rangle$ are equivalent. Therefore the structure may alternatively be thought of as a density wave which propagates along the *a*-axis with moments confined to the *a*-*c*-plane.

The monoclinic space group $C2/m.1'(a0g)0ss$ clearly represents an antiferromagnetic structure in the sense that neighboring Cr moments are flipped. Among all tested models it is the only one which lacks a cycloidal character. In contrast to the hitherto proposed spin cycloid [77, 81] the magnetic moment does not rotate but is fixed at an inclination angle $\delta \approx 50^\circ$ with respect to the hexagonal plane. In turn, the size of the Cr moment is strongly modulated resulting in the periodicity of $7a$. The average moment size may be interpreted as the ordered moment and amounts to $m_s \approx 0.52 \mu_B/\text{Cr}$.

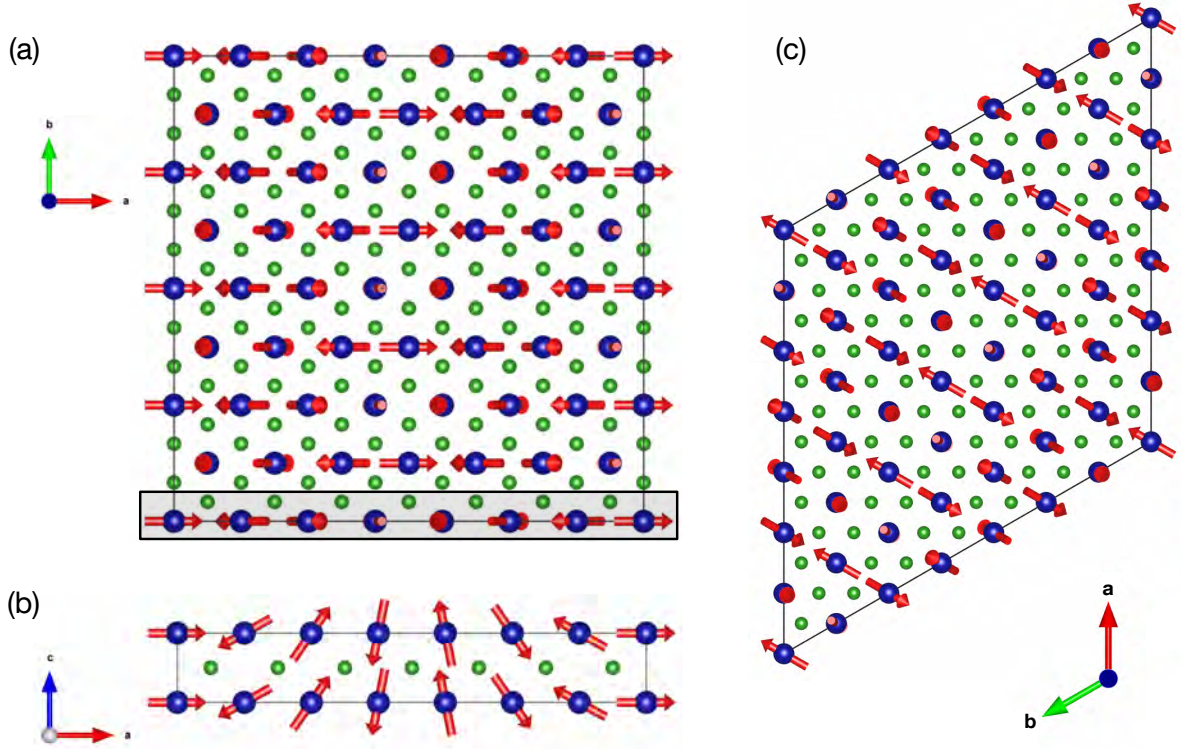


Figure 2.12: Schematic depiction of the $Cmm2(a00)0s0$ structure. (a) Viewing direction along the standard settings c -axis. (b) Viewing direction along the standard settings b axis. (c) Viewing direction along c -axis of the hexagonal nuclear parent cell.

2.4.4.2 Model 2: Orthorhombic Single-k Structure $Cmm2(a00)0s0$

A schematic depiction of the orthorhombic single-k structure $Cmm2(a00)0s0$ is shown in Fig. 2.12. It may be understood in terms of a spin cycloid which propagates along the a -axis of the standard cell. The cycloid exhibits a faint elliptical distortion, i.e., the moment amplitude is slightly modulated, resulting in an average ordered moment $m_s \approx 0.57 \mu_B/\text{Cr}$. The periodicity of the modulation is about $7a$. Note, that the moment vector rotates at a much higher spatial frequency. The $Cmm2(a00)0s0$ superspace group should thus be considered as an antiferromagnetic order and must not be confused with cycloidal or helical ferromagnetic spin textures where the direction of neighboring magnetic moments is changed very little.

In the hexagonal cell, Fig. 2.12c, the cycloid propagates along the $\langle 110 \rangle$ direction with the magnetic moments turning in the $\langle 110 \rangle$ - c -plane. This gives rise to wave fronts perpendicular to $\langle 110 \rangle$ wherein all Cr moments have the same size and direction. Due to the triangular symmetry of the underlying nuclear lattice this spin structure may alternatively be considered as a cycloid that points along the a -axis with moments turning in the a - c -plane.

Thus, the $Cmm2(a00)0s0$ space group is almost equivalent to the simple cycloid that was sug-

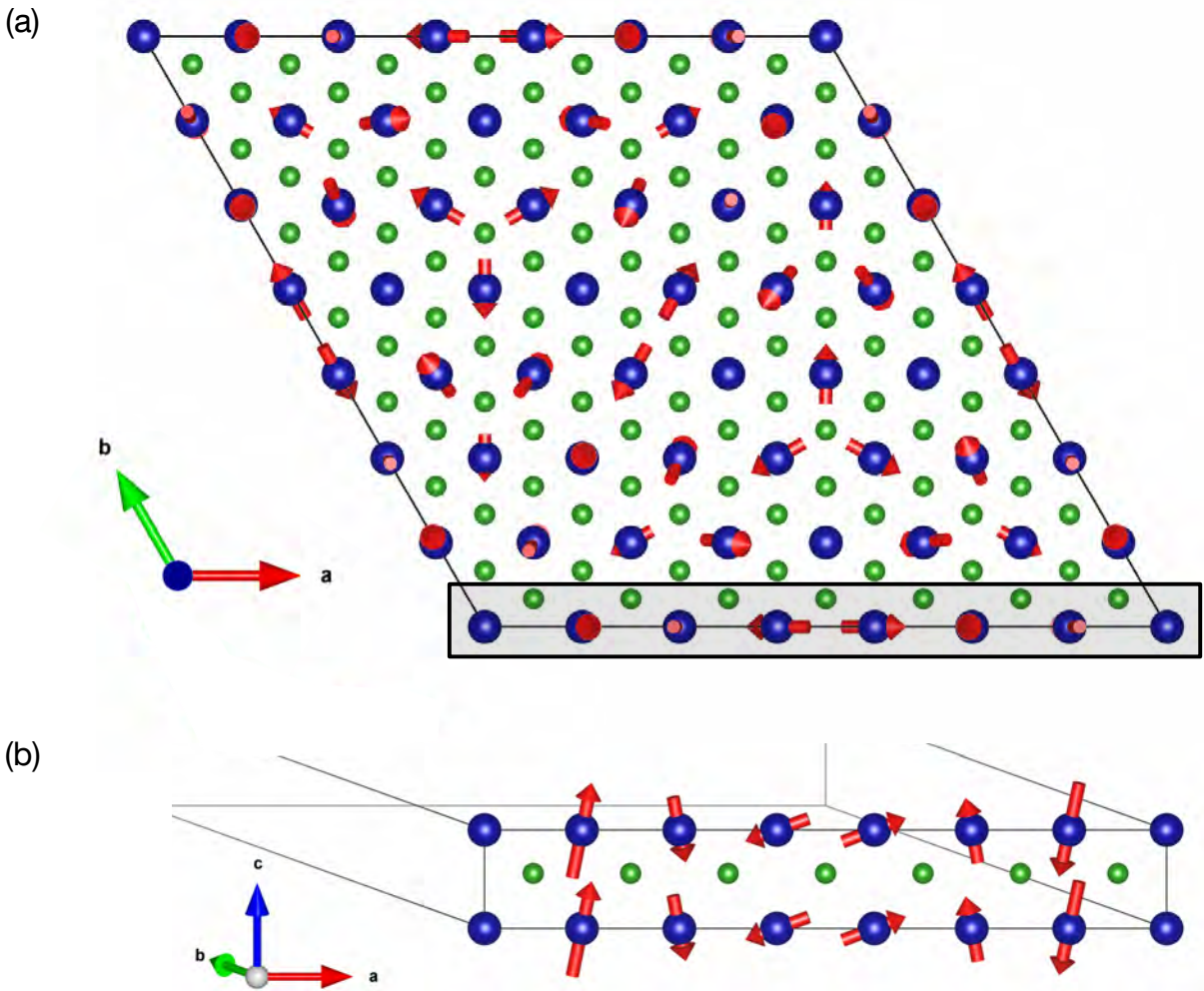


Figure 2.13: Schematic depiction of the $P\bar{3}'1m'$ structure. (a) Viewing direction along the *c*-axis. (b) Modulated spin cycloid along the *a*-axis with moments turning in the *a-c*-plane.

gested by FUNAHASHI and coworkers [77]. It however differs in terms of the small elliptical distortion. The $Cmm2(a00)0s0$ space group is furthermore related to the structure proposed by KAYA ET AL. who, however, reported the best agreement of their polarimetry data with a regular and not an elliptically distorted cycloid. Moreover, their solution was characterized by an inclination of the plane inside which the spins turned by 7.6° from the $\langle 110 \rangle$ -*c* plane [81].

2.4.4.3 Model 3: Trigonal Triple-K Structure $P\bar{3}'1m'$

A schematic depiction of the trigonal triple-k structure $P\bar{3}'1m'$ is shown in Fig. 2.14. It may be understood in terms of a coherent superposition of three independent spin density waves with zero phase shift. This results in a complex arrangement of the Cr moments where elliptically distorted spin cycloids propagate along the $\langle 100 \rangle$ and $\langle 110 \rangle$ directions with the moment vector

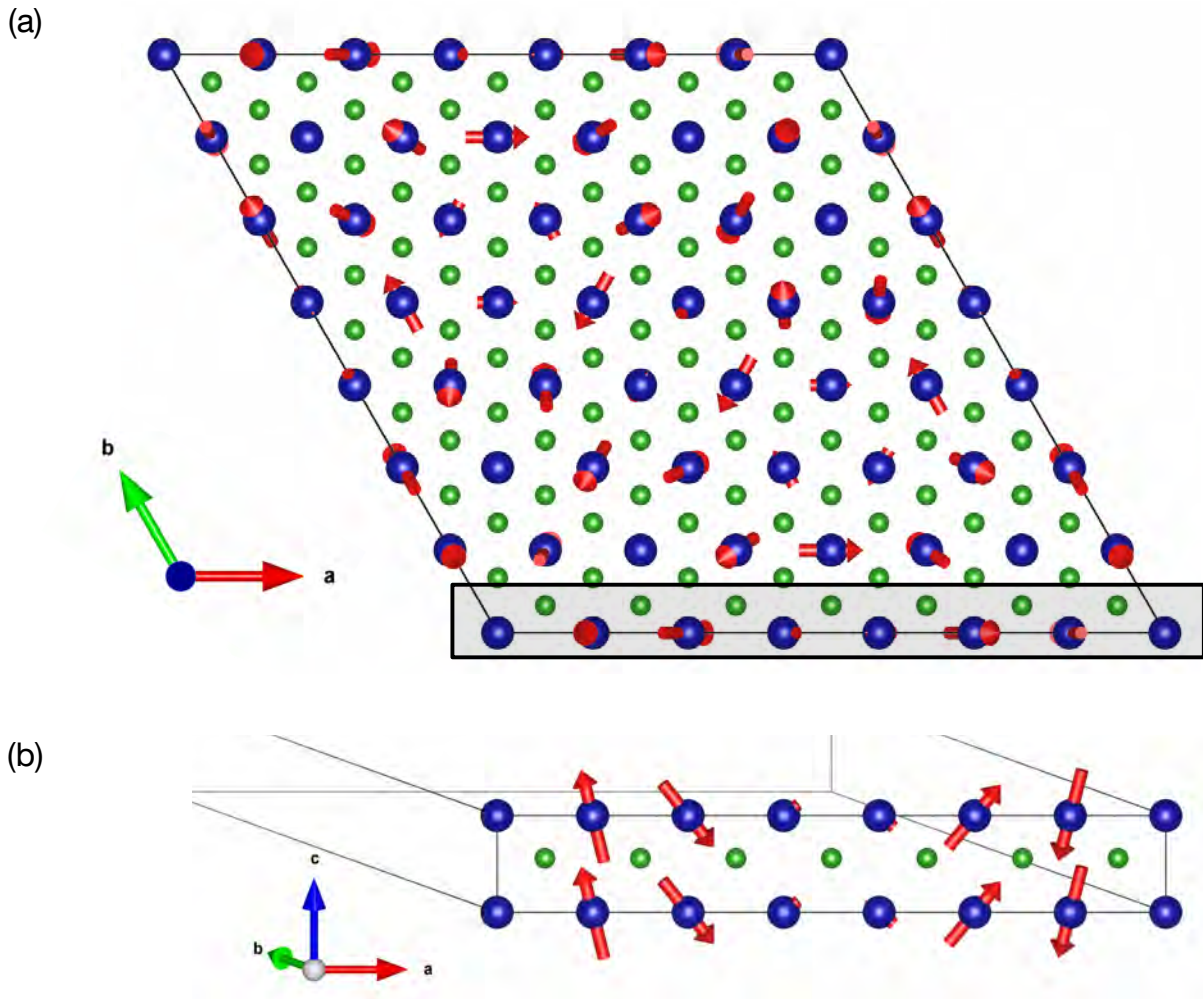


Figure 2.14: Schematic depiction of the $P6'mm'$ structure. (a) Viewing direction along the c -axis. (b) Modulated spin wave along the a -axis with moments turning in the a - c -plane.

confined to the $\langle 100 \rangle$ - c -plane and $\langle 110 \rangle$ - c -plane, respectively. In contrast to the single- k structures, here the phase shift of the cycloids along $\langle 100 \rangle$ and $\langle 110 \rangle$ is such that there are no straight but spherical wavefronts of ferromagnetic Cr moments. The modulation of the magnetic moment corresponds to the observed periodicity of $\sim 7a$. The average moment size may be interpreted as the ordered moment and amounts to $m_s \approx 0.56 \mu_B/\text{Cr}$. As for the $Cmm2(a00)0s0$ superspace group the magnetic moment vector varies at a much shorter distance than $7a$, hence resulting in an antiferromagnetic arrangement.

2.4.4.4 Model 4: Hexagonal Triple-K Structure $P6'mm'$

A schematic depiction of the hexagonal triple- k structure $P6'mm'$ is shown in Fig. 2.14. It may be understood in terms of a coherent superposition of three independent distorted spin cycloids

The Weak Itinerant Antiferromagnet CrB₂

SpGrp	R factors	R	wR	R_{nuc}	wR_{nuc}	R_{mag}	wR_{mag}
Single-k Structures							
C2/m.1'(a0g)0ss	101=101+0/10	4.78	6.76	4.78	6.84	4.78	5.98
Cmm2(a00)0s0	90=90+0/10	4.45	6.26	4.44	6.29	5.03	6.04
Triple-k Structures							
P6'mm'	36=36+0/6	3.7	4.90	3.66	4.60	5.45	6.26
P3'1m'	50=50+0/6	3.76	5.25	3.69	4.65	6.32	7.53

Table 2.5: Magnetic structure refinement of CrB₂ using the four magnetic model structures which showed the best agreement with the experimental data, cf. Tab. 2.3. All fits are based on symmetry averaged data.

with zero phase shift. This results in another complex spin arrangement which is closely related to the P3'1m' structure. Like the latter the P6'mm' structure is characterized by elliptically distorted spin cycloids that propagate along the $\langle 100 \rangle$ and $\langle 110 \rangle$ directions. The orientation of the magnetic moment is again confined to the $\langle 100 \rangle$ - c -plane and $\langle 110 \rangle$ - c -plane, respectively. As for the trigonal P3'1m' structure, the cycloids along $\langle 100 \rangle$ and $\langle 110 \rangle$ are phase shifted such that the structure lacks straight wavefronts of ferromagnetic spins. The modulation of the moment size exhibits again a periodicity of $\sim 7a$. The magnetic moment varies at a high spatial frequency, characteristic of an antiferromagnetic spin arrangement. The ordered moment was estimated as the average Cr moment and amounts to $m_s \approx 0.55 \mu_B/\text{Cr}$.

2.4.4.5 The Puzzle of the Correct Structural Solution

A comparison of the four most promising solutions of the magnetic structure of CrB₂ revealed similarities as well as distinct differences. This naturally raises the question which of the model structures is actually realized. The results of the refinements using the four candidate structures are highlighted in Tab. 2.3 by boldface type. Their magnetic R values range from 5 to 8.6 which is a too small difference to identify the correct magnetic structure of CrB₂.

Averaging of the scattering intensities by taking into account the nuclear and magnetic symmetry of the test structure may be applied to improve the fit quality. In fact, as summarized in Tab. 2.5, symmetry averaging results in a slight enhancement of the reliability factors for all four space groups. However, the difference of the improved R values is even smaller, thus rendering the identification of the correct solution even more difficult.

The following empirical considerations suggest that in CrB₂ one of the triple-k structures, P6'mm' or P3'1m', rather than a single-k structure may be realized:

- (i) Details of the nuclear structure of CrB₂ hint at the formation of a triple-k magnetic structure. As reported in Sec. 2.3.3, Sec. 2.4.2, and 2.4.3, the diffraction data reveal consistently reflections which cannot be accounted for by the C32 crystal lattice. These additional Bragg peaks are distributed along lines of diffuse scattering along the $\langle 100 \rangle$ and $\langle 110 \rangle$ directions.

As they are observed both deep within the magnetically ordered phase, at $T = 2.3$ K, as well as in paramagnetic CrB₂, $T = 100$ K, a purely nuclear origin seems likely. This is corroborated further by polarized neutron diffraction where the additional Bragg peaks were observed exclusively in the non-spin flip scattering signal. Together the experimental data therefore hint at the presence of a nuclear superstructure. Any attempts to index the superstructure peaks using only a single k -vector failed. In contrast, all superstructure reflections could be explained by a set of three propagation vectors which are closely related to the magnetic modulations, cf. Sec. 2.4.3. Thus the putative nuclear superstructure is represented best by a triple- k structure. Finally, the close relationship between the nuclear and magnetic k -vectors suggests an intimate connection of the nuclear modulation and the long-range magnetic order in CrB₂ of yet unknown origin.

- (ii) The formation of a magnetic triple- k structure is consistent with theoretical investigations. For a Heisenberg antiferromagnet on a two-dimensional triangular lattice (Heisenberg-AFT), theory predicts an inherently frustrated magnetic ground state that is characterized by a 120°-structure with SO(3) order parameter [111, 112]. Infinitesimal Kitaev exchange, i.e., infinitesimal deviations from perfectly equivalent exchange interactions between neighboring magnetic atoms located on the edges of a triangle, will result in the formation of a topologically stabilized \mathbb{Z}_2 vortex crystal. In fact, the analysis of the P6'mm' and P $\bar{3}$ '1m' triple- k structures suggests that the latter exhibit both 120° correlations and vortex-like point defects.

For CrB₂ the assumption of a Heisenberg antiferromagnet on a two-dimensional triangular lattice seems to be justified by the distribution of the Cr atoms on a quasi two-dimensional triangular lattice (Fig. 2.1) and the small magnetic anisotropy inferred consistently from our low-temperature bulk and transport measurements (Sec. 2.5). Exchange anisotropies may be introduced by different mechanisms such as, e.g., a magneto-elastic distortion of the nuclear lattice or direct overlap of the d orbitals. Vice versa, the magnetic frustration predicted by the Heisenberg-AFT model agrees extremely well with the experimental observation of strong geometric frustration in CrB₂ inferred from the large negative ratio of the Curie-Weiss and Néel temperature, $f = -\Theta_{CW}/T_N = -8.5$ (Sec. 2.5). In contrast, the observed geometrical frustration cannot be explained by any of the single- k spin structures.

2.4.5 Discussion of the Non-trivial Topology of the Triple- k Structures

It is instructive to perform a more detailed analysis of the P6'mm' and P $\bar{3}$ '1m' triple- k structures in CrB₂. The latter was carried out by ACHIM ROSCH and WOLFGANG SIMETH [113].

Similar results were obtained for both triple- k structures. The presentation will therefore be limited to the case of the P $\bar{3}$ '1m' superspace group, where the key results may be summarized as follows.

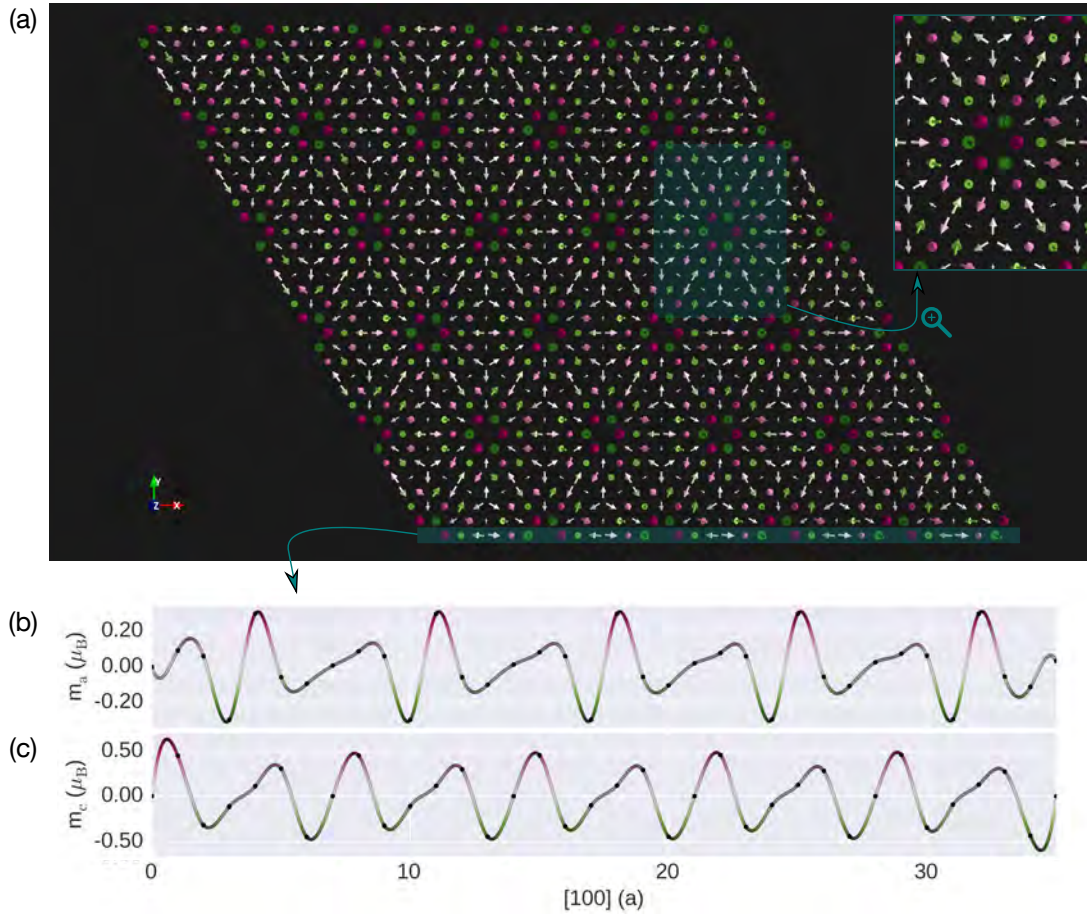


Figure 2.15: Modulation of the magnetic moment in the putative $P\bar{3}'1m'$ triple-k structure of CrB₂. (a) Top view of the magnetic structure highlighting its antiferromagnetic character. The moment vectors are colored according to their z -direction, i.e., green and red vectors point into and out of the drawing plane, respectively. (b) Modulation of m_a and (c) m_c for a cut along the a -direction. The m_b component is zero and therefore not shown. Small black dots indicate the position of the Cr atoms within the modulation wave.

(i) As shown in Fig. 2.15a the magnetic order can be understood in terms of three superposed modulations which propagate in the Cr sheets and which are characterized by the three k -vectors $\boldsymbol{\tau} = (0.286, 0.286, 0)$, $\boldsymbol{\chi} = (-0.572, 0.286, 0)$, and $\boldsymbol{\epsilon} = (0.286, -0.572, 0)$. Fig. 2.15b and Fig. 2.15c show the calculated modulation of the components m_a and m_c of the moment vector, respectively, for a cut along the [100]-direction; the component m_b is zero and therefore not plotted. Small black circles indicate the position of the Cr atoms in the modulation. A comparison of m_a and m_c shows that their modulations exhibit a constant phase shift implying that the structure (along the high-symmetry [100]-, [010]-, and [110]-directions) behaves like a distorted cycloid.

(ii) As indicated by the vanishing l -component of the k -vectors the magnetic moment is not

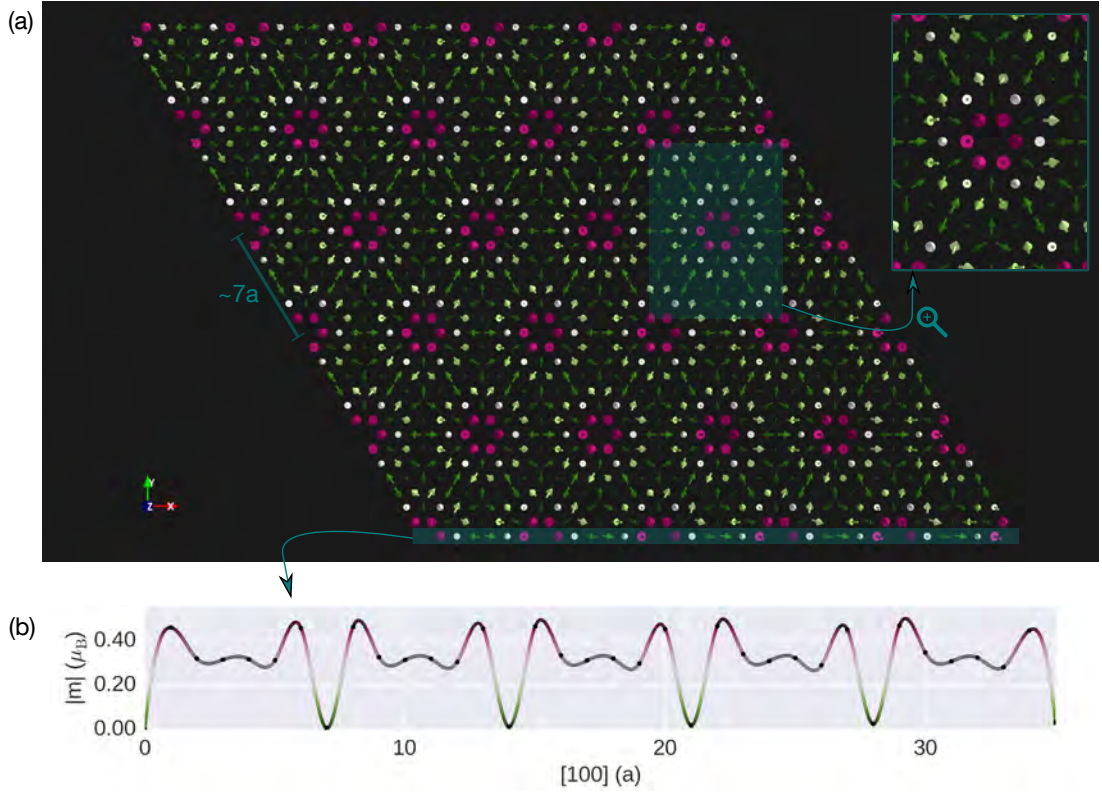


Figure 2.16: Modulation of the magnetic moment for the proposed $P\bar{3}1m'$ triple-k structure of CrB₂. (a) Top view of the magnetic structure highlighting the long-range, $\lambda \approx 7a$, modulation of the magnetic moment amplitude. The moment vectors are colored according to the size of m_c^2 , i.e., green and red vectors correspond to a small and large out-of-plane moment, respectively. (b) Modulation of $|m|$ for a cut along the a -direction. Small black dots indicate the position of the Cr atoms within the modulation wave.

modulated along the crystalline c -axis. Thus Cr atoms which are stacked along the $[001]$ -direction carry an identical magnetic moment.

- (iii) The magnetic structure of CrB₂ is antiferromagnetic in the sense that the direction of the moment vector varies at a high spatial frequency.
- (iv) In addition our refinement suggests a long-range modulation of the moment amplitude with $\lambda \approx 7a$. This is illustrated in Fig. 2.16a where the moment vectors have been colored with respect to their size. This kind of visualization demonstrates that the long-range modulation results in areas which are marked by an enhanced amplitude of the magnetic moment and which form a sixfold hexagonal pattern. In the center of these areas, however, the magnetic moment is essentially zero, resulting in a vortex-like structure. Fig. 2.16b illustrates the long-range modulation of the moment size for a cut along the $[100]$ -direction.

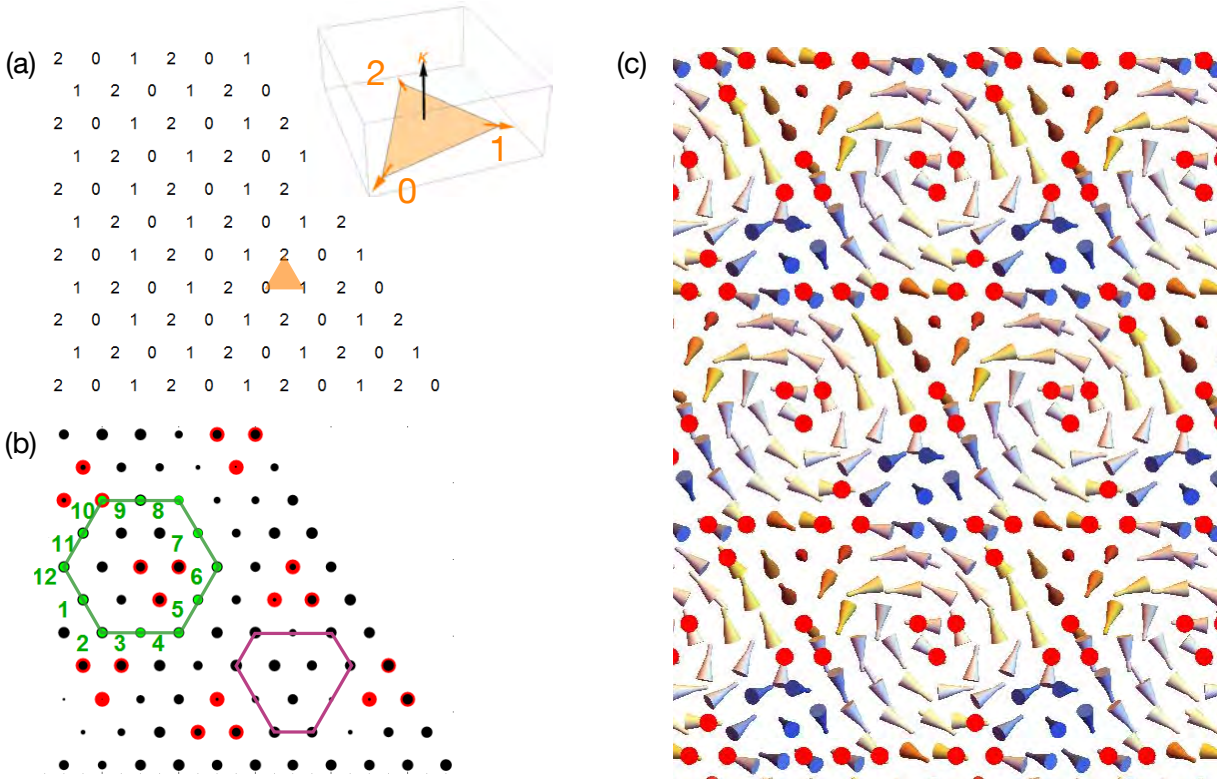


Figure 2.17: Topology of the $P\bar{3}'1m'$ triple-k structure. (a) The quasi two-dimensional spin structure may be considered as a set of upward elementary triangles where each corner is occupied by a Cr atom. Inset: For each triangle the vector κ quantifies the strength of the local 120° spin symmetry. (b) Black dots correspond to the elementary triangles in (a) which form, again, a triangular lattice. Their size indicates the magnitude of κ . Triplets of red dots indicate vortex positions. (c) The κ vector in a larger part of a Cr sheet. Again red dots indicate vortex positions showing the formation of a vortex lattice.

2.4.5.1 Topological Mapping

The regular pattern of vortex-like spin structures formed in the triple-k solutions, shown e.g. for $P\bar{3}'1m'$ in Fig. 2.15 and Fig. 2.17, is reminiscent of the Skyrmion lattice that was recently revealed in various B20 compounds such as MnSi [114], Fe_{1-x}Co_xSi [115, 116], FeGe [117], Cu₂OSeO₃ [118], and some Co-Zn-Mn alloys [119]. In these chiral ferromagnets the magnetic moments turn smoothly at constant amplitude thereby forming helices. The anisotropy of the underlying nuclear lattice pins these helices to high-symmetry directions resulting in a superposition of three helices and, consequently, a regular pattern of magnetic vortices referred to as Skyrmion crystal. The topology of this Skyrmion crystal phase causes some remarkable physical properties, e.g., the topological Hall effect [120–122], and novel collective excitations [123–125].

Even though the triple-k structures discussed here for CrB₂ are characterized by antiferromagnetic moments with a high spatial frequency and a strongly modulated amplitude, thus differing

clearly from the Skyrmion lattice described above, they may as well be understood in terms of a two-dimensional vortex crystal. It is therefore interesting to examine the non-trivial topology of these solutions in more detail. The results of this analysis will be reported in the following.

As only the Cr atoms carry a magnetic moment the honeycomb B sheets were neglected. In analogy with the theoretical investigations of the Heisenberg-AFM model given in Ref. [111] the Cr layers were considered as a set of upward elementary triangles. As shown schematically in Fig. 2.17a each triangle is formed by three counterclockwise numbered nearest Cr neighbors. Then the vector

$$\boldsymbol{\kappa} = \frac{2}{3\sqrt{3}} (\mathbf{S}_0 \times \mathbf{S}_1 + \mathbf{S}_1 \times \mathbf{S}_2 + \mathbf{S}_2 \times \mathbf{S}_0),$$

where the \mathbf{S}_i denote the magnetic moments of the corresponding Cr atoms at the edges of a triangle, measures the quality of the local 120° spin correlations, cf. inset in Fig. 2.17a. $|\boldsymbol{\kappa}| = 1$ if the moment vectors are aligned under 120° with respect to each other. In contrast, $|\boldsymbol{\kappa}| < 1$ if the three spins located at the edge of a triangle exhibit deviations from perfect 120° symmetry. Fig. 2.17b shows $\boldsymbol{\kappa}$ as calculated for the Cr atoms shown in Fig. 2.17a, i.e., each black dot corresponds to an elementary triangle in Fig. 2.17a. The magnitude of $\boldsymbol{\kappa}$ is indicated by the size of the black dots, showing that a local 120° symmetry is present in the greatest part of the structure.

The order parameter space which is suited to describe the present model is isomorphic to the three-dimensional rotation group SO(3). For a two-dimensional system the SO(3) order parameter space is incompatible with topologically stable line defects or Instantons. It allows however the formation of point defects, namely \mathbb{Z}_2 vortices [111].

This may be seen most clearly by considering the rotation of $\boldsymbol{\kappa}$ upon going from one triangle to another. In order to detect a vortex this rotation $R(\Theta, \mathbf{n}) \in \text{SO}(3)$ may be parametrized in terms of the spin rotation group SU(2).

$$U(\Theta, \mathbf{n}) = e^{\frac{\Theta}{2i} \mathbf{n} \boldsymbol{\sigma}}, U \in \text{SU}(2),$$

where Θ and \mathbf{n} are the rotation angle and axis, respectively, and $\boldsymbol{\sigma} = (\sigma_x, \sigma_y, \sigma_z)$ are Pauli matrices. Along any contour C the total change of $\boldsymbol{\kappa}$ is given by the product of the associated rotation matrices

$$\prod_C e^{\frac{\Theta}{2i} \mathbf{n} \boldsymbol{\sigma}}.$$

For a closed contour the so-called vorticity may be calculated from the trace of the latter expression as

$$V[C] = \frac{1}{2} \text{Tr} \prod_C e^{\frac{\Theta}{2i} \mathbf{n} \boldsymbol{\sigma}}.$$

Due to the \mathbb{Z}_2 nature of the vortices $V[C] = \pm 1$, i.e., it adopts only two values depending on whether the path contains a vortex ($V[C] = -1$, green path in Fig. 2.17b) or not ($V[C] = 1$,

purple path in Fig. 2.17b).

Depending on the orientation of κ with respect to the two-dimensional triangular lattice sometimes two types of vortices are distinguished [111]. For “type-I” and “type-II” vortices κ points perpendicular and parallel to the lattice plane, respectively. Fig. 2.17c shows κ for a large portion of a Cr sheet. Clearly κ lies within the metal plane for the vast majority of atoms. Accordingly, the spin arrangement may be identified as type-II vortex structure.

In Fig. 2.17c triplets of red dots mark the positions of vortices which form a two-dimensional hexagonal lattice. As the magnetic modulations of neighboring metal sheets are equivalent each Cr layer of the $P\bar{3}'1m'$ triple-k structure κ exhibits also the same two-dimensional hexagonal vortex lattice. Altogether the structure may hence be considered as a vortex crystal. The analysis of the $P6'mm'$ triple-k structure reveals essentially the same key features, namely 120° spin correlations and the formation of a (slightly different) vortex lattice.

2.4.5.2 Conclusion of the Topological Analysis

In summary the triple-k structures $P6'mm'$ and $P\bar{3}'1m'$ seem to provide the best solution of the magnetic structure of CrB₂. First, they fit the single crystal diffraction data extremely well. Second, superstructure peaks revealed by single crystal neutron diffraction and diffuse neutron scattering suggest the existence of a triple-k nuclear modulation. The associated propagation vectors are closely related to the three magnetic k-vectors of the $P\bar{3}'1m'$ and $P6'mm'$ space groups, hence suggesting an intimate connection of the nuclear superstructure and the magnetic order in CrB₂. The putative interplay of itinerant magnetic order and a weak nuclear modulation constitutes already a surprising result. Perhaps even more importantly, the presence of a triple-k nuclear superstructure and its supposable coupling to the magnetic order suggests, in turn, the existence of a magnetic triple-k structure. Finally, the analysis of the $P6'mm'$ and $P\bar{3}'1m'$ structures reveals a highly non-trivial topology which is characterized by 120° spin correlations and a regular arrangement of vortices, i.e., a vortex crystal phase. These structures can explain quite naturally the strong geometric frustration inferred from low-temperature bulk measurements. Their formation in CrB₂ is consistent with theoretical predictions of the antiferromagnetic Heisenberg-Kitaev model on a triangular lattice. To the best of our knowledge, the measurements carried out as part of this thesis may hence provide the very first example of the realization of the Heisenberg-Kitaev model in an itinerant magnet.

2.4.5.3 Future Experiments

In order to identify a triple-k state in CrB₂ unambiguously additional experimental information will be necessary. As our measurements at both RESI and HEiDi were carried out using unpolarized neutrons the question is whether neutron polarimetry may be suited to clarify this issue. Calculations of the polarization matrices P on the basis of the Blume-Maleev equation were carried out by WOLFGANG SIMETH as part of his Ph.D. thesis for a regular cycloid

	\mathbf{Q}_1		\mathbf{Q}_2		\mathbf{Q}_3	
	P_{11}	P_{22}	P_{11}	P_{22}	P_{11}	P_{22}
regular cycloid (Ref. [77])	-1.000	-0.216	-1.000	-1.000	-1.000	-0.109
C2/m.1'(a0g)0ss	-1.000	-0.349	-1.000	-1.000	-1.000	-0.250
Cmm2(a00)0s0	-1.000	-0.347	-1.000	-1.000	-1.000	-0.240
P6'mm'	-1.000	-0.349	-1.000	-1.000	-1.000	-0.249
P3'1m'	-1.000	-0.324	-1.000	-1.000	-1.000	-0.223
C2/m.1'(a0g)0ss (reg.)	-1.000	-0.216	-1.000	-1.000	-1.000	-0.109
Cmm2(a00)0s0 (reg.)	-1.000	-0.216	-1.000	-1.000	-1.000	-0.109
P6'mm' (reg.)	-1.000	-0.216	-1.000	-1.000	-1.000	-0.109
P3'1m' (reg.)	-1.000	-0.216	-1.000	-1.000	-1.000	-0.109

Table 2.6: Calculated elements P_{ij} of the polarization matrix expected in polarized neutron scattering off the proposed magnetic structures of CrB₂ at the positions of different magnetic satellite peaks $\mathbf{Q}_1 = (0.286, 1 - 2 \cdot 0.286, 0)$, $\mathbf{Q}_2 = (0.286, 0.286, 0)$, and $\mathbf{Q}_3 = (2 \cdot 0.286, 1 - 0.286, 0)$. Off-diagonal elements are zero and therefore not shown. The matrix elements P_{33} can be calculated as $P_{33} = -P_{22}$. They are not listed for lack of space. For all calculations an incident neutron beam of polarization P_i and a scattered neutron beam of polarization P_f were assumed, where $P_f = P_{ij}P_i$ was calculated on the basis of the Blume-Maleev equations.

and the four test structures considered in this thesis, each for the magnetic Bragg peaks at $\mathbf{Q}_1 = (0.286, 1 - 2 \cdot 0.286, 0)$, $\mathbf{Q}_2 = (0.286, 0.286, 0)$, and $\mathbf{Q}_3 = (2 \cdot 0.286, 1 - 0.286, 0)$ [113]. In the case of equally populated domains the off-diagonal elements vanish for all matrices. The non-zero main diagonal elements are summarized in Tab. 2.6. The results obtained for the regular cycloid are fully consistent with calculations reported by KAYA [81] suggesting in turn that our calculations are correct. For the four model structures considered in this thesis a comparison of the individual matrix elements reveals only tiny differences. A discrimination of the model structures by means of neutron polarimetry is therefore ruled out. In fact, neutron polarimetry is extremely sensitive with respect to the out-of-plane component of the magnetic structures. Consequently the differences in the polarization of the regular spin cycloid and any of the four structures considered in this thesis, all of which involve distorted modulation waves, are large. This suggests that neutron polarimetry might allow to distinguish between the regular cycloid and the four distorted structures. During the refinement, however, the structures can be constrained such as to comprise only of regular (undistorted) modulation waves. This results in a significant change of the corresponding polarizations which can no longer be distinguished from the polarization of the simple cycloid, cf. Tab. 2.6. As summarized in Tab. 2.7 the constraint does however not affect the R values too much. Even more importantly, the above-mentioned topological properties of the P6'mm' and P3'1m' triple-k structures remain unaltered. Therefore neutron polarimetry is not suited to provide the necessary experimental underpinning for either a single-k or a triple-k state in magnetic CrB₂.

The Weak Itinerant Antiferromagnet CrB₂

SpCGrp	R factors	R	wR	R_{nuc}	wR_{nuc}	R_{mag}	wR_{mag}
Single-k Structures							
C2/m.1'(a0g)0ss (reg.)	101=101+0/9	4.78	6.82	4.77	6.84	5.19 (4.78)	6.63 (5.98)
Cmm2(a00)0s0 (reg.)	90=90+0/9	4.47	6.36	4.44	6.29	5.63 (5.03)	6.90 (6.04)
Triple-k Structures							
P6'mm' (reg.)	36=36+0/5	3.71	5.11	3.66	4.60	6.52 (5.45)	7.22 (6.26)
P3'1m' (reg.)	50=50+0/5	3.77	5.38	3.69	4.64	6.85 (6.32)	8.03 (7.53)

Table 2.7: Magnetic structure refinement of CrB₂ for the four magnetic model structures exhibiting the best agreement with the experimental data, cf. Tab. 2.3. All fits are based on symmetry averaged data. In contrast to the refinements summarized in Tab. 2.5 only regular modulation waves were permitted, i.e., modulations of the moment amplitude were prohibited. For easier comparison the magnetic reliability factors of the solutions comprising of distorted modulation waves are shown in brackets.

Alternatively, neutron diffraction off a magnetic single-domain state prepared, e.g., by means of uniaxial pressure or a very high symmetry breaking magnetic field may provide an adequate tool to rule out the single-k or the triple-k scenario: In a single-domain state the above-mentioned six-fold scattering pattern around each individual nuclear Bragg peak is expected only for a triple-k structure. In contrast, a single-k structure would be characterized by a two-fold scattering pattern consisting of one Friedel pair. Due to the brittleness of CrB₂ uniaxial pressure experiments are however challenging, particularly in combination with neutron diffraction. Furthermore such experiments will be limited to relatively small pressures of some hundred MPa. Therefore, even if small uniaxial stress was successfully applied to a single crystal sample this would not per se guarantee the generation of a single-domain state, hence complicating the interpretation of experimental results.

The preparation of a single-domain state by means of a high magnetic field is difficult, too. As summarized in Sec. 2.5, the bulk and transport properties of CrB₂ display an extraordinary low magnetic field dependence. This in turn suggests that the energy scale required to affect the long-range magnetic order is very large, i.e., a very strong tuning field which may be provided only by means of pulsed magnets will be needed.

The distinction of single-k and triple-k structures may be possible on the basis of higher order magnetic satellites. For the single-k structures only satellites at positions $\mathbf{Q} = n\mathbf{q}_1$, $n \in \mathbb{N}$ are expected. In contrast, mixed satellites at positions $\mathbf{Q} = \sum_{i=1}^3 n_i \mathbf{q}_i$, $n_i \in \mathbb{N}$, may occur in the case of a triple-k structure. The search for mixed higher order satellites is however complicated by (i) the relatively small ordered moment, (ii) the comparatively large mosaicity, and (iii) the high crystalline symmetry. Due to the small ordered moment and the large mosaicity higher order reflections will have low scattering intensity, demanding in turn long counting times and high neutron flux. Due to the hexagonal crystal symmetry higher order mixed satellites cannot be easily separated from multiple scattering as they share the same positions in reciprocal space.

Hence elaborate techniques such as Renninger scans will be needed to distinguish between mixed higher order magnetic reflections by a multi-k structure and multiple scattering by a single-k structure.

Finally, nuclear magnetic resonance (NMR) may provide additional insights into the magnetic structure of single crystal Cr¹¹B₂. NMR allows to probe microscopically the magnetic interactions, e.g., by studying the hyperfine coupling of ¹¹B with its chemical environment comprising of six nearest neighbor Cr ions. Therefore, NMR fine spectra may allow to distinguish between the simple spin cycloid and the proposed, complex multi-k structures. It is interesting to note, that the the low-temperature NMR spectra reported so far [82, 85] seem to be inconsistent with the formation of a single-k spin cycloid below T_N . Whether the multi-k structures proposed in this thesis may account for these NMR spectra is still an open question and will require further theoretical investigation.

In summary, a clear determination of the magnetic structure of CrB₂ by means of neutron scattering will require sophisticated experimental methods such as neutron diffraction in combination with the preparation of a single-domain state, e.g., by means of uniaxial pressure or very high magnetic fields. Alternatively, NMR may provide further information about the details of the magnetic structure. These additional measurements are beyond the scope of this Ph.D. thesis.

2.4.6 Summary

In summary a comprehensive powder and single crystal neutron diffraction study of the nuclear and magnetic structure of high-quality Cr¹¹B₂ was carried out. These experiments go well beyond earlier measurements both quantitatively and qualitatively. More precisely a large number of distinct nuclear and magnetic Bragg reflections was recorded. Among these numerous Bragg peaks only those were used for the magnetic structure refinement which had extraordinary good counting statistics, meeting a 10σ criterion. Despite this restriction the number of reflections which were eventually included in the refinement was still high enough (67 magnetic peaks) to allow for a statistically meaningful evaluation. Moreover, it exceeded by far the number of reflections considered in earlier investigations. These benefits arise mainly from the high quality of the single crystal samples studied and from their ¹¹B-enrichment which reduces significantly neutron absorption and extinction effects.

All strong Bragg peaks recorded at high and low temperature are consistent with the C32 crystal structure. Consequently, these Bragg peaks must be considered to be nuclear in origin. Both the positions and the intensities of these nuclear peaks are essentially unchanged upon cooling of the sample. Thus there are no indications of a structural phase transition.

In contrast a magnetic phase transition can most clearly be seen from the appearance of multiple satellite peaks below $T_N = 89\text{ K}$. The continuous increase of the satellite intensities with decreasing temperature supports a second order, magnetic phase transition. A closer inspec-

tion and comparison of $I(T)$ for several magnetic satellite peaks suggests that the temperature dependence exhibits a dip between 40 K and 60 K. While cooling through this temperature range the curvature of the intensity curve $I(T)$ changes sign resulting in a faint dent centered around ~ 50 K. This loss of intensity is unambiguously resolved only for a single measurement at RESI, namely the temperature scan of the $(1, \bar{1}, 0) + \chi$ satellite peak, hence raising the question whether the anomaly observed in this measurement is actually a feature of the sample or rather an artifact of the measurement. The faint shoulder in $I(T)$ is, however, most clearly seen in all measurements carried out at HEiDi. Due to the high density of the data points as well as the excellent counting statistics these measurements must be considered more reliable than the ones carried out at RESI. In total the experiments at both instruments therefore suggest that the shoulder in $I(T)$ is not an artifact but a robust feature which is intrinsic to the sample. The microscopic origin of the anomalous temperature dependence is still not clear. In this context it is worth mentioning measurements of the low-temperature magnetic heat capacity of CrB₂. It has been shown that C_{mag} also exhibits a broad shoulder around 50 K [98]. This coincidence suggests that both anomalies may have a common microscopic origin. To clarify this issue conclusively further measurements will be necessary.

Six magnetic satellite peaks surround each nuclear reflection characteristic of a sixfold rotational symmetry about the reciprocal c -axis, $[001]^*$. This clearly demonstrates that the magnetic structure is incommensurate with the nuclear lattice. Consistent with powder neutron diffraction the magnetic satellite peaks can be indexed using three k -vectors of unique length. One of these k -vectors, $\tau = 0.286\tau_{110}^*$, is almost identical to the value suggested by FUNAHASHI. The other k -vectors, χ and ϵ , result from τ by a rotation of $\pm 120^\circ$ about the $[001]^*$ direction.

Refinements of the magnetic structure of CrB₂ were carried out on the basis of a state-of-the-art representation analysis. To the best of our knowledge the nuclear symmetry has not been taken into account in earlier studies. Consistent with Ref. [77] the data recorded as part of this thesis allow rule out a sinusoidal spin structure which had been suggested in an earlier publication [52]. Instead our data are compatible with four possible solutions of the magnetic order of CrB₂, where two are single- k and two are triple- k structures. Even though at present the correct solution cannot be identified unambiguously, empirical considerations suggest that a two-domain triple- k structure, either $P6'mm'$ or $P\bar{3}'1m'$, is realized in CrB₂. First, superstructure peaks revealed by single crystal neutron diffraction and polarized diffuse neutron scattering hint at the formation of a triple- k nuclear modulation and its close connection to the long-range magnetic order. This suggests that the latter is a triple- k structure, too. Second, the inherent frustration of both the $P6'mm'$ and the $P\bar{3}'1m'$ structure can explain quite naturally the strong geometric frustration inferred from the low-temperature bulk measurements. An analysis in the spirit of the antiferromagnetic Heisenberg-Kitaev model on a triangular lattice suggests, that in these structures magnetic frustration manifests in a highly non-trivial topology, characterized by 120° spin correlations and the formation of a \mathbb{Z}_2 vortex crystal. Even

though further investigations will be required to establish a magnetic triple-k structure in CrB₂ conclusively this investigation suggests that the latter may represent the first example of Kitaev physics in an itinerant magnet.

2.5 Low-temperature Bulk and Transport Properties of CrB₂

In the following section the low-temperature bulk and transport properties of high-quality single crystal samples of CrB₂ are reported. The study carried out as part of this thesis comprises measurements of the uniform magnetization, the specific heat, the resistivity, and the Hall effect. These investigations identify CrB₂ consistently as the best candidate material exhibiting weak itinerant antiferromagnetism reported in the literature so far. The measurements also address the role of geometric frustration and magnetic anisotropy in this hexagonal compound and allow to consider implications for superconductivity in non-magnetic CrB₂.

2.5.1 Magnetization

The account of the low-temperature bulk properties of CrB₂ begins with typical magnetization data. Fig. 2.18a shows the uniform magnetization of CrB₂ as a function of temperature for magnetic field up to 9 T. M is small in the paramagnetic as well as in the ordered state. It varies only slightly with temperature and shows a clear cusp at $T_N = 88.5$ K. This value of T_N is perfectly consistent with the measurements of the heat capacity, resistivity, and Hall effect presented below. Both, the qualitative shape of the magnetization curve and the temperature of the maximum do not change in fields up to 9 T for field along $\langle 100 \rangle$ and $\langle 001 \rangle$. Comparing M for both field directions yields a small easy-plane anisotropy of $\sim 10\%$, consistent with an earlier report [92].

Fig. 2.18b shows M/H for 1 T as a function of temperature. M/H serves as an estimate for the susceptibility, $\chi = dM/dH$, and is small and positive for all temperatures studied. This is consistent with the small, strictly linear field dependence, $M(H)$, shown in Fig. 2.19. In contrast to most previous studies [8, 93, 126] M/H does not exhibit a so-called Curie tail, i.e., a low-temperature increase, hence suggesting the absence of any impurity-induced susceptibility enhancement. During single crystal growth such magnetic impurities may be introduced from contaminated starting elements or the growth apparatus. For instance, Fe contaminations are commonly contained in less pure, commercial B powders. The absence of a low-temperature Curie tail in the magnetization data corroborates the excellent quality of the single crystal samples studied in this thesis which have been grown from high purity starting elements.

The inverse normalized magnetization, H/M , is depicted in Fig. 2.18c. In the paramagnetic state it follows a Curie-Weiss temperature dependence. Its slope, $d(H/M)/dT$, is essentially unchanged for the field range studied. Extrapolation of H/M to $T = 0$ yields a large negative Curie-Weiss temperature of $\Theta_{CW} \approx -750(50)$ K and a large fluctuating effective moment,

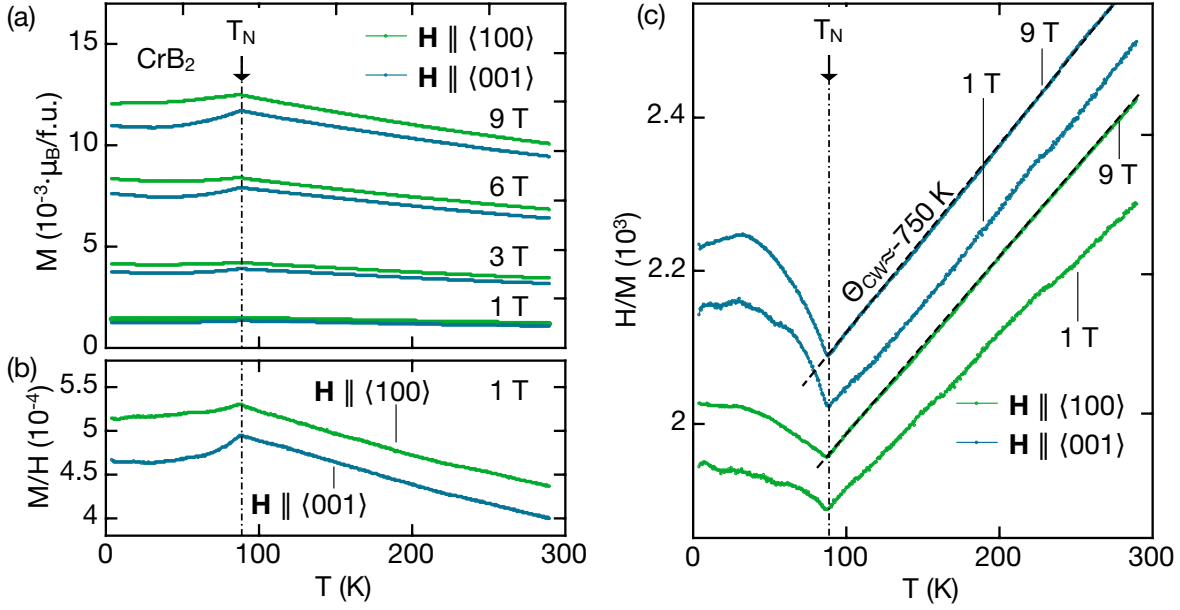


Figure 2.18: Magnetization of CrB₂ as a function of temperature. (a) Uniform magnetization M for various fields applied along the hexagonal a - and c -axis, respectively. (b) Normalized magnetization, M/H , for $\mu_0 H = 1$ T for both field directions. (c) Inverse normalized magnetization, H/M , for $\mu_0 H = 1$ T and 9 T and both field directions. Curie-Weiss fits to the high-temperature paramagnetic part are shown as dashed lines. Dash-dotted lines mark the position of $T_N = 88.5$ K.

$m_{\text{eff}} = 2.2(1) \mu_B$. This value is slightly larger than expected for Cr(III), exhibiting a [Ar]3d³ configuration with $m = 1.94 \mu_B$. In full agreement with the literature [79, 92] the effective fluctuating moment exceeds by far the ordered moment $m_s \approx 0.5 \mu_B/\text{Cr}$ observed by neutron diffraction. The enhancement of m_{eff} over m_s is considered a hallmark of weak itinerant magnetism. The large negative Curie-Weiss temperature and the large value of m_{eff} hint at strong antiferromagnetic interactions and an abundance of spin fluctuations, respectively.

The ratio $f = -\Theta_{\text{CW}}/T_N$ is often considered as a measure of the strength of geometric frustration. Large values of f imply a strong suppression of the long-range magnetic order and hence strong geometric frustration. For CrB₂ $f \approx 8.5$, which is characteristic of strong geometric frustration [127].

Finally, the field dependence $M(H)$ of paramagnetic CrB₂, $T = 100$ K, and antiferromagnetic CrB₂, $T = 2$ K, is shown in Fig. 2.19. The two curves almost coincide and exhibit essentially the same field dependence. As mentioned above $M(H)$ is small and strictly linear. Hence the possibility of a field induced spin-flop transition in the magnetically ordered state may be ruled out. Finally, no saturation of the magnetization is achieved up to the highest field studied which represents, again, a characteristic feature expected of weak itinerant magnetism.

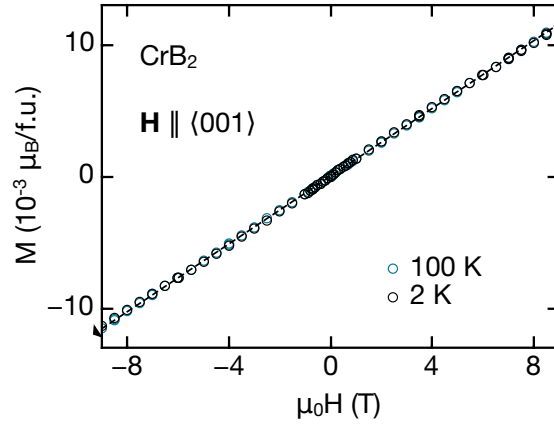


Figure 2.19: Magnetization of CrB₂ as a function of field. The magnetic field dependence, shown here of M for $H \parallel \langle 001 \rangle$, is small and strictly linear in the full field and temperature range studied. No indications for a spin-flop transition are observed. The dashed line serves as a guide to the eye.

2.5.2 Specific Heat

Typical specific heat data are shown in Fig. 2.20. External magnetic fields of up to 9 T were applied in the hexagonal basal plane. A pronounced λ -anomaly is detected at $T_N = 88.5$ K, characteristic of a second order phase transition. Here T_N was determined using an entropy conserving construction and agrees nicely with the transport and magnetization measurements. As expected for an itinerant magnet both T_N and the absolute value of C are essentially unchanged even in the highest field studied, $\mu_0 H = 9$ T. In the low-temperature limit where lattice contributions can be neglected the electronic specific heat C/T extrapolates to a Sommerfeld coefficient of $\gamma_0 = 13 \text{ mJ mol}^{-1} \text{ K}^{-2}$. This is consistent with the value reported in the literature, $\gamma_0 = 13.6 \text{ mJ mol}^{-1} \text{ K}^{-2}$ [72], and typical for d - and f -electron materials with moderate electronic correlations. In the high-temperature Dulong-Petit limit where lattice contributions dominate the specific heat data limits to $C_{DP} = 9R = 74.83 \text{ J mol}^{-1} \text{ K}$, with the universal gas constant R . This is fully consistent with the unit cell of CrB₂ containing three atoms.

For an estimate of the electronic specific heat at intermediate temperatures, e.g., close to T_N , where phonon contribution are already quite substantial, the specific heat of the non-magnetic isostructural sibling VB₂ was subtracted from the specific heat data of CrB₂. The lack of strong electronic correlations in VB₂ is consistent with a low Sommerfeld coefficient, extrapolated to $\gamma_0 = 4 \text{ mJ mol}^{-1} \text{ K}^{-2}$. On the other hand the specific heat of of VB₂ cannot be accounted for by a simple Debye model (cf. the solid curve in Fig. 2.20a). If Θ_D is chosen such that the Debye model approaches the observed high-temperature specific heat of CrB₂ and VB₂ the value $\Theta_D = 950$ K is obtained. This value of Θ_D is similar to values reported for other diborides. Comparison with our specific heat measurements however shows that additional phonon contributions must be taken into account at intermediate temperatures. These contributions potentially originate

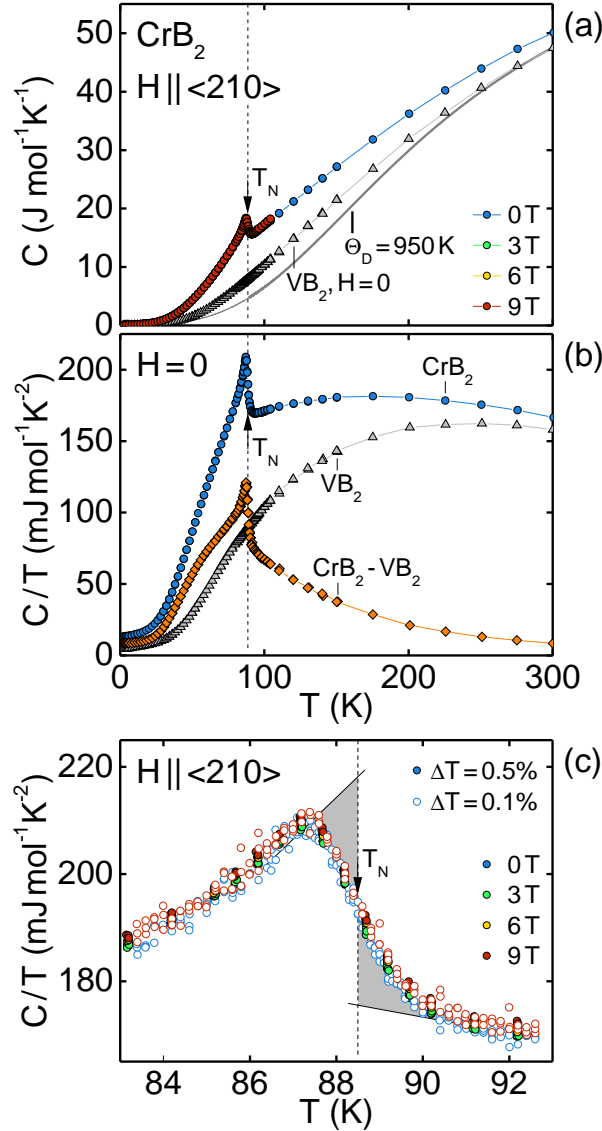


Figure 2.20: Specific heat of CrB₂. The graph was taken from Ref. [98]. (a) Specific heat of CrB₂ for various magnetic fields. The specific heat of non-magnetic VB₂ may serve as an estimate of the lattice contribution to C . (b) Estimate of the electronic specific heat, C/T . (c) Zoom into the λ -anomaly. An entropy conserving construction (grey areas) was used to determine the Néel temperature T_N . A value of $T_N = 88.5$ K was found, irrespective of the external magnetic field and the size of the heat pulses applied.

from the quasi two-dimensional crystal structure.

Subtraction of the specific heat of VB₂ from the specific heat of CrB₂ reveals two features which can be seen best in C/T , Fig. 2.20b. First, the electronic specific heat determined this way is quite large even for $T > T_N$ suggesting strong spin fluctuations well above the onset of long-range magnetic order. This finding is fully consistent with the large effective fluctuating

moment inferred from the temperature dependence of the magnetization. Second, for $T < T_N$ the temperature dependence of the electronic specific heat exhibits a negative curvature resulting in a faint cusp around 50 K.

The unusual shape of the specific heat curve suggests the existence of additional electronic excitations for this intermediate temperature regime. This is supported by our magnetic neutron diffraction: as stated in Secs. 2.4.2 and 2.4.3 the temperature dependence of the magnetic Bragg scattering displays a dent in the same temperature range, $T \sim 50$ K. For many materials the temperature dependence of the electronic specific heat scales as the temperature derivative of the resistivity $d\rho/dT$. In fact this may be expected whenever the same scattering mechanism which determines the electronic transport properties also dominates the specific heat and, further, follows Fermi's golden rule [128]. As will be shown below $d\rho/dT$ does not exhibit a cusp around 50 K and hence does not scale as C/T . This suggests, that the excitations which give rise to the additional electronic specific heat do not affect the electronic transport. Overall, the same charge carriers which cause the specific heat enhancement also participate in the long-range antiferromagnetic order, implying once more the itinerant character of the antiferromagnetism in CrB₂. The microscopic nature of these additional excitations is hitherto unclear. Keeping in mind that in elemental Cr both spin and charge order occur and are intimately connected [129] one may speculate that CrB₂ could be on the verge of a charge order instability or may even exhibit charge order at room temperature already.

2.5.3 Electrical Resistivity and Hall Effect

Fig. 2.21a shows typical resistivity data of single crystal CrB₂. Measurements were carried out for two ingots, SFZ118 and SFZ162, and give essentially identical results. To study the resistivity anisotropy the excitation current was applied along two crystallographic directions, $\langle 100 \rangle$ and $\langle 001 \rangle$, resulting in the resistivity curves ρ_a and ρ_c , respectively. Both ρ_a and ρ_c decrease monotonically with decreasing temperature. Extrapolation to zero temperature yields a residual resistivity of $\rho_0^a = 4.2 \mu\Omega \text{ cm}$ and $\rho_0^c = 3.3 \mu\Omega \text{ cm}$. This corresponds to the highest hitherto reported residual resistivity ratios (RRR) of 16 and 32, respectively.

The resistivity anisotropy is small at low temperatures but strongly increases with increasing temperatures. At room temperature the c -axis resistivity is a factor of two larger than for current along a .

At the magnetic ordering transition the temperature dependence of ρ changes from a sub-linear behavior at high T to a super-linear behavior at low T . This change of slope results in a clear kink and allows the Néel temperature, $T_N = 88.5$ K, to be determined from the derivative of the resistivity with respect to the temperature, $d\rho/dT$. The latter is shown in Fig. 2.21b. As illustrated in Fig. 2.21e both, T_N and the qualitative form of the magnetic ordering transition, are unchanged in magnetic fields up to 14 T, the highest field studied.

A detailed analysis of the temperature dependence of the resistivity in the magnetically ordered

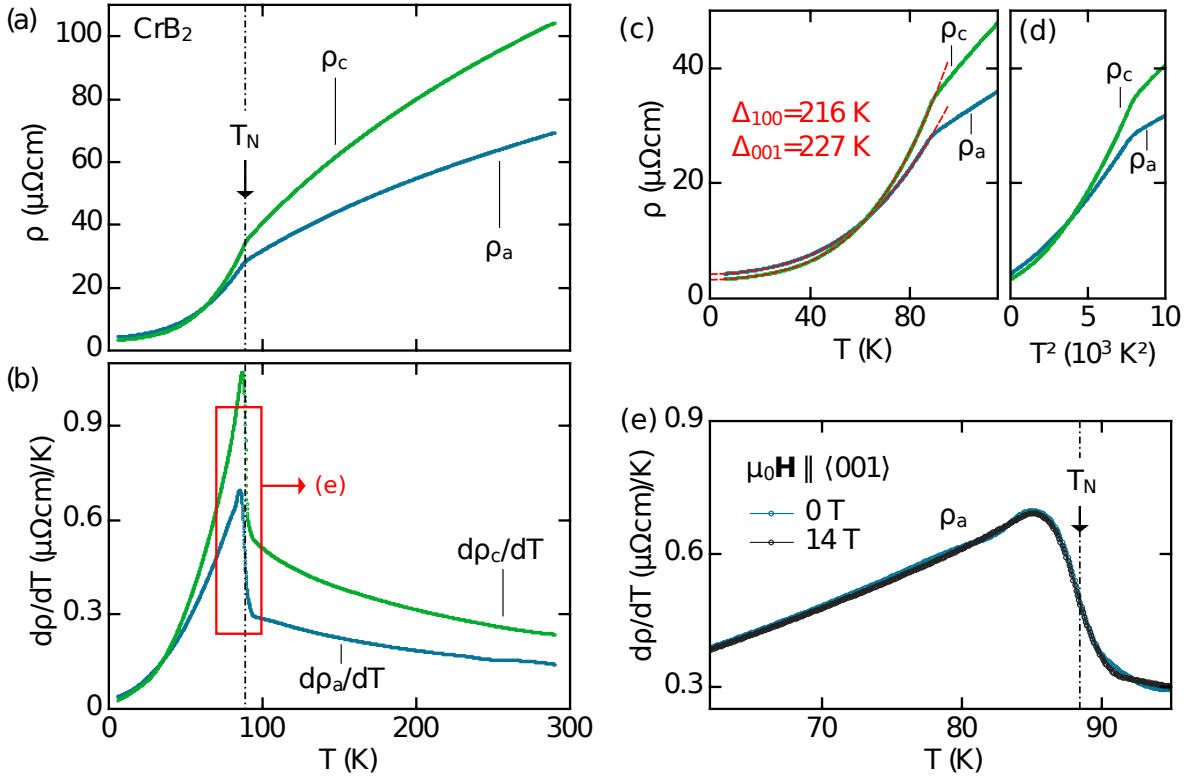


Figure 2.21: Electrical resistivity ρ of single crystal CrB₂. (a) Temperature dependence of ρ_a and ρ_c corresponding to the current directions, $\mathbf{j} \parallel \langle 100 \rangle$ and $\mathbf{j} \parallel \langle 001 \rangle$, respectively. The magnetic ordering transition is indicated by a pronounced kink at $T_N = 88.5$ K. (b) Temperature derivative of the resistivity, $d\rho/dT$, as a function of temperature. T_N is indicated by an abrupt jump. (c) Zoom into the low-temperature part of ρ . Dashed lines correspond to fits of the resistivity according to Eq. 2.2. (d) When plotted against T^2 ρ exhibits a clear curvature. Hence a quadratic temperature dependence must be ruled out. (e) $d\rho/dT$ at zero field and 14 T with current and field applied along the a - and c -axis, respectively. The dash-dotted line marks the position of T_N in all graphs.

state shows that $\rho(T)$ cannot be understood in a simple Fermi liquid picture. In a Fermi liquid scenario electron-electron scattering gives rise to $\rho \propto AT^2$. Fig. 2.21d shows ρ as a function of T^2 . The apparent curvature of both ρ_a and ρ_c in this graph implies that the resistivity below T_N does not follow a quadratic temperature dependence. In fact, the super-linear temperature dependence for $T < T_N$ may be accounted for extremely well by the formation of spin density wave (SDW) order. Here, three contributions to the resistivity were considered, namely (i) a constant term ρ_0 accounting for impurity scattering, (ii) the quadratic Fermi liquid temperature dependence AT^2 , and (iii) an exponential term accounting for scattering of electrons from bosonic excitations. In the case of CrB₂ these bosonic excitations are probably spin waves. Term (iii) is obtained by inserting a dispersion $\omega(\mathbf{k})$ with an excitation gap Δ , into a linearized Boltzmann

2.5 Low-temperature Bulk and Transport Properties of CrB₂

	SFZ118		SFZ162	
	$\mathbf{j} \parallel a$	$\mathbf{j} \parallel c$	$\mathbf{j} \parallel a$	$\mathbf{j} \parallel c$
ρ_0 ($\mu\Omega$ cm)	6.5	4.1	4.2	3.3
A ($\mu\Omega$ cm K ⁻²)	1.74	2.12	1.97	1.86
B ($\mu\Omega$ cm)	127	355	134	298
Δ (K)	210	226	216	227
RRR	11	31	16	32

Table 2.8: Results of the fit of a gapped Fermi liquid ground state as parametrized in Eq. 2.2 to the low-temperature resistivity, $T < T_N$, of CrB₂.

equation for $T < \Delta$. Since the three terms are due to different scattering mechanisms they may be added in the spirit of Matthiessen's rule:

$$\rho(T) = \rho_0 + AT^2 + B\frac{T}{\Delta} \left(1 + 2\frac{T}{\Delta}\right) \exp\left(-\frac{\Delta}{T}\right). \quad (2.2)$$

Fig. 2.21c shows the low-temperature resistivity ρ_a and ρ_c together with a fit according to Eq. 2.2 (dashed lines). The fitted curves agree nicely with the experimental data. As summarized in Tab. 2.8 essentially identical fits were obtained for both single crystal ingots studied, SFZ118 and SFZ162. Therefore the following discussion will be limited to the parameters found for SFZ118. The coefficients of the quadratic term, $A^a = 1.97$ n Ω cm K⁻² and $A^c = 1.86$ n Ω cm K⁻², agree with values of typical d -metals. The gap parameters $\Delta^a = 216$ K and $\Delta^c = 230$ K are slightly anisotropic. This is consistent with the small easy-plane anisotropy of the magnetization and compares with the resistivity anisotropy above T_N . The sub-linear temperature dependence of the resistivity in this paramagnetic temperature regime may be thought of as a result of the scattering of the conduction electrons from phonons and spin fluctuations. The pronounced anisotropy of ρ up to a factor of two at temperatures well above T_N thereby strongly supports a moderate anisotropy of the underlying spin fluctuations and is consistent with the easy-plane anisotropy of the magnetization.

The longitudinal magnetoresistance $\Delta\rho(H)$ of CrB₂ is depicted in Fig. 2.22a for various temperatures and magnetic field up to 14 T. $\Delta\rho(H)$ is small and negative at room temperature. At lower temperatures the magnetoresistance becomes positive and increases with decreasing temperature. For all temperatures studied $\Delta\rho(H)$ follows a conventional quadratic field dependence, $\rho \propto B^2$, over nearly the entire field range with a temperature dependent prefactor.

The Hall resistivity, ρ_{xy} , is shown for various temperatures in Fig. 2.22b. Current and magnetic field were applied along the a - and c -axis, respectively. For all temperatures studied ρ_{xy} is small and displays a strictly linear field dependence. No anomalous Hall contributions were found. This allowed the normal Hall constant, R_0 , to be measured by temperature sweeps at constant magnetic field, $B = \pm 6$ T. As shown in Fig. 2.22c the absolute value of R_0 increases

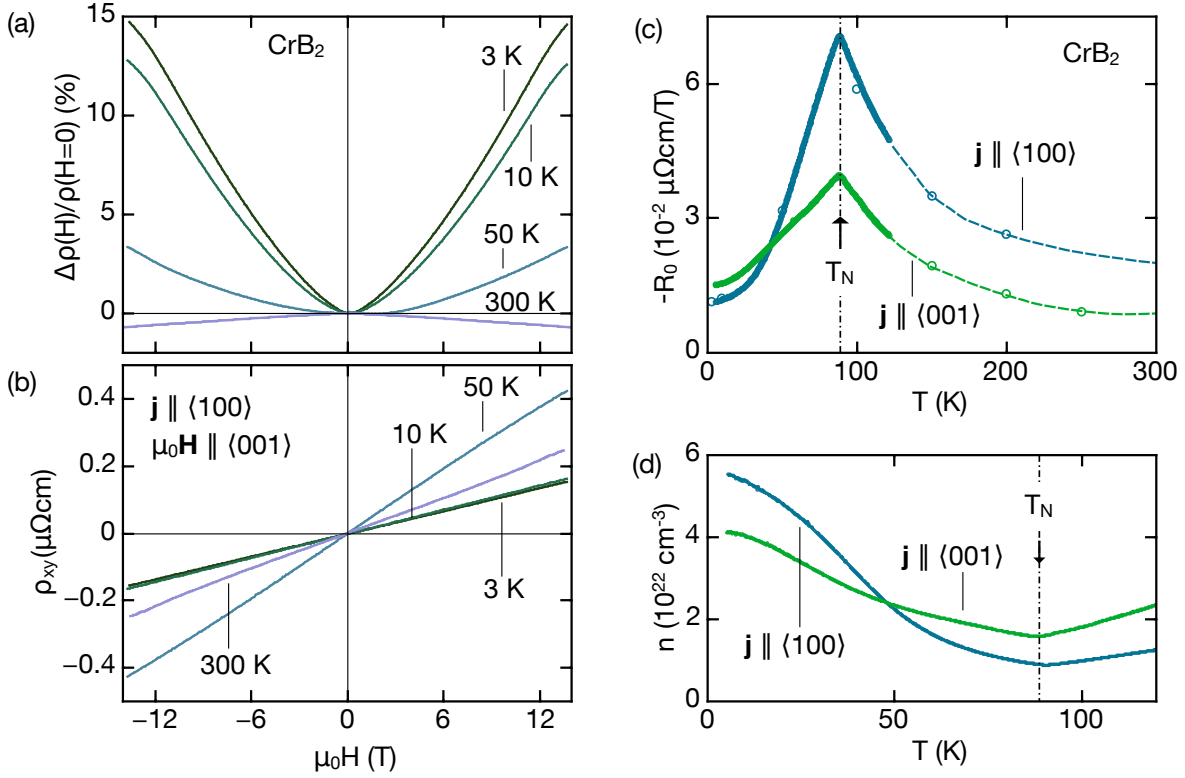


Figure 2.22: Magnetoresistance and Hall effect of CrB₂ for current along $\langle 100 \rangle$. (a) Longitudinal magnetoresistance as a function of magnetic field for various temperatures. (b) Hall resistivity for various temperatures. The magnetic field was applied along $\langle 001 \rangle$. (c) Normal Hall constant R_0 as a function of temperature for two current directions, $j \parallel \langle 100 \rangle$ and $j \parallel \langle 001 \rangle$. Full and open circles correspond to data determined from temperature sweeps and field sweeps, respectively. The dashed lines at high temperatures serve as a guide to the eye. (d) Effective charge carrier density as a function of temperature as calculated from R_0 . Vertical dash-dotted lines mark the position of $T_N = 88.5$ K.

as the temperature is increased, displays a clear cusp at $T_N = 88.5$ K, and then decreases. Data obtained from temperature sweeps and field sweeps are fully consistent and in perfect agreement with literature. The anisotropy with respect to the two current directions studied, $j \parallel \langle 100 \rangle$ and $j \parallel \langle 001 \rangle$, is small. The positive slope of the Hall resistivity indicates electron conduction. Using a simple one-band model the effective carrier density n can be estimated from R_0 . The absolute value found that way, $n \approx 10 \cdot 10^{22} \text{ cm}^{-3}$, is characteristic of a good metal. Fig. 2.22d shows n as a function of temperature. With decreasing temperature n displays a minimum at T_N followed by an increase. This faint S-shape suggests that multiple bands are present at the Fermi level and change differently with temperature.

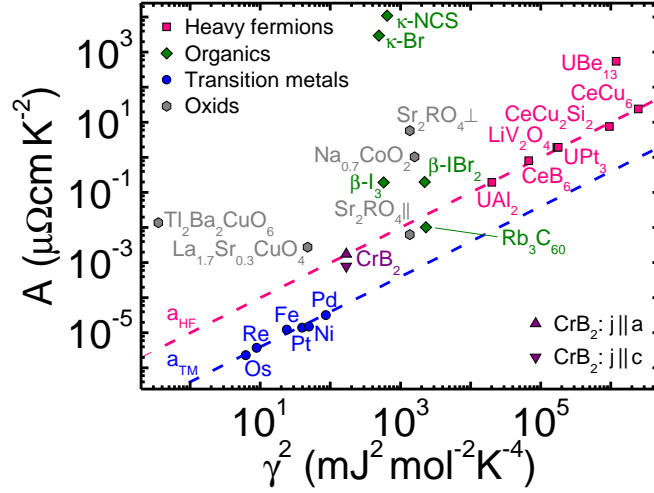


Figure 2.23: Kadowaki-Woods plot of selected d - and f -electron materials as presented in Ref. [130]. The Kadowaki-Woods ratio of CrB₂ differs clearly from typical d -electron compounds but is close to the value of typical heavy-fermion f -metals. The graph was adapted from Ref. [98].

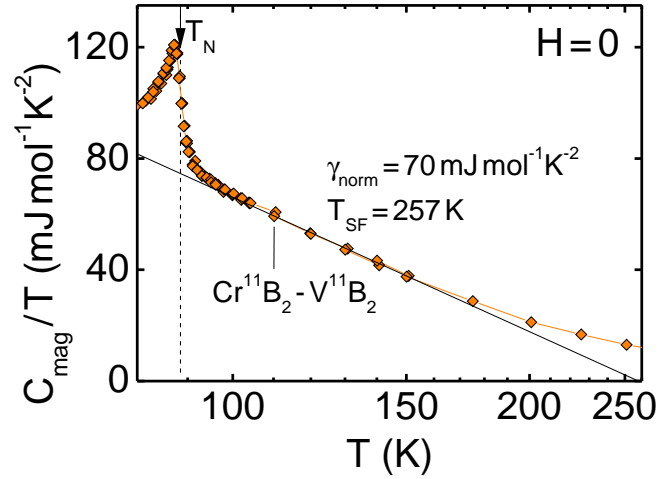


Figure 2.24: Magnetic contribution to the specific heat and the fit of its logarithmic temperature dependence according to Eq. 2.4. Graph adapted from Ref. [5].

2.5.4 Discussion

Turning to a discussion of the key experimental findings and their broader implications, the marked magnetic field independence of the low-temperature bulk and transport properties is addressed. It is then shown, that the ground state of CrB₂ is consistent with a Fermi liquid description and CrB₂ is compared to other correlated materials on the basis of an empirical classification using the Kadowaki-Woods ratio. The importance of spin fluctuations in CrB₂ is

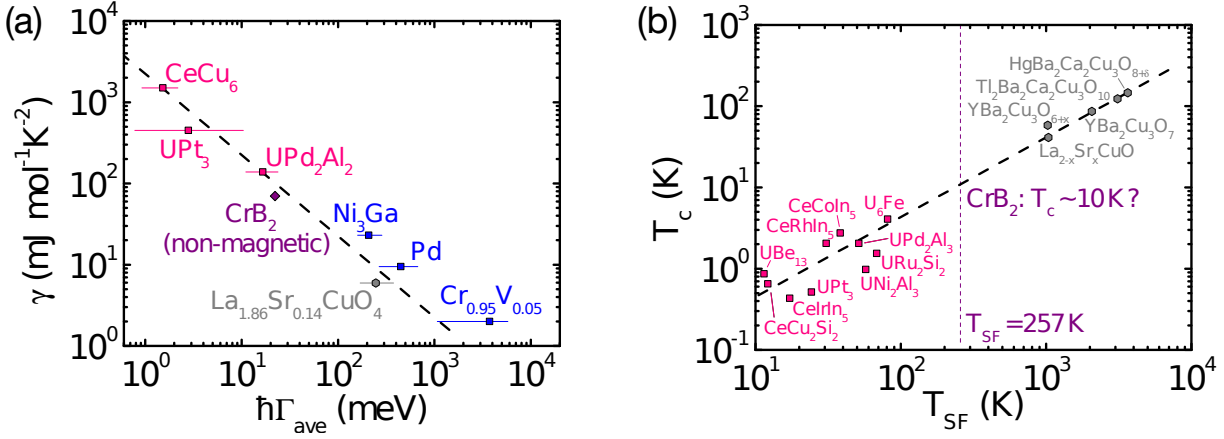


Figure 2.25: Estimate of the average spin fluctuation rate for non-magnetic CrB₂. (a) Empirical relationship of the normal-state Sommerfeld coefficient and the average fluctuating rate. The figure has been reproduced from Ref. [131]. (b) Correlation of the superconducting transition temperature T_c and the spin fluctuation temperature T_{SF} for some heavy-fermion and cuprate superconductors. The estimated fluctuation temperature $T_{\text{SF}} = 257 \text{ K}$ implies a possible critical temperature $T_c \approx 10 \text{ K}$ for magnetically mediated superconductivity in non-magnetic CrB₂. The figure has been reproduced from Ref. [132] Both graphs were adapted from Ref. [5].

outlined and quantified by deriving a high spin fluctuation temperature T_{SF} . Keeping in mind that strong spin fluctuations are widely accepted as a potential pairing mechanism for unconventional, magnetically mediated superconductivity possible scenarios for such superconductivity in non-magnetic CrB₂ are considered.

The discussion begins with an account of the field dependence of the low-temperature bulk and transport properties of CrB₂, which were not studied prior to the investigations carried out as part of this thesis. These measurements show that the effect of an applied magnetic field of up to 14 T is remarkably small. The resistivity exhibits a small quadratic magnetoresistance of a few percent. Yet the Néel temperature is essentially unchanged up to the highest field studied. Consistently, T_N does neither shift as a function of field when deduced from the magnetization and heat capacity data. It is noteworthy that the accuracy of our measurements is sufficient to rule out any changes of T_N within a tenth of a K. The marked independence of T_N of an applied magnetic field demonstrates that the energy scales of the magnetic order are large and typical for band structure effects. Most importantly the field-induced Zeeman splitting of the conduction band is still small at the highest fields studied. Hence the magnetic order must be due to the itinerant electrons which unambiguously identifies CrB₂ as an itinerant magnet. The classification of CrB₂ as an itinerant magnet is also supported by the observation of a gapped Fermi liquid ground state in the resistivity (Sec. 2.5.3) and the reduced ordered moment observed in neutron diffraction (Sec. 2.4) as compared to the large fluctuating Curie-Weiss moment inferred from magnetization measurements (Sec. 2.5.1).

It is interesting to compare CrB₂ to other materials with electronic correlations. The Kadowaki-Woods ratio a allows to classify materials with electronic correlations empirically and to check their consistency with Fermi liquid theory [130, 133]. It can be calculated from the coefficient A of the quadratic term of the temperature dependence $\rho(T)$ and the square of the Sommerfeld coefficient γ . A is proportional to the quasiparticle-quasiparticle scattering cross section, γ represents an effective quasiparticle mass. Thus the former probes the imaginary part of the quasiparticle self-energy and the latter its real part. In turn, the Kadowaki-Woods ratio is only meaningful if the quasiparticle self-energy is momentum independent [130].

From the resistivity measurements the coefficients $A_a = 1.76 \text{ n}\Omega \text{ cm K}^{-2}$ and $A_c = 2.12 \text{ n}\Omega \text{ cm K}^{-2}$ may be inferred, cf. Tab. 2.8. The temperature dependence of the specific heat allows to determine $\gamma_0 = 13 \text{ mJ mol}^{-1} \text{ K}^{-2}$. For the following discussion the A coefficients obtained from the single crystal SFZ118 were used since heat capacity data is only available for that sample. As the variation of the A coefficients for both single crystals studied, SFZ118 and SFZ162, is small, similar results may be expected if the A coefficients of sample SFZ162 were chosen instead. The Kadowaki-Woods ratio

$$a = \begin{cases} A_a/\gamma_0^2 = 10.4 \text{ }\mu\Omega \text{ cm mol}^2 \text{ K}^2 \text{ J}^{-2} \\ A_c/\gamma_0^2 = 12.5 \text{ }\mu\Omega \text{ cm mol}^2 \text{ K}^2 \text{ J}^{-2} \end{cases} \quad (2.3)$$

differs clearly from the Kadowaki-Woods ratio of typical transition metal compounds with $a_{\text{TM}} \approx 0.4 \text{ }\mu\Omega \text{ cm mol}^2 \text{ K}^2 \text{ J}^{-2}$. In fact the value of a corresponds rather to heavy-fermion f -electron systems with $a_{\text{HF}} \approx 10 \text{ }\mu\Omega \text{ cm mol}^2 \text{ K}^2 \text{ J}^{-2}$. As shown in Fig. 2.23 CrB₂ is located in the same regime as the high- T_c cuprate superconductor La_{1.7}Sr_{0.3}CuO₄ and the ruthenate superconductor Sr₂RuO₄. In the final part of this section it will be shown that, besides the Kadowaki-Woods ratio, CrB₂ and the oxide superconductors have another feature in common, namely strong spin fluctuations.

The large negative Curie-Weiss temperature (Sec. 2.5.1) as well as the comparatively large A coefficient of the resistivity (Sec. 2.5.3) already suggested the existence of strong spin fluctuations in CrB₂. The resistivity anisotropy above T_N and its sudden disappearance below T_N suggests, that spin fluctuations dominate the transport properties at intermediate temperatures in the paramagnetic regime. The strength of the spin fluctuations may be estimated from the heat capacity measurements. Assuming two-dimensional fluctuations in a three-dimensional lattice, which seems to be justified by the layered crystalline structure of CrB₂, the self-consistently renormalized spin fluctuation theory predicts a logarithmic scaling of the electronic specific heat with temperature,

$$C_{\text{mag}}/T = \gamma_{\text{norm}} \ln(T_{\text{SF}}/T). \quad (2.4)$$

As has been outlined in Sec. 2.5.2 C_{mag} can be obtained by subtraction of the heat capacity of non-magnetic VB₂ which serves as an estimate of the lattice contribution to the heat capacity.

The normal-state Sommerfeld coefficient may be inferred from the linear extrapolation of C_{mag}/T above T_N to zero temperature, resulting in $\gamma_{\text{norm}} \approx 70 \text{ mJ mol}^{-1} \text{ K}^{-2}$. T_{SF} is the so-called spin fluctuation temperature. It is related to the average fluctuation rate Γ_{ave} as $\hbar\Gamma_{\text{ave}} = k_{\text{B}}T_{\text{SF}}$. As shown in Fig. 2.24, T_{SF} was determined by a least-square fit of Eq. 2.4 to the experimental data. The fit agrees reasonably well; the small deviation at high temperatures may be attributed to the inaccuracy of the subtracted lattice contribution. As spin fluctuation temperature $T_{\text{SF}} = 257 \text{ K}$ is found, corresponding to an average fluctuation rate $\hbar\Gamma_{\text{ave}} \approx 22 \text{ meV}$ or 33 THz . Empirically it has been demonstrated by HAYDEN and coworkers [131] that the normal-state Sommerfeld coefficient γ_{norm} scales with the average fluctuation rate Γ_{ave} . As shown Fig. 2.25a the parameters obtained for CrB₂ agree nicely with this observation. In turn, this suggests that the assumptions made above are indeed justified.

Spin fluctuations are considered as pairing mechanism in a variety of unconventional superconductors [134, 135]. Such unconventional, magnetically mediated superconductivity requires several criteria to be met, namely (i) the spin fluctuation spectra should be focused in energy and momentum, (ii) the dominant momentum contributions should match sections of the Fermi surface as to promote Cooper pairing, and (iii) transverse and longitudinal components should be pair forming. If these conditions are fulfilled the critical temperature T_c may be expected to scale with the width of the fluctuations' relaxation frequency spectrum. Since the latter is measured by the characteristic spin fluctuation temperature T_{SF} it follows $T_c \propto T_{\text{SF}}$ [132]. Empirically this relation has been demonstrated for a large number of heavy-fermion and cuprate superconductors [132, 136]. It is interesting to compare the estimate of $T_{\text{SF}} = 257 \text{ K}$ for CrB₂ with typical spin fluctuation temperatures of these compounds. The result of this comparison is shown in Fig. 2.25b. Excitingly, CrB₂ is placed right in between both material classes: The heavy-fermion superconductors exhibit spin fluctuation temperatures in a range of $10 \text{ K} - 100 \text{ K}$. Consistently, they display relatively low superconducting transition temperatures of a few K at most. In turn the high- T_c cuprates have high spin fluctuation temperatures ranging from $1 \cdot 10^3 \text{ K}$ to $1 \cdot 10^4 \text{ K}$. Assuming now that the above-mentioned criteria for magnetically mediated superconductivity may indeed be met in *non-magnetic* CrB₂ the empirical relationship $T_c \propto T_{\text{SF}}$ suggests a superconducting transition temperature as high as $\sim 10 \text{ K}$.

Note that this consideration requires the suppression of antiferromagnetic order in CrB₂, e.g., by hydrostatic pressure, uniaxial stress, or a combination thereof. If pressure is used to eliminate the magnetic order it is additionally necessary that the low-temperature normal-state properties of the putative non-magnetic high-pressure phase of CrB₂ may be inferred from its normal-state properties at ambient pressure. Moreover the prediction of T_c so far completely ignored effects of geometric frustration which may play a role in CrB₂ as suggested by the magnetization.

Irrespective of these limitations our discussion demonstrates that the discovery of superconductivity in CrB₂ may provide a long sought-after link that bridges the gap between the heavy-fermion and cuprate superconductors and hence identifies magnetically mediated superconduc-

tivity as a universal phenomenon in a broad range of material classes [132].

As a concluding remark and appetizer, the high-pressure transport investigation of CrB₂, which will be presented in Sec. 2.6, in fact suggest that the high-pressure state of CrB₂ develops an incipient electronic instability. Even though the microscopic nature of this instability is yet unclear, its experimental signature, namely a pronounced drop in the resistivity, is highly reminiscent of a superconducting transition.

2.5.5 Summary

In summary low-temperature bulk and transport measurements on high-quality single crystal samples of CrB₂ were carried out. Our investigations identify CrB₂ as weak itinerant antiferromagnet par excellence. Key characteristics of weak itinerant magnetism comprise a relatively low magnetic transition temperature $T_N = 88.5$ K, strong spin fluctuations with a large fluctuating effective moment $\mu_{\text{eff}} = 2\mu_B/\text{Cr}$ exceeding the small ordered moment $\mu_{\text{eff}} \approx 0.5\mu_B/\text{Cr}$, an extraordinary robustness of all physical properties with respect to high external magnetic fields of up to 14 T, and a low-temperature resistivity of a few $\mu\Omega$ cm characteristic of a good metal. Our analysis further suggest a weak easy-plane magnetic anisotropy and strong geometric frustration. Finally, our measurements hint at a putative electronic instability in non-magnetic CrB₂. More precisely, our specific heat data suggest that CrB₂ could exhibit superconductivity at comparatively high transition temperatures when magnetism is suppressed using a non-thermal tuning parameter such as pressure. This motivated the high-pressure study of CrB₂ presented in the Sec. 2.6.

2.6 High-pressure Transport Properties of CrB₂

This section reports on a comprehensive study of the high-pressure transport properties of CrB₂. Consistent with the crystalline and elastic anisotropy of CrB₂ these measurements suggest that the electronic and magnetic properties of CrB₂ are essentially determined by the ratio of the lattice parameters c/a . Perhaps most importantly, an incipient electronic instability at moderate quasi-hydrostatic pressure is revealed.

2.6.1 Piston-cylinder and Uniaxial Pressure Cells

Fig. 2.26 shows typical low-temperature resistivity data of CrB₂ under hydrostatic pressure p and uniaxial stress σ_{\perp} and σ_{\parallel} , where σ_{\perp} and σ_{\parallel} denote uniaxial stress perpendicular and parallel to the c -axis, respectively. In two cases - hydrostatic pressure p and uniaxial stress σ_{\perp} - the excitation current was applied along the c -axis. Conversely, for the measurement with uniaxial stress σ_{\parallel} the excitation current was applied along the a -axis. In the piston-cylinder cell, pressure up to 2.2 GPa was applied to the sample. In the uniaxial pressure experiments, stress as high

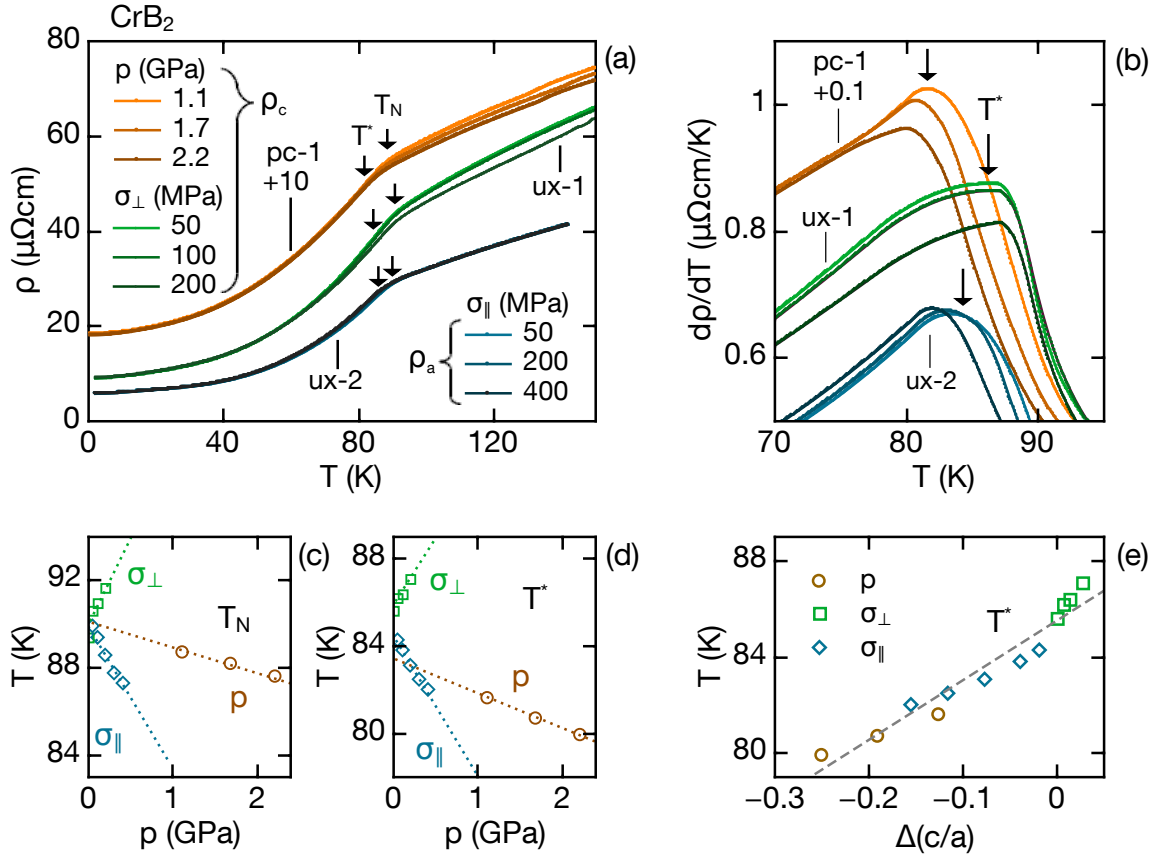


Figure 2.26: Electrical resistivity of CrB₂ measured with a piston-cylinder cell and uniaxial pressure cell, generating essentially hydrostatic pressure and uniaxial stress, respectively. (a) For all pressure conditions ρ drops monotonically with decreasing temperature and displays a pronounced kink at T_N . T^* indicates the temperature of the maximum of the derivative $d\rho/dT$. Data obtained with the piston-cylinder cell (orange) were shifted by adding an offset of 10 $\mu\Omega\text{ cm}$. (b) Temperature derivative $d\rho/dT$. Data obtained with the piston-cylinder cell (orange) were shifted by adding an offset of 0.1 $\mu\Omega\text{ cm K}^{-1}$. (c) Pressure dependence of T_N . (d) Pressure dependence of T^* . (e) The different pressure dependencies of T^* can be accounted for by a single function which is linear in the ratio of the lattice constants c/a .

as 200 MPa and 400 MPa was applied along the a - and c -axis of the sample, respectively. For both measurements further increase of the pressure resulted in bursting of the sample.

2.6.1.1 Piston-cylinder Cell

The account on the high-pressure transport properties begins with the measurements using the piston-cylinder cell. Here the pressure was the most hydrostatic as compared with the other techniques applied. With decreasing temperature ρ drops monotonically to a small residual resistivity of $\rho_0 \approx 8 \mu\Omega\text{ cm}$. Note that in the interest of clarity in Fig. 2.26a the data recorded

2.6 High-pressure Transport Properties of CrB₂

	p_0, σ GPa	T_N K	T^* K	A nΩcm/K ²	B μΩcm	ρ_0 μΩcm	Δ K
pc-1	1.1	88.7	81.6	3.70	23.56	8.48	132.4
	1.7	88.2	80.7	3.72	23.76	8.29	132.9
	2.2	87.6	79.9	3.76	26.49	8.21	140.9
ux-1, σ_{\perp}	0.05	90.6	86.2	2.74	137.48	9.26	200.3
	0.1	91.0	86.4	2.72	135.88	9.21	200.9
	0.2	91.7	87.1	2.76	116.81	9.44	203.0
ux-2, σ_{\parallel}	0.05	89.9	84.3	1.38	158.93	5.97	209.1
	0.1	89.4	83.8	1.38	155.75	5.97	207.8
	0.2	88.6	83.1	1.4	158.39	5.96	207.9
	0.3	87.8	82.5	1.42	153.42	5.95	205.5
	0.4	87.3	82.0	1.45	171.4	5.93	211.4

Table 2.9: Key parameters which describe the temperature dependence of the resistivity of CrB₂ at various pressures for $T < T^*$. The parameters were obtained by fitting a gaped Fermi liquid ground state to the experimental data. T_N was determined from the kink of the temperature dependence of ρ ; T^* corresponds to the temperature of the maximum of $d\rho/dT$.

with the piston-cylinder cell (ρ_c , pc-1) were shifted by adding a constant offset of 10 μΩ cm. Closer inspection of the temperature dependence of ρ reveals the change from a sublinear behaviour above the Néel temperature T_N to a superlinear behaviour below T_N . Consistent with the measurements at zero pressure, this change of slope results in a pronounced kink at T_N and a distinct maximum of the first derivative, $d\rho/dT$, at T^* (Fig. 2.26b). Fig. 2.26c and Fig. 2.26d show T_N and T^* as a function of hydrostatic pressure and uniaxial stress, respectively. Values of T_N and T^* are summarized in Tab. 2.9 for all pressures studied. With increasing pressure both T_N and T^* are suppressed at similar rates. A linear fit of the pressure dependence yields $dT_N/dp \approx -1 \text{ K GPa}^{-1}$ and $dT^*/dp \approx -1.5 \text{ K GPa}^{-1}$, translating into a critical pressure of $\sim 90 \text{ GPa}$ to suppress T_N . This may be compared with the pressure dependence as calculated from Ehrenfest's theorem,

$$\frac{d(\ln T_N)}{dp} = v_m \frac{\Delta\gamma}{\Delta C_p} = -5.7 \text{ K GPa}^{-1}$$

where $\Delta\gamma$ and ΔC_p are the initial changes of the molar volume and the heat capacity at T_N and zero pressure. Data from Ref. [88] were used to carry out the calculation. The observed pressure dependence is of the same order of magnitude as predicted by the Ehrenfest calculation but about a factor of four weaker. This discrepancy may be attributed to non-ideal hydrostatic pressure conditions. For the strongly texturized polycrystal sample studied, additional deviations from the Ehrenfest value may be due to the averaging over the pressure dependencies of crystal grains

with slightly different crystallographic orientations.

2.6.1.2 Uniaxial Pressure Cell

Turning to the measurements under uniaxial stress, ρ displays qualitatively the same temperature dependence as at ambient and hydrostatic pressure. Notably $\rho(T)$ exhibits again the two characteristic temperatures, T_N and T^* . For each individual curve σ_\perp and σ_\parallel , T_N and T^* exhibit similar pressure dependencies. As for the data collected with the piston-cylinder cell, both T_N and T^* decrease with increasing uniaxial stress σ_\parallel , however at a higher rate, $dT_N/d\sigma_\parallel \approx -7.5 \text{ K GPa}^{-1}$ and $dT^*/d\sigma_\parallel \approx -6.5 \text{ K GPa}^{-1}$. The opposite trend is observed for σ_\perp . Both T_N and T^* increase with increasing σ_\perp as $dT_N/d\sigma_\perp \approx 7.3 \text{ K GPa}^{-1}$ and $dT^*/d\sigma_\perp \approx 6.1 \text{ K GPa}^{-1}$.

The anisotropy of the resistivity may be studied by comparing the curves $\rho(T)$ of different current directions, i.e., ρ_c versus ρ_a , corresponding to the measurement series pc-1 and ux-1 versus ux-2 in Fig. 2.26a, respectively. The resistivity anisotropy is small at low temperatures ($\sim 3.5\%$ at 4 K) and increases at high temperatures ($\sim 35\%$ at 100 K). This is again consistent with the measurements at ambient pressure. As stated in Sec. 2.5.3 the anisotropy may be attributed to strong, slightly anisotropic spin fluctuations above the Néel temperature and their freezing out in the magnetically ordered phase. The effect of pressure on the anisotropy of the resistivity is small since with increasing pressure ρ_a is shifted only slightly towards ρ_c and vice versa.

Turning to the temperature dependence of ρ , it has been mentioned above that for both hydrostatic and uniaxial pressure conditions with decreasing temperature a distinct change from a sublinear to a superlinear temperature dependence is observed at T_N . The low-temperature superlinear behaviour can be accounted for by a Fermi liquid ground state which develops a spin-density type order with gaped bosonic excitations, e.g., spin waves:

$$\rho(T) = \rho_0 + AT^2 + B\frac{T}{\Delta} \left(1 + 2\frac{T}{\Delta}\right) \exp\left(-\frac{\Delta}{T}\right) \quad (2.5)$$

This is, again, consistent with the measurements at ambient pressure. A least-square fit of Eq. 2.5 to the resistivity data results in fit parameters which are reasonably consistent with the ones obtained for $p = 0$ and which are summarized in Tab. 2.9. The smaller size of the Δ value observed with the piston-cylinder cell may be attributed to the quality of the texturized polycrystalline sample studied. Note that within the reliability of the least-square fit the pressure dependence of Δ cannot be derived unambiguously.

2.6.1.3 Role of the c/a Ratio

Tracking T_N as a function of pressure may provide insights about how the long-range magnetic order in CrB₂ changes under different pressure conditions. Unfortunately, T_N cannot be tracked for all pressure conditions. As will be shown below some resistivity curves recorded with Bridg-

2.6 High-pressure Transport Properties of CrB₂

	p_0 GPa	σ_{\perp} GPa	σ_{\parallel} GPa	T_{obs}^* K	a Å	c Å	c/a
pc-1	1.1			81.6	2.9665	3.0226	1.0189
	1.7			80.7	2.9647	3.0189	1.0183
	2.2			79.9	2.9630	3.0154	1.0177
ux-1		0.05		86.2	2.9699	3.0301	1.0203
		0.1		86.4	2.9698	3.0302	1.0203
		0.2		87.1	2.9695	3.0303	1.0205
ux-2			0.05	84.3	2.9701	3.0295	1.0200
			0.1	83.8	2.9702	3.029	1.0198
			0.2	83.1	2.9703	3.028	1.0194
			0.3	82.5	2.9705	3.027	1.0190
			0.4	82.0	2.9707	3.026	1.0186

Table 2.10: Estimate of the change of the lattice parameters a and c upon application of hydrostatic pressure and uniaxial stress.

man cells are strongly broadened, hence prohibiting the direct determination of T_{N} . However, T^* may be tracked. Albeit differing in their absolute values both T_{N} and T^* exhibit similar pressure dependencies (cf. Fig. 2.26c and Fig. 2.26d). For a consistent comparison of all high-pressure transport data T^* will be considered in the further analysis .

The strongly differing pressure dependencies of T^* - dT^*/dp , $dT^*/d\sigma_{\perp}$, and $dT^*/d\sigma_{\parallel}$ - raise the question of their common microscopic origin. Strain energy requires that both hydrostatic pressure and uniaxial stress reduce the volume of the unit cell. Therefore it must be ruled out that T^* is a function of the latter, since it cannot account for the opposite trends $dT^*/d\sigma_{\perp} > 0$ and $dT^*/d\sigma_{\parallel} < 0$. In view of the anisotropy of the hexagonal crystal structure it seems likely that the ratio of the lattice parameters, c/a , may play an important role in stabilizing or suppressing the magnetic order in CrB₂. In fact, the importance of c/a for the electronic properties has been demonstrated for a variety of materials and material classes, cf. Sec. 2.6.3.

To study the role of the pressure-induced crystalline anisotropy in more detail, the effect of different pressure conditions on the hexagonal lattice parameters a and c was estimated. Measurements of the elastic constants of CrB₂ were reported in Refs. [95, 96]. Given that the temperature dependence of the elastic constants is small the room temperature values were used for the calculation. Using Voigt's matrix notation the strain tensor ϵ_i is calculated from the elastic modulus c_{ij} and the stress tensor σ_j as $\epsilon_i = (c_{ij})^{-1} \sigma_j$. The new lattice constants were obtained from the strain tensor as $\epsilon_1 = \Delta a/a$, $\epsilon_2 = \Delta b/b$, and $\epsilon_3 = \Delta c/c$. The ratio c/a of the distorted unit cell is approximated as $c/a \approx 2c/(a+b)$ to account for the irregular distortion of a and b upon the application of uniaxial stress. The results of these calculations are summarized in Tab. 2.10. Fig. 2.26d shows T^* as a function of the calculated c/a ratio. In the interest

of readability instead of c/a the relative change of c/a , i.e., $\Delta(c/a) = (c/a)_{p>0}/(c/a)_{p=0}$ was plotted.

Only for uniaxial pressure perpendicular to the c -axis (ux-1), the ratio of lattice parameter is increased with respect to its initial value, i.e., $\Delta(c/a) > 0$. For all other configurations (pc-1, ux-2) c/a is reduced resulting in a negative relative change, $\Delta(c/a) < 0$. It turns out that the different pressure dependencies of T^* can be accounted for by a function which is linear in c/a :

$$T^* = \alpha \cdot \left(\frac{c}{a}\right) + \beta, \quad (2.6)$$

where $\alpha = 2480$ K and $\beta = -2445$ K. By solving Eq. 2.6 for $T^* = 0$ the critical hydrostatic pressure p_0 that is required to suppress T^* may be estimated. The value obtained, $p_0 \approx 29$ GPa, is a factor of three smaller than the value extrapolated directly from the hydrostatic measurement, $p_0 \approx 90$ GPa. This discrepancy is introduced by Eq. 2.6 which averages over all three pressure dependencies (pc-1, ux-1, and ux-2). The fair agreement of Eq. 2.6 with the experimental data, however, suggests that in all high-pressure measurements the c/a ratio controls T^* and hence the onset of long-range magnetic order.

Consistent with the pronounced elastic anisotropy reported in Ref. [95], c_{11} being a factor of 1.7 larger than c_{33} , the c -axis is compressed much stronger under pressure than the a -axis. Given that the application of uniaxial stress is limited to low pressure due to the formation of brittle cracks, our estimate further suggests high hydrostatic or quasi-hydrostatic pressure as a suitable means to suppress the magnetic order in CrB₂. Therefore several Bridgman cells were prepared to study the resistivity of CrB₂ at pressures well above 2 GPa. These measurements will be reported in Sec. 2.6.2.

It is interesting to compare the change of the lattice parameter ratio c/a caused by the application of pressure on the one hand and by the variation of temperature on the other hand. The latter may be inferred from the powder x-ray diffraction of CrB₂ (cf. Sec. 2.3.1, Fig. 2.2d), implying an enhancement of c/a upon cooling from the paramagnetic high-temperature into the low-temperature magnetic phase of $\Delta(c/a) = (c/a)_{300\text{K}}/(c/a)_{12\text{K}} \approx 0.3\%$. This is slightly larger than the the estimate of the (negative) change upon application of moderate hydrostatic pressure up to ~ 3.5 GPa where $\Delta(c/a) \approx -0.25\%$. In a very simple picture, where the onset of long-range magnetic order is determined by c/a only, this comparison suggests that moderate hydrostatic pressure of a few GPa cannot suppress the magnetic order in CrB₂, consistent with our measurements. It will be shown in the following section that, in contrast, high quasi-hydrostatic pressure as it can be generated by means of Bridgman cells may cause changes of $\Delta(c/a) < -0.3\%$. Consequently, the Bridgman technique may represent an adequate tool to tune magnetic CrB₂ into the paramagnetic state, i.e., to suppress the long-range magnetic order.

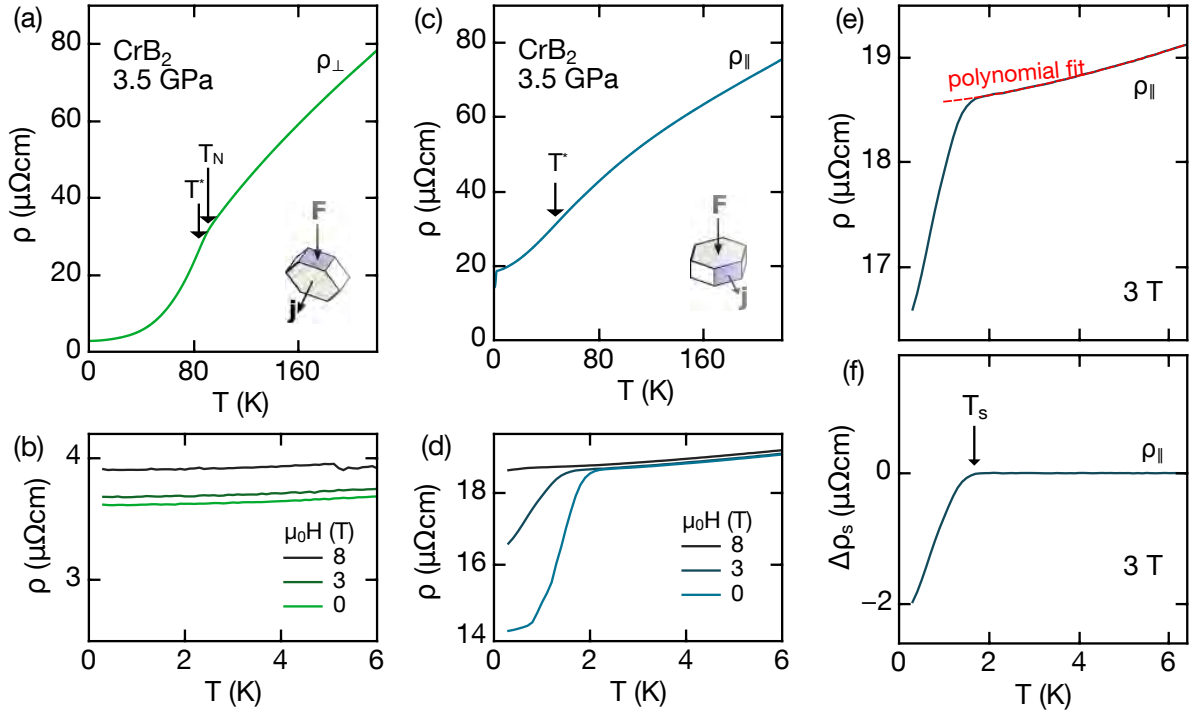


Figure 2.27: Electrical resistivity ρ_{\parallel} and ρ_{\perp} of CrB₂ for current along a and c , respectively. Both measurements were performed simultaneously in a single Bridgman cell using a “crossed” sample geometry. (a) ρ_{\perp} is qualitatively unchanged with respect to measurements at zero pressure, uniaxial strain, and low hydrostatic pressure. Particularly it displays a kink at T_N . (b) ρ_{\perp} drops smoothly down to the lowest temperatures studied. (c) ρ_{\parallel} , in contrast to ρ_{\perp} , is smeared out where the magnetic ordering transition would be expected. (d) The low-temperature resistivity ρ_{\parallel} displays an anomalous drop at $T_s \approx 2.6$ K. This resistivity anomaly is suppressed by magnetic fields. (e, f) Determination of the onset temperature, T_s , and the size $\Delta\rho_s$, of the anomaly of ρ_{\parallel} by subtraction of a polynomial fit.

2.6.2 Bridgman Cells

For all measurements employing Bridgman cells a solid pressure medium (steatite) was used. Steatite has a relatively low hydrostatic limit and thus develops uniaxial stress components. As has been emphasized in Sec. 1.2.3 these cause pressure anisotropies. The pressure generated with this technique is therefore referred to as quasi-hydrostatic in the following, i.e., as a combination of hydrostatic pressure p_0 plus a uniaxial stress component σ_{dev} . Keeping in mind the strong dependence of T^* on uniaxial stress the “crossed” sample geometry introduced in Sec. 1.2.3 was used. This sample arrangement allows to track the presence of a uniaxial pressure component. In the “crossed” geometry two samples are placed within the same Bridgman cell - the first one with its c -axis parallel, the second one with its c -axis perpendicular to the anvil plane. Consequently, the uniaxial stress term σ_{dev} acts as σ_{\perp} in the first case and as σ_{\parallel} in the latter

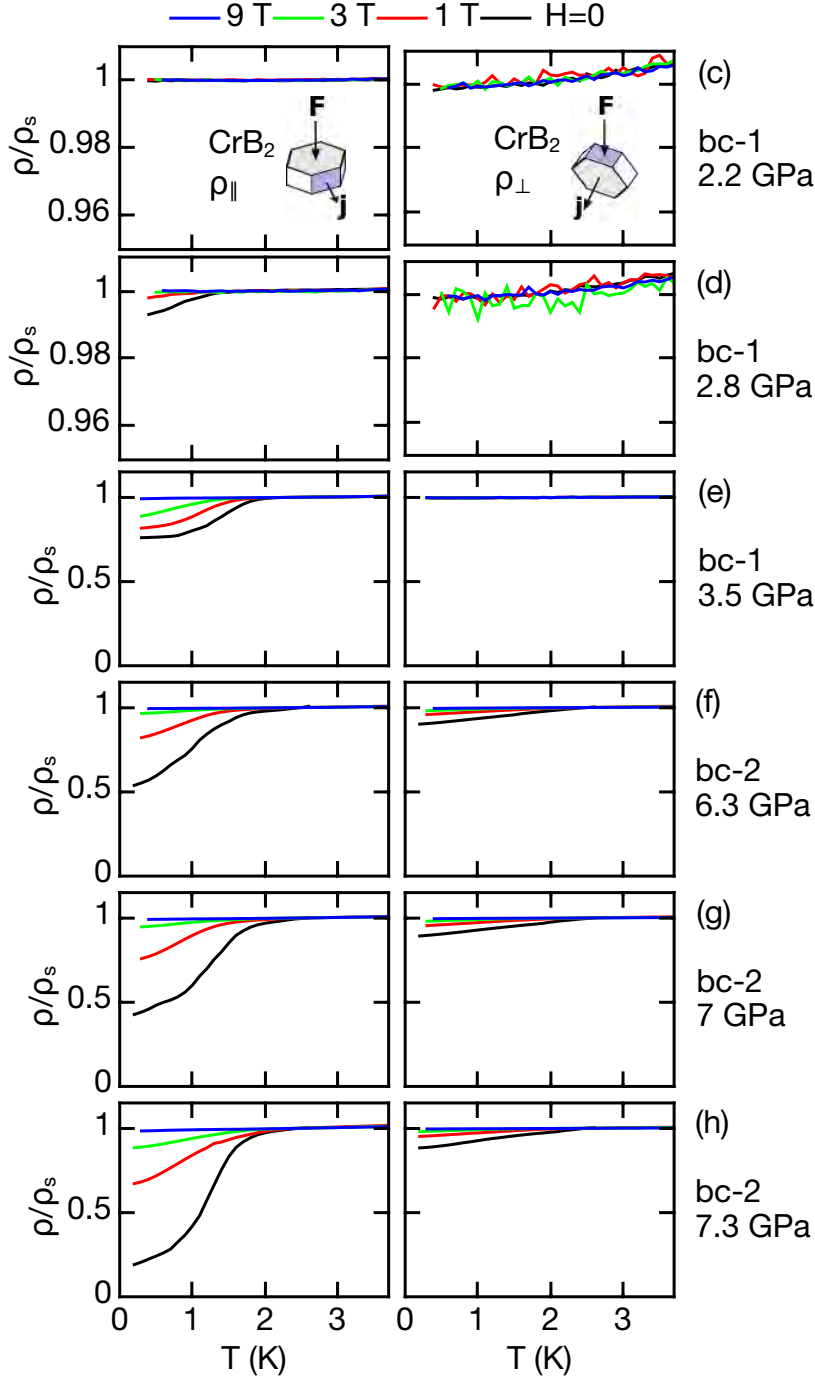


Figure 2.28: Low-temperature resistivity ρ_{\perp} and ρ_{\parallel} of CrB₂ for current along a (left column) and c (right column), respectively. All data were normalized to $\rho_s = \rho(T_s)$. Pressure increases from top to bottom. At each pressure both samples were measured simultaneously in a single Bridgman cell using a "crossed" sample geometry. Above 2.2 GPa ρ_{\parallel} develops an anomalous drop at $T_s \approx 2.2$ K which becomes more pronounced with increasing pressure and which is suppressed with increasing magnetic field. On the other hand, ρ_{\perp} remains almost unchanged up to the highest pressures studied. The small low-temperature drop of ρ_{\perp} at high pressures is observed only for bc-2 and may be attributed to a misalignment of the sample causing a finite uniaxial component σ_{\parallel} .

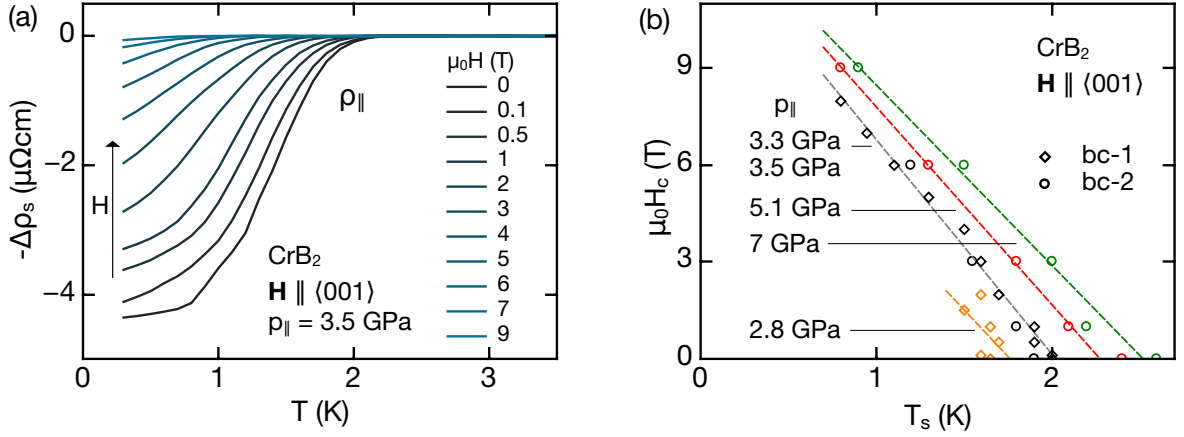


Figure 2.29: Field dependence of the low-temperature resistivity anomaly of ρ_{\parallel} . (a) With increasing field both T_s and the size of the drop in the resistivity $\Delta\rho_s$ decrease. (b) Critical magnetic field H_c which is needed to recover the normal resistivity, i.e., to suppress the anomalous drop. Data have been taken by measuring the onset temperature T_s of the resistivity anomaly at constant magnetic field.

case. In the following the resistivity data recorded under the two different pressure conditions will be denoted p_{\perp} and p_{\parallel} , respectively, where

$$p = p_0 + \sigma_{\text{dev}} = \begin{cases} p_0 + \sigma_{\perp} \equiv p_{\perp}, & \text{if } \mathbf{F} \perp c, \\ p_0 + \sigma_{\parallel} \equiv p_{\parallel}, & \text{if } \mathbf{F} \parallel c, \end{cases} \quad (2.7)$$

and \mathbf{F} is the force used to load the cell.

Fig. 2.27 shows typical resistivity data measured with a Bridgman cell at a pressure of ≈ 3.5 GPa. The excitation current was applied along c and a for the first and the second sample, respectively. In the following the data obtained for the two sample geometries and the corresponding pressure conditions will be reported.

2.6.2.1 Quasi-hydrostatic Pressure p_{\perp}

To begin with, the resistivity of the sample oriented with its c -axis perpendicular to the loading force F is considered. As compared to the temperature dependence of the resistivity recorded with the piston-cylinder and uniaxial pressure cell, ρ_{\perp} is qualitatively unchanged. Notably the magnetic ordering transition is indicated by a clear kink at T_N and a maximum of $d\rho/dT$ at T^* . Below T^* the temperature dependence can be accounted for by the SDW expression given by Eq. 2.5 with similar parameters as for the previously reported data. As shown in in Fig. 2.27b no significant deviation from this behavior is observed down to the lowest temperatures studied. Consistent with our measurements at zero pressure a small normal magnetoresistance,

$\Delta\rho_B \propto B^2$, is found.

2.6.2.2 Quasi-hydrostatic Pressure p_{\parallel}

It is instructive to compare these results with the resistivity of the second sample which was oriented with its c -axis perpendicular to the loading force F and hence exposed to anisotropic pressure p_{\parallel} . It differs from the data reported above in four aspects.

- (i) ρ_{\parallel} again decreases monotonically with decreasing temperature, thereby passing through a point of inflection which is indicated by a maximum of the temperature derivative $d\rho/dT$ at T^* . However, no pronounced kink is observed akin T_N where the onset of long-range magnetic order would be expected. Instead, ρ_{\parallel} appears to be broadened over a wide temperature range. The pressure dependence of the magnetic ordering transition was therefore determined from T^* , i.e., the maximum of $d\rho/dT$.
- (ii) Below T^* the temperature dependence $\rho(T)$ cannot be fitted by a gapped Fermi liquid ground state characterized by the SDW expression given in Eq. 2.5.
- (iii) A distinct low-temperature resistivity anomaly is observed around $T_s = 2.6$ K where ρ_{\parallel} drops abruptly by up to $\sim 24\%$. Even larger drops by up to $\approx 80\%$ were observed with other pressure cells and for higher pressure (cf. Fig. 2.28).

As shown in Fig. 2.27e and Fig. 2.27f T_s and the size of the drop in the resistivity $\Delta\rho_s$ were determined by subtracting a polynomial fit of the high-temperature resistivity above the anomalous drop from the measured temperature dependence $\rho_{\parallel}(T)$,

$$\Delta\rho_s(T) = \rho_{\parallel}(T) - \rho_{\parallel,\text{polyfit}}(T).$$

The size of the drop in the resistivity, $\Delta\rho_s$, may then be inferred directly from the resulting curve. It corresponds to the deviation from the baseline and is non-zero only for $T < T_s$ where T_s was identified using an onset criterion. This procedure allowed to detect and to quantify even very small resistivity drops, e.g., at high magnetic fields.

- (iv) The residual resistivity $\rho_{\parallel,0}$ (determined from the resistivity curve above the anomalous drop at T_s) is almost by a factor of 5 larger than $\rho_{\perp,0}$ hence exceeding strongly the small resistivity anisotropy observed for ρ_a and ρ_c both at zero pressure and uniaxial stress.

To begin with, the strong broadening of ρ_{\parallel} is considered. Such a smearing can be caused by inhomogeneous pressure conditions. These are not uncommon if solid state pressure media such as steatite are used. Two reasons, however, suggest that the observed broadening is not an effect of pressure inhomogeneities but intrinsic to the sample. First, the samples are short when compared to the anvil diameter. Therefore the pressure inhomogeneity over a single sample should be small. Furthermore, for the ‘‘crossed geometry’’ two samples are placed on top of

anvil of the Bridgman cell in a circular arrangement. As the isobars in the sample volume are expected to be ring-shaped both samples should be exposed to very similar pressure conditions, cf. Fig. 1.6. The broadening is however only observed for the second sample. In fact, for all pressure cells studied the broadening has been observed only within a single sample geometry, namely when the sample was exposed to p_{\parallel} with $\mathbf{j} \parallel \mathbf{a}$. Note that apart from the broadening of $\rho(T)$ also the low-temperature resistivity anomaly is observed only under these conditions. If the broadening of $\rho(T)$ was only due to pressure inhomogeneities both samples must be equally affected, which is clearly not the case. Second, the pressure inhomogeneity can be estimated from the width of the superconducting transition of the pressure gauge. As has been described in Sec. 1.2.3 this gives a typical value of $\Delta p/p \approx 15\%$. It was checked that a Gaussian pressure distribution of this width cannot account for the observed smearing. Moreover, the shift of T^* expected from such a putative Gaussian pressure distribution is small compared to the observed pressure dependence dT^*/dp .

As concerns the loss in resistivity observed at low temperature $T < T_s$ (cf. Fig. 2.27d) it is noteworthy, that irrespective of the pressure applied only ρ_{\parallel} displays this resistivity drop. This is shown in more detail in Fig. 2.28 which compares ρ_{\parallel} and ρ_{\perp} over a wide pressure range and for various fields. As can be seen from the right column of Fig. 2.28 the resistivity anomaly varies only little with respect to its onset temperature T_s whereas its size $\Delta\rho_s$ gets significantly enhanced at higher pressure.

Typical data of the field dependence of the low-temperature part of ρ_{\parallel} are shown in Fig. 2.29a. At zero field, $T < T_s$, and with decreasing temperature, the resistivity ρ_{\parallel} exhibits a steep linear drop before it eventually levels off near the lowest temperatures reached. If an external magnetic field is applied the linear temperature decrease below T_s is conserved but its slope becomes smaller as $\mu_0 H$ grows. At the same time both T_s and the size of the drop in the resistivity decrease as the magnetic field is cranked up.

A comparatively high magnetic field $\mu_0 H_c$ is needed to fully suppress the resistivity drop. As shown in Fig. 2.29b both T_s and H_c are smallest at low pressure where $T_s \approx 1.6$ K and $\mu_0 H_c \approx 2$ T. At high pressure, where T_s is enhanced to about 2.6 K, the critical field increases dramatically and even exceeds the highest field studied, $H_c > 9$ T. By measuring T_s at constant magnetic field for all pressures studied the temperature dependence of H_c may be determined. It is linear and amounts to $\mu_0 dH_c/dT_s \approx -6$ T K⁻¹. With increasing pressure both T_s and the critical field H_c increase slightly hence leaving the slope $\mu_0 dH_c/dT_s$ essentially unchanged.

Considering incipient conventional superconductivity with a critical temperature $T_c = T_s = 2.6$ K as the putative origin of the sudden drop in resistivity it is interesting to compare the high critical fields observed to some theoretical predictions.

Pair breaking may be induced due to the Zeeman energy of spin polarization [137]. This Pauli

limit (also: Clogston-Chandrasekhar limit) may be estimated as

$$B_P = 1.84T_c \text{ T K}^{-1} \approx 5 \text{ T}, \quad (2.8)$$

which is about a factor of two smaller than the critical field observed.

In the orbital limit of BCS superconductivity the Cooper pairs are broken as soon as their kinetic energy due to their orbital motion in an applied magnetic field exceeds the pairing energy [138]. The orbital critical field may be estimated from the initial slope of the temperature dependence of $\mu_0 dH_c/dT$ at T_c as

$$B_{\text{orb}} = -0.7T_c \left(\frac{\mu_0 dH_c}{dT} \right)_{T_c} \approx 11 \text{ T}. \quad (2.9)$$

The theoretical limit hence exceeds slightly the observed critical field. This may be due, however, to experimental constraints which prohibit measurements at lower temperatures and higher magnetic field.

The high critical field observed may as well be explained by the nucleation of superconductivity at portions of sample surface that are aligned parallel to the external field. This nucleation field is up to $\sim 70\%$ higher than the bulk critical field,

$$B_{\text{nuk}\parallel} = 1.695B_c, \quad (2.10)$$

which may be well above 9 T [139, 140].

Alternatively, the superconductivity may be not a bulk property but emerge in a thin layer. For thin superconducting films forming parallel to an external magnetic field the critical field may be calculated as

$$B_{c\parallel} = 2\sqrt{6}B_{\text{cth}} \frac{\lambda_L}{d}, \quad (2.11)$$

where λ_L is the London penetration depth, d is the thickness of the layer, and B_{cth} is the thermodynamical critical field [141]. The latter can be estimated from the microscopic theory of BCS superconductivity as $B_{\text{cth}} = 0.06 \text{ T}$. The London penetration depth of metallic superconductors is about 10 nm to 100 nm. Assuming a very thin superconducting layer with $d \approx 1 \text{ nm}$ yields $B_{c\parallel} \approx 30 \text{ T}$, demonstrating that inhomogeneous superconductivity may account for the observed high critical field.

2.6.2.3 Role of the c/a Ratio

Fig. 2.30a shows T^* as a function of pressure for the first (p_{\perp}) and second (p_{\parallel}) sample. For the first sample T^* first increases with growing pressure, passes through a maximum at $\sim 5 \text{ GPa}$, and eventually decreases. The opposite behavior is found for the second sample: T^* first decreases with increasing pressure and then grows again above $\sim 5 \text{ GPa}$.

The different trends of dT^*/dp_{\perp} and dT^*/dp_{\parallel} may be understood in terms of a uniaxial stress

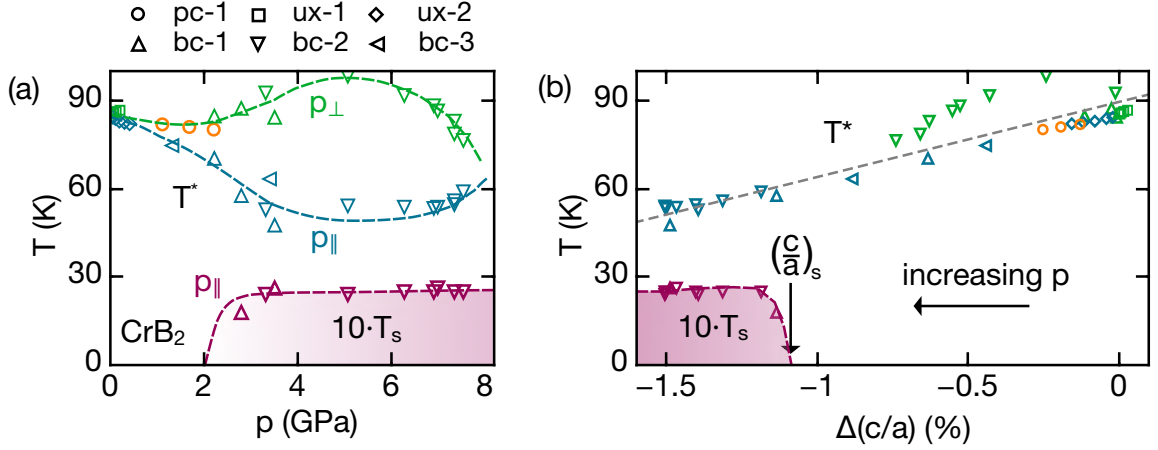


Figure 2.30: (a) Pressure dependence of the point of inflection in $\rho(T)$, T^* , and the onset temperature of the low-temperature resistivity anomaly, T_s , for all pressure cells studied. The latter is only observed for samples exposed to p_{\parallel} . (b) Dependence of T^* and T_s of the calculated relative change of the lattice parameter ratio.

component σ_{dev} . In the Bridgman cells σ_{dev} develops due to the solid pressure medium. Based on the experiments employing hydrostatic pressure and uniaxial stress it is possible to estimate the uniaxial component and the associated change in the lattice parameters for both samples from T^* and p_0 . Assuming perfectly homogeneous pressure conditions over the full sample space, hydrostatic pressure p_0 plus a single stress component σ_{dev} should account for the strain of both samples. For the first sample $\epsilon_{\perp} = c^{-1} \cdot (p_0 + \sigma_{\text{dev}}, p_0, p_0, 0, 0, 0)^T$, while for the second sample $\epsilon_{\parallel} = c^{-1} \cdot (p_0, p_0, p_0 + \sigma_{\text{dev}}, 0, 0, 0)^T$. Extrapolating the linear relation of T^* and c/a inferred from the measurements at uniaxial and hydrostatic pressure (Eq. 2.6) to high pressures, T^* may be calculated from ϵ for both samples. The uniaxial component σ_{dev} may eventually be determined by a least-squares minimization of $\sum_{i=\perp, \parallel} (T_{i,\text{obs}}^* - T_{i,\text{calc}}^*)^2$, where $T_{i,\text{obs}}^*$ and $T_{i,\text{calc}}^*$ correspond to the observed and calculated values of T^* , respectively.

The results of the calculation are summarized in Tab. 2.11. At low pressures p_0 the uniaxial component σ_{dev} is small. With increasing p_0 it first increases and above $p_0 > 3.5$ GPa eventually decreases again. This trend presumably arises from the elastic properties of the powdered solid pressure transmitter (steatite) and of the anvil material used.

Fig. 2.30b shows T^* and T_s from all measurements as a function of the calculated relative change of the lattice parameter ratio, $\Delta(c/a)$. Measurements under hydrostatic and uniaxial pressure are located at large ratios c/a , corresponding to small relative changes $\Delta(c/a)$. Measurements based on Bridgman cell using the first sample orientation, p_{\perp} , are located in an intermediate range of c/a corresponding to a relative reduction of $-\Delta(c/a) \approx 0.5-1\%$. Finally, measurements based on Bridgman cell using the second sample geometry, p_{\parallel} , give the lowest values of c/a thus corresponding to the largest suppression, $-\Delta(c/a) \approx 0.5-1.5\%$. The calculated values for

The Weak Itinerant Antiferromagnet CrB₂

	p_0 GPa	σ_{dev} GPa	$\mathbf{F} \perp c$					$\mathbf{F} \parallel c$					T_s K
			T_{obs}^* K	T_{calc}^* K	a Å	c Å	c/a	T_{obs}^* K	T_{calc}^* K	a Å	c Å	c/a	
bc-1	2.2	1	84.5	82.8	2.9575	3.0170	1.0190	70.3	69.7	2.9647	3.0055	1.0138	1.8
	2.8	2.1	87.4	85.1	2.9494	3.0152	1.02	57.8	57	2.9648	2.9904	1.0086	
	3.5	2.8	84.4	85.5	2.9433	3.0117	1.0201	47.6	48.0	2.9638	2.9786	1.0086	
bc-2	3.3	2.6	92.5	85.4	2.9407	3.0006	1.0177	52.9	50.4	2.9640	2.9817	1.006	2.4
	5.1	2.4	98.1	74.9	2.9407	3.0006	1.0177	54.2	47.6	2.9581	2.9724	1.0048	2.4
	6.3	2.1	91.8	74.9	2.9389	2.9921	1.0158	53.6	47.6	2.9538	2.9681	1.0048	2.5
	6.9	1.9	88.2	72.4	2.9380	2.9876	1.0149	53.3	47.7	2.9515	2.9659	1.0049	2.5
	7.0	1.7	86.4	71.7	2.9638	2.9868	1.0146	53.8	48.6	2.951	2.9665	1.0052	2.6
	7.3	1.5	82.8	69.8	2.9387	2.9841	1.0138	54.7	50.1	2.9495	2.9668	1.0059	2.5
	7.3	1.2	78.8	69	2.9401	2.9837	1.0135	55.9	52.4	2.9491	2.9691	1.0068	2.5
	7.6	0.9	76.4	67.0	2.9416	2.9816	1.0127	59.0	55.7	2.9478	2.9717	1.0081	2.5
bc-3	1.3	0.8						74.5	74.5	2.9671	3.0137	1.0157	
	3.4	1.3						63.3	63.3	2.9616	2.9947	1.0112	

Table 2.11: Estimate of the uniaxial pressure component σ_{dev} and the associated change of the lattice parameters a and c upon application of quasi-hydrostatic pressure. The values of c/a which are printed in boldface correspond to relative changes $\Delta(c/a) < \Delta(c/a)_s = -1.1\%$. See text for details of calculation.

$\Delta(c/a)$ shown in Fig. 2.30b follow roughly Eq. 2.6. The agreement is not too bad considering that Eq. 2.6 was inferred from measurements at rather low pressure. Furthermore, deviations from Eq. 2.6 may be explained to some extent by the uncertainty in p_0 which may be estimated from the width of the superconducting transition of the pressure gauge. Finally the assumption of perfectly homogeneous pressure conditions over the whole sample space may no longer be fulfilled at the highest pressures studied because the diameter of the ring-shaped isobars becomes small as compared to the typical sample dimensions (cf. Sec. 1.2.3).

Turning now to T_s it is remarkable, that the associated resistivity anomaly is observed only if the change of the ratio of the lattice parameters exceeds a critical value, $\Delta(c/a) < 1.1\%$. This suggests that the ratio of the lattice parameters c and a does not only control the onset of long-range magnetic order in CrB₂ but also causes the appearance of the low-temperature resistivity anomaly. The pressure needed to achieve the critical ratio $\Delta(c/a)_s$ in the absence of a uniaxial stress component, i.e., by means of perfectly hydrostatic pressure may be estimated as $p_s \approx 10$ GPa. If instead purely uniaxial pressure was used to achieve the critical ratio $\Delta(c/a)_s$, either by compressing the c -axis or by stretching the a -axis, stress as high as $\sigma_{001} \approx 3$ GPa and $\sigma_{100} \approx 8$ GPa were necessary. The former hydrostatic pressure conditions may be experimentally feasible, e.g., by means of diamond anvil cells with Helium as the pressure medium. In contrast, the latter high uniaxial stress lies presumably beyond the limit imposed by the mechanical stability of CrB₂ meaning that any sample is likely to burst already at much lower uniaxial pressure due to imperfections of the experimental apparatus (such as alignment and smoothness

of the anvils).

2.6.3 Discussion

In the following the main findings of the high-pressure transport experiments will be discussed. First, the limitations and benefits of the high-pressure technique applied are summarized. Next, arguments supporting that the low-temperature resistivity drop in ρ_{\parallel} indicates an incipient electronic instability are presented. By comparing the experimental signatures observed in the reported in this thesis measurements to well-known examples in the literature the nature of such a putative incipient instability is considered. As a result pressure induced superconductivity is identified as the most probable explanation for the anomalous low-temperature resistivity in the high-pressure phase of CrB₂.

Our high-pressure transport investigations suggest that quasi-hydrostatic pressure, i.e., the combination of high hydrostatic pressure with a uniaxial stress component generated by means of Bridgman cells with a solid pressure transmitter, represent a prerequisite to induce some of the most interesting features in the resistivity of CrB₂, notably the broadening of ρ_{\parallel} and its low-temperature resistivity anomaly. Both experimental signatures are observed only under the quasi-hydrostatic pressure conditions. In particular the anomalous low-temperature drop in ρ_{\parallel} occurs only if the distortion of the crystalline lattice exceeds the limit $\Delta(c/a) < -1.1\%$.

Bridgman cells with steatite as a solid pressure medium are an ideal tool to achieve this specific distortion of the crystalline lattice. Aligning an arbitrary crystal axis along with the uniaxial stress component will result in an additional compression of this axis. This effect may even be enhanced by exploiting the crystalline elastic anisotropy of CrB₂. Under hydrostatic pressure the soft c -axis will be compressed stronger than the hard a -axis. If the c -axis is exposed to quasi-hydrostatic pressure $p_{\parallel} = p_0 + \sigma_{\text{dev}}$, where $\sigma_{\text{dev}} \parallel c$, it will be compressed even more effectively. Consequently, high quasi-hydrostatic pressure may be used with low experimental effort in order to tune CrB₂ to small ratios c/a which were otherwise accessible only by means of very high hydrostatic pressure. In fact, the typically undesired deviations from perfectly hydrostatic pressure conditions trigger interesting physical phenomena not only in CrB₂ but in a plurality of materials including, e.g., high-temperature superconductors and heavy-fermion compounds.

Turning to the discussion of the high-pressure resistivity data, some important conclusions can be drawn. Most importantly the data hint at an electronic instability as the origin of the unusual temperature dependence of ρ_{\parallel} . Upon application of pressure significant changes in $\rho(T)$ are only observed under quasi-hydrostatic conditions. ρ_{\perp} is qualitatively unchanged when compared to the ambient pressure resistivity and the resistivity under hydrostatic and uniaxial pressure. In contrast, ρ_{\parallel} exhibits a temperature dependence which strongly differs from these curves. The pressure induced modification of ρ_{\parallel} manifests in two key signatures, namely a broadening of $\rho(T)$ near T_{N} and a pronounced low-temperature drop in the resistivity. Since both the broadening

and the resistivity anomaly are only observed together it is natural to assume a common origin for both features. Whereas an external magnetic field has no effect near T_N on the first feature, the latter shows a pronounced magnetic field dependence (cf. Fig. 2.29), suggesting an electronic rather than a structural origin.

In the absence of more conclusive experimental data the precise nature of the electronic instability is still not clear. The pressure-induced modification of the transport properties could be accounted for by different forms of electronic instability, where the most obvious candidates are magnetic order and superconductivity.

The first scenario, a pressure-induced modification of the original antiferromagnetic order, is consistent with the absence of the signature of T_N in ρ_{\parallel} . Unlike for the resistivity at ambient pressure, under hydrostatic, uniaxial, and quasi-hydrostatic pressure p_{\perp} there is no distinct kink in ρ_{\parallel} indicating the freezing out of spin fluctuations. A magnetic instability seems to be less likely, however, because the low-temperature bulk and transport data unambiguously identify CrB₂ as a weak itinerant antiferromagnet (cf. Sec. 2.5), exhibiting basically no magnetic field dependence of T_N . This is in stark contrast to the high-pressure resistivity where the anomaly in ρ_{\parallel} shows a clear field dependence.

The second scenario, pressure-induced superconductivity, appears to be most likely for several reasons. First, the shape of the resistivity anomaly, i.e., the drop of ρ_{\parallel} with decreasing temperature is strongly reminiscent of an incomplete superconducting transition. Even though ρ_{\parallel} remains finite down to the lowest temperature and for all pressures studied, the size of the drop, $\Delta\rho_s$, has been found to become as large as $\sim 80\%$ at high pressure. This may be understood in terms of a large portion of the sample becoming superconducting, however, without forming a complete superconducting percolation path between the voltage terminals. Similar resistivity drops as the ones shown in Fig. 2.27c and Fig. 2.28 have been recorded, e.g., for CaFe₂As₂ where superconductivity is induced by pressure [142]. Only in the pressure range $3.5 \text{ GPa} \leq p \leq 5.5 \text{ GPa}$ the in-plane resistivity of CaFe₂As₂ exhibits a full superconducting transition. At slightly higher and lower pressure, however, there is a sharp yet incomplete drop in resistivity, strongly suggestive of incipient superconductivity. It seems likely that the drop in ρ_{\parallel} observed in CrB₂ also marks incipient superconductivity. The analogy between CrB₂ and CaFe₂As₂ is further supported by the critical field H_{c2} which displays a linear temperature dependence for both materials, as shown in Fig. 2.29 for CrB₂.

Second, superconductivity is supported by the distinct magnetic field dependence of the resistivity anomaly. Both the onset temperature T_s and the size of the resistivity drop $\Delta\rho_s$ decrease with increasing magnetic field. Note that the observation of a resistivity anomaly at magnetic fields exceeding the Pauli limit typically rules out conventional BCS-type superconductivity. Inhomogeneous conventional superconductivity may, however, exhibit very high critical fields, referred to as H_{c3} . Thus, pressure induced superconductivity in CrB₂ may either be inhomogeneous or unconventional, where the high spin-fluctuation temperature $T_{SF} = 257 \text{ K}$ which is

inferred (for non-magnetic CrB₂) from the heat capacity data, is compatible with an unconventional magnetically mediated superconductivity with a critical temperature as high as $T_c \approx 10$ K, cf. Sec. 2.5. Interestingly, the estimate of T_c is not too far apart from the value of T_s deduced from the high-pressure transport measurements. The absence of the signature of T_N in ρ_{\parallel} may indicate that in the putative superconducting phase the long-range magnetic order of CrB₂ is suppressed justifying our assumption of non-magnetic CrB₂ for our estimate of T_c .

Taken together these arguments identify pressure induced incipient superconductivity as the most likely explanation of the low-temperature resistivity anomaly observed in CrB₂ at high pressure. The appearance of the drop in resistivity only under quasi-hydrostatic pressure p_{\parallel} hints at a strong dependence of the putative superconductivity on an anisotropic distortion of the nuclear lattice.

Despite all arguments for incipient superconductivity in the high-pressure phase of CrB₂ it has to be emphasized, that the precise nature of the electronic instability needs further experimental and theoretical exploration. In particular measurements of the specific heat or magnetization under pressure will be needed to unambiguously identify superconductivity and to determine the superconducting volume fraction of the sample.

Stress Dependence of the Superconducting Properties of Correlated Materials

The delicate dependence of the superconducting transport properties on an anisotropic lattice distortion has been observed in a multitude of materials and material classes with strong electronic correlations. Below a short overview of a few well-established superconductors will be given which have been shown to be extremely sensitive to anisotropic distortion introduced either by pressure or by doping. As a common feature all of these materials display a certain crystallographic anisotropy. In some cases, e.g., the high- T_c superconductors, the materials may even be considered two-dimensional. The importance of the structural anisotropy for unconventional, magnetically mediated superconductivity has been pointed out by MONTHOUX and LONZARICH [143].

Our overview begins with two isostructural siblings of CrB₂, notably MgB₂ and NbB₂. Both exhibit phonon-mediated superconductivity at 39 K and 9 K, respectively. [56, 60] Several high-pressure studies have been carried out on polycrystalline and single crystal MgB₂ and resulted in different pressure dependencies of the superconducting transition temperature, $T_c(p)$ (cf. Refs. 24-34 in Ref. [144]). The variation of $T_c(p)$ can most likely be attributed to differing pressure conditions, in particular to shear stress and lattice defects induced by solid pressure media upon the application of quasi-hydrostatic pressure [144]. On the other hand, superconductivity in non-stoichiometric NbB₂ is known to depend strongly on the precise chemical composition [61, 145, 146]. While in this thesis mechanical pressure was used to tune the ratio of the lattice parameters, c/a , and accordingly the transport properties of CrB₂, “chemical pressure” by means of substitutional doping is commonly used to tune the Nb/B ratio and accordingly the

superconducting properties of NbB₂. Since the Nb/B ratio directly affects the lattice parameter ratio c/a the same mechanism may drive the electronic instability in NbB₂ and CrB₂. In fact, it was shown that NbB_{2+x} becomes superconducting if $c/a > 1.069$, corresponding to a B excess $x > 0.4$ [145].

Only recently superconductivity has also been reported for V-doped ZrB₂ and HfB₂ [147, 148]. Both compounds crystallize in the same AlB₂ structure as CrB₂ and exhibit superconducting transition temperatures as high as 8.33 K and 7.31 K for Zr_{0.96}V_{0.04}B₂ and Hf_{0.97}V_{0.03}B₂, respectively. In these compounds V-doping leaves the a lattice parameter essentially unchanged while it reduces the inter-layer distance c .

From our synopsis superconductivity may be identified as a common feature of the C32 metal diborides. The absence of superconductivity in the undistorted AlB₂ prototype structures (except for MgB₂) and its ubiquitous stress-induced emergence strongly suggest a common origin of the superconductivity in the whole material class. This may be, e.g., a structural instability. In fact, first-principles calculations corroborate for several C32 compounds (including CrB₂ and MnB₂) the metastability of the AlB₂ structure and its destabilization in consequence of B depletion [108, 149]. The application of chemical or mechanical pressure may hence drive these compounds close to a structural transition. This way their phonon spectra as well as their electronic band structure may be altered dramatically, eventually giving rise to phonon or density-wave mediated superconductivity.

The 1-2-2 iron arsenide superconductors are layered metal compounds and exhibit spin density wave (SDW) order at low temperatures. The magnetic ground state of the stoichiometric parent material can be modified by pressure or chemical doping and - in most cases - results in the suppression of SDW order accompanied by the appearance of superconductivity. One example belonging to this material class, CaFe₂As₂ has already been mentioned above. In another case, BaFe₂As₂, it was shown that the phase diagram depends strongly on the precise pressure conditions. For instance, uniaxial pressure reduces the SDW order more effectively than purely hydrostatic pressure and favors superconductivity [150]. A similar connection of the pressure anisotropy and superconductivity has also been reported for SrFe₂As₂ [151].

In close analogy many high- T_c cuprate superconductors under pressure display a strong dependence of their superconducting transition temperature on the exact pressure conditions [152]. In fact, going from truly hydrostatic to quasi-hydrostatic pressure may even change the sign of dT_c/dp . E.g., in YBa₂Cu₃O_{7-y} and Gd_{1-x}Y_xBa₂Cu₃O_{7-y} the sign and size of dT_c/dp were demonstrated to depend on the direction of the uniaxial pressure applied [153, 154].

Finally it is interesting to consider some of the tetragonal heavy-fermion compounds which can be driven superconducting by tuning their c/a ratio. This has been demonstrated, e.g., for PuMg₅, where M=(Co, Rh), and CeMIn₅, where M=(Co, Rh, In), which exhibit a linear dependence of T_c on c/a [136, 155, 156]. Tuning of c/a using “uniaxial chemical pressure” has been discussed as a key parameter for the superconductivity in CeRh_{1-x}Ir_xIn₅ [157]. By means

of a crossed sample geometry DEMUER ET AL. showed that the phase diagram of CePd₂Si₂ is markedly affected by uniaxial stress components, where stress applied along the c -axis enhances superconductivity [158]. In strong analogy uniaxial stress along c has been shown to enhance the superconducting phase transition also in CeCu₂Si₂ [159].

The vast number of superconductors that exhibit a clear dependence of their transport properties on uniaxial stress demonstrates the importance of pressure anisotropies for this material class in general. Consistent with the analysis carried out as part of this thesis, it also underpins that the ratio c/a may crucially determine the transport properties of CrB₂ and perhaps even induce superconductivity in this compound.

2.6.4 Summary

As part of this thesis a comprehensive high-pressure transport study on high-quality single crystal samples of CrB₂ has been carried out. The experiments show that $\rho(T)$ depends strongly on the precise pressure conditions applied. Thus resistivity data taken at moderate hydrostatic pressure, uniaxial stress, and quasi-hydrostatic pressure p_{\perp} display the characteristic features and temperature dependence consistent with the ambient pressure resistivity reported in Sec. 2.5.3. In stark contrast, a clear qualitative change of $\rho(T)$ is observed under quasi-hydrostatic pressure p_{\parallel} , where the uniaxial stress component points along the c -axis of the crystal. The corresponding resistivity curves ρ_{\parallel} are significantly broadened and lack the characteristic signature of T_N , i.e., there is no kink in the resistivity around $T \approx 90$ K. Hence there is no clear indication of long-range magnetic order. Moreover a distinct low-temperature drop of ρ_{\parallel} was detected below $T_s \approx 1.6$ K. Both T_s and the size of the drop in the resistivity get enhanced with increasing pressure, while they are suppressed in magnetic fields of several T.

The pressure dependence of the characteristic temperature T^* which marks the point of inflection in $\rho(T)$ exhibits a pronounced dependence on the specific pressure conditions, too. Differences in dT^*/dp can be attributed to the lattice parameter ratio c/a which is altered unevenly under different pressure conditions studied, p (hydrostatic), $\sigma_{\parallel,\perp}$ (uniaxial), and $p_{\parallel,\perp}$ (quasi-hydrostatic). As a central result the ratio of the lattice parameters c/a was identified as a key parameter to tune the transport and magnetic properties of CrB₂.

The high-pressure experiments allow to quantify the change in c/a and to sketch a phase diagram which depends only on the latter ratio, accounting for the key features of all resistivity data (Fig. 2.30). This analysis particularly demonstrates that as a prerequisite for the occurrence of the low-temperature resistivity drop a critical lattice distortion $\Delta(c/a) < -1.1\%$ must be exceeded.

Due to the limitations of the high-pressure measurement techniques applied in this thesis the microscopic origin of the unusual low-temperature drop in ρ_{\parallel} is still not clear. Empirical considerations, however, suggest that the magnetic field dependence may be attributed to an incipient electronic instability. Several aspects suggest pressure-induced superconductivity as the most

likely cause of the low-temperature resistivity anomaly in CrB₂. Still further experimental and theoretical exploration will be needed to clarify this question.

2.7 Conclusions

A comprehensive investigation of high-quality single crystal CrB₂ has been carried out. X-ray and neutron diffraction data confirm the C32 hexagonal crystal lattice. They also reveal diffuse streaks and faint nuclear satellite peaks which may be attributed to the formation of a short-range defect structure and a nuclear superstructure, respectively. In the absence of more detailed experimental data the ordering of B vacancies was suggested as a microscopic mechanism of both the putative defect structure and the nuclear superstructure.

Weak itinerant antiferromagnetism in CrB₂ is suggested by the small ordered moment and the incommensurability of the long-range antiferromagnetic structure observed in magnetic neutron scattering. The latter may be understood in terms of a magnetic triple-k structure with a highly non-trivial topology characterized by vortices. The structure accounts in an intuitive way for the strong geometrical frustration which has been inferred from the large negative Curie-Weiss temperature and the comparatively low Néel temperature, $T_N = 89$ K.

Low-temperature bulk and transport measurements strongly support the assumption of weak itinerant antiferromagnetism. In fact, CrB₂ may even represent the closest antiferromagnetic analog to the archetypical weak itinerant ferromagnets reported so far. In addition to the above-mentioned incommensurate magnetic structure and the reduced ordered moment, characteristics of itinerant magnetism observed in CrB₂ include a typical metallic resistivity, the comparatively low Néel temperature, a large fluctuating moment which clearly exceeds the ordered moment, and a remarkable stability of T_N with respect to high fields. Moreover, itinerant magnetism is corroborated by inelastic neutron scattering and de Hass-van Alphen oscillations. While the first demonstrates the absence of well-defined magnon dispersions in favor of strongly overdamped spin fluctuations the latter suggest a Fermi surface that clearly contains sheets derived from *d*-electrons [99, 101].

Finally, investigation of the pressure dependence of the magnetic order in CrB₂ carried out as part of this thesis show that the electronic and magnetic properties of this compound are widely determined by the ratio of the hexagonal lattice constants. Moderate quasi-hydrostatic pressure induces a low-temperature resistivity anomaly, where ρ drops abruptly at a pressure-dependent critical temperature $T_s = 1.8$ K to 2.6 K. The characteristic shape as well as the distinct field dependence of the drop in the resistivity is highly reminiscent of incipient superconductivity. A detailed analysis shows similarities with the unconventional superconductivity observed in some iron-arsenide superconductors.

The Local Moment Antiferromagnet MnB₂

3.1 Introduction to MnB₂

MnB₂ crystallizes in the hexagonal AlB₂ structure, Strukturbericht designation C32, space group P6/mmm (#191). It is an isostructural sibling of CrB₂. Room temperature lattice constants of MnB₂ of $a = 3.007 \text{ \AA}$ and $c = 3.037 \text{ \AA}$ were reported by BINDER [160]. Thermal expansion data were recorded by BOWMAN and NERESON using neutron diffraction. They suggest a monotonic temperature dependence of both the a - and c -axis [161] from 5 K to 298 K. To the best of our knowledge, the variation of the lattice constants at higher temperatures has not been reported. A schematic depiction of the C32 structure is shown in Fig. 2.1. Composed from a sequence of alternating Mn and B layers, MnB₂ forms basically a closed-packed structure, which are quite generally prone to stacking faults. Moreover, B deficiency may easily arise due to evaporation losses during the growth of crystalline MnB₂ which requires temperatures of at least 1400 °C to 1500 °C [5, 160]. As in any hexagonal diboride line defects and B vacancies are thus likely to occur also in MnB₂ but have not been subject of previous studies. This is particularly problematic as first-principles calculations imply that for MnB₂ the ReB₂-type structure, space group P6₃/mmc (#194), is energetically more favorable compared to the AlB₂-type structure [149, 162]. Consistent with the binary phase diagram of the Mn-B system [163] experimentally observed AlB₂-type MnB₂ should thus be considered metastable. Interestingly, a stabilization of the ReB₂-type structure was also suggested for CrB₂. But while the ReB₂-type seems to be favorable even in stoichiometric MnB₂, it requires B deficiency in CrB₂, cf. Sec. 2.3.3

The discovery of ferromagnetism in the Mn-B system dates back to the beginning of the 20th century and was claimed by WEDEKIND and HEUSLER in a heated debate [164–166]. Owing to the arguable chemical composition of the Mn-B alloys prepared at that time it was first not

possible to identify the ferromagnetic compound unambiguously. The synthesis of pure MnB₂ by BINET DU JASSONNEIX eventually allowed to trace the ferromagnetic signal to MnB. In contrast MnB₂, which is the topic of this chapter, turned out to be essentially non-magnetic at room temperature [167].

Subsequent investigations of the magnetic properties of MnB₂ at low temperatures by means of susceptibility [79, 168], magnetization [79], and nuclear magnetic resonance [71] measurements reported ferromagnetism with a Curie temperature between $T_c = 140$ K and 148 K, a small saturation moment $m_s = 0.19$ to $0.25 \mu_B/\text{Mn}$, and a large effective fluctuating moment $m_{\text{eff}} = 2.3 \mu_B/\text{Mn}$. Magnetization data by KASAYA and HIHARA indicated additionally that the soft axis of the ferromagnetic moment was the c -axis. The same authors reported a metallic resistivity with a monotonic temperature dependence, exhibiting however a faint anomaly near T_c and a clear change of slope at 760 K [73].

Due to the fluctuating moment exceeding the small saturation moment, the magnetic and transport properties of MnB₂ were first interpreted in terms of weak itinerant ferromagnetism. Later, KASAYA and coworkers questioned this assumption on the basis of ⁵⁵Mn-NMR spectroscopy. In contrast to magnetization measurements, the latter suggested large Mn moments of about $3 \mu_B$ oriented almost perpendicular to the crystallographic c -axis [73, 169]. To account for the apparent mismatch between magnetization and NMR data the authors of Ref. [73] suggested that MnB₂ was in fact antiferromagnetic with an ordering temperature as high as $T_N = 760$ K which they inferred from their resistivity data. The putative weak ferromagnetism was attributed to a canting of the localized Mn moments.

It is well known that in crystals lacking inversion symmetry the spin-orbit (Dzyaloshinskii-Moriya) interaction may cause deviations from a perfectly collinear spin arrangement. Due to the high symmetry of the crystal lattice such a scenario may be ruled out in the case of MnB₂. As an explanation for the spin-canting KASAYA ET AL. have put forward an s - d exchange interaction. Here, similar to the STONER-description of itinerant ferromagnetism, the canting of the localized Mn moments is stabilized by a spontaneous polarization of the conduction electrons. The model differs from STONER's theory in the sense that the molecular field which drives the polarization of the conduction electrons is caused by the localized moments.

Powder neutron diffraction carried out by LEGRAND and NEOV corroborated antiferromagnetism with Mn moments $m_s = 2.6 \mu_B/\text{Mn}$ oriented perpendicular to the c -axis [170]. Additionally, these data indicated that all moments within the same hexagonal plane coupled ferromagnetically while neighboring planes exhibited antiferromagnetic order. Albeit providing a quite comprehensive picture of the magnetic order of MnB₂ the study by LEGRAND and NEOV left several questions unanswered. First, no account of the putative spin-canting transition was given. Second, due to the limited temperature range studied, the Néel temperature could not be determined. The authors of Ref. [170] state however that T_N exceeded the highest temperature studied, 885 K, which is already clearly larger than the originally proposed value, $T_N = 760$ K.

Finally, band structure calculations underpinned the assumption of local-moment magnetism in MnB₂ [74, 171]. The latter was attributed to KÜBLER’s covalency mechanism, i.e., spin-dependent changes in the covalent interactions of neighboring *d*-orbitals [172]. The putative low-temperature spin-canting transition appears to be consistent with these calculations in the sense that small deviations from the perfectly collinear antiferromagnetic arrangement are not prohibited energetically.

Despite the progress that has been made in the understanding of the magnetism of MnB₂ some issues still remain unresolved. Important aspects of the well-established C32 nuclear structure have so far not been addressed at all, namely (i) the variation of the lattice parameters at elevated temperature, (ii) the formation of ReB₂-type MnB₂, and (iii) the role of crystalline defects. As part of this thesis, these questions were addressed by means of powder x-ray diffraction, powder neutron diffraction, and polarized single crystal neutron diffraction, where neutron studies were carried out at the instruments SPODI and DNS at the MLZ, Garching. As will be reported in Sec. 3.2, refinements of these data are fully consistent with the AlB₂-type structure of MnB₂. No indications of ReB₂-type MnB₂ are observed. The analysis of the diffraction data further suggest a monotonic temperature dependence of both the *a*- and *c*-axis over four orders of magnitude in temperature, 4 K to 1130 K. No evidence for nuclear or magnetic diffuse scattering is found, suggesting the absence of defect structures and geometric magnetic frustration, respectively.

Shortcomings in previous measurements arise from the quality of the samples examined. Previous experimental investigations of MnB₂ were mostly carried out on sintered polycrystalline specimens that contained impurity phases, namely MnB₄ or Mn₃B₄. To the best of our knowledge, so far only KASAYA and HIHARA used single crystal material in their analysis of the magnetic anisotropy of MnB₂. These authors examined tiny flux-grown single crystal platelets of $0.5 \times 0.5 \times 0.05 \text{ mm}^3$ with the *c*-axis pointing along the shortest edge [73]. In contrast, for our measurements of the low-temperature bulk and transport properties, including the ac susceptibility, magnetization, specific heat, resistivity and Hall effect, large float-zoned single crystal specimens were employed. As will be reported in Sec. 3.4 the measurements carried out as part of this thesis are essentially consistent with previous investigation of polycrystalline material. In contrast to reports by KASAYA and coworkers our magnetization data indicate a weak easy-plane anisotropy, though. Perhaps most importantly, our measurements corroborate a spin-canting transition at $T_{\text{flop}} \approx 130 \text{ K}$ in otherwise antiferromagnetic MnB₂.

Due to an ¹¹B enrichment which results in a significant reduction of neutron absorption the samples investigated in this thesis are perfectly suited for extensive neutron scattering experiments. Therefore a comprehensive powder and single crystal neutron diffraction study was carried out at the instruments SPODI and RESI at MLZ, Garching. In these experiments open questions concerning the magnetic structure of MnB₂ were addressed, such as (i) the Néel temperature and (ii) experimental evidence for the putative spin-canting transition. The results of the measurements will be presented in Sec. 3.3. The powder neutron data indicate a Néel temperature as

T (K)	$R_{\text{nuc,p}}$	a (Å)	c (Å)	$B_{\text{iso}}(\text{B})$ (Å ²)	$B_{\text{iso}}(\text{Mn})$ (Å ²)
11	1.7	3.006200(17)	3.028790(18)	0.023(2)	0.0111(8)
50	1.71	3.006260(17)	3.028790(18)	0.023(2)	0.0112(8)
100	1.73	3.006550(17)	3.029020(18)	0.023(2)	0.0117(8)
150	1.72	3.006850(17)	3.029840(18)	0.023(2)	0.0119(8)
200	1.72	3.007250(17)	3.031200(18)	0.023(2)	0.0126(8)
250	1.72	3.007800(17)	3.032890(18)	0.023(2)	0.0135(8)
298	1.69	3.008450(17)	3.034760(18)	0.023(2)	0.0142(8)

Table 3.1: Powder x-ray diffraction of MnB₂. The corresponding refinements were carried out assuming the hexagonal C32 crystal structure and isotropic displacements for both the B and Mn atoms.

high as 1130 K. Refinements of the single crystal data are based on a representation analysis and suggest in-plane antiferromagnetic order in MnB₂. Moreover, the diffraction data reported in this thesis appear to be consistent with the proposed low-temperature spin-canting.

3.2 Nuclear Structure of MnB₂

The nuclear structure of MnB₂ was studied by means of standard powder x-ray diffraction. Additionally single crystal neutron diffraction with polarized neutrons was carried out to check the diffuse scattering. Diffuse scattering may arise due to magnetic frustration or crystalline defect structures. In MnB₂ the latter may be caused by stacking faults of the hexagonal crystal structure or short-range order of B vacancies.

This section is outlined as follows. First, the results of the powder x-ray diffraction study will be presented. These data essentially confirm the hexagonal C32 symmetry and allow to infer the temperature dependence of the lattice parameters. Following this the results of the polarized single crystal neutron scattering will be reported. In contrast to the isostructural compound CrB₂ no nuclear diffuse scattering is observed in MnB₂.

3.2.1 Powder X-Ray Diffraction

Powder x-ray diffraction was carried out on a specimen prepared from float-zoned single crystal MnB₂. Fig. 3.1a shows typical diffraction data along with their structural refinement. The hexagonal C32 space group which has been reported in the literature was chosen as nuclear model for all fits. The key results of the refinements are summarized in Tab. 3.1. The discrepancy between the observed and calculated intensity is small, hence confirming the C32 structure of MnB₂ both at room temperature and at cryogenic temperatures. Weak additional Bragg reflections highlighted by red arrows in Fig. 3.1a do not originate from hexagonal MnB₂ but may be attributed to a small (3-5 wt%) volume fraction of a yet unidentified impurity phase.

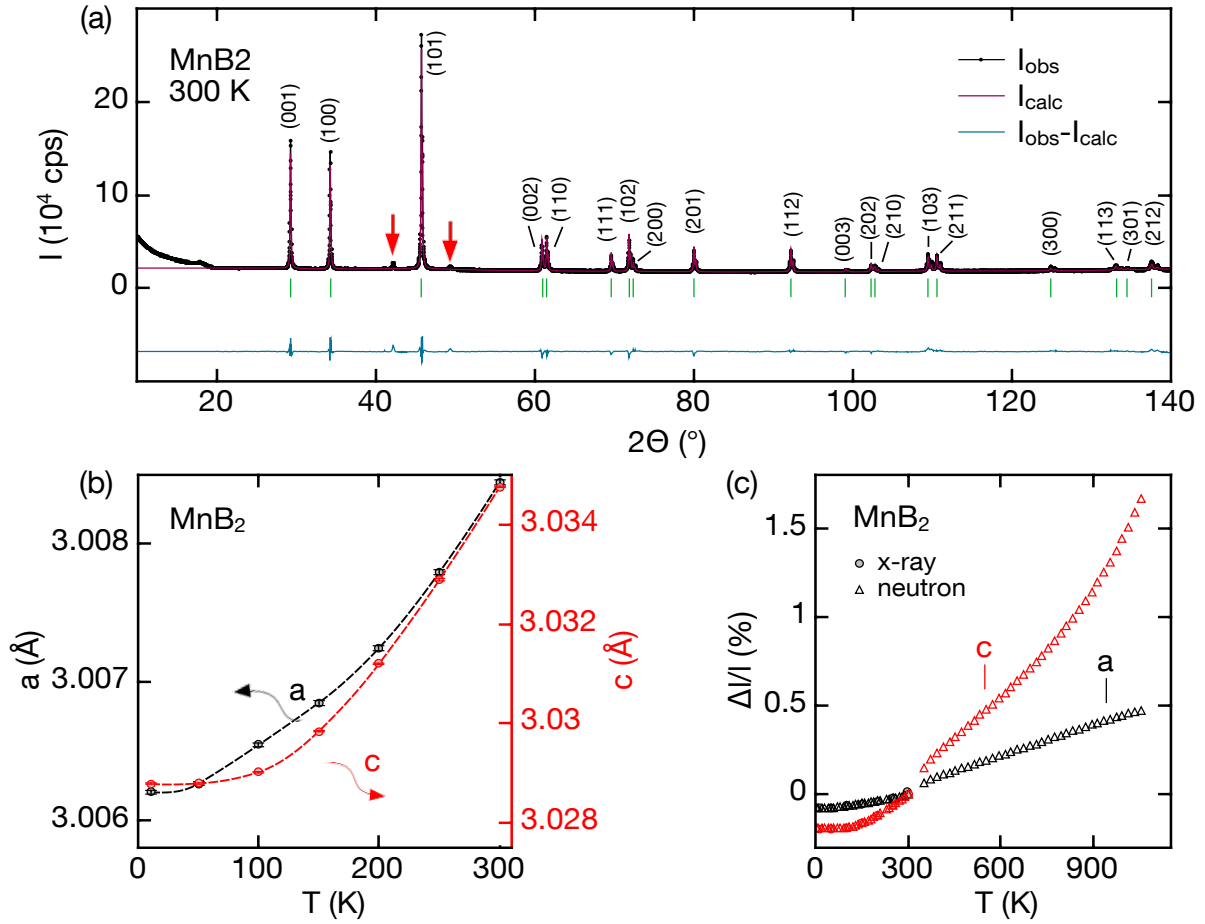


Figure 3.1: Powder x-ray diffraction of MnB₂. (a) Refinement of the diffraction data assuming the hexagonal C32 crystal structure. Red arrows indicate Bragg peaks which cannot be fitted using the model structure. They originate from a small volume fraction (3-5 wt%) of a yet unidentified impurity phase. (b) Lattice parameters as a function of temperature. (c) Relative change of the lattice parameters as a function of temperature. For comparison neutron data were added (triangular symbols). They are fully consistent. See text for details.

Fig. 3.1b shows the change of the lattice parameters of MnB₂ upon cooling to temperatures as low as 10 K. As T is reduced both a and c decrease monotonically. No anomalies are observed in the full temperature range studied.

The lattice parameters inferred from powder neutron data (cf. Sec. 3.3.1) are fully consistent with these findings. Absolute values of a and c differ by no more than 0.02% as compared to the x-ray data. They are summarized in Tab. 3.2. Qualitatively, the same temperature dependence is observed. This is seen most clearly from Fig. 3.1c which shows the relative change $\Delta l/l$ inferred from x-ray and neutron data for both crystal axes as a function of temperature. At low temperatures results from powder x-ray and powder neutron diffraction agree perfectly. They

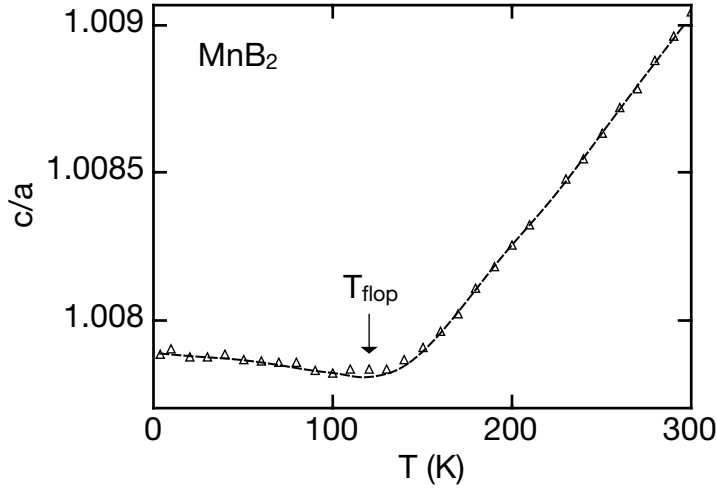


Figure 3.2: Lattice parameter ratio c/a of MnB_2 . Here both a and c were determined by means of powder neutron diffraction, cf. Sec. 3.3.1 for details. X-ray data are qualitatively consistent but exhibit a lower point density. The dashed line is a guide to the eye.

indicate consistently moderate reductions of about 0.08% and 0.2% of the a and c lattice parameter, respectively. In contrast, a 0.18% reduction of the a -axis and a 0.16% expansion of the c -axis are observed in isostructural CrB_2 (cf. Sec. 2.3.1). From 353 K to 1053 K powder neutron diffraction suggests that both a and c grow monotonically reaching a maximum enhancement over their room temperature values of about 0.47% and 1.66%, respectively. At even higher temperatures the incipient decomposition of metastable MnB_2 prevents a reliable refinement of the scattering data.

High-pressure transport measurements of isostructural CrB_2 (cf. Sec. 2.6) as well as systematic doping experiments in isostructural NbB_2 [61, 145, 146] suggest that the ratio of the lattice parameters c/a strongly affects the electronic properties in hexagonal diborides and may even drive instabilities such as superconductivity. It is therefore interesting to study c/a also for MnB_2 . Fig. 3.2 shows the temperature dependence of c/a as determined from powder neutron diffraction. Values obtained from x-ray data are qualitatively consistent but are not shown for clarity. Below room temperature the ratio of the lattice parameters is essentially 1, i.e., deviations from unity are small. With decreasing temperature c/a first drops monotonically, then passes through a faint minimum at about 130 K, and finally increases weakly. It is remarkable that the temperature at which c/a exhibits a minimum matches accurately the temperature of the putative spin-canting transition, $T_{\text{flop}} \approx 130$ K, which may be inferred consistently from ac susceptibility and magnetization data (cf. Sec. 3.4.2 and Sec. 3.4.3). The distinct change in the temperature dependence of c/a may thus be interpreted in terms of a weak magneto-elastic coupling. In turn, uniaxial pressure may be suited to suppress or enhance T_{flop} by compressing the c - or a -axis, respectively.

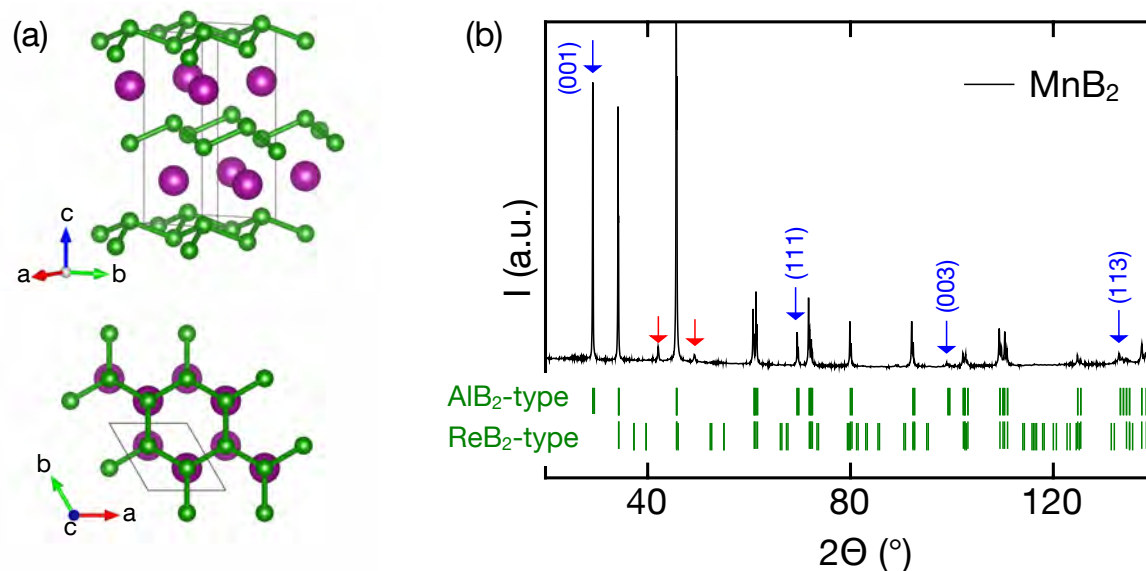


Figure 3.3: X-ray diffraction of MnB₂, $T = 300$ K. (a) Putative ReB₂-type structure of MnB₂. For a comparison with the AlB₂-type structure see Fig. 2.1. (b) Accordance of the ReB₂-type with experimental data. Green vertical lines indicate calculated peak positions of AlB₂-type and ReB₂-type MnB₂. Comparison with the measured powder profile demonstrates the presence of all characteristic reflections of the AlB₂-type (blue arrows). At the same time none of the unique reflections of the ReB₂-type are observed. Red arrows mark reflections caused by a yet unidentified impurity phase. They cannot be fitted using any of the two structure types.

The account on the x-ray diffraction data ends with a short discussion on putative ReB₂-type MnB₂, space group $P6_3/mmc$ (#194), which has been suggested by first-principles calculations [149]. From the same calculations lattice parameters $a \approx 2.77$ Å and $c \approx 6.95$ Å were predicted. A schematic depiction of the proposed structure is shown in Fig. 3.3a. It consists of honeycomb Mn sheets which are neighbored by puckered B layers. Fig. 3.3b shows the observed powder profile along with calculated Bragg peak positions of the well-established AlB₂-type and the proposed ReB₂-type. Comparison of the calculated peak positions shows that the ReB₂-type lacks several reflections which should be present in the scattering off the AlB₂-type and vice versa. In fact, within the angular range studied our experimental data demonstrate the presence of all characteristic reflections of the AlB₂-type. On the other, none of the additional peaks associated with the ReB₂-type are observed, hence suggesting that the data are fully explained by the C32 structure. No experimental evidence of ReB₂-type MnB₂ is found.

3.2.2 Polarized Single Crystal Neutron Diffraction

The diffuse scattering of single crystal MnB₂ was studied using a monochromatic and polarized neutron beam, $\lambda = 4.2$ Å, at the instrument DNS at the MLZ, Garching. The instrument

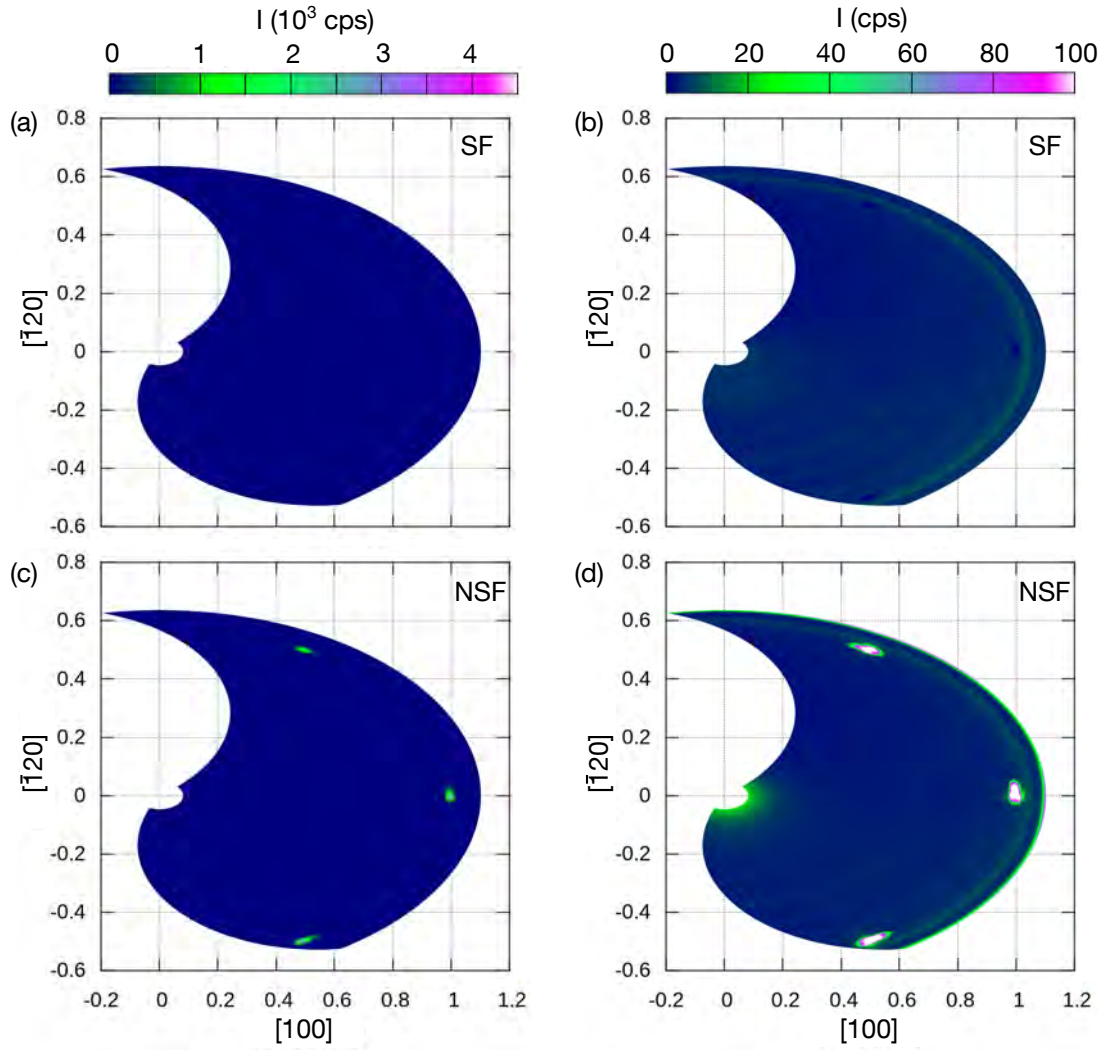


Figure 3.4: Polarized neutron scattering in the $(hk0)$ reciprocal space plane of MnB_2 , $T = 300$ K. A polarization analysis allows to discriminate nuclear and magnetic scattering. Top row: Spin-flip channel showing only magnetic contributions. Consistent with the magnetic propagation vector no scattering is observed $[170]$. Bottom row: Non spin-flip channel containing only nuclear contributions. Three strong Bragg peaks are resolved, namely (clockwise from top to bottom) (010) , (100) , and $(1\bar{1}0)$. Inspection of the low-intensity signal contribution corroborates that neither magnetic (b) nor nuclear (d) diffuse scattering occur.

was configured such as to discriminate magnetic and nuclear scattering. Scattering recorded in the spin-flip channel (SF) was purely magnetic whereas scattering recorded in the non spin-flip channel (NSF) was purely nuclear in origin. The reciprocal hexagonal basal plane $(hk0)$, was studied by rotating the single crystal sample around the axis perpendicular to the scattering plane, i.e., the crystallographic c -axis. Owing to its high Néel temperature, cf. Sec. 3.3, MnB_2 exhibits antiferromagnetic order at room temperature. Therefore all data were recorded at

300 K.

Typical scattering data are shown in Fig. 3.4. As shown in Fig. 3.4a the $(hk0)$ reciprocal space plane contains no magnetic scattering. This is in agreement with the literature [170] and the magnetic neutron diffraction carried out as part of this thesis, which suggest a magnetic propagation vector $\mathbf{k} = 0.5\boldsymbol{\tau}_{001}$. The low-intensity contribution of the scattering signal is shown in Fig. 3.4b. Clearly no magnetic scattering is detected. Within the $(hk0)$ plane thus magnetic diffuse scattering which may arise, e.g., due to magnetic geometrical frustration may be ruled out.

Considering now the non spin-flip nuclear scattering shown in Fig. 3.4c and Fig. 3.4d for high and low scattering intensity, respectively, three strong Bragg peaks are observed. Consistent with the hexagonal symmetry of the C32 crystal lattice and the above-mentioned lattice constants they can be indexed as (clockwise from top to bottom) (010) , (100) , and $(1\bar{1}0)$. The low-intensity contribution to the nuclear scattering signal is shown in Fig. 3.4d. As for the spin-flip channel it contains no diffuse contributions. This finding is in stark contrast to our investigations of CrB₂. As reported in Sec. 2.3.3 the latter exhibits distinct diffuse streaks and faint peaks distributed therein, strongly suggesting the presence of short-range defect order and a nuclear superstructure, respectively. Keeping in mind that CrB₂ and MnB₂ are isostructural siblings and, as outlined in Sec. 1.1, have been synthesized using the same preparation chain and procedure, the absence of similar experimental signatures in the scattering off MnB₂ is surprising. On the other hand, the pronounced difference in the diffuse scattering off CrB₂ and MnB₂ seems to be consistent with our speculations about an interplay between the complex long-range spin order and the putative superstructure in CrB₂. As will be reported in the following section, MnB₂ contrariwise exhibits a rather simple antiferromagnetic order of localized Mn moments.

3.3 Magnetic Structure of MnB₂

The magnetic structure of MnB₂ was studied by means of both powder neutron diffraction and, for the first time, single crystal neutron diffraction. Our account starts with the presentation of the powder neutron data. They confirm the hexagonal C32 nuclear structure of our MnB₂ specimens, consistent with the x-ray diffraction data. Covering four orders of magnitude in temperature, namely from 4 K up to temperatures as high as 1170 K, the comprehensive series of measurements carried out as part of this thesis allowed to track the magnetic ordering transition at $T_N \approx 1130$ K, right at the nuclear phase boundary of MnB₂. All magnetic Bragg peaks were found to be consistent with the proposed propagation vector $\mathbf{k} = 0.5\boldsymbol{\tau}_{001}$ thus corroborating a doubling of the magnetic unit cell with respect to the crystalline c -axis [170]. Assuming ferromagnetic Mn sheets which are mutually coupled antiferromagnetically, the powder neutron diffraction allowed to infer an ordered moment of $2.54 \mu_B/\text{Mn}$ in the low-temperature limit, again in good agreement with Ref. [170].

In the second part of this section the results of the single crystal neutron scattering will be reported. To the best of our knowledge, no such investigations of single crystal MnB₂ have been reported in the literature so far. Using the four-circle diffractometer RESI several nuclear and magnetic Bragg peaks were recorded at 3 K, 225 K, 300 K, 425 K, and 625 K. To determine the magnetic structure of MnB₂ a representation analysis was carried out resulting in six possible solutions. Three of these six candidate structures were ruled out during the subsequent refinement process. The remaining three model structures are all characterized by ferromagnetic Mn sheets that are mutually coupled antiferromagnetically. They differ, however, in the angle of the Mn moment with respect to the hexagonal a -axis, which may be 0°, 30°, or 60°. Unfortunately, the accuracy of the neutron data is at present not sufficient to identify the correct spin alignment among the three alternatives unambiguously. Still the analysis carried out in this thesis allows to track the temperature dependence of the ordered moment which is found to be in good agreement with the one derived from powder neutron data. It suggests, moreover, local-moment magnetism in MnB₂. Finally, the low-temperature ferromagnetism inferred from ac susceptibility and magnetization measurements is taken into account by fitting a canted antiferromagnetic structure to the diffraction data. Though the single crystal neutron data do not provide definite evidence they do not rule out a putative spin-canting at $T_{\text{flip}} \approx 130$ K.

3.3.1 Powder Neutron Diffraction

Powder neutron diffraction was carried out at the instrument SPODI at MLZ, Garching (cf. Sec. 1.4.2). Measurements were carried out under heating from 4 K to 300 K and from 353 K to 1173 K. In order to reduce temperature gradients the sample temperature was stepped and stabilized while data were recorded for about 30 minutes at each setpoint. All measurements are summarized in Fig. 3.5a which shows the scattering intensity as a function of the sample temperature and the scattering angle. The observed intensity distribution is consistent with the C32 nuclear lattice. Additionally magnetic scattering gives rise to several satellite reflections all of which can be indexed using the propagation vector $\mathbf{k} = 0.5\tau_{001}$ proposed in Ref. [170]. A refinement of these data was carried out for each individual temperature to determine the lattice constants and the ordered moment. For all temperatures nuclear scattering off hexagonal MnB₂ and magnetic scattering off a collinear antiferromagnetic structure with in-plane Mn moments as proposed in Ref. [170] was assumed. For the high-temperature measurements, 353 K to 1053 K, additionally scattering due to the Nb powder canister was taken into account. At even higher temperatures the incipient decomposition of metastable MnB₂ prevented a reliable refinement. Isotropic atomic displacements were assumed for both Mn and B. The key results of the refinements are summarized in Tab. 3.2. Small R values indicate a good agreement of the nuclear and magnetic model structures with the experimental data.

As has been discussed already in Sec. 3.2.1 the powder neutron diffraction data allow to infer a monotonic increase of both the a - and c -axis with increasing temperature. Data are shown in

Fig. 3.1c for $4\text{ K} \leq T \leq 1053\text{ K}$. They are in excellent agreement with the values determined by x-rays.

The temperature dependence of the ordered moment is shown in Fig. 3.8 along with values obtained from single crystal neutron diffraction, cf. Sec. 3.3.2. At $T = 4\text{ K}$, the lowest temperature studied, powder data suggest an ordered moment of $2.75\ \mu_{\text{B}}/\text{Mn}$. This is in good agreement with Ref. [170] where an ordered moment of $2.6\ \mu_{\text{B}}/\text{Mn}$ was reported. With increasing temperature m decreases monotonically. From cryogenic temperatures to about 600 K it thereby exhibits a temperature dependence

$$m_s \propto \sqrt{1 - (T/T_{\text{N}})^2}. \quad (3.1)$$

At even higher temperatures the reduction of the ordered moment is less pronounced than it would be expected for a simple local-moment magnet. The discontinuous jump at about 300 K originates most likely from small systematic differences between the measurement series at low and high temperature. The absence of abrupt changes in $m(T)$ near $T_{\text{flop}} \approx 130\text{ K}$ suggests that any changes of the magnetic structure in the corresponding temperature range must occur smoothly. This is consistent with the assumption of a continuous crossover from the high-temperature collinear antiferromagnetic to a low-temperature spin-canted antiferromagnetic state. It is also in agreement with the specific heat data reported in Ref. [5], where no anomalies were observed between 2 K and 300 K , suggesting either the absence of a low-temperature phase transition or a smooth crossover (cf. Sec. 3.4.1). From the fact that the refinements using a collinear antiferromagnetic model structure are in excellent agreement with the experimental data it may be concluded that a putative ferromagnetic canting must be small.

From the continuous decrease with increasing temperature and eventually the disappearance of the $0.5\tau_{001}$ Bragg peak, shown in Fig. 3.5b, a high magnetic ordering temperature, $T_{\text{N}} \approx 1130\text{ K}$, may be estimated. This exceeds strongly the value reported by KASAYA ET AL., $T_{\text{N}} \approx 760\text{ K}$ [73]. The observation of magnetic scattering at temperatures well above 760 K is consistent with Ref. [170]. Due to the smaller temperature range studied, the authors of Ref. [170] were however not able to extrapolate the temperature of the Néel transition.

Inspection of the binary phase diagram of the B-Mn system suggests that at 1075 K metastable MnB₂ decomposes into its neighboring phase Mn₃B₄ and MnB₄ [163, 173]. In good agreement, the sudden appearance of additional Bragg peaks at about 1100 K is observed, which may be attributed to these Mn- and B-rich phases, respectively. Within the experimental error, T_{N} coincides with this decomposition temperature hence suggesting that the long-range magnetic order in MnB₂ develops right upon the condensation of the crystal lattice. The observation of some faint magnetic scattering even at $T > 1100\text{ K}$ may be explained by overheated portions of the MnB₂ sample which have not yet decomposed.

The Local Moment Antiferromagnet MnB₂

T (K)	$R_{\text{nuc,p}}$	$R_{\text{mag,p}}$	a (Å)	c (Å)	$B_{\text{iso}}(\text{B})$ (Å ²)	$B_{\text{iso}}(\text{Mn})$ (Å ²)	m (μ _B /Mn)
4	5.52829	4.04557	3.00677(3)	3.03046(4)	0.27013(1612)	0.09214(2491)	2.75444(2612)
10	5.91107	5.46623	3.00671(3)	3.03047(4)	0.24747(1594)	0.10104(2480)	2.75213(2617)
20	5.73818	4.81012	3.00682(3)	3.03049(4)	0.28425(1581)	0.09363(2436)	2.78301(2557)
30	5.55439	4.05761	3.00676(3)	3.03044(4)	0.25386(1634)	0.04601(2503)	2.77213(2652)
40	5.86309	4.02746	3.00679(3)	3.03049(4)	0.31082(1613)	0.11471(2477)	2.77068(2605)
50	5.32664	5.56142	3.00680(3)	3.03046(4)	0.29358(1573)	0.10013(2416)	2.72916(2544)
60	5.71571	6.67523	3.00682(3)	3.03046(4)	0.29722(1625)	0.07610(2493)	2.74848(2638)
70	5.75315	5.92083	3.00692(3)	3.03054(4)	0.29913(1594)	0.07013(2440)	2.75258(2574)
80	5.18245	6.27718	3.00695(3)	3.03056(4)	0.28987(1620)	0.08113(2489)	2.75010(2615)
90	5.47150	4.63380	3.00702(3)	3.03055(4)	0.28656(1552)	0.12146(2406)	2.73640(2520)
100	5.88783	3.39294	3.00705(3)	3.03056(4)	0.30323(1583)	0.11501(2445)	2.77285(2534)
110	6.11102	5.60894	3.00717(3)	3.03072(4)	0.27331(1603)	0.11078(2479)	2.75594(2600)
120	5.89023	5.52761	3.00724(3)	3.03080(4)	0.27979(1606)	0.09752(2476)	2.77319(2617)
130	5.98285	4.48723	3.00735(3)	3.03090(4)	0.28782(1625)	0.12600(2517)	2.75575(2635)
140	6.01019	4.69041	3.00745(3)	3.03111(4)	0.31551(1621)	0.17797(2528)	2.77832(2615)
150	5.70048	6.41450	3.00751(3)	3.03128(4)	0.30679(1578)	0.17031(2458)	2.71043(2556)
160	5.79638	7.86460	3.00755(3)	3.03149(4)	0.31314(1620)	0.16943(2528)	2.73076(2638)
170	5.99869	4.43203	3.00760(3)	3.03172(4)	0.31376(1578)	0.19595(2473)	2.79152(2569)
180	5.88601	5.18169	3.00771(3)	3.03209(4)	0.32166(1589)	0.21841(2495)	2.75401(2571)
190	5.85270	5.11231	3.00775(3)	3.03235(4)	0.33816(1603)	0.20660(2509)	2.72459(2595)
200	5.73484	4.95563	3.00789(3)	3.03271(4)	0.31749(1584)	0.17200(2476)	2.75507(2567)
210	5.88581	6.42062	3.00798(3)	3.03301(4)	0.31252(1622)	0.20707(2545)	2.73140(2622)
230	5.57776	6.08549	3.00817(3)	3.03367(4)	0.32192(1571)	0.20734(2458)	2.75355(2534)
240	6.29360	6.76517	3.00829(3)	3.03399(4)	0.32737(1584)	0.24929(2509)	2.73507(2565)
250	6.38853	6.97482	3.00840(3)	3.03436(4)	0.34929(1626)	0.22702(2564)	2.74145(2632)
260	5.55253	4.26595	3.00852(3)	3.03476(4)	0.31309(1555)	0.24849(2471)	2.76290(2529)
270	5.96475	4.94495	3.00867(3)	3.03510(4)	0.34345(1615)	0.26964(2555)	2.77214(2606)
280	5.30831	6.00902	3.00872(3)	3.03543(4)	0.35301(1567)	0.27748(2486)	2.76668(2547)
290	4.83640	4.49705	3.00888(3)	3.03584(3)	0.33276(1505)	0.28974(2406)	2.78063(2446)
300	5.19173	4.04769	3.00899(3)	3.03621(3)	0.35332(1503)	0.32434(2421)	2.75990(2430)
353	14.00105	7.37298	3.01105(5)	3.04087(5)	0.46567(2344)	0.37318(3905)	2.60041(3684)
373	7.16295	10.07902	3.01169(3)	3.04230(4)	0.59177(1641)	0.64984(2866)	2.46830(2504)
393	6.43069	13.55852	3.01199(3)	3.04329(4)	0.61056(1545)	0.72977(2747)	2.48972(2388)
413	6.63964	12.54394	3.01237(3)	3.04429(4)	0.61414(1530)	0.75016(2730)	2.47584(2382)
433	6.41166	9.80192	3.01269(3)	3.04521(4)	0.59405(1450)	0.84219(2647)	2.46478(2279)
453	6.70026	11.44292	3.01304(3)	3.04610(4)	0.58753(1488)	0.79168(2690)	2.44813(2319)
473	6.73285	9.78714	3.01344(3)	3.04703(4)	0.59548(1427)	0.84975(2604)	2.44228(2223)
493	6.69413	10.78039	3.01377(3)	3.04797(4)	0.62584(1454)	0.85732(2648)	2.42317(2261)
513	7.02417	9.90065	3.01408(3)	3.04890(4)	0.66609(1482)	0.88707(2706)	2.41619(2296)
533	7.42026	10.94006	3.01447(3)	3.04985(4)	0.64651(1492)	0.88300(2734)	2.38138(2318)
553	8.03357	9.40317	3.01485(3)	3.05072(4)	0.66097(1521)	0.88719(2795)	2.34997(2355)
573	8.20734	11.05662	3.01525(3)	3.05171(4)	0.65920(1553)	0.90707(2855)	2.34808(2405)
593	8.00223	11.10409	3.01560(3)	3.05265(4)	0.68170(1543)	0.93291(2849)	2.35514(2396)
613	8.44613	10.69304	3.01591(3)	3.05364(4)	0.70985(1608)	0.96489(2962)	2.33078(2483)
633	8.63904	10.92309	3.01627(3)	3.05463(4)	0.78249(1618)	0.99794(2959)	2.30453(2461)
653	8.53971	10.71112	3.01663(3)	3.05569(4)	0.76823(1588)	0.97402(2903)	2.27176(2423)
673	8.66298	13.02666	3.01703(3)	3.05680(4)	0.80336(1622)	1.01286(2956)	2.23938(2462)
693	8.11131	14.35310	3.01731(3)	3.05785(4)	0.82673(1589)	1.00571(2872)	2.19751(2423)
713	8.37480	13.41625	3.01769(3)	3.05900(4)	0.82387(1622)	1.04936(2937)	2.22244(2481)
733	7.95196	13.28702	3.01803(3)	3.06016(4)	0.84972(1587)	1.05119(2848)	2.17176(2411)
753	8.27335	13.70698	3.01841(3)	3.06129(4)	0.86001(1645)	1.05970(2951)	2.16770(2510)
773	8.04861	12.31577	3.01881(3)	3.06262(4)	0.90419(1606)	1.13061(2885)	2.11989(2431)
793	8.36530	12.69295	3.01918(3)	3.06392(4)	0.88697(1632)	1.14779(2944)	2.11530(2488)
813	8.34309	11.50318	3.01955(3)	3.06521(4)	0.89774(1597)	1.15516(2883)	2.08538(2447)
833	8.09886	13.85254	3.01989(3)	3.06653(4)	0.92003(1639)	1.21122(2994)	2.07695(2507)
853	8.11687	14.96040	3.02023(3)	3.06801(4)	0.92054(1634)	1.22383(2993)	2.00665(2510)
873	9.42406	15.42871	3.02066(3)	3.06945(4)	0.93122(1721)	1.19508(3155)	2.02672(2664)
893	6.19559	9.23089	3.02085(3)	3.07096(4)	0.82165(1539)	0.83698(2619)	2.04475(2420)
913	6.05072	7.69776	3.02114(3)	3.07260(4)	0.83208(1528)	0.86286(2620)	2.00714(2401)
933	5.84079	7.04580	3.02150(3)	3.07424(4)	0.85044(1547)	0.89110(2659)	1.97997(2447)
953	5.29912	9.13154	3.02186(3)	3.07604(4)	0.85063(1541)	0.86622(2633)	1.93037(2438)
973	5.25441	8.39461	3.02220(3)	3.07797(4)	0.83971(1510)	0.90734(2608)	1.86985(2424)
993	5.57339	8.18760	3.02252(3)	3.08002(4)	0.84456(1556)	0.89790(2687)	1.82603(2490)
1013	5.40953	6.77502	3.02284(3)	3.08210(4)	0.85340(1553)	0.91413(2679)	1.75303(2506)
1033	5.54470	9.11922	3.02307(3)	3.08447(4)	0.86116(1602)	0.88717(2742)	1.65944(2634)
1053	5.78940	10.65826	3.02334(3)	3.08692(4)	0.87121(1609)	0.92786(2774)	1.55088(2698)

Table 3.2: Refinement of powder neutron diffraction data. See text for details.

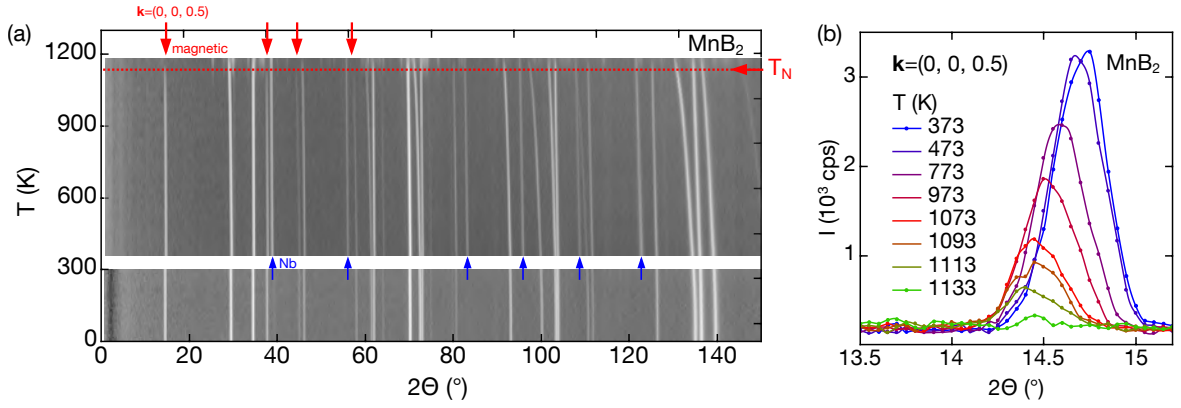


Figure 3.5: Powder neutron diffraction of MnB_2 . (a) Scattering intensity as a function of scattering angle and temperature. Red arrows indicate the strongest magnetic Bragg peaks occurring below $T_N \approx 1130$ K. Blue arrows mark Bragg peaks which originate from scattering off the Nb sample tubes used for all high-temperature measurements. At highest temperatures the sudden appearance of additional reflections suggest the decomposition of metastable MnB_2 , putatively into the Mn- and B-rich neighboring phases Mn_3B_4 and MnB_4 , respectively. (b) Temperature dependence of the strongest magnetic satellite at $\mathbf{k} = 0.5\boldsymbol{\tau}_{001}$ corroborating a high Néel temperature, $T_N \approx 1130$ K.

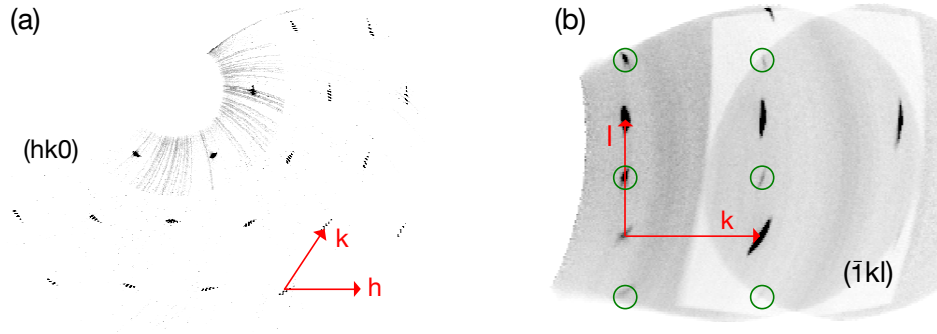


Figure 3.6: Single crystal neutron diffraction of MnB_2 , $T = 300$ K. (a) Scattering in the $(hk0)$ reciprocal space plane. The sixfold pattern is fully consistent with the nuclear hexagonal C32 lattice. (b) Scattering in the $(\bar{1}kl)$ reciprocal space plane demonstrating the presence of additional magnetic Bragg peaks. Consistent with powder neutron diffraction, they can be indexed using the magnetic propagation vector $\mathbf{k} = 0.5\boldsymbol{\tau}_{001}$ (green circles).

3.3.2 Single Crystal Neutron Diffraction

Single crystal neutron diffraction was carried out at the four-circle diffractometer RESI at the MLZ, Garching, using unpolarized thermal neutrons at a wavelength of 1.0408 \AA . An image plate detector rather than a counter tube detector was used to cope with the large in-plane peak broadening of about 7° . The anisotropic mosaicity originates from the c -axis slowly turning by

about 1° over the total length of 2.6 mm of the sample studied, cf. Sec. 1.1. Fig. 3.6 shows typical room temperature diffraction data. The $(hk0)$ reciprocal space plane, Fig. 3.6a, displays a sixfold scattering pattern, consistent with the scattering off the nuclear C32 structure determined by powder x-ray and neutron data. Additional weaker reflections are observed, e.g., in the $(\bar{1}kl)$ reciprocal space plane shown in Fig. 3.6b. These peaks cannot be indexed unless an additional propagation vector $\mathbf{k} = 0.5\boldsymbol{\tau}_{001}$ is used. In fact, any Bragg peaks which cannot be indexed by means of the nuclear primitive translations can be indexed using $\mathbf{k} = 0.5\boldsymbol{\tau}_{001}$. As the latter is the magnetic propagation vector which has been inferred already from the powder neutron data all associated peaks were attributed to scattering off the antiferromagnetic order that emerges below $T_N \approx 1130$ K.

In order to determine the magnetic structure of single crystal MnB₂ the nuclear and magnetic scattering at various temperatures, 3 K, 225 K, 300 K, 425 K, and 625 K, was studied. These data suggest that the magnetic structure of MnB₂ is essentially unchanged in the temperature range covered.

3.3.3 Representation Analysis and Magnetic Structure Refinement

Based on the nuclear C32 structure and the magnetic modulation vector $\mathbf{k} = 0.5\boldsymbol{\tau}_{001}$ a representation analysis was carried out using the crystallographic software JANA2006 in order to identify compatible magnetic isotropy subgroups. The magnetic moment was thereby assumed to be located exclusively at the Mn site. Subsequently, again JANA2006 was employed to fit the candidate structures obtained from the representation analysis to the single crystal neutron scattering data. For the fitting procedure the atomic positions were kept constant, i.e., deviations from the C32 nuclear symmetry were prohibited. To account for the ¹¹B-enrichment of the sample the coherent scattering length of the B atoms was set to $b_{\text{coh}} = 6.65$ fm. An isotropic extinction model (type 1, Lorentzian) was chosen to account for extinction effects and the magnetic form factor of the Mn²⁺ ion was used to calculate the magnetic scattering. In order to account for magnetic domains the structures were assumed to be twinned. Finally, for each individual isotropy subgroup under test scattering intensities originating from equivalent positions were averaged.

From the representation analysis six magnetic superspace groups were identified as potential solutions of the magnetic structure of MnB₂. Fig. 3.7 shows these candidate structures in their standards settings and (for better comparison) in hexagonal settings. As a common feature all six model structures are characterized by a ferromagnetic in-plane coupling and an antiferromagnetic inter-plane coupling of the Mn moments. Closer inspection reveals that among the six models three - C[c]ccm, P[c]6/mmc, and P[b]2/m - are equivalent. These structures exhibit Mn moments which point along the crystallographic c -axis. In contrast, in the remaining candidate structures the Mn moments lie within the hexagonal basal plane. They differ in terms of the angle of the moment vector with respect to the crystallographic a -axis, namely 30° (C[c]mcm (1)), 0°

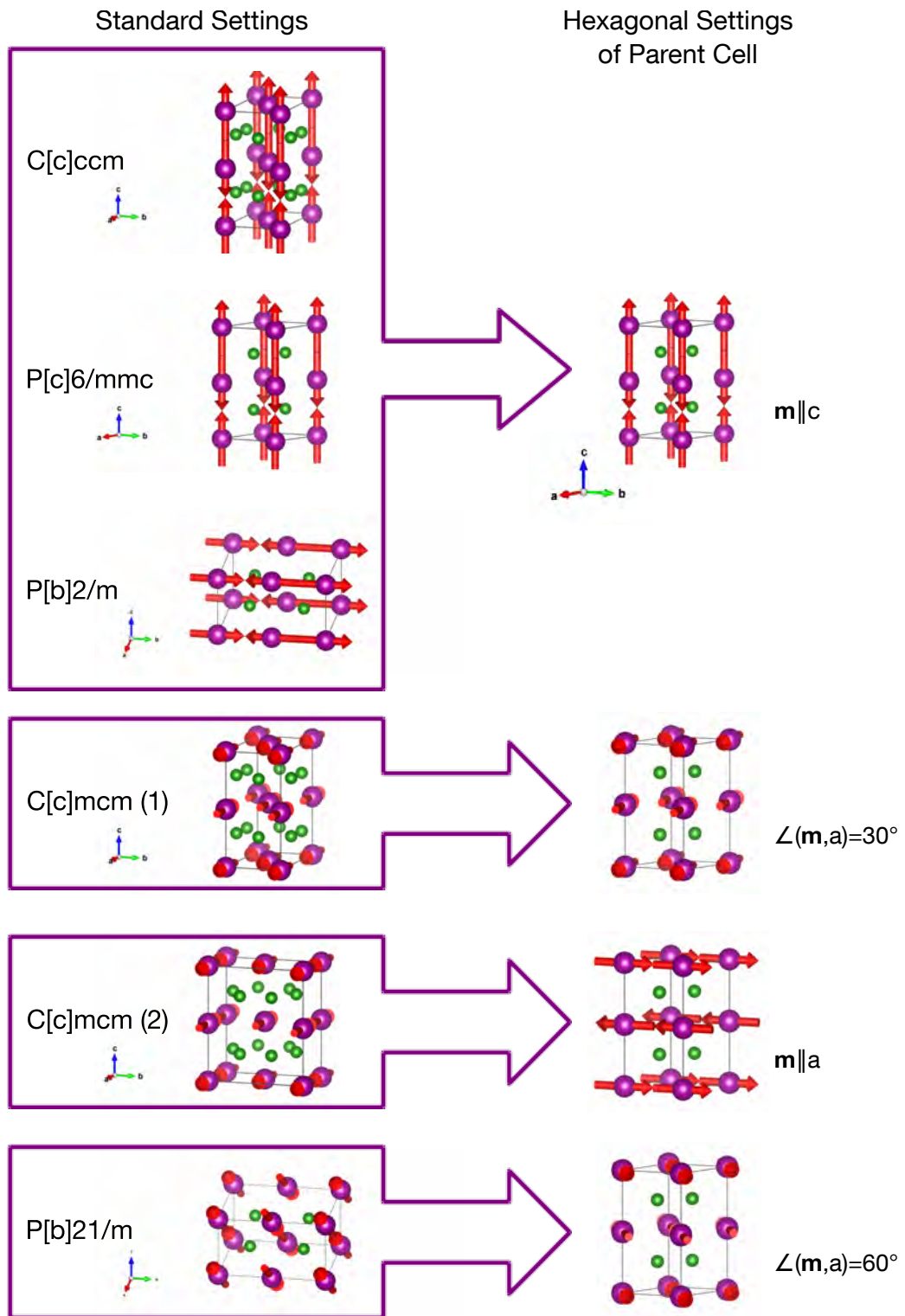


Figure 3.7: Representation analysis of MnB₂. The tested six magnetic space groups are shown in their standard settings (left column) and in the settings of the hexagonal parent cell (right column). The block arrows group space groups which share the same direction of the magnetic moment with respect to the hexagonal cell. For three groups the moment vectors is oriented parallel to the *c*-axis; for the other three groups the moment vector lies in the hexagonal basal plane.

SpGrp	Cell		#(all)	R(obs)	R(all)	R _{nuc} (obs)	R _{nuc} (all)	R _{mag} (obs)	R _{mag} (all)
C[c]ccm	5.2083 3.0070 6.0740 90 90 90		32+12	28.55	39.43	21.19	32.92	57.64	63.30
P[c]6/mcc	3.0070 3.0070 6.0740 90 90 120		22+12	35.31	50.46	25.80	42.62	70.45	77.13
P[b]2/m	3.0070 3.0070 6.0740 90 90 120		32+12	28.71	39.37	21.39	32.96	57.65	63.29
C[c]mcm (1)	5.2083 3.0070 6.0740 90 90 90		32+12	17.99	28.20	17.60	28.18	19.54	28.28
C[c]mcm (2)	3.0070 5.2083 6.0740 90 90 90		32+12	17.99	28.20	17.60	28.18	19.54	28.28
P[b]21/m	3.0070 6.0740 3.0070 90 120 90		32+12	17.99	28.20	17.60	28.18	19.54	28.28
C2'2'21	5.2083 3.0070 6.0740 90 90 90		33+13	18.22	27.88	18.59	29.28	8.52	8.52

Table 3.3: Single crystal neutron diffraction of MnB₂. Refinements of the dataset recorded at 3 K using different magnetic superspace groups. The number of reflections after averaging, i.e., the number of fitted reflections, is broken down in observed (“obs”) and weak ($I < 3\sigma$) reflections.

T (K)	#(all)	$R(\text{obs})$	$R(\text{all})$	$R_{\text{nuc}}(\text{obs})$	$R_{\text{nuc}}(\text{all})$	$R_{\text{mag}}(\text{obs})$	$R_{\text{mag}}(\text{all})$	m (μ_{B}/Mn)
SpcGrp C[c]mcm (1)								
3	32+12	17.99	28.20	17.60	28.18	19.54	28.28	2.764(327)
225	37+6	7.05	9.01	6.27	6.27	11.63	24.65	2.545(158)
300	23+1	7.07	8.18	6.60	6.60	9.49	16.34	2.937(278)
425	38+7	10.91	13.07	9.31	9.31	22.81	37.95	2.458(250)
625	41+4	12.14	13.74	9.45	10.44	31.21	36.48	1.915(188)
SpcGrp C2'2'21								
3	33+13	18.22	27.88	18.59	29.28	8.52	8.52	2.043(280)

Table 3.4: Single crystal neutron diffraction of MnB₂. Refinements of the dataset recorded at different temperatures using the C[c]mcm and C2'2'21 superspace groups. The corresponding cell parameters are summarized in Tab. 3.3. The number of reflections after averaging, i.e., the number of fitted reflections, is broken down in observed (“obs”) and weak ($I < 3\sigma$) reflections.

(C[c]mcm (2)), and 60° (P[b]21/m).

At first the presentation of the fit results will focus on the low-temperature limit, $T = 3\text{K}$, where the most comprehensive dataset consisting of 31 nuclear and 28 magnetic Bragg peaks was recorded and where the largest ordered moment is expected. The main results of the refinements using the six candidate structures are summarized in Tab. 3.3. A comparison of the R factors shows that the three structures which exhibit magnetic moments along the c -axis must be ruled out. The fits employing any of the remaining three model structures result in identical R values and the same ordered moment of $2.76 \mu_{\text{B}}/\text{Mn}$. On the one hand, this is in excellent agreement with the powder neutron data. On the other hand, the correct magnetic structure thus cannot be identified on the basis of the unpolarized neutron data. Consistent with literature it is possible to state, however, that the antiferromagnetic long-range order of MnB₂ is characterized by Mn moments with a large in-plane component.

Fig. 3.8 shows the refined ordered moment as a function of temperature. As indicated by the solid red line $m(T)$ agrees reasonably well with Eq. 3.1, i.e., the temperature dependence expected for a local-moment magnet. Local-moment magnetism is also suggested from the large size of m which exceeds clearly the saturation moment determined from magnetization data. In fact, a local-moment picture of the magnetic order of MnB₂ has also been put forward in Ref. [74] where band structure calculations suggest that the splitting of the spin-up and spin-down bands is as large as 2 eV and thus exceeds the respective band widths. As reported in Sec. 3.3.1 comparable values of the ordered moment may be inferred from refinements of the powder neutron data.

As a consequence of the collinear antiferromagnetic spin arrangement one would expect the magnetization \mathbf{M} of MnB₂ to vanish, or to be extremely small at least. In particular \mathbf{M} should lack ferromagnetic contributions. In accordance with Ref. [73], the low-temperature magnetization

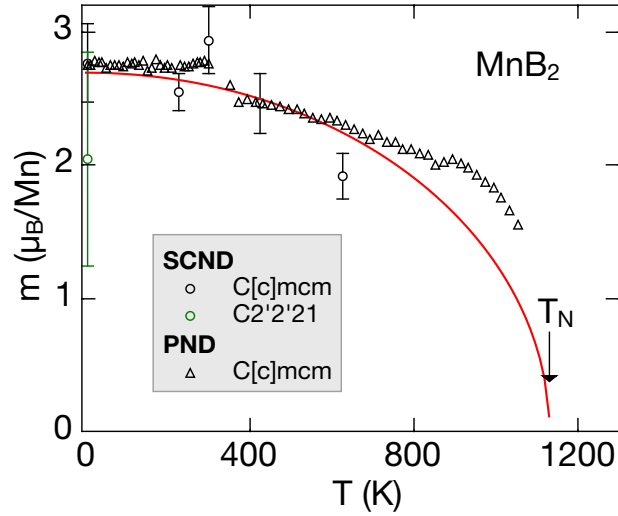


Figure 3.8: Temperature dependence of the ordered magnetic moment as inferred from refinements using the $C[c]mcm$ and $C2'2'21$ superspace groups, i.e., assuming a perfectly collinear in-plane antiferromagnetic spin structure and a canted antiferromagnet, respectively. Open circles refer to single crystal diffraction data. Open triangles indicate powder neutron data. Corresponding errorbars are of the symbol size and omitted in the interest of clarity. The solid red lines was calculated according to Eq. 3.1, showing the temperature dependence expected for a local-moment magnet.

and susceptibility measurements carried out as part of this thesis however clearly suggest the development of a small ferromagnetic component below $T_{\text{flop}} \approx 130$ K. As will be reported in Sec. 3.4.3 these data imply a small but finite magnetic moment of about $0.1 \mu_B/\text{Mn}$ and, most importantly, ferromagnetic hysteresis. To resolve the discrepancy of an antiferromagnetic spin order, on the one hand, and weak low-temperature ferromagnetism, on the other hand, a small spin canting was proposed [73]. The latter may account for a small ferromagnetic component while leaving the antiferromagnetic structure basically unaltered, consistent with both the finite magnetization and the ferromagnetic hysteresis observed at low temperatures. Moreover, calculations confirm that a small inclination of the Mn moment with respect to the hexagonal plane, $\delta \approx 6^\circ$, [74] is energetically equivalent to the collinear antiferromagnet.

To check the low-temperature neutron diffraction data for consistency with the suggested spin-flop transition, the data recorded at 3 K were fitted using the magnetic superspace group $C2'2'21$ as model structure. $C2'2'21$ is a subgroup of the above-mentioned magnetic superspace group $C[c]mcm$ (1). As shown in Fig. 3.9 $C2'2'21$ results from $C[c]mcm$ (1) by a canting of the Mn moments out of the hexagonal basal plane hence giving rise to a net ferromagnetic component. Similar subgroups can be derived from $C[c]mcm$ (2) and $P[b]21/m$. Anticipating that, like their parent groups, these subgroups would be indistinguishable, e.g., due to the formation of magnetic domains and thus would result in identical refinements of the experimental data, in

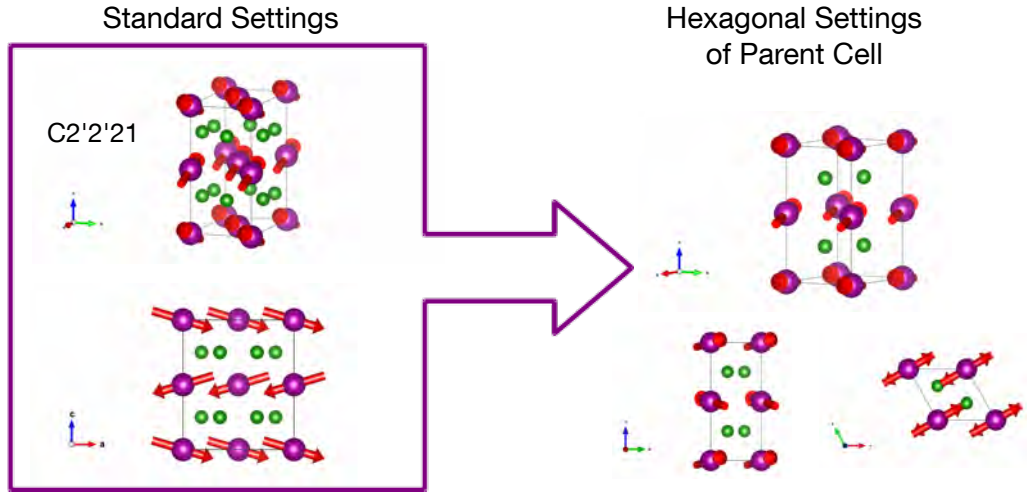


Figure 3.9: Representation analysis of MnB_2 . The subgroup $C2'2'21$ derived from $C[c]mcm$ is compatible with a finite ferromagnetic component arising from a canting of neighboring antiferromagnetic sheets.

the following only the $C2'2'21$ model structure will be considered. The main results of the refinement are also summarized in Tab. 3.3. Comparison of the R values shows that the fit using the $C2'2'21$ structure gives a comparably good agreement with the experimental data as the refinements discussed above. Note that due to the specific method used in the JANA2006 refinement software to label the fitted reflections values of R_{mag} obtained from $C2'2'21$ and from the above-mentioned model structures cannot be compared directly. Instead R should be considered. Keeping in mind that the number of fitted Bragg peaks is relatively small while the number of fit parameters is even larger than for the refinements reported above, because m_c was added as a free parameter, the fit quality is acceptable. Due to these limitations, however, the uncertainty of the fit is substantial and no definitiv conclusions should be drawn from this single refinement.

In comparison to the collinear antiferromagnetic spin structure a smaller ordered moment of $2.04 \mu_B/\text{Mn}$ is found, in excellent agreement with ab-initio calculations [74, 171]. Its large, almost integer size hints again at a localization of the Mn moment. Admittedly the errorbar associated with m is large. Thus chances are that refinements of the $C2'2'21$ spin-canted structure on the basis of a more comprehensive dataset will result in a larger value of the ordered moment, similar to the one determined from the $C[c]mcm$ superspace groups. From the ratio of the in-plane and out-of-plane components, $m_a = 2.018 \mu_B/\text{Mn}$ and $m_c = 0.32 \mu_B/\text{Mn}$, the inclination angle of \mathbf{m} with respect to the hexagonal plane was estimated as $\delta \approx 9^\circ$. Due to the uncertainty in m , smaller values of δ as proposed, e.g., in Ref. [171] where $\delta \approx 6^\circ$, cannot be ruled out, though.

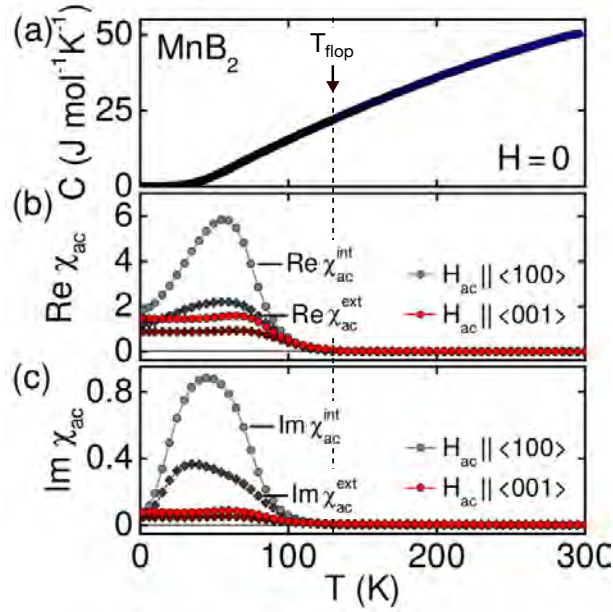


Figure 3.10: Specific heat and ac susceptibility of MnB₂. (a) Specific heat as a function of temperature. No anomalies are observed between 2 K and 300 K. (b) Real part of the ac susceptibility in zero field. A broad maximum appears at $T_{\text{flop}} \approx 130$ K. (c) Imaginary part of the ac susceptibility in zero field. At low temperatures significant dissipation occurs. Graph taken from Ref. [5].

3.4 Low-temperature Bulk Properties of MnB₂

In the following section the low-temperature bulk and transport properties of float-zoned single crystal MnB₂ will be reported. Measurements of the ac susceptibility and the uniform magnetization were carried out, addressing also the magnetic anisotropies in MnB₂. The study further comprises measurements of the specific heat, the resistivity, and the Hall effect.

3.4.1 Specific Heat

The specific heat C of single crystal MnB₂ has been measured by ANDREAS BAUER as part of his Ph.D. thesis [5]. Its temperature dependence is shown in Fig. 3.10a. With decreasing temperature C drops monotonically. The Sommerfeld coefficient was determined from the low-temperature limit of the electronic specific heat C/T and amounts to $\gamma = 3 \text{ mJ mol}^{-1} \text{ K}^2$. This value is characteristic of a metal with little to no electronic correlations. No anomalies are observed in the full temperature range studied suggesting the absence of a low-temperature phase transition. However, a smooth crossover between two similar magnetic structures cannot be ruled out on the basis of the specific heat data.

3.4.2 AC Susceptibility

The real and imaginary part of the ac susceptibility have been measured by ANDREAS BAUER as part of his Ph.D. thesis [5]. They are shown in Fig. 3.10b and Fig. 3.10c, respectively. With decreasing temperature both $\text{Re}(\chi)$ and $\text{Im}(\chi)$ increase slightly. Consistent with literature, a pronounced enhancement sets in at $T_{\text{flop}} \approx 130$ K.

It is well-known that anomalies in the ac susceptibility can be caused by magnetic impurities. For instance, in antiferromagnetic CuMnSb a ferrimagnetic impurity phase, Mn₂Sb, gives rise to a significant gain in $\chi(T)$ (cf. Sec. 4.3.1). It seems plausible that in a similar way the susceptibility enhancement in MnB₂ may originate from Mn-B-based impurity phases. However, an inspection of the neighboring metallurgical phases allows to rule out this assumption as they either exhibit a high magnetic ordering temperatures $T_c \gg T_{\text{flop}}$ or lack a net ferromagnetic magnetization.

- (i) MnB exhibits ferromagnetic order at 578 K [174].
- (ii) For MnB₄ first-principles calculations suggest one-dimensional metallic behavior and local-moment ferromagnetism [175]. Experimental investigations of tiny single crystals synthesized at high pressures and temperatures indicate ferromagnetic correlations but find no magnetic order down to 2 K [176]. A susceptibility enhancement near 100 K as well as the net ferromagnetic moment observed in Ref. [176] are probably extrinsic.
- (iii) Antiferromagnetic order with a complex temperature dependence is observed in Mn₃B₄. It displays collinear antiferromagnetism of its Mn(2c) atoms at 392 K. At 226 K also the Mn(4g) atoms take part in the ordering and a spin-spiral develops. As the temperature is further decreased, the original collinear antiferromagnetic structure is eventually recovered at about 120 K [177, 178]. In fact the latter transition coincides with a 20 % susceptibility gain, which however seems to occur only in phase-pure single crystal Mn₃B₄ and only if the ac field is applied along the orthorhombic *a*-axis [179]. Enhancements in the ac susceptibility have also been reported for Co- and Ni-doped Mn₃B₄, but only for doping concentrations $x > 4.5\%$ and $x > 6\%$, respectively [180, 181].

Therefore a Mn₃B₄ impurity phase cannot account for the observed susceptibility anomaly. First, x-ray diffraction shows no indication of significant amounts of Mn₃B₄. Second, even if the samples studied contained some Mn₃B₄ the associated susceptibility anomaly should be much smaller for two reasons. (i) A much smaller gain in χ was reported for Mn₃B₄. (ii) The latter was observed only along a specific axis, namely the orthorhombic *a*-axis. As any impurity phase will most likely exhibit a random crystallographic orientation, the susceptibility contribution of this phase should be even smaller. (iii) The use of high-purity elements during the growth of the MnB₂ crystals studied in this thesis rules out the presence of Co or Ni and consequently also of Co- or Ni-doped Mn₃B₄. (iv) The recovery of collinear antiferromagnetism in Mn₃B₄ is clearly inconsistent with the low-temperature

magnetization measurements reported in this thesis, which suggest a net ferromagnetic moment and ferromagnetic hysteresis.

Altogether our discussion suggests that the increase of the susceptibility below 130 K represents an intrinsic feature of MnB₂. In combination with the absence of anomalies in the temperature dependence of the specific heat the gain in χ may then be explained by a magnetic phase transition in antiferromagnetic MnB₂ which is either strongly broadened, e.g., due to geometrical frustration, or which releases only little entropy. Alternatively, the rise in the low-temperature ac susceptibility may be due to a smooth transformation of the long-range magnetic structure via a crossover. As reported in Sec. 3.3 neutron diffraction data rule out significant changes of the antiferromagnetic spin order of MnB₂ in the full temperature range studied. In particular no abrupt change of the ordered moment is observed near T_{flop} . Instead the diffraction experiments suggest that the ordered moment increases continuously as T is lowered, cf. Fig. 3.8. These data are also consistent with a slightly canted antiferromagnetic order developing gradually from the high-temperature collinear antiferromagnetic spin structure. In summary, neutron scattering hints at a smooth modification of the magnetic order via a crossover as the most likely explanation for the low-temperature gain of the ac susceptibility.

Turning finally to the anisotropy of the zero field ac susceptibility, χ is slightly larger if the driving ac field is applied along $\langle 100 \rangle$ rather than along $\langle 001 \rangle$. This finding contradicts the report of a soft c -axis given in Ref. [73]. It is however consistent with the magnetization measurements carried out as part of this thesis, where the slope dM/dH in small fields is larger for field along the a -axis. These data will be reported in Sec. 3.4.3.

3.4.3 Magnetization

Fig. 3.11 shows typical magnetization data of single crystal MnB₂ as a function of temperature and field. As expected for an antiferromagnetically ordered compound the absolute value of M is small for all temperatures and fields studied. With increasing field M grows monotonically. No saturation is observed even at the highest field and lowest temperatures studied. At 300 K the field dependence of the magnetization is linear and flat. As shown in Fig. 3.11c and Fig. 3.11d no ferromagnetic hysteresis is detected. When T is reduced $M(H)$ first develops a faint curvature at small fields which eventually turns into a distinct change of slope. For instance, at 3 K the magnetization as a function of field increases steeply below 10 mT and 40 mT for field applied along $\langle 100 \rangle$ and $\langle 001 \rangle$, respectively. Perhaps most importantly, below 150 K for both field directions a ferromagnetic hysteresis with an approximate coercivity of 5 mT is observed.

Turning to the magnetic anisotropy of MnB₂, data shown in Fig. 3.11e for a single temperature, 3 K, suggest that both M and dM/dH are larger for field applied along $\langle 100 \rangle$, i.e., the crystallographic a -axis. At the highest field and the lowest temperature studied the anisotropy of M thereby amounts to 14%. These findings are consistent with the susceptibility measurements

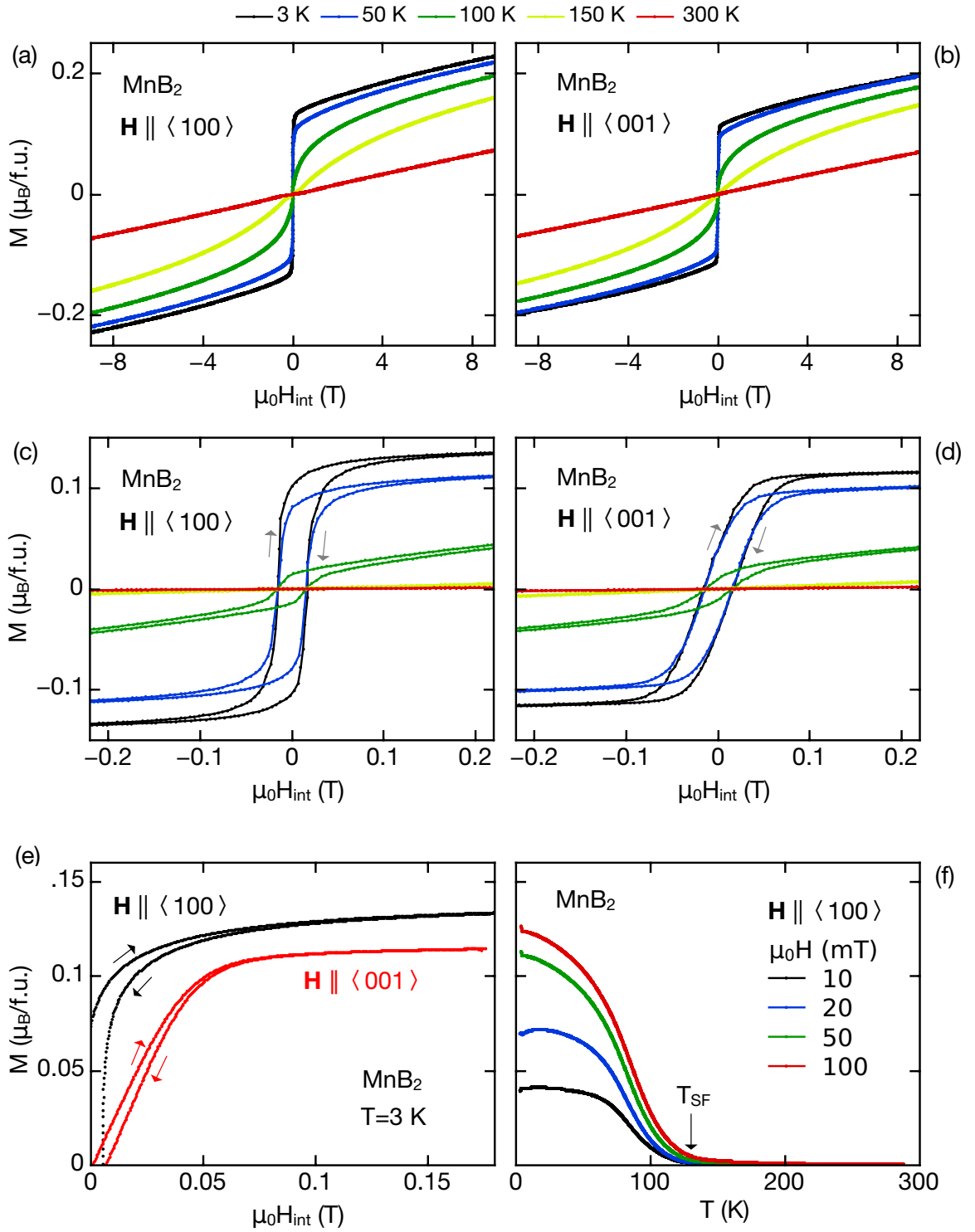


Figure 3.11: Magnetization of MnB₂ as a function of magnetic field and temperature. (a,b) Field dependence $M(H)$ for field applied along $\langle 100 \rangle$ and $\langle 001 \rangle$, respectively. (c,d) A zoom into the low field range reveals a ferromagnetic hysteresis for $T < 150$ K, consistent with the putative spin-flop transition at $T_{\text{flop}} \approx 130$ K. (e) Comparison of the field dependence $M(H)$ for field applied along $\langle 100 \rangle$ and $\langle 001 \rangle$ indicating a small easy-plane anisotropy. (f) Temperature dependence $M(T)$ for small fields applied along $\langle 100 \rangle$. For all measurements a strong enhancement of M at $T_{\text{flop}} \approx 130$ K is observed.

reported in Sec. 3.4.2 and the planar magnetic structure reported in Sec. 3.3 but disagree with the report of a soft c -axis of the magnetization given in Ref. [73].

The temperature dependence $M(T)$ for various small fields along $\langle 100 \rangle$ is shown in Fig. 3.11f. Consistent with what has been discussed above M is small at high temperatures. With decreasing temperature a pronounced enhancement sets in near $T_{\text{flop}} \approx 130$ K. This agrees nicely with the ac susceptibility which exhibits a strong increase of both $\text{Re}\{\chi\}$ and $\text{Im}\{\chi\}$ at the same temperature.

It is interesting to discuss the magnetization data presented above in view of the magnetic structure of MnB₂. As reported in Sec. 3.3 the latter may be understood in terms of an antiferromagnetic arrangement of in-plane Mn moments. The observation of a ferromagnetic hysteresis and an increasing magnetic moment at low temperatures is clearly incompatible with collinear antiferromagnetism. But the effective moment determined from the magnetization data is still much smaller than the ordered moment of $\sim 2 \mu_B$ inferred from neutron diffraction, hence ruling out significant deviations from the antiferromagnetic order. The magnetization data may be explained, however, by a spin-flop transition at $T_{\text{flop}} \approx 130$ K, where the small ferromagnetic net moment observed results from a slight canting of the Mn moments out of the hexagonal planes.

3.4.4 Electrical Resistivity and Hall Effect

To the best of our knowledge, previous studies of the resistivity of MnB₂ have relied exclusively on polycrystalline material. No measurements of the Hall effect have been reported so far. In the investigations of the electrical transport properties of MnB₂ carried out as part of this thesis single crystal material has been examined. All measurements were carried out using the same thin rectangular sample with the excitation current applied along the long and field applied along the short edge, corresponding to $\langle 100 \rangle$ and $\langle 110 \rangle$, respectively.

Fig. 3.12a shows the resistivity of single crystal MnB₂ as function of temperature. With decreasing temperature ρ drops monotonically thereby exhibiting an almost constant slope. As for the specific heat no anomalies occur in the full temperature range studied. In contrast to the report by KASAYA and HIHARA no kink is observed near the putative spin-canting transition T_{flop} [73]. The absolute values of the resistivity are characteristic of a good metal. Discrepancies with the numbers given in Ref. [73] are probably due to differences in the sample qualities as a polycrystalline specimen was examined Ref. [73]. From the room temperature resistivity, $51.8 \mu\Omega \text{ cm}$, and the low-temperature limit $\rho_0 = 9.25 \mu\Omega \text{ cm}$ the ratio $\text{RRR} = 5.6$ can be calculated, indicating a good crystalline quality.

The field dependence of the resistivity shown in Fig. 3.12b supports a longitudinal magnetoresistance $\Delta\rho_B = \rho(B > 0)/\rho(B = 0)$ which is small and negative at high temperature. With increasing temperature $\Delta\rho_B$ gets more pronounced and eventually becomes positive. Thus at 4 K, the lowest temperature studied, a marked difference of $\rho(B = 14 \text{ T})$ and $\rho(B = 0)$ of about

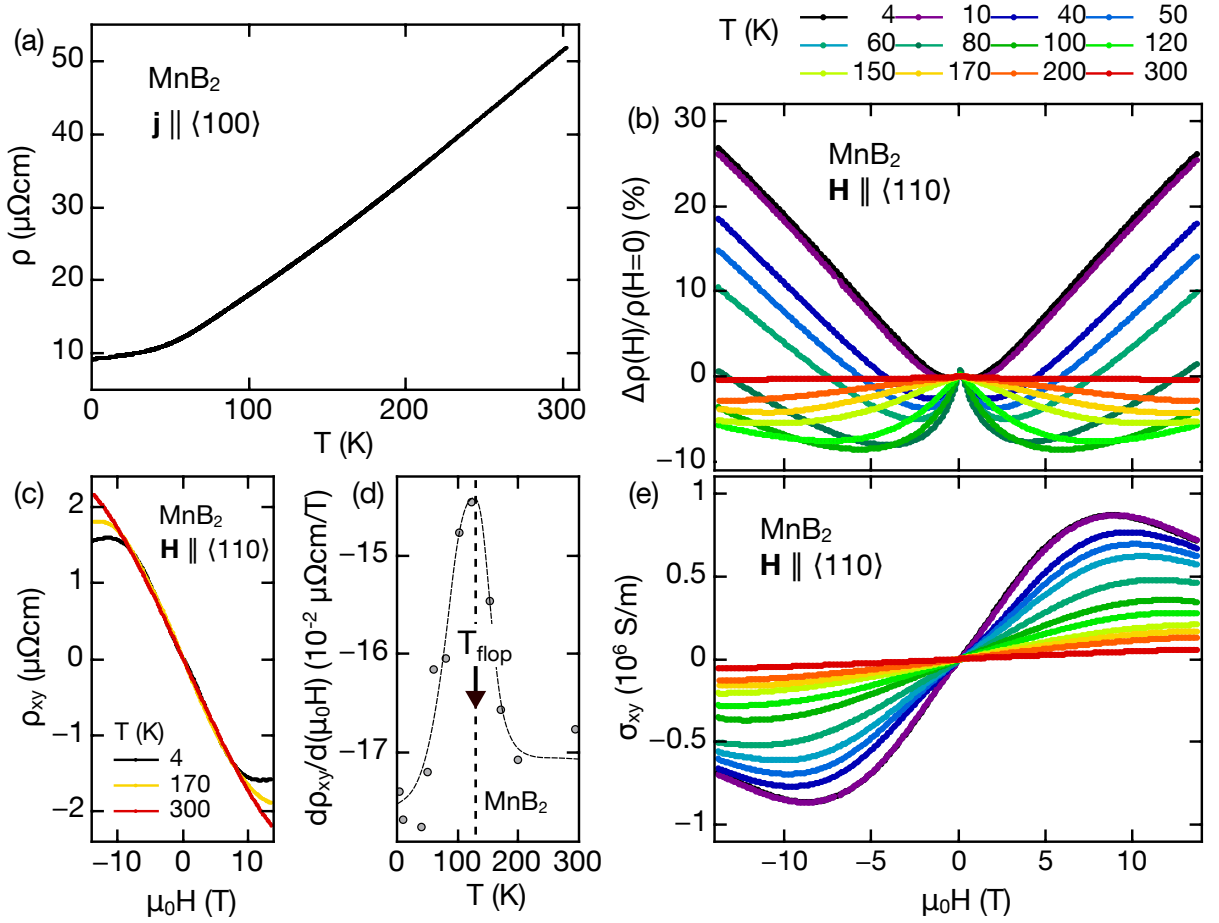


Figure 3.12: Electrical resistivity of MnB₂. For all measurements the excitation current and magnetic field were applied along $\langle 100 \rangle$ and $\langle 110 \rangle$, respectively. (a) Temperature dependence $\rho(T)$ at zero field. No anomalies are observed between 0.2 K to 300 K. (b) Magnetoresistance $\Delta\rho_H$ between 4 K and 300 K. (c) The Hall resistivity ρ_{xy} exhibits a linear field dependence over almost the whole field range studied. At high fields, $\mu_0 H > 9$ T, its slope $d\rho_{xy}/d(\mu_0 H)$ is strongly reduced. (d) Slope $d\rho_{xy}/d(\mu_0 H)$ as deduced from linear fits of the Hall resistivity at small fields, $-5 \text{ T} \leq \mu_0 H \leq 5 \text{ T}$. Its overall small variation displays a maximum near $T_{\text{flop}} \approx 130$ K. The solid line is a guide to the eye. (e) Hall conductivity σ_{xy} between 4 K and 300 K.

25 % is observed.

The Hall resistivity ρ_{xy} is shown in Fig. 3.12c as a function of field. It exhibits a constant negative slope in almost the full field range studied. Only at high field, $B > 9$ T, slight deviations from linearity occur which get more pronounced as T is lowered. Assuming a simple single-band model, the negative slope of the Hall resistivity is consistent with hole conduction. Fig. 3.12d shows $d\rho_{xy}/dB$ as a function of temperature. The data were obtained by fitting ρ_{xy} in the low-field region where its field dependence is linear. A faint maximum is centered around $T_{\text{flop}} \approx 130$ K suggesting the presence of a tiny anomalous Hall contribution which may arise

from the canting of the spin structure. Finally, our measurements allow to determine the Hall conductivity σ_{xy} . As shown in Fig. 3.12e σ_{xy} as a function of field is small at high temperature. With decreasing temperature the Hall conductivity increases gradually and exhibits a broad maximum around 9 T.

3.5 Summary

In summary, a comprehensive study of the bulk, transport, and structural properties of float-zoned single crystal MnB₂ has been carried out as part of this thesis. The x-ray and neutron data confirm the previously reported metastable C32 crystal structure in a temperature range covering four orders of magnitude, namely between ~ 1130 K and cryogenic temperatures. No indications of ReB₂-type MnB₂ are found. Investigations of the diffuse scattering in the $(hk0)$ scattering plane reveal strong nuclear coherent scattering which is, again, fully explained by the C32 nuclear lattice. In contrast to isostructural CrB₂ which exhibits distinct streaks of nuclear diffuse scattering in the $(hk0)$ reciprocal space plane, in MnB₂ no nuclear diffuse scattering is detected. No magnetic diffuse scattering is observed either, suggesting that magnetic frustration, if present at all, may play a minor role in this compound.

The magnetic structure of MnB₂ has been studied by means of powder and single crystal neutron diffraction. These investigations identify MnB₂ as antiferromagnet with high Néel temperature, $T_N \approx 1130$ K. Consistent with previous reports the spin structure of this compound may be understood in terms of ferromagnetic Mn sheets which mutually couple antiferromagnetically. It is characterized by collinear Mn moments of about $2.76 \mu_B/\text{Mn}$ that are essentially confined to the hexagonal planes, i.e., their out-of-plane component is negligible. At low temperatures the diffraction data are explained satisfactorily by the same collinear antiferromagnetic structure which, however, cannot account for the net ferromagnetic moment and ferromagnetic hysteresis observed in the magnetization measurements in the temperature range $T < T_{\text{flop}} \approx 130$ K. The latter may be explained in terms of a canted antiferromagnet developing below T_{flop} , which is not ruled out by our scattering data. The canted antiferromagnet is characterized by a finite out-of-plane component of \mathbf{m} hence giving rise to a net ferromagnetic moment. The transformation from the collinear to the canted structure happens gradually as may be seen, e.g., from the smooth increase of the ordered moment \mathbf{m} upon cooling, notably near T_{flop} . The large size of \mathbf{m} and its temperature dependence suggest that the magnetism in MnB₂ arises from localized Mn moments.

Local-moment magnetism is also supported by the low-temperature bulk and transport measurements. The temperature dependence of the specific heat shows no indications of a low-temperature phase transition, consistent with the assumption of a $T_N \approx 1130$ K high-temperature antiferromagnetic order which is essentially unchanged down to the lowest temperatures studied. The low-temperature limit of the electronic specific heat suggests weak electronic correlations.

The monotonic temperature dependence of the specific heat is contrasted by measurements of the ac susceptibility which show a strong enhancement for $T < T_{\text{flop}} \approx 130$ K. In combination with the absence of anomalies in the specific heat the pronounced gain in χ may be interpreted in terms of the above-mentioned smooth transformation of the magnetic structure from a collinear to a canted antiferromagnetic spin order, where the latter develops a small ferromagnetic net moment. A spin-canted antiferromagnetic state is consistently supported by our low-temperature magnetization measurements. For $T < T_{\text{flop}}$ the latter reveal a significant increase and a ferromagnetic hysteresis in the temperature dependence $M(T)$ and field dependence $M(H)$, respectively.

Resistivity measurements establish the good metallic conductivity of MnB_2 . As for the specific heat no anomalies are observed in the full temperature range studied. As a function of magnetic field, the Hall resistivity exhibits a negative slope hence suggesting holes as the dominant charge carriers. A faint local maximum is observed near T_{flop} in the field-dependence of the Hall resistivity. It may be interpreted as a weak anomalous Hall contribution arising from the small net ferromagnetic moment of the canted spin structure.

Along with the findings on CrB_2 , cf. Sec. 2, our investigation of MnB_2 suggests that by adding of one electron the weak $T_{\text{N}} = 89$ K itinerant antiferromagnet CrB_2 is transformed into the high-temperature $T_{\text{N}} \approx 1130$ K local-moment antiferromagnet MnB_2 . This illustrates the great potential of the hexagonal transition metal diborides to serve as a playground for exploring and tuning a variety of physical properties within a common crystalline environment.

4.1 Introduction to Heusler Compounds

The material class of the so-called Heusler compounds is formed by a group of intermetallics which share a generic chemical composition and crystal structure. According to these criteria two sub-classes are distinguished. Full-Heuslers form with the constitutional formula X_2YZ and crystallize in the $L2_1$ structure with space group $Fm\bar{3}m$. This structure can be described as four interpenetrating face-centered cubic (fcc) lattices that are shifted by a quarter of a room diagonal with respect to each other. Half-Heuslers have an empirical constitutional formula XYZ which may be denoted as $(XY)X'Z$ for quaternary compounds, where different elements may occupy the X and X' sites. They share the $C1_b$ structure with space group $F\bar{4}3m$. Compared to the full-Heusler structure one of the four fcc sublattices is not occupied. As a consequence the half-Heusler structure lacks inversion symmetry. For both sub-classes X , Y , and Z atoms may be selected from an extremely wide range of elements including, amongst others, transition metals and post-transition metals. Consequently, an enormous variety of compounds and a cornucopia of physical properties may be realized. Not surprisingly, Heusler compounds are therefore intensively studied in different research areas.

Despite their common nuclear structure Heuslers exhibit a variety of different physical properties which makes them promising candidates for future technical applications. For instance, future spintronic devices require magnetic metals with high spin polarization at the Fermi level. This requirement could be met by half-metallic Heusler compounds which have been predicted in the 1980ies and which could allow for the construction of fully integrated all-Heusler-devices. In this area half-metallic antiferromagnets are even more desirable as they do not give rise to stray fields and are less sensitive to magnetic fields. Half-metallic materials are metallic for one spin

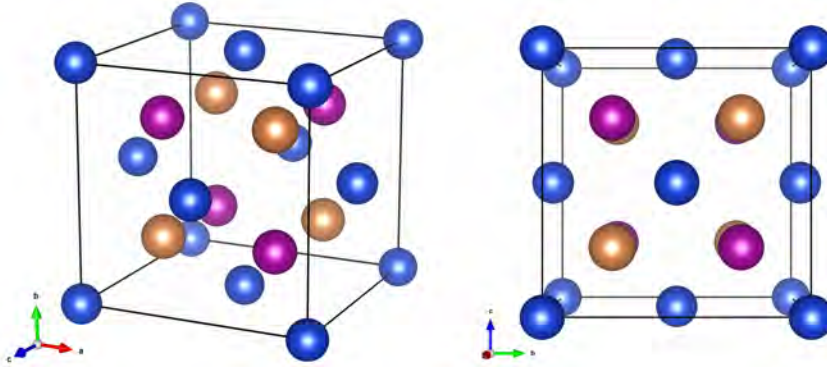


Figure 4.1: Schematic depiction of the half-Heusler $C1_b$ structure of CuMnSb. The cubic unit cell is indicated by black lines and contains no center of inversion. Cu, Mn, and Sb atoms are colored blue, brown, and purple, respectively.

polarization but semiconducting for the other and hence exhibit a complete spin polarization at the Fermi level. Itinerant ferromagnetism as observed, e.g., in NiMnSb, is quite obviously compatible with a half-metallic electronic density of states. Here, the majority charge carriers have a high density of states at the Fermi level while E_F is located in a gap of the minority charge carrier's band structure. Thus the majority band remains metallic while the minority band is semiconducting resulting in a full spin polarization. In contrast the full spin polarization which is a key characteristic of the half-metallicity seems to rule out half-metallic *antiferromagnetism* at first sight. In fact half-metallic antiferromagnets may still be accomplished as delicately balanced ferrimagnets where multiple bands contribute to the majority density of states at the Fermi surface. Thus the magnetic moments corresponding to different bands may cancel out while leading to a full spin polarization at E_F .

CuMnSb is one of few antiferromagnetic metals crystallizing in the half-Heusler structure. It is an interesting material for the following reasons. (i) The nature of the antiferromagnetic order exhibiting hallmarks of both local-moment and itinerant electron magnetism, (ii) the lack of inversion symmetry, which potentially permits the formation of complex magnetic structures due to the Dzyaloshinskii-Moriya interaction, (iii) the comparatively low Néel temperature, and (iv) its chemical and structural proximity to half-Heusler metallic ferromagnets with high ordering temperatures, e.g., NiMnSb, also suggesting the importance of spin fluctuations. Closer examination of the antiferromagnetic order in CuMnSb may hence support the design of antiferromagnetic Heuslers for future applications. Perhaps even more important, it might provide new insights into the physics of other materials with strong antiferromagnetic spin fluctuations and pave the way to a more fundamental understanding of local-moment and itinerant magnetism and their mutual interplay.

4.2 Introduction to CuMnSb

CuMnSb was reported to crystallize in the half-Heusler $C1_b$ structure, space group $F\bar{4}3m$ (#216), with a lattice constant $a = 6.07(2)$ Å consistently by several authors [6, 182, 183]. Even though CASTELLIZ realized already in 1952 [182] that the macroscopic magnetization of ferromagnetic NiMnSb was continuously reduced when Cu was doped on the Ni site it took more than ten more years until ENDO and coworkers identified CuMnSb as perhaps the first antiferromagnetic Heusler compound. From their ac susceptibility measurements ENDO ET AL. inferred a moderate Néel temperature, $T_N = 55$ K, a moderate negative Curie-Weiss temperature, $\Theta_{CW} \approx -160$ K, as well as a large fluctuating moment $m_{\text{eff}} = 5.6 \mu_B/\text{Mn}$ [6, 7]. Varying values of the Néel temperature (50 K, 62 K), Curie-Weiss temperature (-250 K, -120 K), and the effective fluctuating moment ($6.3 \mu_B/\text{Mn}$, $5.2 \mu_B/\text{Mn}$) were further reported by BŒUF and HELMHOLDT, respectively [8, 184, 185]. The large scatter of T_N , Θ_{CW} , and m_{eff} may be due to slightly varying chemical compositions of the samples studied.

In any case, the large negative Curie-Weiss temperatures confirmed by all authors suggest strong antiferromagnetic interactions. As summarized below this is consistent with the antiferromagnetic long-range magnetic ordering observed in neutron scattering [186]. Strong magnetic fluctuations are suggested by the relatively large coefficient of the temperature dependence of the resistivity, $A = 0.053 \mu\Omega \text{ cm K}^{-2}$, and a Sommerfeld coefficient of the specific heat, $\gamma = 17 \text{ mJ mol}^{-1} \text{ K}^2$ [8, 184, 187] which is typical for transition metal compounds and suggests a moderate mass enhancement of the charge carriers. The latter is also consistent with theoretical work by JEONG ET AL. who find a large enhancement of the dynamic thermal mass $m^*/m \approx 4.2$ due to spin fluctuations [188]. Moreover, inelastic neutron scattering of single crystal CuMnSb carried out by GEORG BRANDL as part of his Ph.D. thesis revealed an abundance of heavily damped magnetic fluctuations at temperatures even far above T_N which are gapped by $\Delta E \approx 2.5 \text{ meV}$ below T_N [99].

Measurements of the resistivity, magnetization, and specific heat reveal consistently a pronounced independence of the magnetic ordering temperature on magnetic fields [8, 184, 189, 190]. Strong spin fluctuations, a large fluctuating effective moment, and most importantly a very small dependence of T_N of magnetic fields are widely considered as hallmarks of itinerant magnetism. On the other hand CuMnSb exhibits also features which are commonly attributed to local magnetism, notably an almost integer ordered moment, $m_s = 3.9 \mu_B/\text{Mn}$, and a commensurate spin order [186] as well as a large (yet unsaturated) magnetization at high magnetic fields [189].

Half-metallicity of CuMnSb is suggested by the almost integer ordered moment and the recovery of ferromagnetism by doping of only a few percent of Ni or Pd on the Cu site [7, 190, 191]. The latter is expected for a half-metallic antiferromagnet as it is actually a thoroughly balanced ferrimagnet. Ab-initio calculations, however, suggest that CuMnSb is a semi-metal (not to be confused with a half-metal), where the Mn atoms are chemically isolated and magnetically

coupled via an indirect exchange interaction. The latter is mediated through heavy conduction electrons and light valence band holes which may account at least to some degree for the peculiar combination of features characteristic of itinerant and local-moment magnetism [188]. The pressure dependence of the long-range magnetic order in CuMnSb has been studied by BŒUF who reported a slight increase of T_N upon the application of pressure, $dT_N/dp \approx 4.1 \text{ K GPa}^{-1}$, in good agreement with the Ehrenfest prediction ($dT_N/dp \approx 5 \text{ K GPa}^{-1}$).

The ratio $f = -\Theta_{CW}/T_N \approx 3$ suggests that geometric frustration may play a role in CuMnSb. In fact, frustration in this cubic metal compound may arise from disorder, notably from point defects such as anti-site disorder or interstitial atoms. In previous studies, the presence of a significant degree of disorder was also supported by a relatively high residual resistivity $\rho_0 \approx 50 \mu\Omega \text{ cm}$ and large residual resistivity ratios, $\text{RRR} \approx 4$ [8, 184, 192–194]. Moreover, the importance of atomic disorder in CuMnSb is suggested by a large high-temperature volume collapse $\Delta V/V \approx 1.5\%$ observed at about 740 K [195]. The latter may be understood in terms of an order-disorder transition where atoms randomly populate the fourth fcc sublattice of the $C1_b$ structure at $T > 740 \text{ K}$ (which is vacant at $T < 740 \text{ K}$). Finally, as pointed out later by MÁCA ET AL., magnetic frustration may originate from the antiferromagnetic spin arrangement [196].

The magnetic structure of CuMnSb has first been studied by FORSTER ET AL. by means of powder neutron diffraction [186]. Magnetic Bragg reflections appearing at cryogenic temperatures can be indexed using the k-vector $0.5\tau_{111}$, where $\tau_{111} = 2\pi\sqrt{3}/a$, and may be attributed to the formation of a type-II long-range antiferromagnetic order. In this spin arrangement the magnetic cell is doubled with respect to the nuclear cell along all three crystal axes. Because neighboring ferromagnetic (111) sheets are coupled antiferromagnetically the structure is sometimes also termed AFM(111) [197]. In the notion of magnetic space groups the structure may be referred to as R[I]3c. A schematic drawing of the structure is shown in Fig. 4.10a. From the fact that the magnetic structure factor F_{111} was found to vanish it was concluded that within the (111) sheets the magnetic moment points along a $\langle 111 \rangle$ direction. Both the antiferromagnetic order and the experimentally observed ordered moment, $m_s = 3.9 \pm 0.1 \mu_B/\text{Mn}$ are supported by ab-initio calculations [188].

The observation of collinear antiferromagnetism is somewhat surprising as in materials lacking inversion symmetry, such as CuMnSb, the antisymmetric (Dzyaloshinskii-Moriya) exchange interaction favors a canting of the magnetic moments. Hence one might expect deviations from a perfectly collinear spin alignment. In fact, MÁCA ET AL. argued that the AFM(111) structure is *not* the magnetic ground state of *pure* CuMnSb. It may be stabilized however due to crystalline disorder. For instance, Cu-Mn anti-sites at small concentrations of a few percent should already be sufficient to favor the AFM(111) ordering [197]. The presence of anti-site disorder is consistent with the relatively large residual resistivity of about $50 \mu\Omega \text{ cm}$ reported in the literature. The pronounced sensitivity of the physical properties on defects and disorder is a common phenomenon in Heusler compounds, resulting in modified or even drastically altered

physical properties as compared to the expectations for the perfectly ordered host material [198–201]. Unraveling this intimate connection, in turn, seems to be essential for both technological applications and the fundamental understanding of the underlying physics.

The properties of CuMnSb as reported so far raise the following questions: As essentially all previous studies were carried out on polycrystalline CuMnSb no account on the effects of geometric frustration, crystalline anisotropies, or magnetic anisotropies was given yet. In addition, the crystalline quality and composition of the polycrystalline material studied to date differs strongly. This is seen most clearly from the large scatter in important material parameters reported. For instance, the Néel temperature, fluctuating moment, and Curie-Weiss temperature given in different studies vary significantly. As part of this thesis, these issues have been addressed for the first time by investigating high-quality single crystal CuMnSb.

Single crystal growth was carried out by ANDREAS BAUER as part of his Ph.D. thesis, resulting in two single crystal ingots referred to as CuMnSb-A and CuMnSb-B, cf. Sec. 1.1.3. While CuMnSb-A was synthesized from a stoichiometric mixture of starting elements CuMnSb-B was grown from a mixture that contained 3.5% Sb excess. From powder x-ray diffraction and ac susceptibility measurements it was concluded that CuMnSb-A contained a small volume fraction of a ferrimagnetic impurity phase, $< 1\%$ Mn_2Sb , whereas CuMnSb-B was phase-pure [5]. The suppression of the Mn_2Sb impurity phase in the second crystal suggested that CuMnSb-B displays the intrinsic physical properties of this semi-Heusler compound. A comparison of the low-temperature bulk and transport properties of samples prepared from both crystals reveals, in fact, distinct differences which will be reported below.

The main results of the low-temperature ac susceptibility and heat capacity measurements reported in Ref. [5] will be summarized (Sec. 4.3.1 and Sec. 4.3.2). Following this, the measurements of the magnetization (Sec. 4.3.3), resistivity, and Hall effect (Sec. 4.3.4) which have been carried out as part of this thesis are reported. All low-temperature bulk and transport measurements suggest antiferromagnetic order developing below $T_N = 55\text{ K}$ and $T_N = 49\text{ K}$ for CuMnSb-A and CuMnSb-B, respectively. Magnetic anisotropies are small as expected for a cubic compound. The relatively large ratio of the Curie-Weiss and the Néel temperature, $f = -\Theta_{\text{CW}}/T_N \approx 3$ suggests moderate geometric frustration. Further, all data demonstrate a remarkable lack of field-dependence of the Néel temperature. This is widely considered as a characteristic of itinerant magnetism. Perhaps most importantly, for CuMnSb-B signatures of a second phase transition at $T^* \approx 35\text{ K}$ were observed consistently in all low-temperature measurements. In contrast no indications of a second transition were detected for CuMnSb-A. The observation of a second phase transition suggests that the long-range magnetic order in CuMnSb-B may differ from the magnetic ordering of CuMnSb-A as well as the type-II antiferromagnetism proposed for CuMnSb in general.

This issues will be addressed in the final sections of this chapter where the nuclear (Sec. 4.4) and magnetic (Sec. 4.5) structure of CuMnSb-A and CuMnSb-B are reported. For our study

powder x-ray diffraction, powder neutron diffraction, and single crystal neutron diffraction were used. The diffraction data imply that both CuMnSb-A and CuMnSb-B crystallize in the same $C1_b$ half-Heusler structure. Elastic polarized neutron scattering of CuMnSb-B was employed to check for putative defect structures and magnetic frustration which may both give rise to diffuse scattering. While the Bragg scattering observed in these measurements is consistent with the nuclear and magnetic structure inferred from single crystal unpolarized neutron diffraction there were no indications of diffuse scattering. This demonstrates that in CuMnSb-B defect structure formation and geometric frustration, if present at all, play only a minor role. Large ordered moments were observed for both single crystal ingots studied. They are almost identical with the effective fluctuating moment, suggesting together a local-moment character of the antiferromagnetic order. However, CuMnSb-A and CuMnSb-B develop slightly different magnetic structures. While CuMnSb-A exhibits the type-II antiferromagnetic order which has been reported in the literature, CuMnSb-B undergoes an additional spin reorientation transition at $T^* \approx 35$ K. More precisely, at $T < T^*$ the magnetic moments in CuMnSb-B are no longer aligned along the crystallographic $\langle 111 \rangle$ direction but are tilted out of that direction by a small angle $\alpha \approx 11^\circ$. Even though the magnetic structure below T^* does not correspond to a structure predicted by M \acute{A} CA our measurements suggest that the magnetic ground state of *phase-pure* CuMnSb actually differs from the hitherto accepted type-II antiferromagnetic spin arrangement.

4.3 Low-temperature Bulk and Transport Properties of CuMnSb

4.3.1 AC Susceptibility

Measurements of the zero field ac susceptibility of CuMnSb-A and CuMnSb-B were carried out by ANDREAS BAUER as part of his Ph.D. thesis [5]. Consistent with the above-mentioned metallurgical characterization (Sec. 1.1.3) they suggest the presence of a small volume fraction of the ferrimagnetic Mn_2Sb impurity phase in CuMnSb-A and, in contrast, the phase purity of CuMnSb-B. The presence of the Mn_2Sb contamination in CuMnSb-A leads to the emergence of a broad maximum of the ac susceptibility at about 240 K. At that temperature the magnetic anisotropy of Mn_2Sb changes from an easy c -axis at high T to an easy basal plane at low T giving rise to a strongly enhanced susceptibility. No such enhancement is observed in CuMnSb-B hence suggesting its phase purity.

4.3.2 Specific Heat

Measurements of the specific heat of CuMnSb-A and CuMnSb-B have been carried out by ANDREAS BAUER as part of his Ph.D. thesis [5]. Typical data are shown in Fig. 4.2 and may be summarized as follows. As a clear hallmark of a second order phase transition both CuMnSb-A and CuMnSb-B display a pronounced lambda anomaly at $T_N = 55$ K and $T_N = 49$ K, respectively. T_N does not shift by more than ~ 0.5 K in magnetic fields up to 14 T.

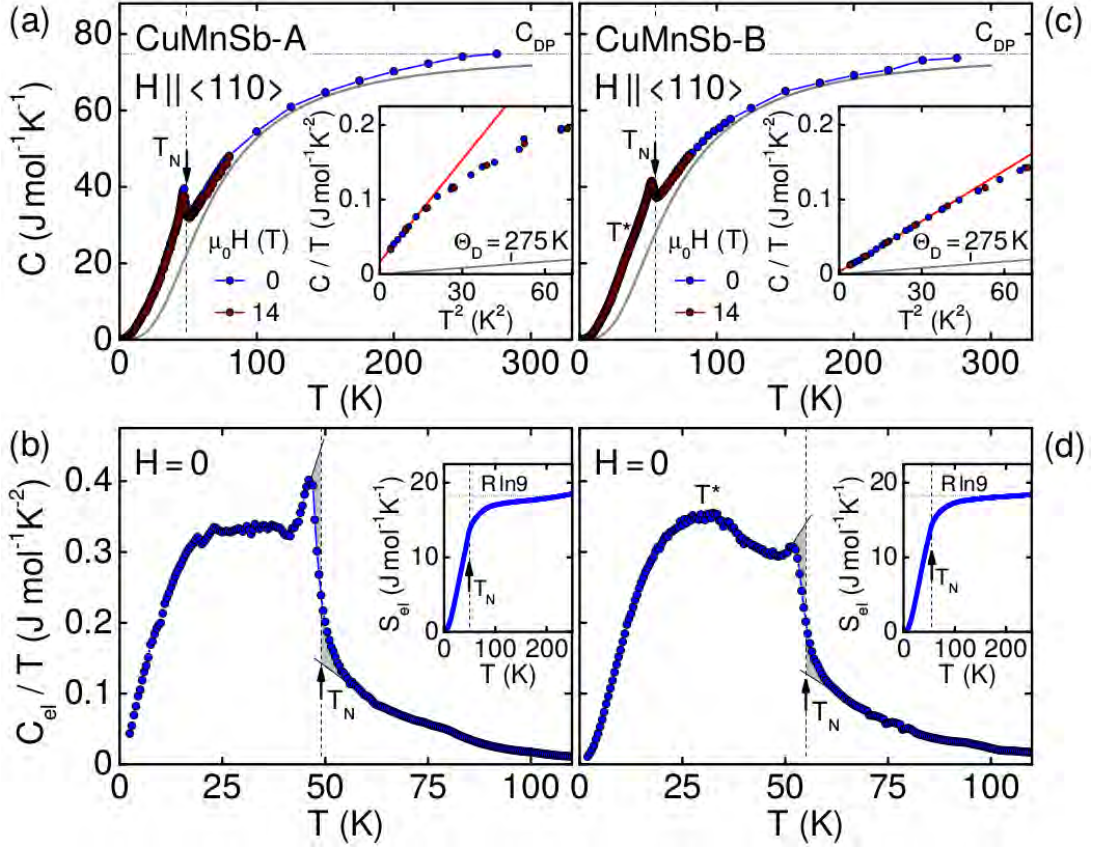


Figure 4.2: Specific heat of CuMnSb as a function of temperature. (a) Specific heat of CuMnSb-A. A pronounced lambda anomaly is present at $T_N = 49$ K. Its position is essentially unchanged up to 14 T, the highest field studied. The high-temperature Dulong-Petit limit extrapolates to $9R = 74.83 \text{ J mol}^{-1} \text{ K}$. The phonon contribution may be fitted using a Debye model (solid gray lines) with $\Theta_D = 275$ K (b) Electronic contribution to the specific heat divided by temperature. C_{el} exhibits a steep increase and a maximum near T_N as well as a broad plateau from 25 K to 40 K. Its numerical integration yields the entropy S which extrapolates to $R \ln 9$, corresponding to $J = 4 \mu_B$ magnetic moments. (c) Specific heat of CuMnSb-B showing the same salient features as CuMnSb-A, however with a slightly higher Néel temperature $T_N = 55$ K. (d) Electronic specific heat of CuMnSb-B divided by temperature. Besides the steep increase and local maximum near T_N a broad maximum around $T^* = 30$ K occurs. Graphs taken from Ref. [5].

The lack of field-dependence of the ordering temperature is widely accepted as a hallmark of itinerant magnetism. The Sommerfeld coefficients of both ingots differ strongly. For CuMnSb-A $\gamma_0 = 15.4 \text{ mJ mol}^{-1} \text{ K}^2$, which is typical for d -electron systems with moderate or strong electronic correlations. This is also consistent with earlier measurements of polycrystalline samples. The Sommerfeld coefficient of CuMnSb-B is significantly smaller, $\gamma_0 = 3.2 \text{ mJ mol}^{-1} \text{ K}^2$, suggesting weak electronic correlations. The discrepancy in γ_0 is not reflected in any other physical property

and its origin is still not clear. For both CuMnSb-A and CuMnSb-B the high-temperature phonon contribution to the specific heat can be approximated by a Debye model with $\Theta_D = 275$ K and a Dulong-Petit limit of $9R = 74.8 \text{ J mol}^{-1} \text{ K}$, where R is the universal gas constant. The electronic contribution to the specific heat C_{el}/T is finite even far above T_N , suggesting the presence of strong magnetic fluctuations at high temperatures. Moreover, C_{el}/T exhibits a broad plateau around $T^* \approx 30$ K for CuMnSb-A and a clear maximum for CuMnSb-B.

Powder and single crystal neutron diffraction carried out as part of this thesis suggest that the latter two features result from a reorientation of the magnetic moments in antiferromagnetic CuMnSb. As will be reported in Sec. 4.5 in CuMnSb-B the spin reorientation has been observed directly by neutron diffraction. In contrast, in CuMnSb-A no evidence of a spin reorientation has been observed so far. Keeping in mind the plateau-like temperature dependence of the electronic specific heat around $T^* \approx 30$ K the spin reorientation in CuMnSb-A may be incipient.

4.3.3 Magnetization

Fig. 4.3 shows the uniform magnetization of single crystal CuMnSb-A and CuMnSb-B as a function of temperature and for field applied along the $\langle 100 \rangle$ direction. The account of the magnetization data begins with the results for CuMnSb-A, i.e., single crystal CuMnSb as grown from a stoichiometric mixture of the starting elements. As expected for an antiferromagnet M is small for all fields and temperatures studied. As shown in Fig. 4.3a M increases slightly with decreasing temperature and passes through a distinct maximum at $T_N = 51.5$ K. This value is in good agreement with the Néel temperature reported by BŒUF [184]. For $T < T_N$ the magnetization decreases monotonically. In particular no Curie tail is observed down to the lowest temperatures studied suggesting the absence of ferromagnetic impurities. By comparing M for the different values of H an almost linear field dependence is found.

Hence, despite the pronounced field dependence, the magnetization data may be plotted in a compact and clear way when considering the normalized magnetization M/H , which also serves as an estimate for the magnetic susceptibility, $\chi = dM/dH$. As shown in Fig. 4.3b the absolute value of M/H is slightly suppressed with increasing magnetic field. Moreover, M/H exhibits a qualitatively different behavior at $T > T_N$ in small and high magnetic fields: At high fields, $\mu_0 H \geq 6$ T, M/H increases monotonically as T is lowered. In contrast, for $\mu_0 H = 1$ T and $\mu_0 H = 3$ T a clear maximum and a cusp are observed, respectively, around $T \approx 150$ K. Both features are presumably attributed to a ferrimagnetic impurity phase, Mn_2Sb , which changes its magnetic anisotropy from an easy c -axis to an easy basal plane at $T = 240$ K. Our data suggest that the associated magnetic fluctuations get quenched in a sufficiently high magnetic field $\mu_0 H > 3$ T and, in lower fields, freeze out below $T \approx 100$ K. As summarized in Sec. 1.1.3 the presence of a small volume fraction ($\leq 1\%$) of Mn_2Sb in CuMnSb-A has been confirmed by means of powder x-ray diffraction and ac susceptibility measurements [5].

Fig. 4.3c shows the inverse normalized magnetization H/M as a function of temperature. At

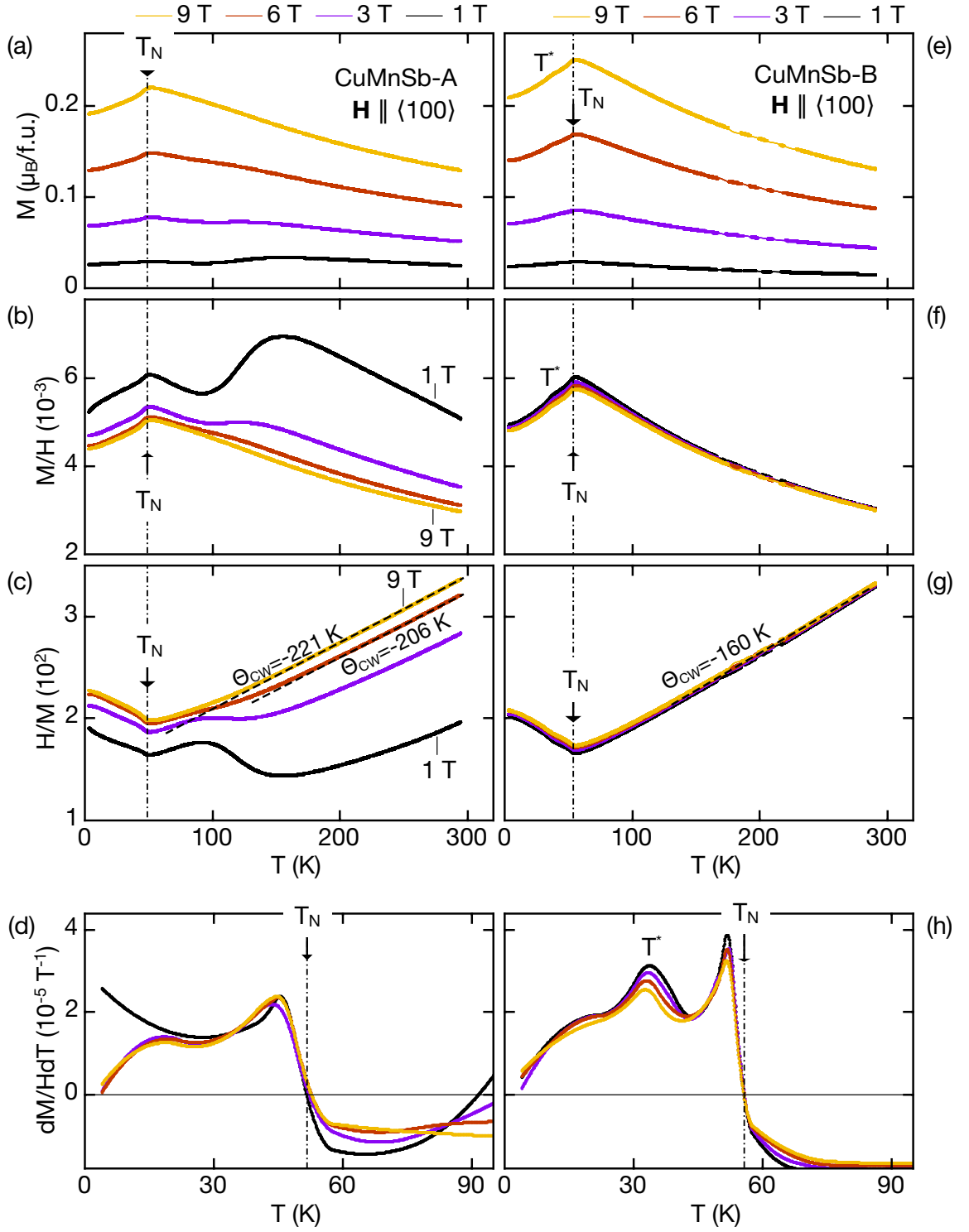


Figure 4.3: Uniform magnetization M , normalized magnetization M/H , inverse normalized magnetization H/M , and temperature derivative of the normalized magnetization, $dM/(HdT)$, each for CuMnSb-A (left column) and CuMnSb-B (right column). The magnetic field was applied along the $\langle 100 \rangle$ direction. Missing data points for CuMnSb-B at about 200 K are due to temperature instabilities that occurred during the measurement.

high magnetic fields, where the Mn₂Sb impurity signal is suppressed, H/M follows a Curie-Weiss behavior with a fluctuating effective moment of $m_{\text{eff}} = 3.4 \mu_{\text{B}}/\text{f.u.}$ and a negative Curie-Weiss temperature $\Theta_{\text{CW}} \approx -215(10)$ K, implying antiferromagnetic correlations.

Magnetization measurements of polycrystalline CuMnSb which, like the single crystal CuMnSb-A, was prepared from a stoichiometric initial composition were reported by BœUF [184]. A comparison of the results obtained from the magnetization measurements carried out as part of this thesis with the values reported in the latter study, $\Theta_{\text{CW}} \approx -250(10)$ K and $m_{\text{eff}} = 5.6 \mu_{\text{B}}/\text{f.u.}$, shows that for single crystal CuMnSb-A both the Curie-Weiss temperature and the fluctuating moment are smaller. Still m_{eff} is large when compared with typical itinerant antiferromagnets, for instance, CrB₂ (cf. Sec. 2) and only slightly smaller than the ordered moment of $m_{\text{s}} \approx 3.8 \mu_{\text{B}}/\text{f.u.}$ which, for CuMnSb-B, is deduced from neutron diffraction measurements (cf. Sec. 4.5). Together with the almost integer value of m_{s} this observation suggests a local-moment character of the antiferromagnetism in CuMnSb, in contrast to the weak field dependence of T_{N} which suggests itinerant magnetism.

The ratio $f = -\Theta_{\text{CW}}/T_{\text{N}} \approx 4$ hints at the possibility of moderate geometric frustration [127]. Despite the cubic structure geometric frustration can be induced in Heusler compounds, e.g., due to disorder, which appears to be unlikely here. However, magnetic frustration may result from the antiferromagnetic spin arrangement as has been pointed out by MÁCA and coworkers [196].

Fig. 4.3d shows the derivative of the normalized magnetization with respect to the temperature, $dM/(HdT)$, as a function of T . This corresponds to the magnetocaloric effect. Its temperature dependence is essentially unchanged in the full field range studied, with a minor exception. While the curves recorded at high magnetic field, $\mu_0 H = 3, 6, \text{ and } 9$ T display the same temperature dependence down to the lowest temperatures studied, the data recorded at 1 T exhibit a slight upturn of $dM/(HdT)$ below 20 K. Two aspects suggest that this feature is not intrinsic but results again from the tiny Mn₂Sb contamination: (i) the low-temperature upturn in $dM/(HdT)$ is suppressed in a sufficiently high magnetic field, consistent with the field-induced suppression of the broad hump observed in M around 150 K which has been attributed to Mn₂Sb impurities already, and (ii) the absence of an upturn of $dM/(HdT)$ in phase-pure CuMnSb-B, cf. Fig. 4.3h.

Irrespective of the applied magnetic field the Mn₂Sb contamination does not influence $dM/(HdT)$ at intermediate temperatures, in particular not around T_{N} . T_{N} may hence also be derived from $dM/(HdT)$. The same value for the Néel temperature as inferred from $M(T)$ beforehand, $T_{\text{N}} = 51.5$ K, is recovered if T_{N} is chosen as the temperature where $dM/(HdT) = 0$. As shown in the Fig. 4.3h and Fig. 4.4a, in fields up to 9 T the Néel temperature is slightly increased and shifts by up to 1.2 K. This is slightly more than the field-induced shift of the lambda anomaly observed in the above-mentioned heat capacity measurements of CuMnSb-A and also exceeds the field-induced change of T_{N} of CuMnSb-B. Below it will be shown that the latter amounts to

no more than 0.5 K.

Turning now to CuMnSb-B, Fig. 4.3e shows that again M is small for all fields and temperatures studied and follows an almost linear field dependence. With decreasing temperature M first increases monotonically up to a maximum at $T_N = 55.6$ K and then decreases. No Curie tail is detected down to the lowest temperatures studied suggesting once more the absence of ferromagnetic impurities. The value of T_N agrees nicely with the one reported by ENDO for CuMnSb as grown from an initial composition with 3-4 % Sb excess [6, 7].

In contrast to CuMnSb-A, no additional features are observed in small fields in the paramagnetic phase. This can most clearly be seen from the normalized magnetization, M/H , shown in Fig. 4.3f. Consistent with the powder x-ray diffraction and ac susceptibility measurements carried out in Ref. [5] this supports that no impurity phase is present in CuMnSb-B. However, a small hump which is not present in CuMnSb-A can be found in the antiferromagnetic phase of CuMnSb-B at $T^* = 33.8$ K. The occurrence of this additional feature in CuMnSb-B and its absence in CuMnSb-A is highlighted in Fig. 4.5a which shows M under a magnetic field of 9 T for both samples. As shown in Fig. 4.5c the hump at T^* is observed irrespective of the direction of the magnetic field and, moreover, appears at all fields studied. The latter is most clearly seen from the temperature derivative of the normalized magnetization, dM/HdT . As shown in Fig. 4.3h dM/HdT exhibits a distinct cusp at T^* for all fields studied. As will be reported in Sec. 4.5 neutron diffraction confirms that the additional feature at T^* is due to a slight reorientation of the antiferromagnetically aligned magnetic moments.

Returning now to the normalized magnetization of CuMnSb-B, the absolute size of M/H remains essentially unchanged in fields up to 9 T. Consequently, the inverse normalized magnetization is almost identical for all fields studied. As shown in Fig. 4.3g the high-temperature part of H/M follows a Curie-Weiss temperature dependence. Here, an effective fluctuating moment of $m_{\text{eff}} \approx 3.95 \mu_B/\text{f.u.}$ and a negative Curie-Weiss temperature of $\Theta_{\text{CW}} \approx -160(8)$ K may be deduced. The values of m_{eff} is in excellent agreement with susceptibility data of CuMnSb-B reported in Ref. [5], $m_{\text{eff}} = 3.99 \mu_B/\text{f.u.}$, but smaller than the result of ENDO, $m_{\text{eff}} \approx 5.7 \mu_B/\text{f.u.}$ [6, 7]. Θ_{CW} matches almost exactly the value reported by ENDO and is somewhat smaller than the one derived from ac susceptibility measurements in Ref. [5] where $\Theta_{\text{CW}} \approx -132$ K. The ratio $f = -\Theta_{\text{CW}}/T_N \approx 3$ is slightly smaller than in CuMnSb-A. Still a value of $f \approx 3$ suggest the presence of moderate geometric frustration.

Fig. 4.3h finally shows the temperature derivative of the normalized magnetization, $dM/(HdT)$ as a function of T . The Néel temperature extracted from the derivative is identical to the one extracted from M directly, $T_N = 55.6$ K. Fig. 4.4a compares the field dependence of the Néel temperatures of CuMnSb-A and CuMnSb-B. Unlike in CuMnSb-A where T_N was slightly increased with increasing field, in CuMnSb-B T_N is essentially unchanged up to the highest fields studied.

As mentioned above, consistent with magnetic neutron diffraction, CuMnSb-B undergoes a

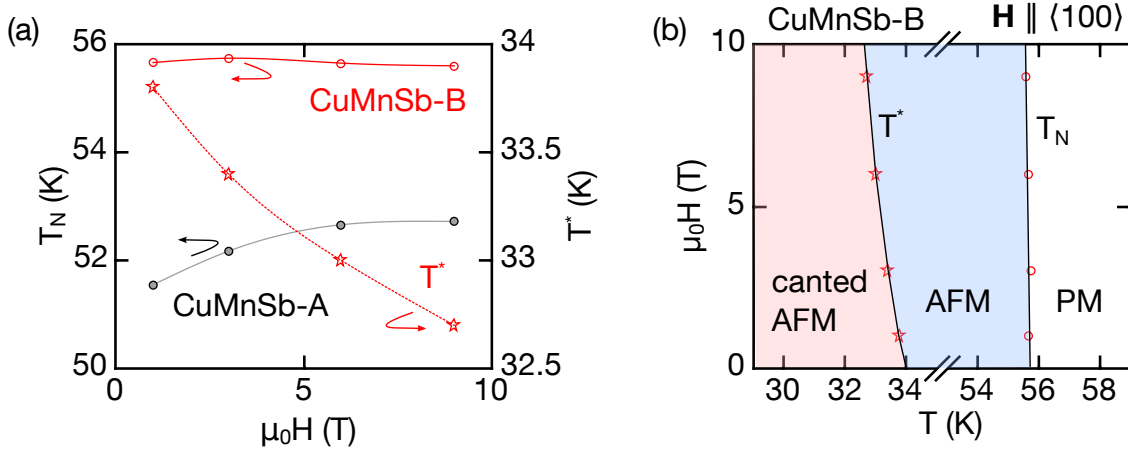


Figure 4.4: (a) Magnetic transition temperatures of CuMnSb-A and CuMnSb-B. Both T_N and T^* were inferred from the temperature derivative of the normalized magnetization $dM/(HdT)$. (b) Magnetic phase diagram of CuMnSb-B comprising a paramagnetic (PM) and antiferromagnetic (AFM) phase. Below T^* the reorientation of the Mn moments results in a canted antiferromagnet with no net moment.

spin-reorientation transition at $T^* = 33.8$ K resulting in a faint cusp in M . In turn, $dM/(HdT)$ displays a distinct maximum around T^* . A comparison of $dM/(HdT)$ for CuMnSb-A and CuMnSb-B demonstrates that this additional peak is observed only in CuMnSb-B. Its field dependence is again shown in Fig. 4.4a and may be characterized as follows. (i) First, with increasing magnetic field the size of the cusp in M and hence of the associated peak in $dM/(HdT)$ is slightly suppressed. (ii) Second, T^* is shifted towards lower temperatures, namely from 33.8 K at 1 T to about 32.7 K at 9 T. This suggests that the external field suppresses the spin reorientation and favors the untilted antiferromagnetic spin alignment.

The measurements carried out as part of this thesis suggest the magnetic phase diagram of CuMnSb-B shown in Fig. 4.4b. Paramagnetic (PM) CuMnSb-B orders antiferromagnetically (AFM) at $T_N = 55.6$ K, where the latter transition temperature is essentially unchanged up to the highest fields studied. At temperatures $T < T^*$ the reorientation of the magnetic moments results in a canted antiferromagnet with no net moment. In contrast to T_N the canting transition at T^* displays a slight dependence on the applied magnetic field.

The account of the magnetization of CuMnSb is finished with a closer inspection of the magnetic anisotropy. The magnetic anisotropy has been studied only for CuMnSb-B where measurements of the magnetization with the external magnetic field applied along the $\langle 100 \rangle$, $\langle 110 \rangle$, and $\langle 111 \rangle$ direction were carried out. The results of these measurements are shown in Fig. 4.5b. For all field directions the temperature dependence of the magnetization is qualitatively identical. As stated above it displays a pronounced maximum at $T_N = 55.6$ K and a hump around $T^* = 33.8$ K. A close-up of both features is shown in Fig. 4.5c for $\mu_0 H = 9$ T. M is largest for $H \parallel \langle 100 \rangle$ and smallest for $H \parallel \langle 110 \rangle$. As expected for a cubic compound this anisotropy is small and amounts

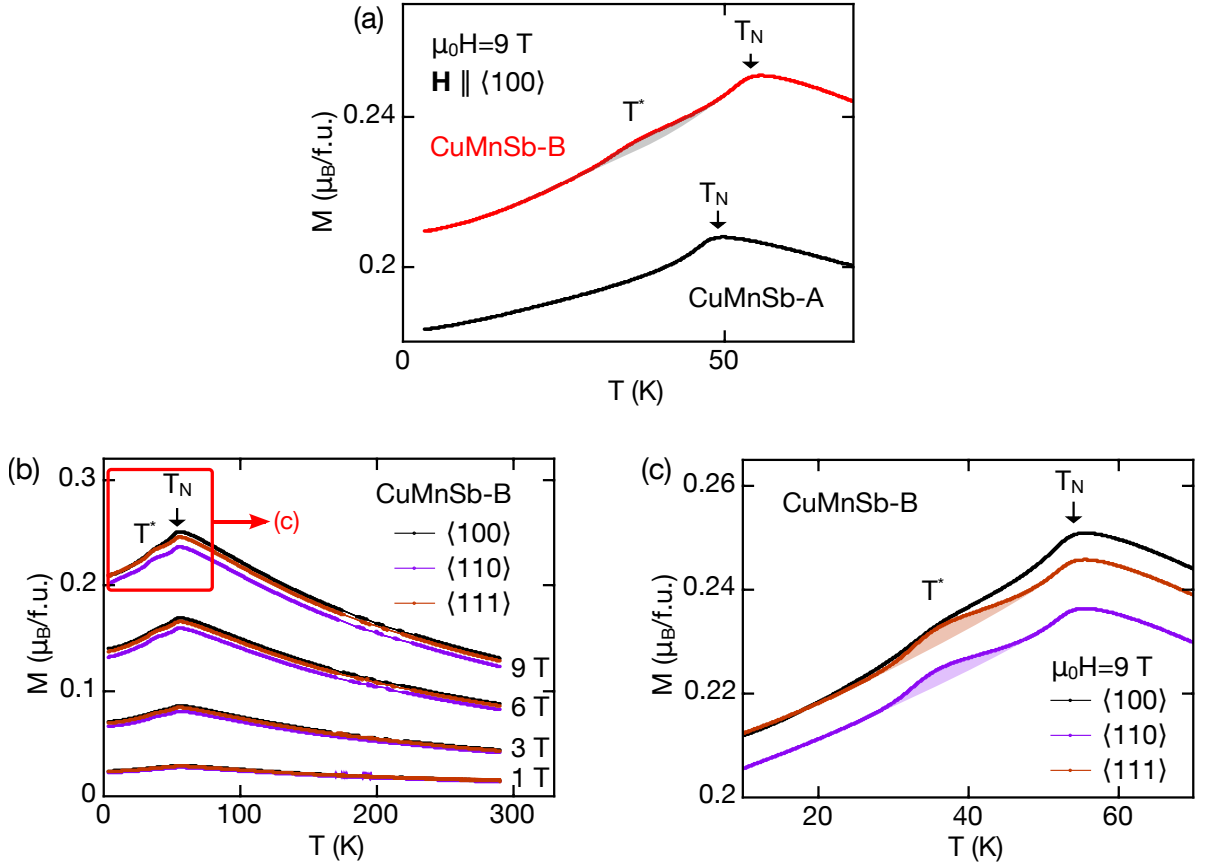


Figure 4.5: (a) Comparison of the low-temperature magnetization of CuMnSb-A and CuMnSb-B at 9 T revealing an additional small hump at $T^* = 33.8$ K in CuMnSb-B which is not observed in CuMnSb-A. (b) Magnetization of CuMnSb-B for various magnetic fields applied along high-symmetry directions. Missing data points at about 200 K are due to temperature instabilities that occurred during the measurement. (c) Low-temperature magnetization of CuMnSb-B for a field of 9 T applied along high-symmetry directions.

to $\sim 5\%$.

4.3.4 Electrical Resistivity and Hall Effect

The zero field resistivity of CuMnSb-A and CuMnSb-B are shown in Fig. 4.6 as a function of temperature. For both samples the temperature dependence $\rho(T)$ is qualitatively very similar. Starting from a room temperature value of $203 \mu\Omega \text{ cm}$ and $250 \mu\Omega \text{ cm}$ for CuMnSb-A and CuMnSb-B, respectively, ρ decreases monotonically with decreasing temperature. At the lowest temperatures studied the residual resistivity extrapolates to $\rho_0 = 49.3 \mu\Omega \text{ cm}$ and $\rho_0 = 61.5 \mu\Omega \text{ cm}$ for CuMnSb-A and CuMnSb-B, respectively. Thus the same residual resistivity ratio is obtained for both samples, $\text{RRR} = 4.2$. The residual resistivities ρ_0 seem to be large for transition metal

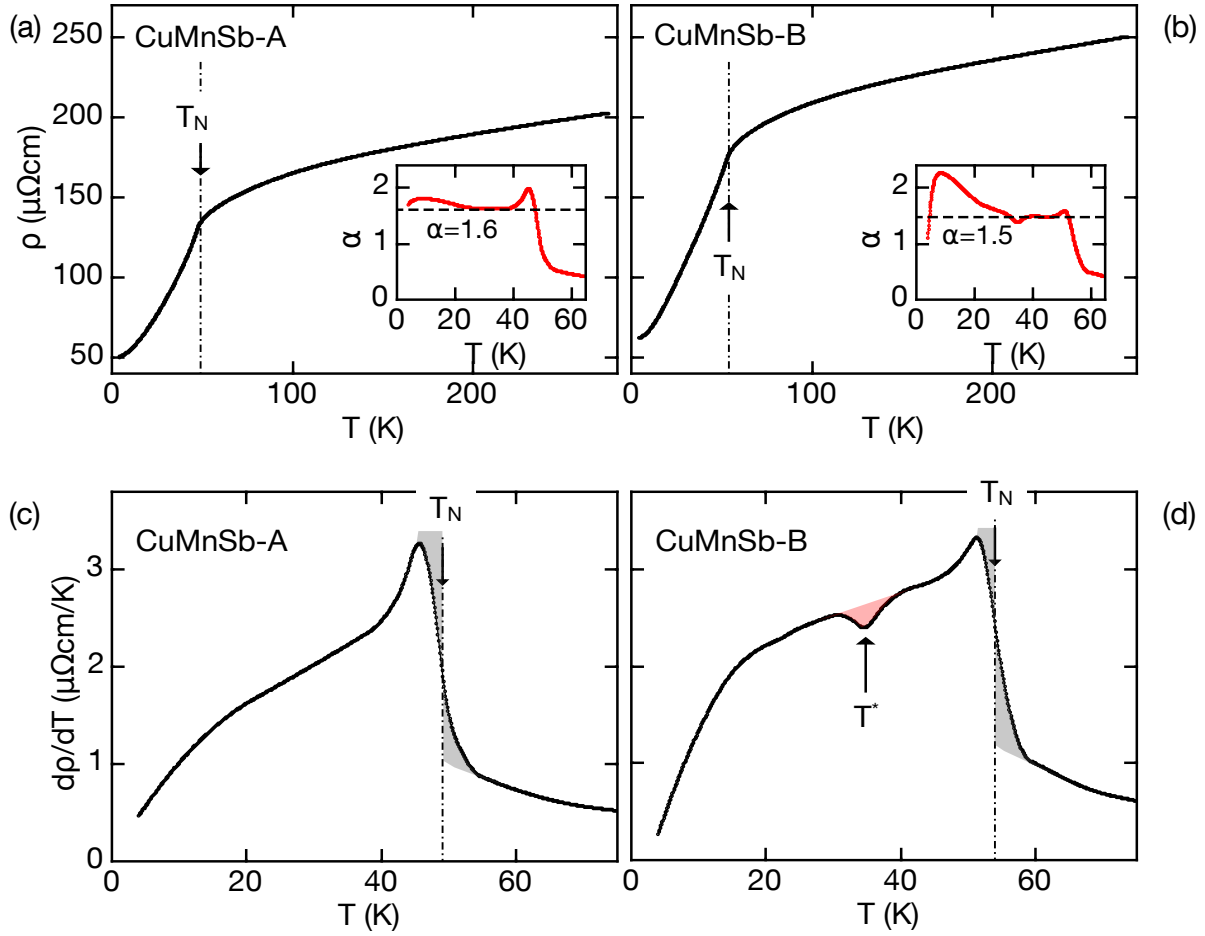


Figure 4.6: (a,b) Resistivity ρ of CuMnSb-A and CuMnSb-B as a function of temperature. The insets show the exponent of a powerlaw fit to the low-temperature part of $\rho(T)$. (c,d) Derivatives of the resistivity with respect to the temperature. Only for CuMnSb-B a dip in $d\rho/dT$ is observed at $T^* \approx 34$ K (red shaded area).

compounds in general. They are however typical for Heusler compounds which are prone to defects and anti-site disorder.

Due to the freezing-out of spin fluctuations the onset of long-range magnetic order is accompanied by a distinct drop of the resistivity at T_N . This change of slope is most easily seen when considering the temperature derivative of the resistivity, $d\rho/dT$, which is also shown in Fig. 4.6. In the analysis of the specific heat data T_N was based on an entropy conserving construction. The application of a similar criterion to the resistivity data gives $T_N = 49$ K and $T_N = 55$ K for CuMnSb-A and CuMnSb-B, respectively, which is in fair agreement with the magnetization data. Note that near T_N the shape of $d\rho/dT$ strongly resembles the electronic specific heat C_{el}/T . This suggests that the scattering mechanism which accounts for the electrical resistivity obeys Fermi's golden rule with the corresponding density of state dominating the specific heat [128].

The temperature dependence of the resistivity of antiferromagnetic CuMnSb was fitted using a power-law expression

$$\rho(T) = \rho_0 + AT^\alpha. \quad (4.1)$$

Here, ρ_0 is the residual resistivity arising due to electron scattering from defects. The second term accounts for electron-electron scattering and, for $\alpha = 2$, corresponds to a Fermi liquid ground state. In turn, deviations from a quadratic behavior may indicate a breakdown of the Fermi liquid scenario. The exponent α can be calculated from ρ and its derivative with respect to the temperature, $\rho' = d\rho/dT$, as

$$\alpha = T \cdot \frac{\rho'}{\rho - \rho_0}. \quad (4.2)$$

The insets in Fig. 4.6 show α as a function of temperature. For CuMnSb-A $\alpha \approx 1.6$ over a wide temperature range. A slight enhancement is observed only below 20 K where $\alpha \approx 1.8$. This compares to the value reported by BØUF [184]. For CuMnSb-B $\alpha \approx 1.5$ for $T^* \leq T \leq T_N$. Around $T^* \approx 34$ K an additional weak anomaly is observed. Below T^* the exponent first increases with decreasing temperature. After passing through a maximum at 8.5 K α finally drops again, thereby reaching almost a value of 1 at the lowest temperature studied. Altogether, the temperature dependence of ρ for both CuMnSb-A and CuMnSb-B clearly differ from the Fermi liquid behavior. Interestingly a value of $\alpha = 5/3 \approx 1.6$ is also observed in a marginal Fermi liquid at the border of three dimensional metallic ferromagnetism [202]. The strong variation of α with changes of the sample temperature indicates that the simple power-law (4.1) cannot fully account for the resistivity of CuMnSb.

Measurements of the longitudinal magnetoresistance and Hall effect of CuMnSb-B have been carried out using the same sample geometry, where the excitation current was applied along $\langle 100 \rangle$ and the field along $\langle 110 \rangle$. As shown in Fig. 4.7a the normal magnetoresistance is small and negative at high temperatures. Below $T \approx 100$ K it becomes positive and with increasing temperature and field grows up to $\sim 6\%$. For all temperatures studied a quadratic field dependence of the magnetoresistance is observed.

The Hall resistivity ρ_{xy} is strictly linear in field (small deviations from the linear behavior in Fig. 4.7b are due to temperature instabilities). Consequently, the Hall effect in CuMnSb can be fully characterized by a normal Hall constant R_0 which is most effectively measured using temperature sweeps at fixed field. Fig. 4.7c shows R_0 as a function of temperature. The data have been extracted from temperature scans of ρ_{xy} at constant field $\mu_0 H = \pm 3$ T. Data obtained from field sweeps at constant temperature are perfectly consistent. With decreasing temperature R_0 first increases, then passes through a maximum at $T_N = 55$ K, and finally decreases again. A very weak anomaly is observed around $T^* = 34$ K. Assuming a simple single band model the effective carrier concentration may be estimated as $n = (R_0 e)^{-1} \approx 2 \cdot 10^{21} \text{ cm}^{-3}$. This value is rather small for a metal and indicates a low density of states at the Fermi level. In agreement with the positive value of R_0 , the positive sign of n suggests holes as the dominant charge

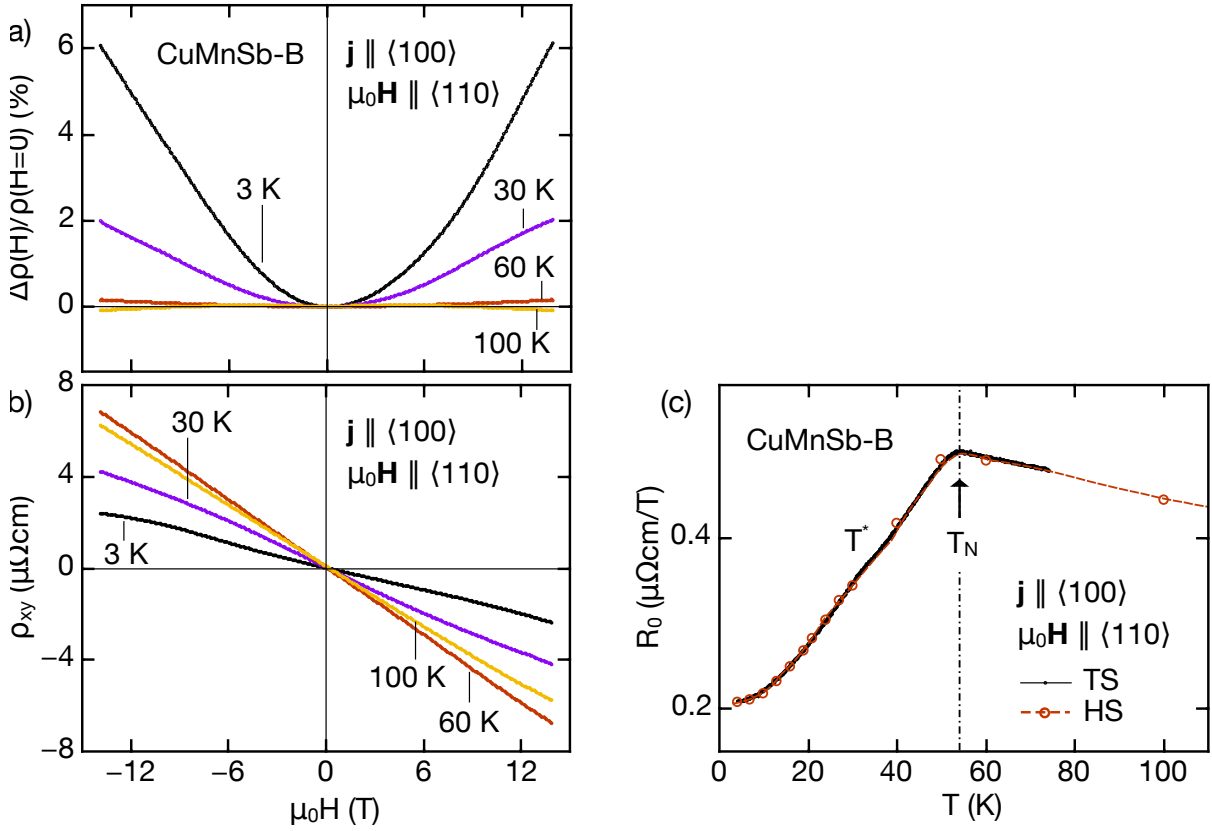


Figure 4.7: Magnetoresistance and Hall effect of CuMnSb-B. (a) Longitudinal magnetoresistance at various temperatures as a function of magnetic field. (b) Hall resistivity at various temperatures as a function of magnetic field. (c) Temperature dependence of the normal Hall constant R_0 as measured by temperature sweeps (TS) and field sweeps (HS). The dashed line serves as a guide to the eye.

carriers. In total, these results are consistent with the prediction of semi-metallicity with heavy electron masses and normal hole masses by JEONG [188].

4.4 Nuclear Structure of CuMnSb

4.4.1 Powder X-ray and Neutron Diffraction

As part of this thesis the nuclear structure of CuMnSb-B was investigated by means of powder x-ray diffraction and powder neutron diffraction. These measurements clearly confirm the reported $C1_b$ structure both at room temperature and at cryogenic temperatures. Structural parameters were obtained from refinements of diffraction data collected at various temperatures. These findings are summarized in Tab. 4.3 and will be briefly discussed below.

Powder x-ray diffraction of CuMnSb-B was carried out at temperatures between 12 K and 300 K. Typical data are shown in Fig. 4.8a along with their refinement. The $C1_b$ half-Heusler structure

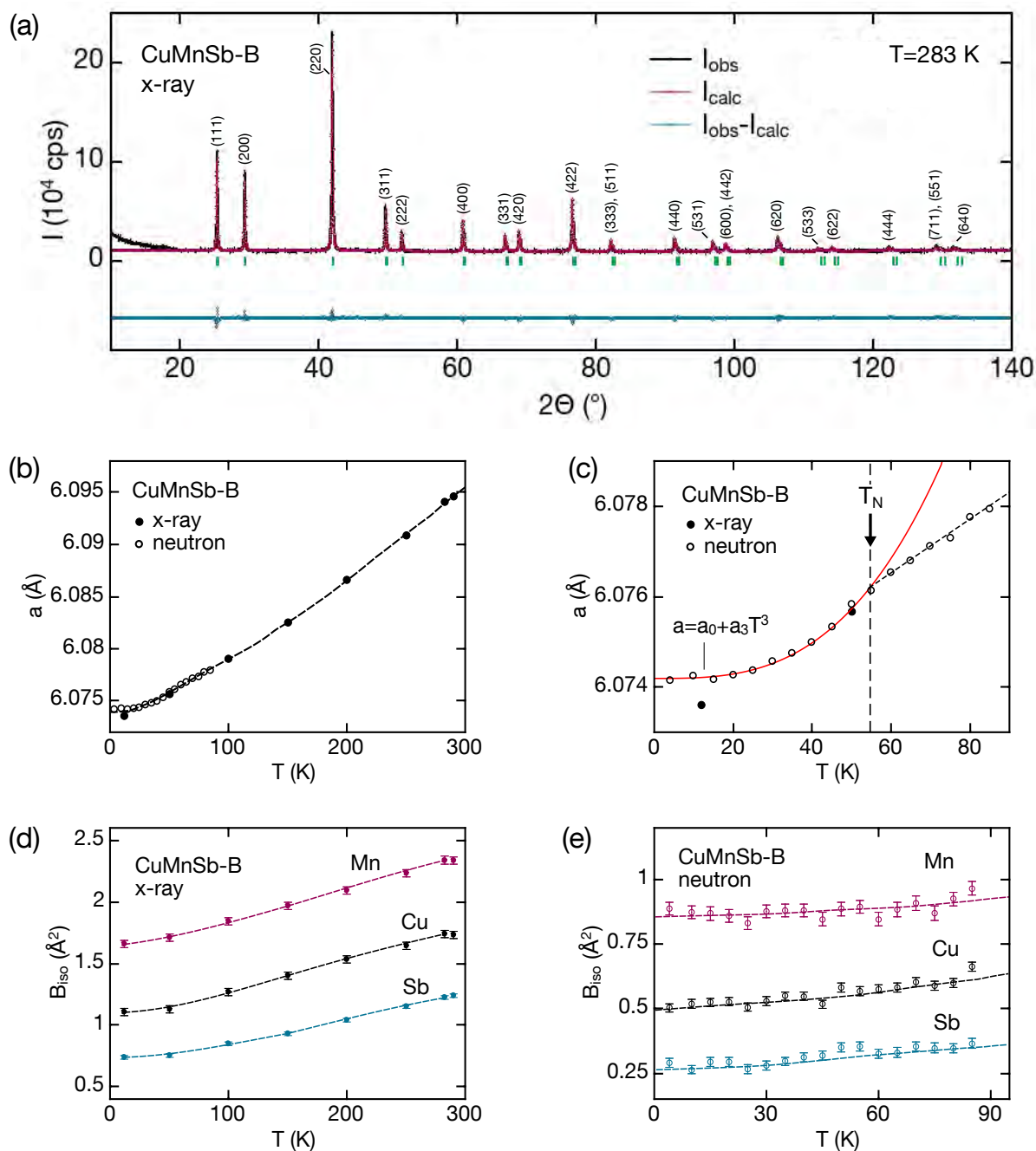


Figure 4.8: Nuclear structure refinement of CuMnSb-B from powder x-ray and neutron diffraction data. (a) Powder x-ray diffraction pattern consistent with the $C1_b$ half-Heusler structure. (b) Cubic lattice parameter a as a function of temperature. Errorbars are smaller than the symbol size. (c) Variation of the lattice parameter a at low temperatures. (d) Isotropic displacement parameters B_{iso} extracted from refinements of powder x-ray data. (e) Isotropic displacement parameters B_{iso} extracted from refinements of powder neutron data. Data have not been corrected for absorption. Dashed lines serve as a guide to the eye.

accounts for all observed Bragg peaks. Fig. 4.8b shows the lattice parameter a as a function of temperature. Values obtained from both powder x-ray and powder neutron diffraction agree very well. With decreasing temperature a decreases monotonically from 6.095 Å at room temperature to 6.074 Å at 4 K, corresponding to a relative change of approximately 0.3%. The isotropic displacement parameters B_{iso} which were inferred from the refinement of the x-ray data are comparatively large. This may indicate the presence of structural disorder, notably point defects such as anti-site disorder. Fig. 4.8d shows B_{iso} as a function of temperature. For all temperatures $B_{\text{iso,Sb}} < B_{\text{iso,Cu}} < B_{\text{iso,Mn}}$. Considering CuMnSb as self-doped $\text{Cu}^+\text{Mn}^{2+}\text{Sb}^{3-}$ [188] and assuming that large (small) ionic radii and atomic masses hinder (favor) the thermal motion of the corresponding ions, this observation is consistent with the reverse order of the atomic radii $r_{\text{Sb}^{3-}} > r_{\text{Cu}^+} > r_{\text{Mn}^{2+}}$ and $m_{\text{Sb}} > m_{\text{Cu}} > m_{\text{Mn}}$, respectively. As the temperature is lowered all three displacement parameters decrease monotonically.

Results obtained from powder x-ray diffraction are qualitatively consistent with our powder neutron investigation, where measurements have been carried out in a temperature range from 4 K to 85 K. As shown in Fig. 4.8c high-resolution temperature scans in the neutron study reveal additionally a weak change of slope of the temperature dependence of the lattice parameter near T_{N} . Presumably due to magnetostriction $a(T)$ changes from a linear behavior in the paramagnetic regime to a cubic behavior in the antiferromagnetic phase. The results of the refinement of the isotropic displacement parameters observed by neutron diffraction are shown in Fig. 4.8e. Qualitatively B_{iso} inferred from x-ray and neutron diffraction agree nicely. Yet the absolute values obtained from x-ray data are larger than corresponding results extracted from neutron diffraction. This occurs naturally as the scattering centers are different for both methods. Moreover, the discrepancy of the isotropic displacement parameters could presumably be reduced by means of an absorption correction of both x-ray and neutron data which is, however, beyond the scope of this thesis.

An estimate of the dominant type of anti-site defects and its concentration may be deduced from a combined analysis of the powder x-ray and neutron data carried out by ANATOLIY SENYSHYN. For these refinements the site occupancy for one atom type - Cu, Mn, or Sb - was fixed at 100% while the occupancies of the remaining two atoms sites were chosen as parameters of the fit. As summarized in Tab. 4.4.1 our data are in agreement with a small amount (1.5%) of Cu/Mn anti-sites. In contrast, both Cu/Sb and Mn/Sb swaps result in a poorer fit quality and hence explain the observed scattering less well. This finding is in excellent agreement with experimental results by MÁCA and coworkers who report a value of 1.6% for the Cu/Mn mix/occupancy ratio [197].

4.4.2 Polarized Neutron Scattering

The spectrometer DNS at the MLZ, Garching, was used to study the diffuse scattering in CuMnSb-B. Due to a misalignment of the instrument the observed scattering intensities are

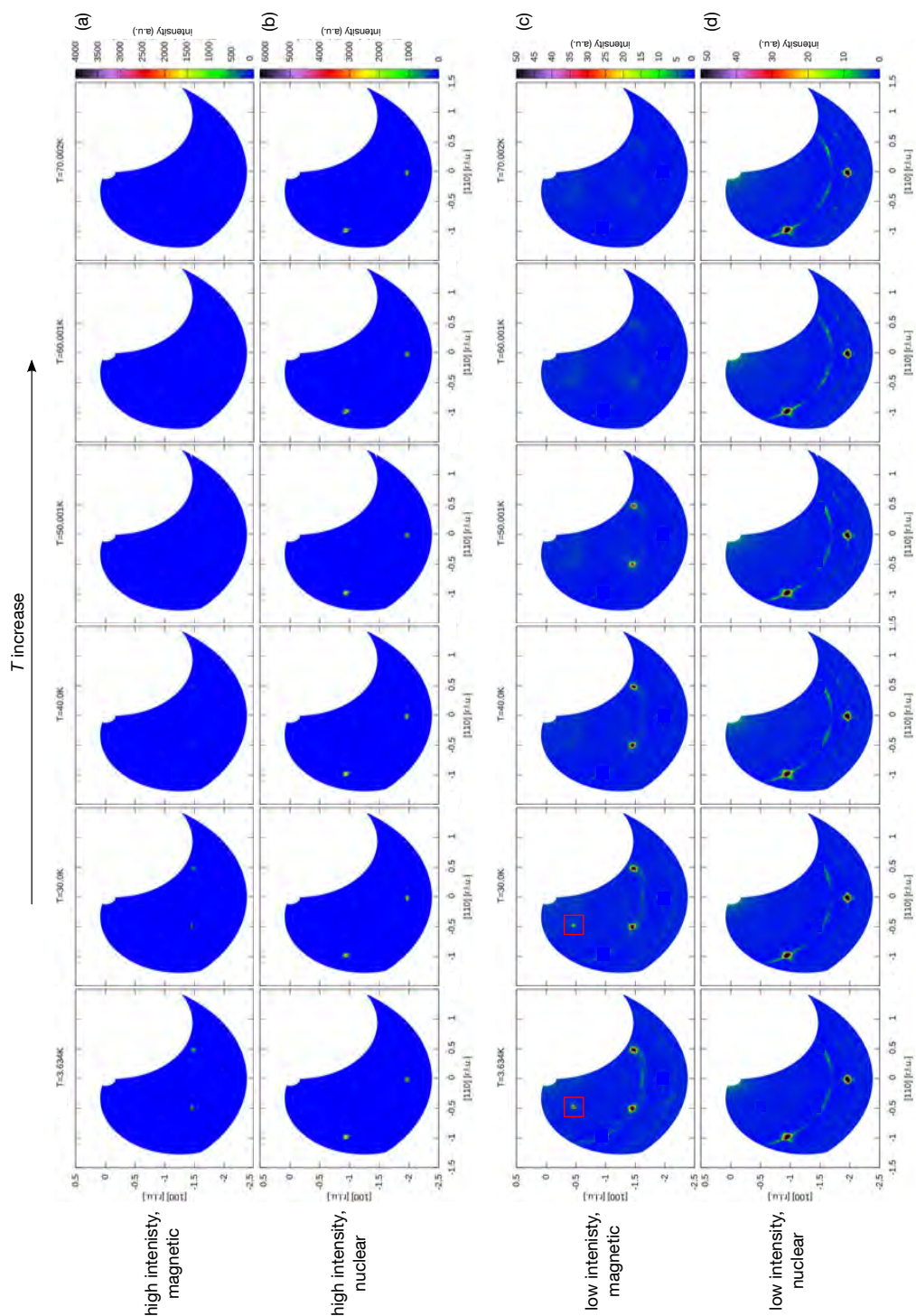


Figure 4.9: Polarized neutron scattering of CuMnSb-B as recorded at the DNS spectrometer at various temperatures. Temperature increases from left to right. (a) Magnetic scattering of high intensity. (b) Nuclear scattering of high intensity. (c) Magnetic scattering of low intensity. (d) Nuclear scattering of low intensity. For $T < 30$ K the $(0.5, 0.5, 0.5)$ satellite peak is observed (red box). The diffuse rings observed at low intensities arise most likely from a thin layer of powdered CuMnSb on the sample surface.

The Half-Heusler Antiferromagnet CuMnSb

Cu	Mn	Sb	R, R_w
Cu 100 %	Mn 100 %	Sb 100 %	3.19, 4.10
Cu 100 %	Mn/Sb 98.4/1.6, %	Sb/Mn 98.4/1.6, %	3.34, 4.27
Cu/Sb 100.3/0.3 %	Mn 100, %	Sb/Cu 100.3/0.3 %	3.19, 4.10
Cu/Mn 98.5/1.5 %	Mn/Cu 98.5/1.5 %	Sb 100 %	3.20, 4.08

Table 4.1: Combined refinement of the powder x-ray and neutron data assuming the full occupation of one atom site while occupancies of the remaining two atom sites are parameters of the fit.

incorrect and the data could not be evaluated quantitatively. Consequently, while the scattering signal in the NSF channel is truly non spin-flip in origin those events which were recorded in the SF channel are mixed and therefore include a substantial portion of non spin-flip scattering. Although all measurements were done using polarized neutrons a discrimination of nuclear and magnetic scattering is thus *not* possible by means of a polarization analysis. However, this classification can be done at least for the coherent Bragg scattering on the basis of the sample temperature. Bragg peaks which were observed at $T > T_N$ must be nuclear in origin whereas magnetic satellites appear only at $T < T_N$. This classification procedure is facilitated by the fact that the magnetic satellite peaks are incommensurate with the nuclear scattering and therefore occupy distinct positions in reciprocal space. Despite the instrumental issues a qualitative examination of the data is therefore still possible and will be presented in the following.

Fig. 4.9 shows the nuclear and magnetic scattering in the $\langle 110 \rangle \times \langle 001 \rangle$ reciprocal space plane for various temperatures. The magnetic signal of high intensity is shown in Fig. 4.9a. For paramagnetic CuMnSb, $T > T_N$, no magnetic Bragg reflections are detected. In contrast, below T_N scattering from the long-range magnetic order sets in, manifesting in the observation of two magnetic satellite peaks at the positions $(\frac{\bar{1}}{2} \frac{\bar{1}}{2} \frac{\bar{3}}{2})$ and $(\frac{1}{2} \frac{1}{2} \frac{\bar{3}}{2})$. Both positions are compatible with the reported k-vector $\mathbf{k} = (0.5, 0.5, 0.5)$. Fig. 4.9b presents the nuclear scattering signal of high intensity. Strong nuclear scattering is observed at two Bragg positions, $(\bar{1}\bar{1}\bar{1})$ and $(00\bar{2})$, in accordance with the extinction rules of the $C1_b$ structure. As expected for the nuclear scattering the intensity of these peaks does not change significantly as a function of temperature.

Turning now to the magnetic signal of low intensity shown in Fig. 4.9c, again, no magnetic Bragg scattering is seen at high $T > T_N$ where CuMnSb is a paramagnet. For $T^* < T < T_N$ the above-mentioned magnetic Bragg reflections are observed. When the temperature is lowered below $T^* \approx 30$ K an additional peak occurs at $(\frac{\bar{1}}{2} \frac{\bar{1}}{2} \frac{\bar{1}}{2})$. As will be discussed in more detail

below the appearance of this satellite peak is attributed to a spin reorientation transition and fully consistent with the other diffraction experiments. Considering the occurrence of diffuse scattering, the diffuse rings seen in Fig. 4.9c and Fig. 4.9d do not arise from the sample bulk but are presumably due to tiny amounts of CuMnSb powder at the surface of the specimen studied. Thus no diffuse scattering is observed in either scattering channel and at any temperature. The absence of diffuse scattering may indicate that any defects present in the sample are distributed rather randomly and do not form a short-range ordered defect structure.

4.5 Magnetic Structure of CuMnSb

Theoretical investigations in the magnetic order of CuMnSb suggested that antiferromagnetism is energetically favored over paramagnetic or ferromagnetic correlations [188]. This is consistent with the report of commensurate antiferromagnetic order with a propagation vector $\mathbf{k} = (0.5, 0.5, 0.5)$ and an ordered moment of $m_s = 3.9(1) \mu_B/\text{Mn}$ [186]. The magnetic unit cell is thus doubled with respect to the nuclear cell along all three coordinate axes. This kind of modulation is commonly referred to as type-II antiferromagnetism [203]. Both the commensurability and the almost integer ordered moment are characteristic of local-moment magnetism. A microscopic model of the spin order was inferred from the magnetic structure factor. Due to the selection rule for magnetic neutron scattering the intensity of the $(0.5, 0.5, 0.5)$ satellite must vanish for an arrangement where the magnetic moments point along the $\langle 111 \rangle$ direction. This has indeed been observed by FORSTER and coworkers who inferred the magnetic ground state that is shown schematically on the right-hand side of Fig. 4.10a. It consists of ferromagnetic (111) planes in which the Mn moments point along the $\langle 111 \rangle$ direction; adjacent (111) layers couple antiferromagnetically. This spin arrangement was therefore also denoted AFM(111) [197].

Since the experimental observation by FORSTER the AFM(111) order is widely accepted as the magnetic ground state of CuMnSb. On the other hand, deviations from a perfectly collinear spin alignment may be expected due to spin-orbit coupling. In materials lacking inversion symmetry the latter gives rise to the so-called antisymmetric Dzyaloshinskii-Moriya exchange interaction which favors a canting of the magnetic moments. The AFM(111) is also questioned by more recent ab-initio calculations by MÁCA and coworkers. Their study suggest that other antiferromagnetic states with moments oriented along $\langle 100 \rangle$, a tetragonal arrangement with alternating double layers of opposite spins along the $\langle 210 \rangle$ directions, or even more complex spin states are expected. However, crystal defects such as Cu-Mn anti-site disorder may stabilize the experimentally observed AFM(111) state already at small defect concentrations of a few percent [197]. The latter are consistent with the relatively large residual resistivity of $\sim 50 \mu\Omega \text{ cm}$ reported in the literature.

The low-temperature magnetization and transport data reported in this thesis as well as specific

Magnetic Super- space Group	Axes	Origin Shift
R[I]3c	$(\frac{1}{2}, -\frac{1}{2}, 0 0, \frac{1}{2}, -\frac{1}{2} 2, 2, 2)$	(0, 0, 0)
R[I]3m	$(\frac{1}{2}, -\frac{1}{2}, 0 0, \frac{1}{2}, -\frac{1}{2} 2, 2, 2)$	(0, 0, 0)
C[B]m	$(-1, \frac{1}{2}, \frac{1}{2} 0, -\frac{1}{2}, \frac{1}{2} 1, \frac{1}{2}, \frac{1}{2})$	(0, 0, 0)
C[B]c	$(-1, \frac{1}{2}, \frac{1}{2} 0, -\frac{1}{2}, \frac{1}{2} 1, \frac{1}{2}, \frac{1}{2})$	$(0, \frac{1}{4}, 0)$
P[I]1	$(0, \frac{1}{2}, -\frac{1}{2} -\frac{1}{2}, \frac{1}{2}, 0 \frac{1}{2}, 1, \frac{1}{2})$	(0, 0, 0)

Table 4.2: Magnetic superspace groups of CuMnSb for $\mathbf{k} = (0.5, 0.5, 0.5)$. The groups are listed together with the transformation which brings the unit cell to the standard settings.

heat measurements by ANDREAS BAUER [5] strongly suggest that the magnetic ground state of CuMnSb-B differs from the reported AFM(111) structure. This is further corroborated by our powder and single crystal neutron diffraction which will be presented below. In contrast to Ref. [186] these measurements on CuMnSb-B clearly demonstrate that the intensity of the (0.5, 0.5, 0.5) satellite is finite below $T^* \approx 34$ K, hence supporting a spin reorientation transition. Magnetic structure refinements suggest that for $T < T^*$ the AFM(111) arrangement is slightly modified as the magnetic moments are tilted out of their original $\langle 111 \rangle$ direction. Our observations provide for the first time an experimental underpinning for the deviation of the magnetic ground state from the hitherto accepted AFM(111) spin structure.

4.5.1 Representation Analysis

In order to identify possible magnetic structures of CuMnSb a representation analysis was carried out. Consistent with literature [186] as well as the powder neutron data presented below the magnetic propagation vector $\mathbf{k} = (0.5, 0.5, 0.5)$ was assumed. The representation analysis was performed using the crystallographic software JANA2006, resulting in five non-centrosymmetric superspace groups. Their properties are summarized in Tab. 4.2. Group R[I]3m is non-magnetic and will not be considered any further. Fits using groups P[I]1 as the model structure did not converge and were hence rejected. The remaining model structures are shown schematically in Fig. 4.10 using hexagonal standard settings and parent-like cubic settings, $(2a, 2b, 2c; 90, 90, 90)$. In the Shubnikov group R[I]3c the magnetic moment points along the c -axis of the standard cell, its a - and b -component vanish. In cubic settings this corresponds to the antiferromagnetic arrangement proposed by FORSTER, i.e., the moment vector components are equal in size, $m_a = m_b = m_c$. Consequently, \mathbf{m} is oriented perpendicular to the (111) planes. In group C[B]m \mathbf{m} points along the b -axis of the standard cell, both m_a and m_c vanish. In cubic settings this corresponds to an arrangement where the moments lie in the (111) planes and point along the $\langle 110 \rangle$ direction. Finally, in group C[B]c the magnetic moment may have finite a -, b -, and c -components. Fitting the data using the C[B]c superspace group results in a spin arrangement

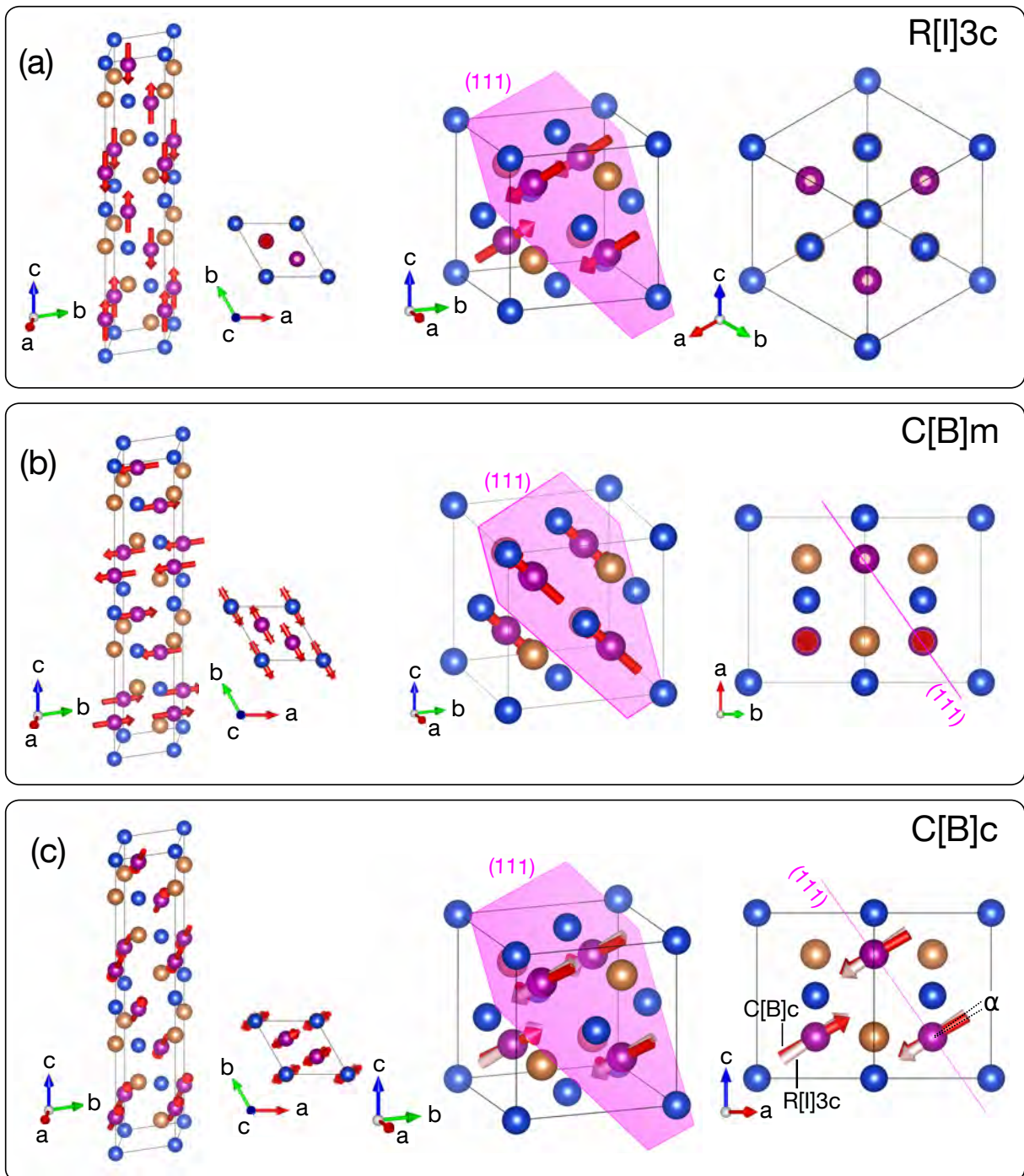


Figure 4.10: Magnetic superspace groups of CuMnSb with $\mathbf{k} = (0.5, 0.5, 0.5)$ in standard settings and cubic parent-like settings. (a) R[1]3c, the magnetic moments is perpendicular on the cubic (111) planes. (b) C[B]m, the magnetic moments lie in the cubic (111) planes and point along $\langle 110 \rangle$. (c) C[B]c, the magnetic moments are tilted with respect to the cubic $\langle 111 \rangle$ direction by an angle α .

that strongly resembles the one derived from space group R[$\bar{1}$]3c. The moment vector, however, is not oriented perpendicular to the (111) sheets but under an angle $90^\circ + \alpha$, where

$$\mathbf{m} \cdot \mathbf{n}_{111} = |\mathbf{m}| |\mathbf{n}_{111}| \cos(\alpha), \quad (4.3)$$

and \mathbf{n}_{111} points along $\langle 111 \rangle$.

Below it will be shown that this slightly canted antiferromagnetic structure accounts best for the observed scattering intensities in both powder and single crystal neutron diffraction. Our data allow to infer a tilting angle of $\alpha \approx 11^\circ$ of the moment vector with respect to the cubic $\langle 111 \rangle$ direction.

4.5.2 Powder Neutron Diffraction

Powder neutron diffraction was carried out at the instrument SPODI at the MLZ, Garching. Fig. 4.11a shows typical diffraction pattern of CuMnSb-B for three temperatures, $80 \text{ K} > T_N$, $T_N > 40 \text{ K} > T^*$, and $4 \text{ K} < T^*$. Bragg scattering observed above T_N is consistent with the x-ray diffraction data and may be indexed according to the $C1_b$ half-Heusler structure of CuMnSb. Hence, this scattering is nuclear in origin. Below T_N magnetic Bragg peaks appear at low scattering angles, cf. Fig. 4.11b. They can be indexed using the k-vector originally proposed by FORSTER, $\mathbf{k} = (0.5, 0.5, 0.5)$ [186]. Consistent with Ref. [186] no $(0.5, 0.5, 0.5)$ satellite is observed at this temperature, suggesting $\mathbf{m} \parallel \langle 111 \rangle$. As shown in the inset in Fig. 4.11b a faint $(0.5, 0.5, 0.5)$ Bragg reflection eventually appears when T is further reduced. From Fig. 4.11c $T^* \approx 30 \text{ K}$ may be extracted as the onset temperature of the $(0.5, 0.5, 0.5)$ satellite, in good agreement with the low-temperature bulk and transport measurements. The observation of a $(0.5, 0.5, 0.5)$ satellite peak clearly rules out any arrangement where $\mathbf{m} \parallel \langle 111 \rangle$, notably the R[$\bar{1}$]3c structure is disallowed. Refinements of the powder neutron data were carried out for the three Shubnikov superspace groups, R[$\bar{1}$]3c, C[B]m, and C[B]c. The program FULLPROF was used [36]. Parent-like cubic cell settings were employed and the directions of the magnetic moment vectors were constrained according to the symmetry of the individual magnetic superspace groups. The magnetic moment was assumed to be located exclusively on the Mn atoms. Following the argumentation by JEONG who classified CuMnSb heuristically as self-doped $\text{Cu}^{1+}\text{Mn}^{2+}\text{Sb}^{3-}$ the magnetic form factor of the Mn^{2+} ion was used for all fits.

Fitting space group C[B]m to the data results in significantly worse R factors than fits employing the R[$\bar{1}$]3c and C[B]c structures. This model structure is therefore rejected and the corresponding refinements will not be shown below. The magnetic reliability factors obtained from refinements with the two remaining space groups, R[$\bar{1}$]3c and C[B]c, are shown in Fig. 4.12a as a function of temperature. They do not differ significantly quantitatively or qualitatively and thus cannot conclusively identify the correct magnetic structure. However, the appearance of the $(0.5, 0.5, 0.5)$ satellite peak below T^* may only be explained within the C[B]c space group, cf. Fig. 4.12b.

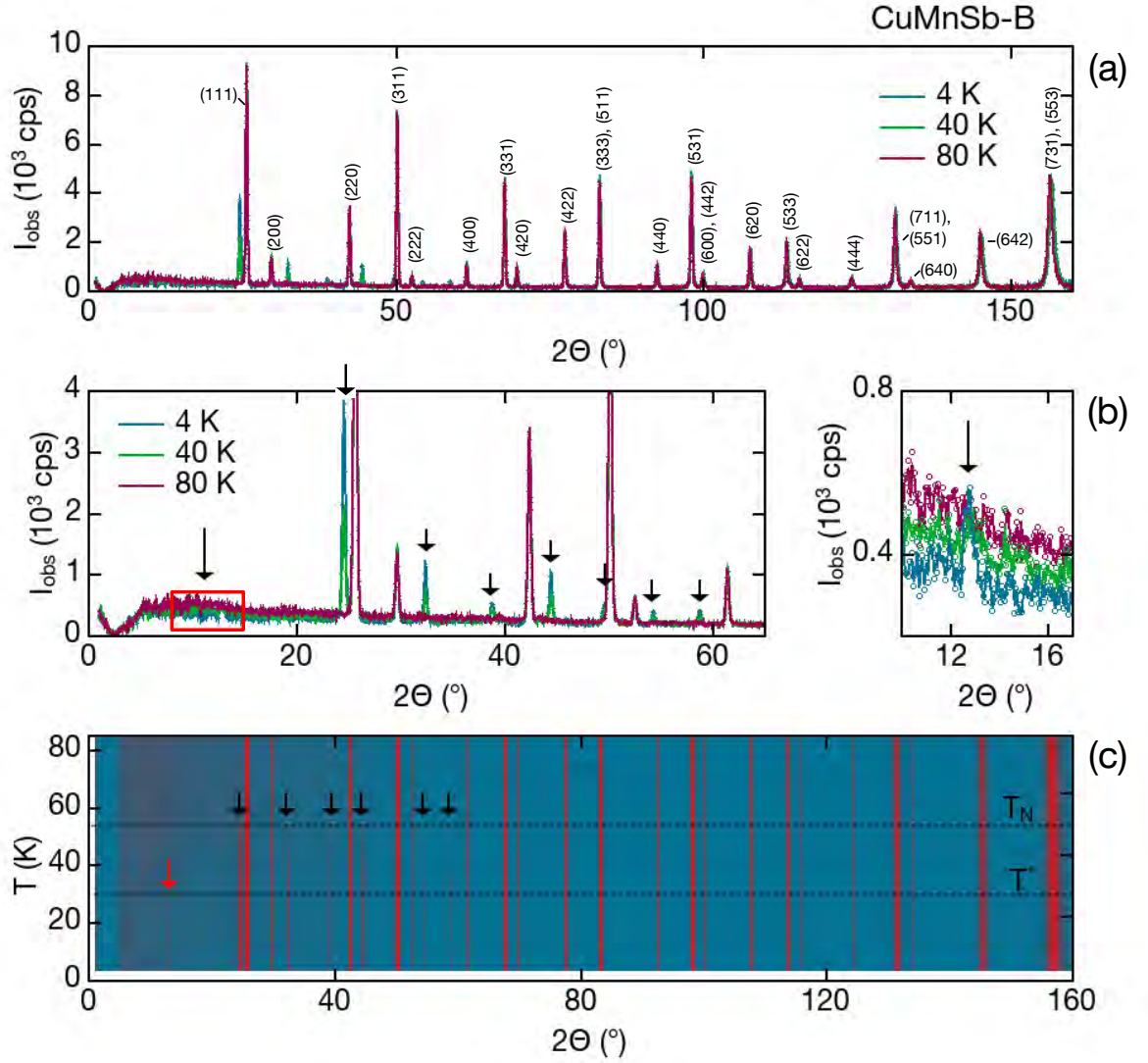


Figure 4.11: Powder neutron diffraction of CuMnSb-B. (a) Typical diffraction data for $T > T_N$, $T^* < T < T_N$, and $T < T^*$. Labels correspond to the $C1_b$ structure. (b) Blow-up of the diffraction pattern at small angles where magnetic Bragg scattering is abundant. Arrows indicate the strongest magnetic satellites. The region surrounded by the red box is enlarged on the right-hand side. It shows the appearance of an additional (0.5, 0.5, 0.5) satellite peak below T^* . (c) Scattering intensity as a function of temperature and scattering angle. Black arrows indicate the strongest magnetic reflections. The red arrow marks the weak (0.5, 0.5, 0.5) satellite peak that occurs below T^* .

Therefore, for $T < T^*$, the magnetic structure of CuMnSb-B is described by the Shubnikov group $C[B]c$ with a non-zero tilting angle α . At intermediate temperatures $T^* \leq T \leq T_N$ both test structures $R[I]3c$ and $C[B]c$ with $\alpha \approx 0$ account similarly well for the experimental data. This finding is also corroborated by the single crystal data presented below.

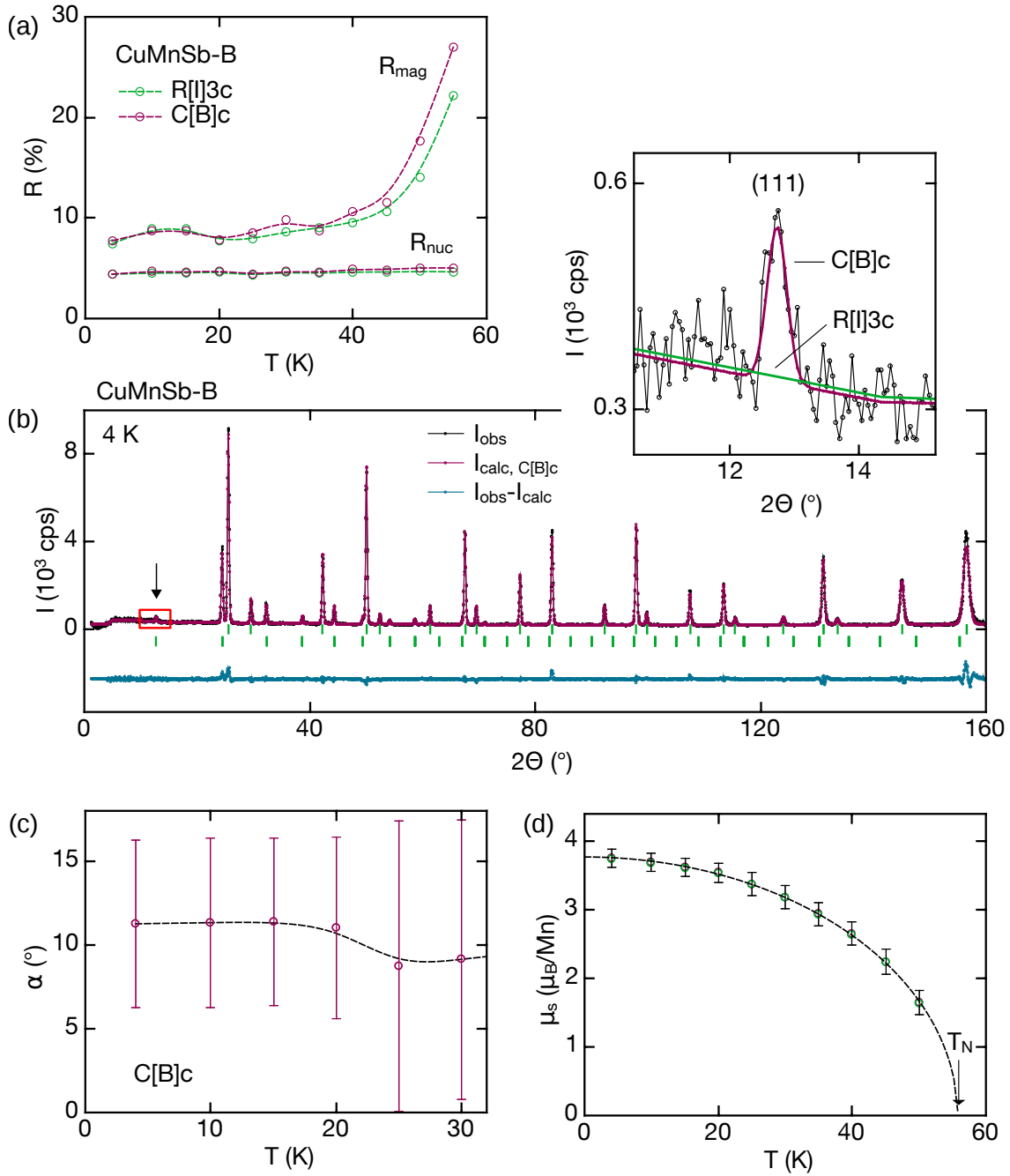


Figure 4.12: Magnetic structure refinement for CuMnSb-B on the basis of powder neutron data. (a) R factors for superspace groups $R[\text{I}]3c$ and $C[\text{B}]c$ as a function of temperature. Dashed lines serve as a guide to the eye. (b) Magnetic structure refinement for $T = 4$ K using the $C[\text{B}]c$ Shubnikov group. The region surrounded by the red box is enlarged in the inset and shows the (0.5, 0.5, 0.5) magnetic satellite peak. The latter cannot be explained by the $R[\text{I}]3c$ structure. (c) Tilting angle α of the magnetic moments in the $C[\text{B}]c$ structure as a function of temperature. (d) Ordered moment as a function of temperature. Values determined from refinements employing space groups $R[\text{I}]3c$ and $C[\text{B}]c$ are essentially identical. The dashed line corresponds to Eq. 4.4. Above 50 K R_{mag} clearly exceeds 20%, prohibiting a conclusive analysis of these refinements. Corresponding data points were removed from the graphs.

Tab. 4.3 summarizes the key results of the magnetic structure refinements based on the C[B]c space group. It also lists the individual components of the magnetic moment, $m_a = m_b$, and m_c , which were used to calculate the tilting angle α by means of Eq. 4.3. As shown in Fig. 4.12c α remains essentially unchanged as a function of temperature. At 4 K, the lowest temperature studied, $\alpha \approx 11^\circ$. Fig. 4.12d shows m_s , the ordered moment per Mn, as a function of temperature. At 4 K $m_s = 3.77 \mu_B/\text{Mn}$, in good agreement with the literature. Below T_N the magnetic moment increases rapidly with decreasing temperature as

$$m_s \propto \sqrt{1 - (T/T_N)^2}. \quad (4.4)$$

By fitting Eq. 4.4 to $m_s(T)$ the Néel temperature $T_N \approx 55.8$ K is obtained, in excellent agreement with the bulk data.

4.5.3 Single Crystal Neutron Diffraction

Single crystal data were recorded at the diffractometers RESI and HEiDi at the MLZ, Garching, using an image plate and a single counter detector, respectively. Fig. 4.13 shows typical nuclear and magnetic scattering data obtained from both instruments. Consistent with the modulation vector determined from powder neutron diffraction, $\mathbf{k} = (0.5, 0.5, 0.5)$, the $(hk0)$ reciprocal space plane contains only nuclear Bragg peaks at positions consistent with the $C1_b$ structure (Fig. 4.13a). In contrast, the $(0, 0, 0.5)$ reciprocal space plane contains only magnetic satellite peaks (Fig. 4.13b). Compared to the nuclear scattering their intensity is reduced much stronger with increasing scattering angle. All data show a faint peak splitting suggestive of small angle grain boundaries or a small second crystal grain. This is seen even better from the peak profiles recorded at HEiDi. With a typical full width of half maximum of about 1° the nuclear peak profiles are still comparatively narrow for a half-Heusler compound and, for this material class, indicate a small crystalline mosaicity and hence a good sample quality. The same peak splitting and peak width are observed for the magnetic scattering suggesting that both the splitting and the mosaicity are fully determined by the nuclear structure, whereas a magnetic origin such as a second k-vector may be ruled out. This justifies the approach used in the data analysis, where during the indexing and integration of the scattering intensities the peak splitting was not taken into account. Instead the double Bragg peaks were treated as single, slightly broader reflections. The magnetic structure factors obtained were subsequently refined in order to infer the long-range magnetic structure of CuMnSb-B.

All refinements were carried out by means of the JANA2006 crystallographic software [37]. For all magnetic test structures the same hexagonal standard cell was used, namely $a = b = 4.319 \text{ \AA}$, $c = 21.157 \text{ \AA}$ with $\alpha = \beta = 90^\circ$, $\gamma = 120^\circ$. The atomic positions were fixed according to the nuclear parent structure. Furthermore peaks with intensity $I < 3\sigma$ were classified as weak reflections. Consistent with the analysis of the powder neutron data the magnetic form factor

The Half-Heusler Antiferromagnet CuMnSb

CuMnSb-B									
powder x-ray diffraction, SpcGrp F $\bar{4}3m$									
T (K)	a (Å)	$B_{\text{iso}}^{\text{Cu}}$ (Å ²)	$B_{\text{iso}}^{\text{Mn}}$ (Å ²)	$B_{\text{iso}}^{\text{Sb}}$ (Å ²)	R_{nuc}				
290	6.0946054	1.7321280	2.3360784	1.2400336	3.35				
283	6.0940576	1.7382636	2.3369305	1.2215097	3.18				
250	6.0908952	1.6397172	2.2323575	1.1447823	3.31				
200	6.0866399	1.5280147	2.0920947	1.0343242	3.36				
150	6.0825348	1.3976427	1.9622812	0.9278152	3.34				
100	6.0790243	1.2689319	1.8370175	0.8482639	3.26				
50	6.0756688	1.1270149	1.7106214	0.7520527	3.23				
12	6.0736046	1.1024860	1.6548150	0.7377928	3.18				
powder neutron diffraction, SpcGrp F $\bar{4}3m$									
T (K)	a (Å)	$B_{\text{iso}}^{\text{Cu}}$ (Å ²)	$B_{\text{iso}}^{\text{Mn}}$ (Å ²)	$B_{\text{iso}}^{\text{Sb}}$ (Å ²)	R_{nuc}				
85	6.0779653	0.65795833	0.95152503	0.35718012	4.24				
80	6.0777321	0.59855419	0.91628677	0.34175348	3.83				
75	6.0773106	0.58627641	0.86407739	0.34212914	4.30				
70	6.0771194	0.59918815	0.89507103	0.34544820	4.23				
65	6.0767927	0.57898068	0.87367493	0.32370168	4.37				
60	6.0765209	0.57294643	0.83462000	0.31785670	4.46				
powder neutron diffraction, SpcGrp R[$\bar{1}$]3c									
T (K)	a (Å)	$B_{\text{iso}}^{\text{Cu}}$ (Å ²)	$B_{\text{iso}}^{\text{Mn}}$ (Å ²)	$B_{\text{iso}}^{\text{Sb}}$ (Å ²)	R_{nuc}	$m_{a,b,c}$ (μ _B)	m (μ _B)	R_{mag}	
55	6.0761375	0.55538946	0.87160283	0.33572549	4.64	0.8824031	1.53	22.2	
50	6.0758452	0.57158273	0.85801607	0.33124414	4.68	0.9458514	1.64	14.1	
45	6.0753608	0.50707996	0.82209074	0.30104858	4.62	1.2876655	2.23	10.6	
40	6.0750122	0.5381735	0.85540265	0.29325449	4.63	1.5244581	2.64	9.53	
35	6.0747514	0.53550601	0.84114712	0.26936966	4.49	1.6888101	2.93	9.01	
30	6.0745711	0.51787847	0.8446672	0.25756755	4.6	1.8317351	3.17	8.62	
25	6.0743785	0.4959996	0.80084479	0.24453378	4.29	1.9441457	3.37	7.91	
20	6.0742779	0.51415223	0.82305288	0.26998121	4.63	2.0392451	3.53	7.72	
15	6.0741687	0.51202041	0.83483869	0.27248457	4.53	2.0806825	3.6	8.97	
10	6.0742092	0.50852162	0.8382498	0.24220073	4.53	2.1251934	3.68	8.96	
4	6.0741782	0.48903257	0.85139018	0.26591691	4.4	2.158474	3.74	7.45	
powder neutron diffraction, SpcGrp C[B]c									
T (K)	a (Å)	$B_{\text{iso}}^{\text{Cu}}$ (Å ²)	$B_{\text{iso}}^{\text{Mn}}$ (Å ²)	$B_{\text{iso}}^{\text{Sb}}$ (Å ²)	R_{nuc}	$m_{a,b}$ (μ _B)	m_c (μ _B)	m (μ _B)	R_{mag}
55	6.0761395	0.55404925	0.86544943	0.33230948	5.03	0.4350411	1.5054926	1.63	27
50	6.0758438	0.5701288	0.85184997	0.32774517	5.04	0.7752367	1.2371805	1.65	17.7
45	6.0753589	0.50617528	0.81798643	0.29873309	4.86	1.1086326	1.6002047	2.24	11.6
40	6.0750084	0.53705788	0.85115272	0.29085901	4.89	1.3141669	1.8929108	2.65	10.7
35	6.0747461	0.53516823	0.84036738	0.268794	4.58	1.474211	2.0713174	2.94	8.75
30	6.074573	0.51749611	0.84345013	0.25679979	4.7	1.6062658	2.2250774	3.18	9.8
25	6.0743775	0.4956817	0.79997218	0.24398129	4.39	1.7169864	2.3448274	3.38	8.5
20	6.0742788	0.51341236	0.82194215	0.26902881	4.77	1.7323627	2.5610607	3.54	7.8
15	6.0741715	0.51168239	0.83479244	0.27205244	4.58	1.7560335	2.6301689	3.62	8.74
10	6.0742121	0.50761414	0.8365652	0.24099679	4.71	1.7942567	2.6828904	3.69	8.71
4	6.0741796	0.48846105	0.85190696	0.26582801	4.42	1.8248875	2.721916	3.75	7.73

Table 4.3: Refinement of powder x-ray and neutron diffraction data. Errors are small and therefore not noted individually. Typical deviations are $\Delta a < 0.2 \cdot 10^{-4}$ Å, $\Delta B_{\text{iso}} < 3 \cdot 10^{-2}$ Å², and $\Delta m_a, \Delta m_c < 0.1$ μ_B.

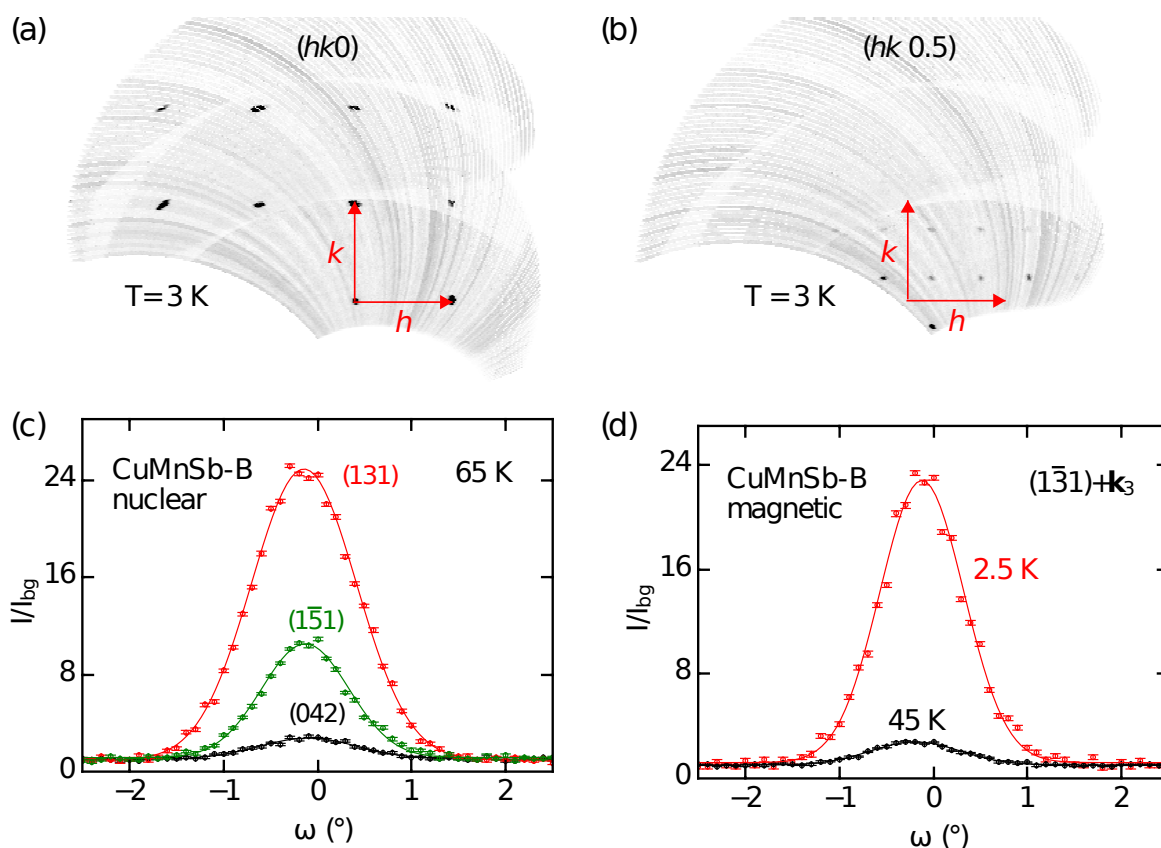


Figure 4.13: Neutron scattering of single crystal CuMnSb-B. (a) Nuclear scattering in the $(hk0)$ scattering plane. (b) Magnetic scattering in the $(hk 0.5)$ scattering plane. Data have been recorded at the RESI diffractometer using an image plate detector, $T = 3$ K. (c) Typical peak profiles of some nuclear reflections recorded at HEiDi, $T = 65$ K. (d) Peak profiles of the magnetic $(1\bar{3}1)$ satellite peak recorded at HEiDi at $T = 45$ K and $T = 2.5$ K.

of the Mn^{2+} ion was used, further assuming that the magnetic moments are located at the Mn sites only. For all refinements extinction effects were found to be negligible. Consequently, any extinction correction was omitted in the interest of simplicity. Tab. 4.4 and Tab. 4.5 summarize the datasets collected at both diffractometers, RESI and HEiDi, and list the key results of the structural refinements. In both Tab. 4.4 and Tab. 4.5 the numbers of nuclear and magnetic reflections fitted are broken down in observed and weak ($I < 3\sigma$) reflections.

The nuclear scattering observed at both instruments is consistent with the $C1_b$ structure as reported in the literature and as confirmed by the powder x-ray and powder neutron diffraction measurements carried out as part of this thesis. The magnetic structure was determined in the spirit of the representation analysis given above, i.e., the three model structures shown in Fig. 4.10 - $R[\text{I}]3c$, $C[\text{B}]c$, and $C[\text{B}]m$ - were checked for their agreement with the experimental data.

The Half-Heusler Antiferromagnet CuMnSb

CuMnSb-B									
SpcGrp SpcGrp $F\bar{4}3m$									
T (K)	#(nuc)	#(mag)	$R(\text{obs})$	$R(\text{all})$	$R_{\text{nuc}}(\text{obs})$	$R_{\text{nuc}}(\text{all})$	$R_{\text{mag}}(\text{obs})$	$R_{\text{mag}}(\text{all})$	
300	37+0		1.44	1.44	1.44	1.44			
160	37+0		3.06	3.06	3.06	3.06			
60	142+0		4.33	4.33	4.33	4.33			
SpcGrp R[$\bar{1}$]3c									
T (K)	#(nuc)	#(mag)	$R(\text{obs})$	$R(\text{all})$	$R_{\text{nuc}}(\text{obs})$	$R_{\text{nuc}}(\text{all})$	$R_{\text{mag}}(\text{obs})$	$R_{\text{mag}}(\text{all})$	
40	83+0	9+0	6.77	6.77	5.27	5.27	46.02	46.02	
3	76+0	21+16	5.17	5.86	4.30	4.30	24.11	36.92	
SpcGrp C[B]m									
T (K)	#(nuc)	#(mag)	$R(\text{obs})$	$R(\text{all})$	$R_{\text{nuc}}(\text{obs})$	$R_{\text{nuc}}(\text{all})$	$R_{\text{mag}}(\text{obs})$	$R_{\text{mag}}(\text{all})$	
40	83+0	10+0	6.69	6.69	5.27	5.27	39.44	39.44	
3	76+0	27+19	5.78	6.72	4.29	4.29	29.53	41.95	
SpcGrp C[B]c									
T (K)	#(nuc)	#(mag)	$R(\text{obs})$	$R(\text{all})$	$R_{\text{nuc}}(\text{obs})$	$R_{\text{nuc}}(\text{all})$	$R_{\text{mag}}(\text{obs})$	$R_{\text{mag}}(\text{all})$	
40	83+0	10+0	6.68	6.68	5.28	5.28	39.15	39.15	
3	76+0	27+19	5.30	6.12	4.30	4.30	21.26	32.61	

Table 4.4: Single crystal neutron diffraction of CuMnSb-B at RESI. Overview of the collected data and the main results of the nuclear and magnetic structure refinement. Values of R_{mag} which are printed in boldface type mark the best magnetic structure refinement for each temperature.

CuMnSb-B									
SpcGrp $F\bar{4}3m$									
T (K)	#(nuc)	#(mag)	$R(\text{obs})$	$R(\text{all})$	$R_{\text{nuc}}(\text{obs})$	$R_{\text{nuc}}(\text{all})$	$R_{\text{mag}}(\text{obs})$	$R_{\text{mag}}(\text{all})$	
65	38+0		2.59	2.59	2.59	2.59			
SpcGrp R[$\bar{1}$]3c									
T (K)	#(nuc)	#(mag)	$R(\text{obs})$	$R(\text{all})$	$R_{\text{nuc}}(\text{obs})$	$R_{\text{nuc}}(\text{all})$	$R_{\text{mag}}(\text{obs})$	$R_{\text{mag}}(\text{all})$	
45	181+0	12+6	4.63	4.75	4.62	4.62	5.28	13.18	
2.5	259+0	15+51	5.04	5.76	4.96	4.96	10.64	34.49	
SpcGrp C[B]m									
T (K)	#(nuc)	#(mag)	$R(\text{obs})$	$R(\text{all})$	$R_{\text{nuc}}(\text{obs})$	$R_{\text{nuc}}(\text{all})$	$R_{\text{mag}}(\text{obs})$	$R_{\text{mag}}(\text{all})$	
45	181+0	14+8	4.77	5.30	4.62	4.62	14.49	42.80	
2.5	259+0	15+51	5.45	6.54	4.96	4.96	39.57	63.28	
SpcGrp C[B]c									
T (K)	#(nuc)	#(mag)	$R(\text{obs})$	$R(\text{all})$	$R_{\text{nuc}}(\text{obs})$	$R_{\text{nuc}}(\text{all})$	$R_{\text{mag}}(\text{obs})$	$R_{\text{mag}}(\text{all})$	
45	181+0	14+8	4.65	4.81	4.62	4.62	6.43	15.19	
2.5	259+0	15+51	4.99	5.73	4.96	4.96	7.47	33.39	

Table 4.5: Single crystal neutron diffraction of CuMnSb-B at HEiDi. Overview of the collected data and the main results of the nuclear and magnetic structure refinement. Values of R_{mag} which are printed in boldface type mark the best magnetic structure refinement for each temperature.

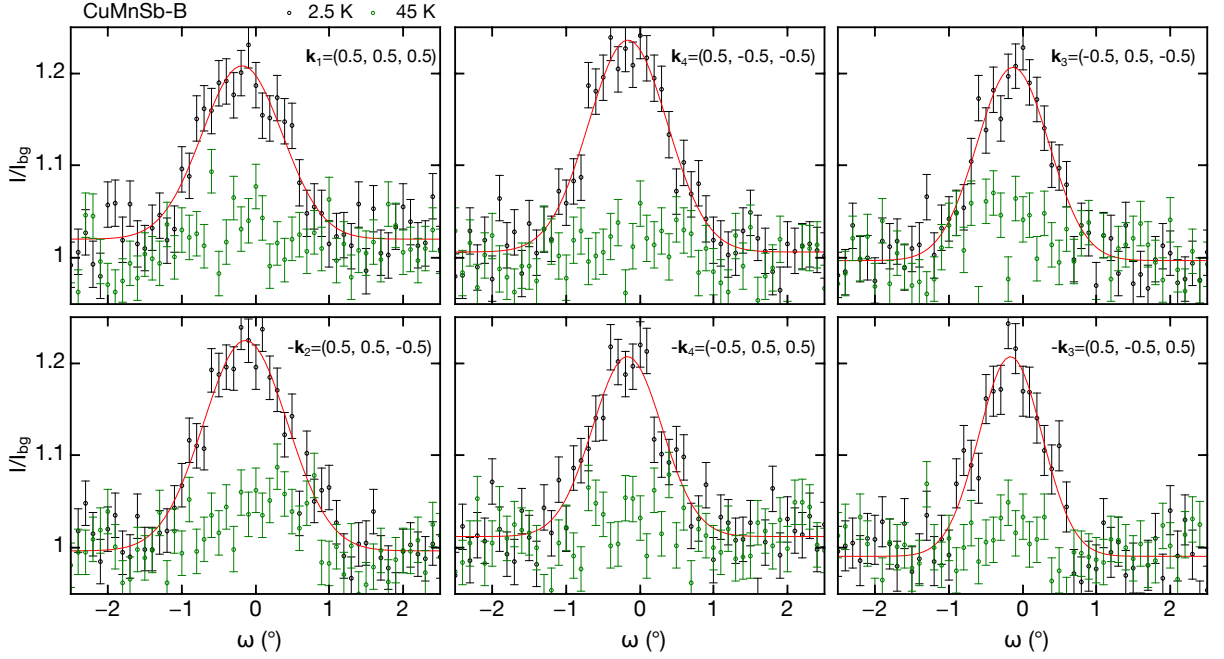


Figure 4.14: Scattering signal of the $\mathbf{k}_1 = (0.5, 0.5, 0.5)$ satellite peak and several equivalent positions for $T = 2.5$ K (black symbols) and $T = 45$ K (green symbols). For comparison data have been normalized to the background intensity. Solid red lines are Gaussian fits to the data at 2.5 K.

Considering first the case of intermediate temperatures, $T^* < T < T_N$, data have been taken at 40 K and 45 K at RESI and HEiDi, respectively. Consistent with the powder diffraction the refinement of both datasets using the C[B]m superspace group results in significantly worse fits than the other Shubnikov groups. Consequently, the magnetic superspace group C[B]m is ruled out as a solution of the magnetic structure.

The R values obtained from refinements based on the R[I]3c and C[B]c superspace groups are ambiguous. While the RESI data favors C[B]c the data recorded at HEiDi is fitted more accurately using the R[I]3c model. The latter solution, i.e., the R[I]3c superspace group, is likely to be the correct one for two reasons. First, slightly more Bragg reflections are included in the refinement of the HEiDi data. Moreover, since these Bragg peaks have been recorded individually using a counter tube detector they are more accurate than the peaks recorded at RESI by means of the image plate detector. Second, even more importantly, the R[I]3c magnetic model structure requires that the Bragg peak at $\mathbf{k} = (0.5, 0.5, 0.5)$ and at all equivalent positions vanishes whereas it may be non-zero for the C[B]c solution. (The C[B]c solution where the intensity at $\mathbf{k} = (0.5, 0.5, 0.5)$ is zero is essentially identical with R[I]3c.) During the experiment carried out at HEiDi the scattering intensity at $(0.5, 0.5, 0.5)$ and several equivalent positions in reciprocal space was therefore carefully checked. As shown in Fig. 4.14 the scattering intensity at all equivalent positions is zero at $T = 45$ K, clearly supporting the R[I]3c structure.

In stark contrast at $T = 2.5$ K distinct Bragg peaks are observed at all equivalent positions. This is consistent with the powder neutron experiments as well as the refinements of the low-temperature single crystal diffraction presented below. Most importantly the appearance of the $(0.5, 0.5, 0.5)$ Bragg peaks unambiguously rules out the $R[\bar{1}]3c$ solution as the magnetic ground state of CuMnSb-B in favor of the $C[B]c$ model, where the magnetic moments are tilted out of the $\langle 111 \rangle$ directions.

Turning now to the low-temperature limit, $T < T^* < T_N$, data have been taken at 3 K and 2.5 K at RESI and HEiDi, respectively. Again refinements on the basis of the $C[B]m$ super-space group are considerably worse than refinements using the other Shubnikov groups. Group $C[B]m$ is hence again ruled out as a solution of the magnetic structure. A comparison of the R values inferred from the refinements using the remaining two space groups, $C[B]c$ and $R[\bar{1}]3c$, demonstrates that the $C[B]c$ symmetry provides better results for both datasets.

The dataset taken at RESI is fitted with a reliability factor $R(\text{obs})=24.11$ for $R[\bar{1}]3c$ but $R(\text{obs})=21.26$ for $C[B]c$, corresponding to an improvement of almost 12 %. From the refinement the ordered moment is inferred as $\mathbf{m}_s = (1.504, 0.752, 3.645) \mu_B/\text{Mn}$ (in hexagonal standard settings), i.e., $m_s = 3.871 \mu_B/\text{Mn}$. This is only slightly larger than suggested by powder neutron diffraction and agrees nicely with the value reported in Ref. [186]. The tilting angle $\alpha = 24.8^\circ$ of the magnetic moment vector with respect to the $\langle 111 \rangle$ direction of the cubic parent cell is large compared to both the powder neutron data and the value obtained from the HEiDi dataset ($\alpha = 14.3^\circ$, see below). This discrepancy may be due to the lower quality of the RESI data which is also suggested by the rather large R factors of the corresponding refinements.

For the dataset recorded at HEiDi, which contains more Bragg reflections and should hence be considered to be statistically more reliable than the RESI data, the R values are much smaller. Here the improvement of $C[B]c$ over $R[\bar{1}]3c$ is even more significant than for the RESI data and amounts to almost 30 %. The ordered moment which may be inferred from the refinement as $\mathbf{m}_s = 0.859, 0.430, 3.767) \mu_B/\text{Mn}$, $m_s = 3.840 \mu_B/\text{Mn}$, is consistent with the findings from the RESI dataset; here the components of the moment vector are again given in hexagonal standard settings. The corresponding tilting angle $\alpha = 14.3^\circ$ agrees nicely with the powder neutron measurements.

Altogether the refinements of the diffraction data recorded at RESI and HEiDi both favor the $C[B]c$ space group as the magnetic ground state of CuMnSb-B. As for the powder neutron data, the $C[B]c$ symmetry is in addition suggested by the appearance of the otherwise forbidden $(0.5, 0.5, 0.5)$ satellite peaks shown in Fig. 4.14.

The temperature dependence of selected nuclear reflections and magnetic satellite peaks was tracked while cooling or heating the sample. Fig. 4.15b shows typical data collected at HEiDi where slow temperature scans of the $(\bar{1}\bar{1}1) - \mathbf{k}_4 = (0.5, -0.5, 1.5)$ magnetic satellite peak were carried out. Data taken upon cooling (empty symbols) and heating (filled symbols) are fully consistent. The onset of long-range magnetic order is marked by a continuous increase of the

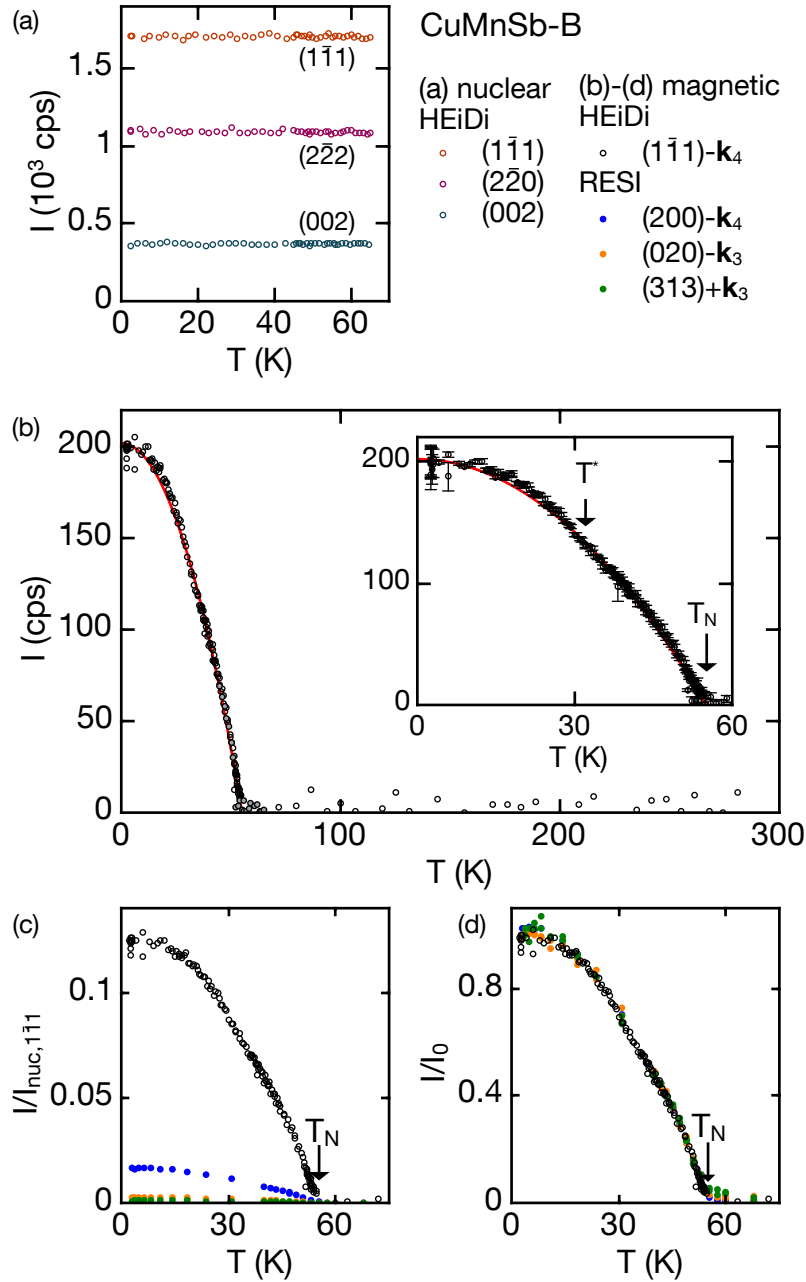


Figure 4.15: Temperature dependence of the elastic neutron scattering of CuMnSb-B. (a) Nuclear scattering close to the onset of long-range magnetic order. No anomalies are observed near T_N . (b) Temperature dependence of a $(1\bar{1}1)$ magnetic satellite peak. The solid red curve corresponds to a parabolic trend, $I \propto 1 - (T/T_N)^2$. Deviations from that curve occur below $T^* = 32$ K (inset). (c) Comparison of several magnetic satellite peaks. Their intensities were scaled to the one of the $(1\bar{1}1)$ nuclear reflection. (d) Scaling the scattering intensity of each individual satellite peak to $I_0 = \lim_{T \rightarrow 0} I$ demonstrates that the temperature dependence is qualitatively identical for all magnetic reflection studied.

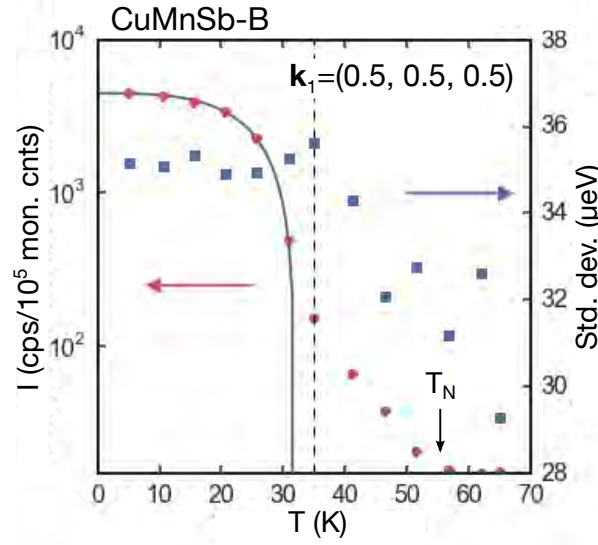


Figure 4.16: Temperature dependence of the $\mathbf{k}_1 = (0.5, 0.5, 0.5)$ magnetic Bragg peak in CuMnSb-B. Figure adapted from Ref. [22].

magnetic scattering below $T_N = 55$ K, characteristic of a second order, magnetic phase transition. No residual intensity is observed above T_N . The value of T_N inferred from the diffraction experiment agrees nicely with the low-temperature bulk and transport data. Below T_N the temperature dependence can be accounted for extremely well by the square of Eq. 4.4 hence suggesting that $I \propto m_s^2 \propto 1 - (T/T_N)^2$ (solid red curve).

As shown in Fig. 4.15c and Fig. 4.15d all satellite peaks studied exhibit the same temperature dependence. This is also in perfect agreement with the temperature dependence of the ordered magnetic moment inferred from powder neutron diffraction, cf. Eq. 4.4. As highlighted in the inset of 4.15b small deviations from the trend occur below $T^* = 32$ K and are presumably attributed to the above-mentioned spin reorientation transition.

As mentioned above the tilting of the magnetic moments below T^* is accompanied by the emergence of the $(0.5, 0.5, 0.5)$ satellite peak, cf. Fig. 4.14. The powder diffraction data allowed to track the reorientation transition temperature to ~ 30 K, suggesting that the re-arrangement of the spin structure also drives the numerous features observed in the bulk and transport data at about $T \approx 35$ K. Due to limitations of beam time, on the one hand, and the low intensity of the $(0.5, 0.5, 0.5)$ satellite peak, on the other hand, it was unfortunately not possible to measure the temperature dependence of this additional Bragg peak in more detail using single crystal samples. However, as part of his Ph.D. thesis PAU JORBA carried out inelastic neutron measurements at the instrument MIRA at the MLZ, Garching [22]. Part of his results are summarized in Fig. 4.16. As indicated by the solid line the intensity of the satellite peak at $\mathbf{k}_1 = (0.5, 0.5, 0.5)$ increases quickly below $T^* = 32$ K. If the standard deviation of the peak is

chosen as criterion for T^* one finds $T^* = 34$ K (vertical dashed line). Both values are in good agreement with the bulk and transport measurements. Consequently the scattering experiment at MIRA underpins the assumption so far inferred only from the powder neutron data, namely that the spin-reorientation transition which was unambiguously identified at low temperatures, can be tracked continuously to an intermediate temperature range. Most importantly the onset temperature T^* coincides with the value of T^* deduced from the bulk and transport data. This finally suggests that the anomalous behavior observed in essentially all low-temperature properties around 32 K originates from the spin reorientation.

Returning to Fig. 4.16 it is noteworthy that on a logarithmic intensity scale the (0.5, 0.5, 0.5) satellite peak is non-zero even in the intermediate temperature range $T^* \leq T \leq T_N$. Its scattering amplitude is extremely small and can therefore only be resolved using large samples in conjunction with a high neutron flux. This prerequisite is typically met in inelastic neutron scattering experiments but rarely during single crystal neutron diffraction, which may explain why the faint satellite at intermediate temperatures could be observed at MIRA but not at RESI, HEiDi, or SPODI. It is interesting to consider possible implications of this finding. In fact the emergence of the (0.5, 0.5, 0.5) satellite peak right below T_N suggests that in the intermediate temperature range $T^* \leq T \leq T_N$ the physical properties of CuMnSb-B are strongly influenced by magnetic fluctuations. This may explain, for instance, the peculiar temperature dependence of the electronic specific heat reported by ANDREAS BAUER [5]. For a deeper understanding of the role of spin fluctuations in CuMnSb further investigation, including neutron diffraction at finite magnetic field as well as detailed inelastic neutron scattering, will be necessary.

In summary the powder and single crystal neutron data recorded as part of this thesis suggest that the magnetic structure of CuMnSb-B changes as a function of temperature. In the temperature range $T^* \leq T \leq T_N$, the spin structure is described by the previously reported type-II AFM(111) arrangement [186]. As shown schematically in Fig. 4.10a this structure is characterized by ferromagnetic (111) planes which are mutually coupled antiferromagnetically, where the moment vectors are oriented perpendicular to the (111) planes. Below T^* the magnetic structure may still be understood in terms of an AFM(111) spin arrangement, i.e., it consists again of ferromagnetic (111) sheets with neighboring sheets coupled antiferromagnetically. However the moment vector is no longer perpendicular on the (111) planes but slightly tilted. The angle of the spin reorientation α is about 14° as inferred from the powder and single crystal neutron diffraction data. The sign of α changes between neighboring (111) planes. Consequently, the spin re-orientation does not result in a net ferromagnetic moment, in contrast to a spin-flop transition.

Altogether our measurements demonstrate that the magnetic ground state of CuMnSb-B differs from the hitherto accepted spin arrangement. Due to the higher crystalline quality of CuMnSb-B when compared to CuMnSb-A or even polycrystalline samples studied elsewhere it seems likely that the magnetic properties of CuMnSb-B are the intrinsic properties of phase-pure CuMnSb

in general. The absence of the T^* spin reorientation transition in previous studies may then be a result of the lower crystalline quality of the previously studied samples.

4.6 Summary

The first experimental investigation of high-quality single crystal CuMnSb were reported. Measurements of the low-temperature bulk and transport properties were carried out on two single crystal ingots CuMnSb-A and CuMnSb-B, grown from a stoichiometric and Sb-rich initial weight, respectively. Distinct differences in the physical properties of both samples may be attributed to the presence of a small Mn_2Sb impurity phase in CuMnSb-A. In contrast the second ingot studied, CuMnSb-B, was phase-pure and hence seems to account best for the intrinsic properties of CuMnSb which will be summarized below.

CuMnSb exhibits the $C1_b$ half-Heusler structure at both ambient and cryogenic temperatures. The onset of long-range magnetic order is reflected in the temperature dependence of the cubic lattice parameter which changes from linear to cubic at $T_N = 55$ K, presumably due to magnetostriction.

The same Néel temperature and a second order, antiferromagnetic phase transition are suggested consistently from the susceptibility, magnetization, electrical transport, and specific heat data. Interestingly, the antiferromagnetic order in CuMnSb features characteristics which are believed to be hallmarks of either local-moment or itinerant magnetism. The following experimental findings are consistent with local-moment magnetism. (i) The temperature dependence of the susceptibility, estimated from the normalized magnetization M/H , exhibits a Curie-Weiss behavior and implies a large, almost integer size of the fluctuating effective moment, $m_{\text{eff}} = 3.95 \mu_B / (\text{f.u.})$. (ii) The latter matches the ordered moment inferred from neutron diffraction data. It is also consistent with the magnetic entropy released at high temperatures. (iii) The Sommerfeld limit of the electronic specific heat is small - characteristic of a metal with weak electronic correlations. (iv) Finally, the long-range magnetic order revealed by neutron diffraction is commensurate with the nuclear lattice. These signatures of local-moment magnetism are contrasted by the comparatively high stability of T_N with respect to high magnetic fields and contributions of magnetic fluctuations in the magnetic entropy and inelastic neutron scattering at temperatures well above T_N , which are characteristic of itinerant electron magnetism.

Magnetization measurements with the magnetic field applied along different high-symmetry directions demonstrate that the magnetic anisotropies are small, as expected for a cubic compound. The ratio $f = \Theta_{CW}/T_N = 3$ suggests moderate geometric frustration, potentially arising from the antiferromagnetic order. Point defects such as vacancies, interstitials, or anti-sites are quite common for Heusler compounds, owing to the good chemical miscibility of the alloyed elements. Consistently a combined analysis of our powder x-ray and neutron data suggests that the dominant point defect in CuMnSb are Cu/Mn swaps which occur with a probability of $\sim 1.5\%$.

No nuclear or magnetic diffuse scattering has been observed, hence ruling out both short-range defect ordering and substantial magnetic frustration.

From pronounced anomalies at $T^* \approx 34$ K in all low-temperature properties studied an additional magnetic transition within the antiferromagnetic phase was identified which has not been reported before. Powder and single crystal neutron diffraction suggest that it is associated with a reorientation of the Mn moment. Below T_N the long-range spin order can be described using the magnetic superspace group $R[\Gamma]3c$. This corresponds to a type-II antiferromagnet where the Mn moments point along $\langle 111 \rangle$, consistent with the literature [186]. At T^* the magnetic moment is canted by about 14° with respect to the initial $\langle 111 \rangle$ orientation and the antiferromagnetic order is described by the Shubnikov group $C[B]c$. The magnetization data corroborate that the spin reorientation does not result in a net ferromagnetic moment, i.e., antiferromagnetically coupled spins are tilted in opposite directions. This very first experimental observation of deviations from the hitherto accepted type-II antiferromagnetism in CuMnSb agrees extremely well with theoretical considerations about the magnetic ground state of CuMnSb put forward by MACA and coworkers [197]. The authors of Ref. [197] argue that the type-II antiferromagnetic order in CuMnSb is in fact energetically unfavorable but gets stabilized in real samples due to crystal defects, notably anti-site disorder. Our findings therefore prove that high-quality samples are essential in order to determine the intrinsic properties of materials which are sensitive to crystalline imperfections, such as many Heusler compounds.

Conclusions

In this thesis three metallic antiferromagnets - CrB₂, MnB₂, and CuMnSb - have been studied. The main results may be summarized as follows.

Our low-temperature bulk, transport, and diffraction measurements establish consistently CrB₂ as a weak itinerant antiferromagnet per excellence. Characteristic features of itinerant magnetism observed in this thesis include a typical metallic resistivity, a comparatively low Néel temperature, a large fluctuating moment which clearly exceeds the ordered moment observed in neutron scattering, incommensurate long-range order, and a remarkable stability of the magnetic order with respect to high fields. CrB₂ may perhaps be the best antiferromagnetic analog of archetypical weak itinerant ferromagnets such as ZrZn₂, Ni₃Al, and MnSi reported so far. Our magnetic neutron diffraction of CrB₂ may be interpreted in terms of a complex triple-k structure which is characterized by 120° correlations and a vortex lattice. As suggested from diffuse neutron scattering the magnetic order may be connected to a nuclear superstructure and short range ordering of defects. A comprehensive series of high-pressure transport measurements finally demonstrates that the itinerant magnetism in CrB₂ is essentially determined by the ratio of the hexagonal lattice constants and may be tuned by means of hydrostatic, uniaxial, and quasi-hydrostatic pressure. Using moderate quasi-hydrostatic pressure CrB₂ can be tuned towards an electronic instability which manifests in the occurrence of a low-temperature resistivity drop. Though ρ stays finite down to the lowest temperatures studied the characteristic shape and magnetic field dependence are strongly suggestive of incipient superconductivity.

Completely different magnetic properties were found in MnB₂, an isostructural sibling of CrB₂. Replacing Cr by Mn, i.e., by adding just one electron, the weak itinerant antiferromagnet CrB₂ is transformed into a high-temperature $T_N \approx 1130$ K local-moment antiferromagnet. This is consistently inferred from low-temperature bulk measurements and neutron scattering data which indicate weak electronic correlations, a large ordered moment and a commensurate antiferromagnetic structure. The seeming inconsistency of a very small low-temperature magnetization

Conclusions

and a ferromagnetic hysteresis below $T_{\text{flop}} \approx 130$ K can be accounted for by a slight spin canting of the otherwise planar magnetic structure formed by Mn moments that lie in the hexagonal basal plane. Moreover, this very first study on large single crystal material allowed to determine the magnetic anisotropies. Consistent with in-plane Mn moments a small easy-plane magnetic anisotropy is observed.

The examination of two single crystal ingots of CuMnSb, where the first one (CuMnSb-A) was grown from a stoichiometric initial composition and the second one (CuMnSb-B) from a Sb-rich mixture of starting elements, revealed distinct differences of their electronic and magnetic properties. These discrepancies arise from tiny amounts of a ferrimagnetic impurity phase, Mn_2Sb , identified in the first sample. In contrast, the second crystal is found to be phase-pure. This suggests that the latter sample displays the intrinsic properties of CuMnSb. Measurements of its low-temperature bulk and transport properties, which were also compared to the properties of CuMnSb-A, reveal characteristics of both local-moment and itinerant antiferromagnetism. Itinerant electron magnetism is suggested by a comparatively low magnetic transition temperature, $T_N = 55$ K, and its weak magnetic field dependence. Several strong arguments, however, corroborate local-moment magnetism. Magnetization measurements on paramagnetic CuMnSb indicate Curie-Weiss behavior and a large effective fluctuating moment which matches the ordered moment almost perfectly. A small Sommerfeld coefficient suggest weak electronic correlations. A local-moment picture is consistently inferred from our magnetic neutron scattering data. The latter can be understood in terms of large Mn moments of $\sim 4 \mu_B$ which develop a commensurate type-II antiferromagnetic order. This structure is characterized by ferromagnetic (111) layers which are mutually coupled antiferromagnetically. The moments are oriented perpendicular to these sheets, i.e., they point along the $\langle 111 \rangle$ directions. In contrast to previous reports on (mostly polycrystalline) CuMnSb, distinct anomalies in essentially all properties studied were observed at $T^* \approx 34$ K in the phase-pure single crystal specimens. These features may be attributed to a low-temperature spin canting transition with no net moment. In fact, our neutron diffraction data demonstrate the spin reorientation unambiguously as the otherwise forbidden (0.5, 0.5, 0.5) magnetic satellite peaks are observed. This first experimental evidence of deviations of the magnetic ground state of CuMnSb from the hitherto accepted type-II antiferromagnetic order is in excellent agreement with a theoretical investigation which claims that the type-II antiferromagnetism in CuMnSb is energetically unfavorable but stabilized in real samples due to crystal defects, notably anti-site disorder [197]. The findings reported in this thesis thus illustrate the strong effect of crystalline imperfections on the electronic and magnetic properties of condensed matter, particularly of Heusler alloys.

Acknowledgments

This thesis would not have been possible without the support, assistance, advice, and collaboration of many helpful colleagues. Particularly I would like to thank the following supporters.

- My Ph.D. supervisor, CHRISTIAN PFLEIDERER, who has always been a great mentor since I joined his work group in 2009. Thank you for giving me all time, scientific and financial support, and motivation needed to carry out this long-term Ph.D. project as well as time-consuming technical side-projects such as the joint development of a novel ADR cryostat.
- PETER BÖNI for providing perfect working conditions at his chair E21 where this Ph.D. project started eight years ago, sharing his entrepreneurial experience, and the awesome speeches at our Christmas parties.
- The E21/E51 work group for providing a fantastic, fruitful working atmosphere which often felt like after-work. Thank you guys for the great technical and scientific exchange. Thank you also for many happy hours, coffee breaks full of provoking political incorrectness, plenty of cake, Weißwurst breakfasts, Burgers, BBQ, birthday parties, Christmas parties, summer parties, triple-d-days, Oktoberfests, and wonderful trips (amongst others) to Cambridge and Tokyo. In particular, I would like to thank ANREAS BAUER for the excellent collaboration on the antiferromagnets and his great support in the paper writing, WOLFGANG SIMETH for providing an analysis of the complex topology of CrB₂ and his support in the analysis of the underlying neutron data, GEORG BENKA for the crystal growth and his measurements of polycrystalline CrB₂, PAU JORBA for his inelastic measurements of CuMnSb and the collaboration on the high-pressure techniques, ALFONSO CHACÓN for long philosophic discussions and his support with the uniaxial pressure apparatus, CHRISTIAN FRANZ and ROBERT RITZ for their advice on high-pressure transport measurements using piston-cylinder and Bridgman pressure cells, TIM ADAMS for his advice on the analysis of the neutron diffraction data, MARKUS KLEINHANS for

Acknowledgments

the magnetization measurements of the frustrated magnets used as cooling media in the ADR cryostats, CHRISTOPHER DUVINAGE and FELIX RUCKER for their advice on measurement techniques but also on family logistics, their excellent technical assistance and the harmonic joint management of the low-temperature laboratories, MICHAEL WAGNER and MARCO HALDER for their support with the vibrating sample magnetometer, once more MARCO HALDER for abundant hands-on coding workshops and wiring tips, and JAN SPALLEK for the great and successful teamwork on the ADR cryostats.

- The working students and Bachelor students I was allowed to work with and who have greatly supported the development of the experimental methods used in this thesis, notably JULIAN BECKER, FLORIAN BUSCHEK, FLORIAN SIGGER, CAROLINA BURGER, LAURA LOHR, NICO HUBER, KLAUS EIBENSTEINER, ANH TONG, SIMON STEINHAUSER, and MICHAEL LAMPL.

STEFAN GIEMSA and ANDREAS MANTWILL for their hands-on help in the laboratories and the machining of mechanical parts on short notice whenever the weekend or a beam time approached.

- The workshop of the Department of Physics, in particular MANFRED PFALLER, MANFRED REITER, and NORBERT HEIMERL, for improving my technical designs and drawings, and the high-quality machining of essentially all parts required for the many experiments and technical developments I carried out during the last years.
- MICHAEL STANGER, KATARZYNA DANIELEWICZ, CLAUDIA SCHWEIGER, and SUSANNE MAYR from the central crystal laboratory of the Department of Physics for cutting, polishing, and orienting numerous samples studied in this thesis as well as the preparation of vast amounts of spare parts used in my high-pressure investigations.
- KARL SYASSEN (Max Planck Institute for Solid State Research, Stuttgart) for his suggestions on the design of the ruby fluorescence manometer set-up during this Ph.D. project. JAMES "JIM" SCHILLING (Washington University in St. Louis) and ANNA KUSMARTSEVA (Loughborough University) for their recommendations for improvements of our Bridgman pressure technique. Thanks to Jim and his Post-Doc PALLAVI MALAVI also for the excellent collaboration on the high-pressure study of CuMnSb.
- The instrument responsables at MLZ involved in the measurements carried out as part of this thesis for their great support during the neutron scattering experiments as well as the data treatment and data analysis thereafter, notably ANATOLIY SENYSHYN (SPODI), BJÖRN PEDERSEN (RESI), MARTIN MEVEN (HEiDi), YIXI SU, and KIRILL NEMKOVSKI (both DNS). Thanks to KLAUDIA HRADIL (X-Ray Center, Technische Universität Wien) and, again, to ANATOLIY SENYSHYN for carrying out the x-ray experiments and for their assistance with the data analysis by means of the FullProf software suite. Moreover, I

would like to thank GEORG BRANDL for the inelastic neutron measurements of CrB₂ and his support with the NICOS instrument control software. Thanks a lot to JÜRGEN PETERS for his great advice and assistance on the installation, operation, and maintenance of our closed-cycle cryocoolers.

- Special thanks go to VACLAV PETŘÍČEK (Institute of Physics of the Czech Academy of Sciences, Prague) who has provided a detailed tutorial on the refinement of the complex magnetic structure of CrB₂ using Jana2006. I am deeply grateful for his commitment, assistance and many fruitful discussions. Without his support the state-of-the-art treatment of our single crystal neutron scattering would not have been possible.
- ACHIM ROSCH (University of Cologne), TED FORGAN (University of Birmingham) and CHRISTIAN BATISTA (University of Tennessee), who strongly supported the study of the topological order of CrB₂.
- Last but not least, my wife and family for their patience and support, notably for days and hours of babysitting which gave me the spare time and ease to finish this project.

Bibliography

- [1] T. Moriya, *Spin Fluctuations in Itinerant Electron Magnetism* (Springer Berlin Heidelberg, 1985).
- [2] G. G. Lonzarich and L. Taillefer, Effect of spin fluctuations on the magnetic equation of state of ferromagnetic or nearly ferromagnetic metals, *J. Phys. C: Solid State Physics* 18, 4339 (1985).
- [3] G. A. Benka, *UHV-compatible arc melting furnace and annealing oven for materials with exotic electronic properties*, Master's thesis, Technische Universität München (2013).
- [4] G. A. Benka, Upcoming Ph.D. thesis, Technische Universität München.
- [5] A. Bauer, *Investigation of itinerant antiferromagnets and cubic chiral helimagnets*, Ph.D. thesis, Technische Universität München (2014).
- [6] K. Endo, T. Ohoyama, and R. Kimura, Antiferromagnetism of CuMnSb, *Journal of the Physical Society of Japan* 25, 907 (1968).
- [7] K. Endo, Magnetic studies of $C1_b$ -compounds CuMnSb, PdMnSb, and $Cu_{1-x}(Ni \text{ or } Pd)_xMnSb$, *Journal of the Physical Society of Japan* 29, 643 (1970).
- [8] J. Bœuf, *Untersuchungen an den antiferromagnetischen Übergangsmetallverbindungen Mn_3Si , $CuMnSb$ und $PdMnTe$* , Ph.d. thesis, Universität (TH) Karlsruhe (2003).
- [9] A. Regnat, *Hochdruckexperimente am itineranten Antiferromagneten CrB_2* , Diploma thesis, Technische Universität München (2010).
- [10] A. Aharoni, Demagnetizing factors for rectangular ferromagnetic prisms, [Journal of Applied Physics](#) 83, 3432 (1998).

Bibliography

- [11] C. Pfeleiderer, A. D. Huxley, and S. M. Hayden, On the use of Cu:Be clamp cells in magnetization and neutron scattering studies, *Journal of Physics: Condensed Matter* **17**, S3111 (2005).
- [12] G. J. Piermarini, S. Block, and J. Barnett, Hydrostatic limits in liquids and solids to 100 kbar, *Journal of Applied Physics* **44**, 5377 (1973).
- [13] V. A. Sidorov and R. A. Sadykov, Hydrostatic limits of fluorinert liquids used for neutron and transport studies at high pressure, *Journal of Physics: Condensed Matter* **17**, S3005 (2005).
- [14] S. Klotz, J.-C. Chervin, P. Munsch, and G. L. Marchand, Hydrostatic limits of 11 pressure transmitting media, *Journal of Physics D: Applied Physics* **42**, 075413 (2009).
- [15] A. Chacón Roldán, *Neutron scattering and susceptibility studies of skyrmion lattices under uniaxial pressure*, Master's thesis, Technische Universität München (2011).
- [16] J. Becker, *Uniaxiale Druckexperimente bei tiefen Temperaturen*, Bachelor's thesis, Technische Universität München (2014).
- [17] C. Pfeleiderer, E. Bedin, and B. Salce, He-activated loading device for low temperature uniaxial and anvil cell pressure experiments, *Review of Scientific Instruments* **68**, 3120 (1997).
- [18] K. Nassau, Synthetic moissanite: a new man-made jewel, *Current Science* **79**, 1572 (2000).
- [19] J.-a. Xu and H.-k. Mao, Moissanite: a window for high-pressure experiments, *Science* **290**, 783 (2000).
- [20] J.-a. Xu, H.-k. Mao, R. J. Hemley, and E. Hines, The moissanite anvil cell: a new tool for high-pressure research, *Journal of Physics: Condensed Matter* **14**, 11543–11548 (2002).
- [21] J.-a. Xu, H.-k. Mao, R. J. Hemley, and E. Hines, Large volume high pressure cell with supported moissanite anvils, *Review of Scientific Instruments* **75** (2004), 10.1063/1.1651634.
- [22] P. Jorba, Upcoming Ph.D. thesis, Technische Universität München.
- [23] M. Wakatsuki, K. Ichinose, and T. Aoki, Notes on compressible gasket and Bridgman-anvil type high pressure apparatus, *Japanese Journal of Applied Physics* **11**, 578 (1972).
- [24] A. K. Bandyopadhyay, S. Chatterjee, E. S. R. Gopal, and S. V. Subramanyam, Optimization of gasket thickness in a bridgman anvil system, *Review of Scientific Instruments* **52**, 1232 (1981).
- [25] T. F. Smith and C. W. Chu, Will pressure destroy superconductivity? *Physical Review* **159**, 353 (1967).

-
- [26] B. Bireckhoven and J. Wittig, A diamond anvil cell for the investigation of superconductivity under pressures of up to 50 GPa: Pb as a low temperature manometer, *Journal of Physics E: Scientific Instruments* 21, 841 (1988).
- [27] G. J. Piermarini, S. Block, J. D. Barnett, and R. A. Forman, Calibration of the pressure dependence of the R1 ruby fluorescence line to 195 kbar, *Journal of Applied Physics* 46, 2774 (1975).
- [28] K. Syassen, Ruby under pressure, *High Pressure Research* 28, 75 (2008).
- [29] F. Sigger, *Rubin-Fluoreszenz-Manometrie bei tiefen Temperaturen*, Bachelor's thesis, Technische Universität München (2013).
- [30] P. Debye, Einige Bemerkungen zur Magnetisierung bei tiefer Temperatur, *Annalen der Physik* 386, 1154 (1926).
- [31] W. F. Giaque, A thermodynamic treatment of certain magnetic effects. A proposed method of producing temperatures considerably below 1° absolute, *Journal of the American Chemical Society* 49, 1864 (1927).
- [32] J. Spallek, *Apparatur für kryogenfreie Experimente bei Temperaturen bis 1 mK*, Bachelor's thesis, Technische Universität München (2011).
- [33] J. Spallek, *Kryogenfreie Experimente an stark korrelierten Elektronensystemen*, Master's thesis, Technische Universität München (2014).
- [34] C. Burger, *A Compact AC Susceptibility Module for Ultra Low Temperatures*, Bachelor's thesis, Technische Universität München (2017).
- [35] C. Duvinage, Upcoming Ph.D. thesis, Technische Universität München.
- [36] J. Rodríguez-Carvajal, Recent advances in magnetic structure determination by neutron powder diffraction, *Physica B* 192, 55 (1993).
- [37] V. Petříček, M. Dušek, and L. Palatinus, Crystallographic computing system JANA2006: General features, *Zeitschrift für Kristallographie - Crystalline Materials* 229, 345–352 (2014).
- [38] M. Hoelzel, A. Senyshyn, and O. Dolotko, SPODI: High resolution powder diffractometer, *Journal of large-scale research facilities* 1 (2015).
- [39] B. Pedersen, RESI: Thermal neutron single crystal diffractometer, *Journal of large-scale research facilities* 1 (2015).
- [40] M. Meven and A. Sazonov, HEiDi: Single crystal diffractometer at hot source, *Journal of large-scale research facilities* 1 (2015).

Bibliography

- [41] A. J. M. Duisenberg, L. M. J. Kroon-Batenburg, and A. M. M. Schreurs, An intensity evaluation method: *EVAl-14*, *Journal of Applied Crystallography* **36**, 220 (2003).
- [42] M. S. Lehmann and F. K. Larsen, A method for location of the peaks in step-scan measured Bragg reflexions, *Acta Crystallographica Section A* **30**, 580 (1974).
- [43] Y. Su, K. Nemkovskiy, and S. Demirdiř, DNS: Diffuse scattering neutron time-of-flight spectrometer, *Journal of large-scale research facilities* **1** (2015).
- [44] O. Schärpf and H. Capellmann, The XYZ-difference method with polarized neutrons and the separation of coherent, spin incoherent, and magnetic scattering cross sections in a multidetector, *Physica Status Solidi (a)* **135**, 359 (1993).
- [45] R. Schedler, U. Witte, M. Rotter, M. Doerr, M. Loewenhaupt, and J. Kulda, CeCu₂-crystal field transition matrix elements determined by polarized neutron spectroscopy, *Physica B: Condensed Matter* **350**, E107 (2004), proceedings of the Third European Conference on Neutron Scattering.
- [46] P. M. De Wolff, The pseudo-symmetry of modulated crystal structures, *Acta Crystallographica Section A* **30**, 777 (1974).
- [47] P. M. De Wolff, Symmetry operations for displacively modulated structures, *Acta Crystallographica Section A* **33**, 493 (1977).
- [48] T. Wagner and A. Schönleber, A non-mathematical introduction to the superspace description of modulated structures, *Acta Crystallographica Section B* **65**, 249 (2009).
- [49] B. J. Campbell, H. T. Stokes, D. E. Tanner, and D. M. Hatch, *ISODISPLACE*: a web-based tool for exploring structural distortions, *Journal of Applied Crystallography* **39**, 607 (2006).
- [50] E. A. Knyshev, V. M. Novgorodtsev, U. S. Plyshevski, V. A. Kobayakov, Z. G. Stepanova, V. V. Svistunov, and A. R. Becketov, Synthesis of transition metal borides and their properties, *Journal of the Less-Common Metals* **47**, 273 (1976).
- [51] W. Gordon Jr. and S. B. Soffer, A galvanomagnetic investigation of TiB₂, NbB₂ and ZrB₂, *Journal of Physics and Chemistry of Solids* **36**, 627 (1975).
- [52] S. H. Liu, L. Kopp, W. B. England, and H. W. Myron, Energy bands, electronic properties and magnetic ordering of CrB₂, *Physical Review B* **11**, 3463 (1975).
- [53] D. R. Armstrong, The electronic structure of the first-row transition-metal diborides, *Theoretica Chimica Acta* **64**, 137 (1983).

-
- [54] X.-B. Wang, D.-C. Tian, and L.-L. Wang, The electronic structure and chemical stability of the AlB_2 -type transition-metal diborides, *Journal of Physics: Condensed Matter* **6**, 10185 (1994).
- [55] P. Vajeeston, P. Ravindran, C. Ravi, and R. Asokamani, Electronic structure, bonding, and ground-state properties of AlB_2 -type transition-metal diborides, *Physical Review B* **63**, 045115 (2001).
- [56] J. Nagamatsu, N. Nakagawa, T. Muranaka, Y. Zenitani, and J. Akimitsu, Superconductivity at 39 K in MgB_2 , *Nature* **410**, 63 (2001).
- [57] C. Buzea and T. Yamashita, Review of the superconducting properties of MgB_2 , *Superconductor Science and Technology* **14**, R115 (2001).
- [58] L. Leyarovska and E. Leyarovski, A search for superconductivity below 1 K in transition metal borides, *Journal of the Less-Common Metals* **67**, 249 (1979).
- [59] A. Yamamoto, C. Takao, T. Masui, M. Izumi, and S. Tajima, High-pressure synthesis of superconducting $Nb_{1-x}B_2$ ($x=0-0.48$) with the maximum $T_c = 9.2$ K, *Physica C: Superconductivity* **383**, 197 (2002).
- [60] H. Takeya, K. Togano, Y. S. Sung, T. Mochiku, and K. Hirata, Metastable superconductivity in niobium diborides, *Physica C* **408–410**, 144 (2004).
- [61] C. A. Nunes, D. Kaczorowski, P. Rogl, M. R. Baldissera, P. A. Suzuki, G. C. Coelho, A. Grytsiv, G. André, F. Boureé, and S. Okada, The NbB_2 -phase revisited: Homogeneity range, defect structure, superconductivity, *Acta Materialia* **53**, 3679 (2005).
- [62] V. A. Gasparov, N. S. Sidorov, I. I. Zver'kova, and M. P. Kulakov, Electron transport in diborides: Observation of superconductivity in ZrB_2 , *Pis'ma v ZhETF* **73**, 601 (2001).
- [63] V. A. Gasparov, N. S. Sidorov, and I. I. Zver'kova, Two-gap superconductivity in ZrB_{12} : Temperature dependence of critical magnetic fields in single crystals, *Physical Review B* **73**, 094510 (2006).
- [64] Y. Singh, A. Niazi, M. D. Vannette, R. Prozorov, and D. C. Johnston, Superconducting and normal-state properties of the layered boride OsB_2 , *Physical Review B* **76**, 214510 (2007).
- [65] Y. Singh, C. Martin, S. L. Bud'ko, A. Ellern, R. Prozorov, and D. C. Johnston, Multi-gap superconductivity and Shubnikov-de Haas oscillations in single crystals of the layered boride OsB_2 , arXiv:1006.5651 (2010).
- [66] V. V. Novikov and A. V. Matovnikov, Low-temperature heat capacity of dysprosium diboride, *Journal of Thermal Analysis and Calorimetry* **88**, 597 (2007).

Bibliography

- [67] V. Novikov and T. Chukina, Anomalies of thermal expansion and change of entropy of rare-earth diborides at the temperatures of magnetic transitions, *Physica Status Solidi B* **248**, 136 (2011).
- [68] T. Mori, T. Takimoto, A. Leithe-Jasper, R. Cardoso-Gil, W. Schnelle, G. Auffermann, H. Rosner, and Y. Grin, Ferromagnetism and electronic structure of TmB_2 , *Physical Review B* **79**, 104418 (2009).
- [69] T. Mori, Boron rich solids - sensors, ultra high temperature ceramics, thermoelectrics, armor, (OS Press, Amsterdam, and Springer, Dordrecht, in conjunction with the NATO Public Diplomacy Division, 2009) Chap. Magnetic and Thermoelectric Properties of Boron-Rich Solids, pp. 63–82.
- [70] M. Avila, S. Bud'ko, C. Petrovic, R. Ribeiro, P. Canfield, A. Tsvyashchenko, and L. Fomicheva, Synthesis and properties of YbB_2 , *Journal of Alloys and Compounds* **358**, 56 (2003).
- [71] R. G. Barnes and R. B. Creel, Chromium-like antiferromagnetic behavior of CrB_2 , *Physics Letters* **29 A**, 203 (1969), also shows NMR data an MnB_2 .
- [72] J. Castaing, R. Caudron, G. Toupance, and P. Costa, Electronic structure of transition metal diborides, *Solid State Communications* **7**, 1453 (1969).
- [73] M. Kasaya and T. Hihara, Magnetic structure of MnB_2 , *Journal of the Physical Society of Japan* **29**, 336 (1970).
- [74] S. Khmelevskiy and P. Mohn, Magnetic ordering in MnB_2 : an ab initio study, *Solid State Communications* **113**, 509–512 (2000).
- [75] R. Kiessling, The binary system Chromium-Boron. I. phase analysis and structure of the ζ - and θ -phases, *Acta Chemica Scandinavica* **3**, 160 (1949).
- [76] R. Kiessling, The borides of some transition elements, *Acta Chemica Scandinavica* **4**, 160 (1950).
- [77] S. Funahashi, Y. Hamaguchi, T. Tanaka, and E. Bannai, Helical magnetic structure in CrB_2 , *Solid State Communications* **23**, 859 (1977).
- [78] S. Okada, K. Kudou, K. Iizumi, K. Kudaka, I. Higashi, and T. Lundström, Single-crystal growth and properties of CrB , Cr_3B_4 , Cr_2B_3 and CrB_2 from high-temperature aluminum solutions, *Journal of Crystal Growth* **166**, 429 (1996).
- [79] M. C. Cadeville, Propriétés magnetiques des diborures de manganese et de chrome: MnB_2 et CrB_2 , *Journal of Physics and Chemistry of Solids* **27**, 667 (1965).

- [80] J. Castaing, Ph.D. thesis, University of Paris (1971).
- [81] E. Kaya, Y. Kousaka, K. Kakurai, M. Takeda, and J. Akimitsu, Spherical neutron polarimetry studies on the magnetic structure of single crystal $\text{Cr}_{1-x}\text{Mo}_x\text{B}_2$ ($x=0, 0.15$), [Physica B: Condensed Matter 404, 2524 \(2009\)](#), proceedings of the 7th International Workshop on Polarized Neutrons for Condensed Matter Investigations and 2nd International Symposium of Quantum Beam Science Directorate.
- [82] C. Michioka, Y. Itoh, K. Yoshimura, Y. Watabe, Y. Kousaka, H. Ichikawa, and J. Akimitsu, NMR studies of single crystal chromium diboride, [Journal of Magnetic Materials 310, 620 \(2007\)](#).
- [83] F. Borsa and R. G. Lecander, Enhancement of the ^{11}B nuclear relaxation in CrB_2 near the antiferromagnetic transition, [Solid State Communications 20, 389 \(1976\)](#).
- [84] Y. Kitaoka, H. Yasuoka, T. Tanaka, and Y. Ishizawa, Nuclear magnetic resonance of ^{11}B in CrB_2 , [Solid State Communications 26, 87 \(1978\)](#).
- [85] Y. Kitaoka and H. Yasuoka, NMR-investigations on the spin fluctuations in itinerant antiferromagnets. III. CrB_2 , [Journal of the Physical Society of Japan 49, 493 \(1980\)](#).
- [86] S. Ogawa, Thermal expansion of ZrZn_2 , [Physica B 119, 68 \(1983\)](#).
- [87] M. Shimizu, Magnetovolume effects in itinerant electron ferromagnets, [Journal of Magnetism and Magnetic Materials 20, 47 \(1980\)](#).
- [88] Y. Nishihara, M. Tokumoto, Y. Yamaguchi, and S. Ogawa, Magneto-volume effect of the itinerant-electron antiferromagnet CrB_2 , [Journal of the Physical Society of Japan 4, 1562 \(1987\)](#).
- [89] J. Castaing, J. Danan, and M. Rieux, Calorimetric and resistive investigation of the magnetic properties of CrB_2 , [Solid State Communications 10, 563 \(1972\)](#).
- [90] J. Castaing, P. Costa, M. Heriter, and P. Lederer, Spin fluctuation effects in nearly antiferromagnetic vanadium and chromium diborides, [Journal of Physics and Chemistry of Solids 33, 533 \(1972\)](#).
- [91] C. N. Guy, The electronic properties of chromium borides, [Journal of Physics and Chemistry of Solids 37, 1005 \(1976\)](#).
- [92] T. Tanaka, H. Nozaki, E. Bannai, Y. Ishizawa, S. Kawai, and T. Yamane, Preparation and properties of CrB_2 single crystals, [Journal of the Less-Common Metals 50, 15 \(1976\)](#).
- [93] G. Balakrishnan, S. Majumdar, M. R. Lees, and D. Mck. Paul, Single crystal growth of CrB_2 using a high-temperature image furnace, [Journal of Crystal Growth 274, 294 \(2005\)](#).

Bibliography

- [94] G. E. Grechnev, A. V. Fedorchenko, A. V. Logosha, A. S. Panfilov, I. V. Svechkarev, V. B. Filippov, A. B. Lyashchenko, and A. V. Evdokimanov, Electronic structure and magnetic properties of transition metal diborides, *Journal of Alloys and Compounds* 481, 75 (2009).
- [95] N. L. Okamoto, M. Kusakari, K. Tanaka, H. Inui, and S. Otani, Anisotropic elastic constants and thermal expansivities in monocrystal CrB₂, TiB₂, and ZrB₂, *Acta Materialia* 58, 76 (2010).
- [96] K. Tanaka, S. Tsutsui, N. L. Okamoto, H. Inui, and A. Q. Baron, Difference in elastic properties of CrB₂ determined by microscopic and macroscopic measurements, in *Material Research Society Symposium Proceedings*, Vol. 1528 (2013).
- [97] G. E. Grechnev, A. S. Panfilov, A. V. Fedorchenko, V. B. Filippov, A. B. Lyashchenko, and A. N. Visiliev, Effect of pressure on the magnetic properties of CrB₂, *Low Temperature Physics* 35, 531 (2009).
- [98] A. Bauer, A. Regnat, C. G. F. Blum, S. Gottlieb-Schönmeyer, B. Pedersen, M. Meven, S. Wurmehl, J. Kuneš, and C. Pfleiderer, Low-temperature properties of single-crystal CrB₂, *Physical Review B* 90, 064414 (2014).
- [99] G. Brandl, Upcoming Ph.D. thesis, Technische Universität München.
- [100] M. Brasse, L. Chioncel, J. Kuneš, A. Bauer, A. Regnat, C. G. F. Blum, S. Wurmehl, C. Pfleiderer, M. A. Wilde, and D. Grundler, De Haas-van Alphen effect and Fermi surface properties of single-crystal CrB₂, *Physical Review B* 88, 155138 (2013).
- [101] M. Brasse, *Magnetization of correlated electron systems: MnSi thin films, CrB₂ single crystals and two-dimensional electron systems in MgZnO/ZnO*, Ph.D. thesis, Technische Universität München, München (2014).
- [102] P. A. Sharma, N. Hur, Y. Horibe, C. H. Chen, B. G. Kim, S. Guha, M. Z. Cieplak, and S.-W. Cheong, Percolative superconductivity in Mg_{1-x}B₂, *Physical Review Letters* 89, 167003 (2002).
- [103] G. Venturini, I. Ijjaali, and B. Malaman, Vacancy ordering in AlB₂-type RGe_{2-x} compounds (R=Y,Nd,Sm,Gd-Lu), *Journal of Alloys and Compounds* 284(1-2), 262 (1999).
- [104] P. H. Tobash, D. Lins, S. Bobev, N. Hur, J. D. Thompson, and J. L. Sarrao, Vacancy ordering in SmGe_{2-x} and GdGe_{2-x} (x = 0.33): Structure and properties of two Sm₃Ge₅ polymorphs and of Gd₃Ge₅, *Inorganic Chemistry* 48, 7286–7294 (2006).
- [105] E. S. Penev, S. Bhowmick, A. Sadrzadeh, and B. I. Yakobson, Polymorphism of two-dimensional boron, *Nano Letters* 12, 2441 (2012).

-
- [106] M. Widom and M. Mihalkovič, Symmetry-broken crystal structure of elemental boron at low temperature, [Physical Review B 77, 064113 \(2008\)](#).
- [107] J. Christensen, S. Lidin, B. Malaman, and G. Venturini, Vacancy-ordering effects in AlB_2 -type $ErGe_{2-x}$ ($0.4 < x \leq 0.5$), [Acta Crystallographica B64, 272 \(2008\)](#).
- [108] M. Dahlqvist, U. Jansson, and J. Rosen, Influence of boron vacancies on phase stability, bonding and structure of MB_2 ($M=Ti, Zr, Hf, V, Nb, Ta, Cr, Mo, W$) with AlB_2 type structure, [Journal of Physics: Condensed Matter 27, 435702 \(2015\)](#).
- [109] G. Oszlányi and A. Süto, Ab initio structure solution by charge flipping, [Acta Crystallographica Section A 60, 134 \(2004\)](#).
- [110] L. Palatinus and G. Chapuis, *SUPERFLIP* – a computer program for the solution of crystal structures by charge flipping in arbitrary dimensions, [Journal of Applied Crystallography 40, 786 \(2007\)](#).
- [111] H. Kawamura and S. Miyashita, Phase transition of the two-dimensional Heisenberg antiferromagnet on the triangular lattice, [Journal of the Physical Society of Japan 53, 4138 \(1984\)](#).
- [112] M. Becker, M. Hermanns, B. Bauer, M. Garst, and S. Trebst, [Spin-orbit physics of \$j=1/2\$ mott insulators on the triangular lattice](#), (2015).
- [113] W. Simeth, Upcoming Ph.D. thesis, Technische Universität München.
- [114] S. Mühlbauer, B. Binz, F. Jonietz, C. Pfleiderer, A. Rosch, A. Neubauer, R. Georgii, and P. Böni, Skyrmion lattice in a chiral magnet, [Science 323, 915 \(2009\)](#).
- [115] W. Münzer, A. Neubauer, T. Adams, S. Mühlbauer, C. Franz, F. Jonietz, R. Georgii, P. Böni, B. Pedersen, M. Schmidt, A. Rosch, and C. Pfleiderer, Skyrmion lattice in the doped semiconductor $Fe_{1-x}Co_xSi$, [Phys. Rev. B 81, 041203 \(R\) \(2010\)](#).
- [116] X. Z. Yu, Y. Onose, N. Kanazawa, J. H. Park, J. H. Han, Y. Matsui, N. Nagaosa, and Y. Tokura, Real-space observation of a two-dimensional skyrmion crystal, [Nature 465, 901 \(2010\)](#).
- [117] X. Z. Yu, N. Kanazawa, Y. Onose, K. Kimoto, W. Z. Zhang, S. Ishiwata, Y. Matsui, and Y. Tokura, Near room-temperature formation of a skyrmion crystal in thin-films of the helimagnet FeGe, [Nat. Mater. 10, 106 \(2011\)](#).
- [118] S. Seki, X. Z. Yu, S. Ishiwata, and Y. Tokura, Observation of skyrmions in a multiferroic material, [Science 336 \(2012\), 10.1126/science.1214143](#).

Bibliography

- [119] Y. Tokunaga, X. Z. Yu, J. S. White, H. M. Rønnow, D. Morikawa, Y. Taguchi, and Y. Tokura, A new class of chiral materials hosting magnetic skyrmions beyond room temperature, *Nat. Commun.* **6**, 7638 (2015).
- [120] A. Neubauer, C. Pfleiderer, B. Binz, A. Rosch, R. Ritz, P. G. Niklowitz, and P. Böni, Topological hall effect in the A phase of MnSi, *Phys. Rev. Lett.* **102**, 186602 (2009).
- [121] T. Schulz, R. Ritz, A. Bauer, M. Halder, M. Wagner, C. Franz, C. Pfleiderer, K. Everschor, M. Garst, and A. Rosch, Emergent electrodynamics of skyrmions in a chiral magnet, *Nature Phys.* **8**, 301 (2012).
- [122] C. Franz, F. Freimuth, A. Bauer, R. Ritz, C. Schnarr, C. Duvinage, T. Adams, S. Blügel, A. Rosch, Y. Mokrousov, and C. Pfleiderer, Real-space and reciprocal-space berry phases in the hall effect of $\text{Mn}_{1-x}\text{Fe}_x\text{Si}$, *Phys. Rev. Lett.* **112**, 186601 (2014).
- [123] M. Mochizuki, Spin-wave modes and their intense excitation effects in skyrmion crystals, *Phys. Rev. Lett.* **108**, 017601 (2012).
- [124] Y. Onose, Y. Okamura, S. Seki, S. Ishiwata, and Y. Tokura, Observation of magnetic excitations of skyrmion crystal in a helimagnetic insulator Cu_2OSeO_3 , *Phys. Rev. Lett.* **109**, 037603 (2012).
- [125] T. Schwarze, J. Waizner, M. Garst, A. Bauer, I. Stasinopoulos, H. Berger, A. Rosch, C. Pfleiderer, and D. Grundler, Universal helimagnon and skyrmion excitations in metallic, semiconducting and insulating chiral magnets, *Nature Mater.* **14**, 478 (2015).
- [126] A. V. Fedorchenko, G. E. Grechnev, A. S. Panfilov, A. V. Logosha, I. V. Svechkarev, V. B. Filippov, A. B. Lyashchenko, and A. V. Evdokimanov, Anisotropy of the magnetic properties and the electronic structure of transition-metal diborides, *Low Temperature Physics* **35**, 862 (2009).
- [127] A. P. Ramirez, Strongly geometrically frustrated magnets, *Annual Review of Materials Science* **24**, 453 (1994).
- [128] M. E. Fisher and J. S. Langer, Resistive anomalies at magnetic critical points, *Physical Review Letters* **20**, 665 (1968).
- [129] E. Fawcett, Spin-density-wave antiferromagnetism in chromium, *Review of Modern Physics* **60**, 209 (1988).
- [130] A. C. Jacko, J. O. Fjaerestad, and B. J. Powell, A unified explanation of the Kadowaki-Woods ratio in strongly correlated metals, *Nature Physics* **5**, 422 (2009).

-
- [131] S. M. Hayden, R. Double, G. Aeppli, T. G. Perring, and E. Fawcett, Strongly enhanced magnetic excitations near the quantum critical point of $\text{Cr}_{1-x}\text{V}_x$ and why strong exchange enhancement need not imply heavy-fermion behavior, [Physical Review Letters](#) **84**, 999 (2000).
- [132] T. Moriya and K. Ueda, Antiferromagnetic spin fluctuation and superconductivity, [Reports on Progress in Physics](#) **66**, 1299 (2003).
- [133] K. Kadowaki and S. B. Woods, Universal relationship of the resistivity and specific heat in heavy-fermion compounds, *Solid State Communications* **58**, 507 (1986).
- [134] P. Monthoux, D. Pines, and L. G. G., Superconductivity without phonons, *Nature* **450**, 1177 (2007).
- [135] C. Pfeleiderer, Superconducting phases of f -electron compounds, *Review of Modern Physics* **81**, 1551 (2009).
- [136] J. L. Sarrao and J. D. Thompson, Superconductivity in cerium- and plutonium-based '115' materials, *Journal of the Physical Society of Japan* **76**, 051013 (2007).
- [137] A. M. Clogston, Upper limit for the critical field in hard superconductors, *Physical Review Letters* **9**, 266 (1962).
- [138] N. R. Werthamer, E. Helfand, and P. C. Hohenberg, Temperature and purity dependence of superconducting critical field, H_{c2} . III. Electron spin and spin-orbit effects, *Physical Review* **147**, 295 (1966).
- [139] D. Saint-James and P. G. de Gennes, Onset of superconductivity in decreasing fields, *Physics Letters* **7**, 306 (1963).
- [140] J. R. Waldram, *Superconductivity of metals and cuprates*, edited by Institute of Physics Publishing (Institute of Physics Publishing, 1996).
- [141] M. Tinkham, *Introduction to superconductivity*, edited by B. Bayne and M. Gardner (McGraw-Hill, 1975).
- [142] M. S. Torikachvili, S. L. Bud'ko, N. Ni, and P. C. Canfield, Pressure induced superconductivity in CaFe_2As_2 , [Physical Review Letters](#) **101**, 057006 (2008).
- [143] P. Monthoux and G. G. Lonzarich, Density-fluctuation-mediated superconductivity, [Physical Review B](#) **69**, 064517 (2004).
- [144] S. Deemyad, T. Tomita, J. Hamlin, B. Beckett, J. Schilling, D. Hinks, J. Jorgensen, S. Lee, and S. Tajima, Dependence of the superconducting transition temperature of single and polycrystalline MgB_2 on hydrostatic pressure, [Physica C](#) **385**, 105 (2003).

Bibliography

- [145] M. Mudgel, V. Awana, G. Bhalla, and H. Kishan, Superconductivity of non-stoichiometric intermetallic compound NbB₂, [Solid State Communications 147, 439 \(2008\)](#).
- [146] T. Takahashi, S. Kawamata, S. Noguchi, and T. Ishida, Superconductivity and crystal growth of NbB₂, [Physica C 426–431, Part 1, 478 \(2005\)](#).
- [147] S. T. Renosto, H. Consonline, C. A. M. dos Santos, J. Albino Aguiar, S.-G. Jung, J. Vanacken, V. V. Moshchalkov, Z. Fisk, and A. J. S. Machado, Evidence of multiband behavior in the superconducting alloy Zr_{0.96}V_{0.04}B₂, [Physical Review B 87, 174502 \(2013\)](#).
- [148] N. Barbero, T. Shiroka, B. Delley, T. Grant, A. J. S. Machado, Z. Fisk, H.-R. Ott, and J. Mesot, Doping-induced superconductivity of ZrB₂ and HfB₂, [Physical Review B 95, 094505 \(2017\)](#).
- [149] S. Aydin and M. Simsek, First-principles calculations of MnB₂, TcB₂, and ReB₂ within the ReB₂-type structure, [Physical Review B 80, 134107 \(2009\)](#).
- [150] W. J. Duncan, O. P. Welzel, X. F. Wang, X. H. Chen, F. M. Grosche, and P. G. Niklowitz, High pressure study of BaFe₂As₂ - the role of hydrostaticity and uniaxial stress, [Journal of Physics: Condensed Matter 22, 1 \(2010\)](#).
- [151] H. Kotegawa, T. Kawazoe, H. Sugawara, K. Murata, and H. Tou, Effect of uniaxial stress for pressure-induced superconductor SrFe₂As₂, [Journal of the Physical Society of Japan 78, 083702 \(2009\)](#).
- [152] J. S. Schilling and S. Klotz, The influence of high pressure on the superconducting and normal properties of high temperature superconductors, in *Physical Properties of High Temperature Superconductors III*, edited by D. M. Ginsberg (World Scientific Publishing Co. Pte. Ltd., 1992) Chap. 2, pp. 59–158.
- [153] S. Bud'ko, O. Nakamura, J. Guimpel, M. Maple, and I. K. Schuller, Anisotropic pressure dependence of the critical temperature of REBa₂Cu₃O_{7- δ} , [Physica C 185, 1947 \(1991\)](#).
- [154] A. A. R. Fernandes, J. Santamaria, S. L. Bud'ko, O. Nakamura, J. Guimpel, and I. K. Schuller, Effect of physical and chemical pressure on the superconductivity of high-temperature oxide superconductors, [Physical Review B 44, 7601 \(1991\)](#).
- [155] E. D. Bauer, J. D. Thompson, J. L. Sarrao, L. A. Morales, F. Wastin, J. Rebizant, J. C. Griveau, P. Javorsky, P. Boulet, E. Colineau, G. H. Lander, and G. R. Stewart, Structural tuning of unconventional superconductivity in PuMGa₅ (M=Co, Rh), [Physical Review Letters 93, 147005 \(2004\)](#).

-
- [156] F. Wastin, P. Boulet, J. Rebizant, E. Colineau, and G. H. Lander, Advances in the preparation and characterization of transuranium systems, *Journal of Physics: Condensed Matter* **15**, S2279 (2003).
- [157] P. G. Pagliuso, C. Petrovic, R. Movshovich, D. Hall, M. F. Hundley, J. L. Sarrao, J. D. Thompson, and Z. Fisk, Coexistence of magnetism and superconductivity in $\text{CrRh}_{1-x}\text{Ir}_x\text{In}_5$, *Physical Review B* **64**, 100503 (2001).
- [158] A. Demuer, A. T. Holmes, and D. Jaccard, Strain enhancement of superconductivity in CePd_2Si_2 under pressure, *Journal of Physics: Condensed Matter* **14**, 529 (2002).
- [159] A. T. Holmes, D. Jaccard, H. S. Jeevan, C. Geibel, and M. Ishikawa, Anisotropy, disorder, and superconductivity in CeCu_2Si_2 under high pressure, *Journal of Physics: Condensed Matter* **17**, 5423 (2005).
- [160] I. Binder and B. Post, Manganese diboride, *Acta Crystallographica* **13**, 356 (1960).
- [161] A. L. Bowman and N. G. Nereson, Low-temperature thermal expansion of MnB_2 , *AIP Conference Proceedings* **17**, 34 (1974).
- [162] B. Wang, X. Li, Y. X. Wang, and Y. F. Tu, Phase stability and physical properties of manganese borides: A first-principles study, *The Journal of Physical Chemistry C* **115**, 21429 (2011).
- [163] H. Okamoto, *Desk Handbook: Phase Diagrams for Binary Alloys* (ASM International, 2010).
- [164] E. Wedekind, Magnetochemische Untersuchungen. 1. Mitteilung: Die ferromagnetischen Die Ferromagnetischen Verbindungen des Mangans mit Bor, Antimon und Phosphor, *Berichte der deutschen chemischen Gesellschaft* **40**, 1259 (1907).
- [165] F. Heusler and E. Take, The nature of the Heusler alloys, *Trans. Faraday Soc.* **8**, 169 (1912).
- [166] F. Heusler, Zur Geschichte der Heuslerschen ferromagnetischen Manganlegierungen. II. *Angewandte Chemie* **26**, 96 (1913).
- [167] A. Binet du Jassonneix, Über die Darstellung und die Eigenschaften der Manganboride MnB und MnB_2 , *Berichte der deutschen chemischen Gesellschaft* **40**, 3193 (1907).
- [168] L. Andersson, B. Dellby, and H. P. Myers, Ferromagnetic mnb_2 , *Solid State Communications* **4**, 77 (1966).
- [169] M. Kasaya, T. Hihara, and Y. Kōi, NMR study in MnB_2 , *Journal of the Physical Society of Japan* **26**, 1549 (1969).

Bibliography

- [170] E. Legrand and S. Neov, Neutron diffraction study of MnB_2 , *Solid State Communications* 10, 883 (1972).
- [171] S. Khmelevskiy and P. Mohn, Covalent magnetism, exchange interactions and anisotropy of the high temperature layered antiferromagnet MnB_2 , *Journal of Physics: Condensed Matter* 24, 016001 (2011).
- [172] A. R. Williams, R. Zeller, V. L. Moruzzi, C. D. G. Jr., and J. Kübler, Covalent magnetism: An alternative to the Stoner model, *Journal of Applied Physics* 52, 2067 (1981).
- [173] A. Cely, L.-E. Tergenius, and T. Lundstrom, Microhardness measurements and phase analytical studies in the Mn-B system, *Journal of the Less-Common Metals* 61, 193 (1978).
- [174] T. Hihara and E. Hirahara, Nuclear magnetic resonance in ferromagnetic MnB , *Journal of the Physical Society of Japan* 20, 873 (1965).
- [175] S. Khmelevskiy, J. Redinger, A. Shick, and P. Mohn, [One-dimensional magnetism in one-dimensional metallic chains in bulk \$\text{MnB}_4\$](#) , (2013).
- [176] H. Gou, A. A. Tsirlin, E. Bykova, A. M. Abakumov, G. Van Tendeloo, A. Richter, S. V. Ovsyannikov, A. V. Kurnosov, D. M. Trots, Z. Konôpková, H.-P. Liermann, L. Dubrovinsky, and N. Dubrovinskaya, Peierls distortion, magnetism, and high hardness of manganese tetraboride, *Physical Review B* 89, 064108 (2014).
- [177] S. Neov and E. Legrand, Neutron diffraction study of the magnetic structure of Mn_3B_4 , *Physica Status Solidi (b)* 49, 589 (1972).
- [178] T. Ishii, M. Shimada, M. Koizumi, T. Sakakibara, and M. Date, Magnetic properties of Mn_3B_4 under high magnetic field, *Solid State Communications* 51, 103 (1984).
- [179] M. Kasaya, T. Hihara, and Y. Kōi, Magnetic susceptibility of single crystal Mn_3B_4 , *Journal of the Physical Society of Japan* 30, 286 (1971).
- [180] H. Hirota and A. Yanase, Magnetic properties of Mn_3B_4 , *Journal of the Physical Society of Japan* 20, 1596 (1965).
- [181] H. Hirota and A. Yanase, Magnetic properties of $\text{Mn}_{3-x}\text{Ni}_x\text{B}_4$ and $\text{Mn}_{3-x}\text{Co}_x\text{B}_4$, *Journal of the Physical Society of Japan* 21, 433 (1966).
- [182] L. Castelliz, Über eine Mischkristallreihe zwischen zwei ternären Vertretern des $C1$ -Typs, *Monatshefte für Chemie und verwandte Teile anderer Wissenschaften* 83, 1314 (1952).
- [183] H. Nowotny and B. Glatzl, Neue Vertreter ternärer Verbindungen mit $C1$ -Struktur, *Monatshefte für Chemie und verwandte Teile anderer Wissenschaften* 83, 237 (1952).

-
- [184] J. Boeuf, C. Pfeiderer, and A. Faißt, Low-temperature properties of the semi-Heusler compound CuMnSb, *Physical Review B* 74, 024428 (2006).
- [185] R. Helmholdt, R. Groot, F. Mueller, P. Engen, and K. Buschow, Magnetic and crystallographic properties of several $C1_b$ type Heusler compounds, *Journal of Magnetism and Magnetic Materials* 43 (1984).
- [186] R. H. Forster, G. B. Johnston, and D. A. Wheeler, Studies of the Heusler alloys - III. The antiferromagnetic phase in the Cu-Mn-Sb system, *Journal of Physics and Chemistry of Solids* 29, 855 (1968).
- [187] S. M. Podgornykh, S. V. Streltsov, V. A. Kazantsev, and E. I. Shreder, Heat capacity of Heusler alloys: Ferromagnetic Ni₂MnSb, Ni₂MnSn, NiMnSb and antiferromagnetic CuMnSb, *Journal of Magnetism and Magnetic Materials* 311, 530 (2007).
- [188] T. Jeong, R. Weht, and W. E. Pickett, Semimetallic antiferromagnetism in the half-Heusler compound CuMnSb, *Physical Review B* 71, 184103 (2005).
- [189] M. Doerr, J. Boeuf, C. Pfeiderer, M. Rotter, N. Kozlova, D. Eckert, P. Kersch, K.-H. Müller, and M. Loewenhaupt, Search for half-metallic antiferromagnetism using pulsed magnetic fields: experimental investigation of Mn₃Si, CuMnSb and PdMnTe, *Physica B* 346-347, 137 (2004).
- [190] C. Pfeiderer, Are Mn₃Si and CuMnSb antiferromagnetic half-metals? *Physica B* 329-333, 1085 (2003).
- [191] I. Galanakis, E. Şaşıoğlu, and K. Özdoğan, Magnetic phase transition in half-metallic CoMnSb and NiMnSb semi-Heusler alloys upon Cu doping: First-principles calculations, *Physical Review B* 77, 214417 (2008).
- [192] W. Schreiner and D. Brandão, Electrical resistivity of the $C1_b$ alloy CuMnSb, *Solid State Communications* 43, 463 (1982).
- [193] M. J. Otto, R. A. M. van Woerden, P. J. van der Valk, J. Wijngaard, C. F. van Bruggen, C. Haas, and K. H. J. Buschow, Half-metallic ferromagnets. I. Structure and magnetic properties of NiMnSb and related inter-metallic compounds, *Journal of Physics: Condensed Matter* 1, 2341 (1989).
- [194] M. M. Kirillova, A. A. Makhnev, E. I. Shreder, V. P. Dyakina, and N. B. Gorina, Interband optical absorption and plasma effects in half-metallic XMnY ferromagnets, *Physica Status Solidi (b)* 187, 231 (1995).
- [195] S. M. Podgornykh, V. A. Kazantsev, and E. I. Shreder, Thermal expansion of Heusler alloys NiMnSb, CuMnSb, and Ni₂MnSb, *Fizika Metallov I Metallovedenie* 86, 69 (1998).

bibliography

- [196] F. Maca, J. Mašek, O. Stelmakhovych, X. Martı, H. Reichlova, K. Uhlıřova, P. Beran, P. Wadley, V. Novak, and T. Jungwirth, Room-temperature antiferromagnetism in CuMnAs, *Journal of Magnetism and Magnetic Materials* **324**, 1606 (2012).
- [197] F. Maca, J. Kudrnovsky, V. Drchal, I. Turek, O. Stelmakhovych, P. Beran, A. Llobet, and X. Marti, Defect-induced magnetic structure of CuMnSb, (2016), [arXiv:1606.04238 \[cond-mat.mtrl-sci\]](https://arxiv.org/abs/1606.04238) .
- [198] D. Orgassa, H. Fujiwara, T. C. Schulthess, and W. H. Butler, First-principles calculation of the effect of atomic disorder on the electronic structure of the half-metallic ferromagnet NiMnSb, *Physical Review B* **60**, 13237 (1999).
- [199] Y. Miura, K. Nagao, and M. Shirai, Atomic disorder effects on half-metallicity of the full-Heusler alloys $\text{Co}_2\text{Cr}_{1-x}\text{Fe}_x\text{Al}$: A first-principles study, *Physical Review B* **69**, 144413 (2004).
- [200] S. Picozzi, A. Continenza, and A. J. Freeman, Role of structural defects on the half-metallic character of Co_2MnGe and Co_2MnSi Heusler alloys, *Physical Review B* **69**, 094423 (2004).
- [201] T. Graf, C. Felser, and S. S. Parkin, Simple rules for the understanding of Heusler compounds, *Progress in Solid State Chemistry* **39**, 1 (2011).
- [202] R. P. Smith, M. Sutherland, G. G. Lonzarich, S. S. Saxena, N. Kimura, S. Takashima, M. Nohara, and H. Takagi, Marginal breakdown of the Fermi-liquid state on the border of metallic ferromagnetism, *Nature* **455**, 1220 (2008).
- [203] T. Chatterji, Magnetic structures, in *Neutron Scattering from Magnetic Materials*, edited by T. Chatterji (Elsevier Science, Amsterdam, 2006) Chap. 2, pp. 25 – 91.